Paleomagnetism and Geochemistry of Basalts in the North American Cordillera, Davis Strait, and Antarctica

Thesis by

Joseph Anthony Biasi

In Partial Fulfillment of the Requirements for

the Degree of

Doctor of Philosophy

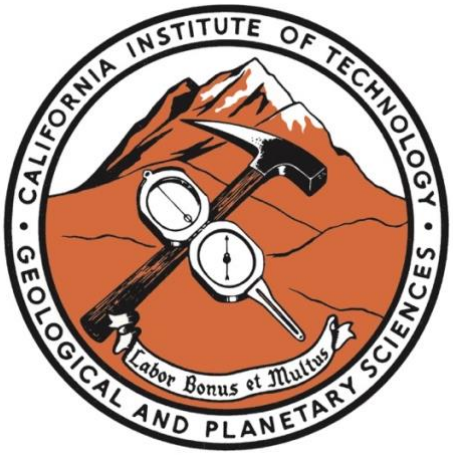

CALIFORNIA INSTITUTE OF TECHNOLOGY

Pasadena, California

2021

(Defended May 20, 2021)

Joseph Anthony Biasi
ORCID: 0000-0003-1196-7877

ACKNOWLEDGEMENTS

In addition to acknowledgements in each chapter, I'd like to show some additional thankfulness here.

Firstly, I want to thank my wife Madeline Lewis for her support and patience over many years, many long days of lab work, and many long absences during fieldwork.

I'd also like to thank my advisors: Paul Asimow, Claire Bucholz, and Joe Kirschvink, for their intellectual guidance, financial support, and for answering many questions over the last six years.

Hard work alone did not bring me to this point. Coincidence, circumstance, and the help of others were major factors in my life. To properly thank all of the friends, enemies, acquaintances, strangers, collaborators, field assistants, co-authors, teachers, professors, and family that have helped me reach this point would be impossible. Therefore, I will express my gratitude all at once:

Thank you, may you each get everything that you deserve.

ABSTRACT

Chapter 1 is an introduction to the thesis and contains a brief summary on how the chapters relate to each other.

In Chapter 2, we present new whole-rock geochemical data from the Brooks Range Ophiolite (BRO) together with new mineral chemistry data from the BRO, South Sandwich forearc, Izu-Bonin forearc, and Hess Deep. The analyses reveal that the BRO was most likely created in a forearc setting. We show that this tectonic classification requires the Brookian orogeny to begin at ~163-169 Ma.

In Chapter 3, we use a combination of paleomagnetic data and thermal modeling to create a magnetic geothermometer (MGT) that can constrain the active transport lifetime of magmatic conduits and igneous intrusions. We apply the MGT technique to eight feeder dikes of the Columbia River basalts (CRB), demonstrating that some dike segments may have been active for less than two weeks, while other segments may have been active for several years. Results suggest that eruption rates, localized spatially along strike of dike segments, were as high as 1–8 km^3 day^{-1}. These results help contextualize field evidence for contrasting CRB eruption durations, and suggest a pathway for constraining the tempo of global flood basalt magmatism that is beyond the resolution of geochronology.

In Chapter 4, we present new stratigraphic and paleomagnetic data from Paleocene flood basalts on Baffin Island. This study focuses on new data from 38 paleomagnetic sites. The average pole does not overlap with the expected pole for a stable North American site at 60 Ma, suggesting that the eruptive sequence at Baffin was emplaced in less time than needed to ‘average out’ secular variation. Secular variation paths generated by our data, combined with an expected rate of secular variation, are used to calculate the eruptive

tempo of lava flow sequences. We find a total eruption duration of ~1.7 kyr and average eruption interval of ~22 years per flow for the thickest sequence of exposed lavas. It appears that the entire package of volcanic deposits was emplaced in a relatively short 'burst' of activity, which has also been inferred at similar deposits in western Greenland. We estimate the total volume of Paleocene Baffin lavas to be 176 km^3. When combined with the ~1.7 kyr eruption duration estimate, this implies an average eruption rate of ~0.1 $km^3\ yr^{-1}$, which is greater than rates found in West Greenland but less than larger flood basalts that are associated with mass extinctions.

In Chapter 5, we present new paleomagnetic and paleointensity data from the James Ross Island volcanic group, located on the Antarctic Peninsula. We collected 251 samples from 31 sites, spanning 0.99 – 6.8 Ma in age, and include positive fold, conglomerate, and baked contact tests. Alternating-field and thermal demagnetization of these samples yields an average pole of -87.7º, 271.1º, α95=7º. When combined with preexisting data from an earlier study on James Ross Island and two studies from Deception Island, we present a revised paleomagnetic pole of -87.5º, 025º, α95=3.6º for the Antarctic Peninsula over the last ~5 Ma. In addition, the C2r/C2n transition may have been recorded at a site on JRI, and further geochronological and paleomagnetic study of these units will refine the age of this reversal. Finally, paleointensity data from three methods (Thellier-Thellier, pseudo-Thellier, and Tsunakawa-Shaw) were collected from all sites. The Thellier-Thellier method had low yields and produced unreliable data, likely due to sample alteration during heating. Results from the Tsunakawa-Shaw and pseudo-Thellier methods were more consistent, and we found average paleointensities of 35 and 65 μT at two sites.

PUBLISHED CONTENT AND CONTRIBUTIONS

Biasi, J., Asimow, P., and Harris, R., 2020, Tectonochemistry of the Brooks Range Ophiolite, Alaska: Lithosphere, v. 2020, doi:10.2113/2020/7866789.

TABLE OF CONTENTS

LIST OF ILLUSTRATIONS AND/OR TABLES

Chapter 4: Baffin Island *Page*

Chapter 1

Introduction

Each of the chapters in this thesis are focused on large quantities of mafic material. Chapter 2 focuses on the geochemistry of the Brooks Range Ophiolite, which is possibly the largest ophiolite in the western hemisphere. Chapter 3 shows how paleomagnetic data can be used to determine the duration of individual flood basalt eruptions, using the Columbia River basalts as a test-case. Chapter 4 focuses on the tempo of flood basalt eruptions, using the Paleocene flood basalts of Baffin Island. Finally, Chapter 5 explores the paleomagnetic record at James Ross Island, the largest volcano in Antarctica.

The importance of large volcanic events may not be immediately apparent. They are rather uncommon compared to 'normal' volcanic events and their magnitude is difficult to understand or even conceptualize in many cases. However, volcanic phenomena have repeatedly changed the course of human history and the history of life on this planet.

For example, the year 536 C.E. is often described as the 'worst year to be alive' due to the sudden onset of a volcanic winter that year, which caused widespread famine, war, plague, and civilizational collapse (Gibbons, 2018). However, 536 C.E. pales in comparison to much larger volcanic events, such as flood basalts. Such events are highly correlated with mass extinctions, ocean anoxic events, and other climatic shifts (Clapham and Renne, 2019). Flood basalts have shaped the diversity and abundance of life on earth in profound ways, yet many aspects of these events remain poorly understood. This work aims to advance our understanding of volcanic and igneous processes, and by extension, advance our growing awareness that life overall is very resilient, even if individual life forms like ourselves are very fragile.

References

Clapham, M.E., and Renne, P.R., 2019, Flood basalts and mass extinctions: Annual Review of Earth and Planetary Sciences, v. 47, p. 275–303, doi:10.1146/annurev-earth-053018-060136.

Gibbons, A., 2018, Eruption made 536 ‘the worst year to be alive’: Science, v. 362, p. 733, doi:10.1126/science.362.6416.733.

Chapter 2

Tectono-Chemistry of the Brooks Range Ophiolite, Alaska

Originally published in: Biasi, J., Asimow, P., and Harris, R., 2020, Tectonochemistry of the Brooks Range Ophiolite, Alaska: Lithosphere, v. 2020, doi:10.2113/2020/7866789.

ABSTRACT

We present new whole-rock geochemical data from the Brooks Range ophiolite (BRO) together with new mineral chemistry data from the BRO, South Sandwich forearc, Izu-Bonin forearc, and Hess Deep. The analyses reveal that the BRO was most likely created in a forearc setting. We show that this tectonic classification requires the Brookian orogeny to begin at ~163-169 Ma.

The middle-Jurassic BRO contains abundant gabbros and other intrusive rocks that are geochemically similar to lithologies found in other forearc settings. Based on major, minor, and trace element geochemistry, we conclude that the BRO has clear signals of a subduction-related origin. High-precision olivine data from the BRO have a forearc signature, with possible geochemical input from a nearby arc.

The Koyukuk terrane lies to the south of the Brooks Range; previous studies have concluded that the BRO is the forearc remnant of this arc-related terrane. These studies also conclude that collision between the Koyukuk arc and the Arctic Alaska continental margin marks the beginning of the Brookian orogeny. Since the BRO is a forearc ophiolite, the collision between the Koyukuk arc and the continental margin must have coincided with obduction of the BRO. Previously determined $^{40}Ar/^{39}Ar$ ages from the BRO's metamorphic sole yield an obduction age of 163-169 Ma. Since the same collisional event that obducts the BRO also is responsible for the Brookian orogeny, we conclude that the BRO's obduction age of ~163-169 Ma marks the beginning of this orogenic event.

1. Introduction

Subduction is one of the defining processes that allows plate tectonics to operate and thereby determines the whole character of our planet. It is now well established that the majority of ophiolites are produced via subduction-related processes (Wakabayashi and Dilek, 2003). Although our understanding of supra-subduction zone (SSZ) ophiolites has advanced greatly over the last 30 years — due in part to ocean-drilling campaigns (e.g., Pearce et al., 2015; Reagan et al., 2017) — many aspects of these ophiolites are still poorly understood. This is especially true when it comes to processes occurring below the extrusive layer.

In the North American Cordillera, most ophiolites have experienced complex syn- and post-emplacement deformation and alteration (Whattam and Stern, 2011). This greatly complicates their geochemical characterization, which is required to identify the tectonic setting in which they are generated (Pearce, 2014). Previous studies of *in situ* forearcs, arcs, and back-arcs have mostly focused on the extrusive layer (pillow basalts and sheeted dikes), as the extrusive section is readily sampled by seafloor drilling and features characteristic rock types such as boninites and forearc basalts (e.g., Reagan et al., 2010). It therefore follows that most tectono-chemical indicators for ophiolites and seafloor basalts have been developed with the extrusive layer in mind (Pearce, 2014).

In this study, we present novel geochemical data from the Brooks Range ophiolite, South Sandwich forearc, Izu-Bonin forearc, and Hess Deep. With these data, we show that the *intrusive* section of the Brooks Range ophiolite (BRO) (Fig. 1) in northern Alaska preserves a forearc geochemical signature. We then use the forearc model of the BRO to resolve several outstanding issues regarding the Mesozoic tectonic history of northern

Alaska. Notably, the tectonic history of the BRO requires that the Brookian orogeny begin at ~163-169 Ma, when the BRO is obducted onto the Arctic Alaska margin.

2. Geological Background

2.1 Brooks Range Ophiolite (BRO)

The Brooks Range ophiolite (BRO) lies in northwestern Alaska (Fig. 1), and is likely middle-Jurassic in age (Harris, 2004). As it is currently (and conservatively) mapped, the BRO covers 1800 km^2. It is composed of six klippe-like massifs. Most studies have focused on three of these massifs (Misheguk, Avan, and Siniktanneyak) (Harris, 2004). Complete ophiolitic sections (from metamorphic sole to pillow basalts/chert) can be found in these three massifs. Glacial erosion of the ophiolite bodies provides nearly 100% exposure in many places.

Only a handful of papers have been published on the BRO, and most studies were published pre-2000. Early reconnaissance-level studies of the western Brooks Range produced various models for the tectonic evolution of the BRO (Martin, 1970; Tailleur, 1970; Roeder and Mull, 1978; Churkin et al., 1979; Gealey, 1980; Moores, 1982; Mayfield et al., 1988; Box and Patton, 1989; Miller and Hudson, 1991; Karl, 1992; Wirth and Bird, 1992). The most recent and thorough work on the BRO was done in the late 1980s and 1990s, and focused mostly on the Siniktanneyak and Misheguk massifs (Harris, 1992, 1995, 1998, 2004; Bickerstaff, 1994). This work mainly involved structural mapping, petrology, and age analysis. Some major and trace element geochemical data were also reported. Hornblende $^{40}Ar/^{39}Ar$ plateau ages were reported for gabbro and metamorphic

sole rocks from the Avan, Asik, Misheguk, and Siniktanneyak massifs. The conclusions most relevant to this study are as follows:

1. The Brooks Range ophiolite contains a complete section of oceanic lithosphere composed, from bottom to top, of a metamorphic sole with partial melts, dunitic and harzburgitic peridotite (serpentinized near the sole but otherwise pristine), transitional ultramafic cumulates (petrologic Moho), thick sections (~4 km) of layered gabbro, massive gabbro, intermediate intrusives, ultramafic/mafic late-stage intrusives, sheeted dikes, pillow basalts, and sedimentary deposits (Harris, 2004).
2. The geochemistry of the BRO is most consistent with formation in a SSZ setting, followed by obduction during arc-continent collision and incorporation into the Brooks Range fold-and-thrust belt (Harris, 1995).
3. The metamorphic sole beneath the BRO is composed mostly of Angayucham (Copter Peak) basalt and intercalated sedimentary rocks. The geochemistry and age of these basalts preclude any genetic relations between them and the BRO (Harris, 1998).
4. The BRO is at the structurally highest position in the Brooks Range, and strain was localized in the serpentinized structural base of the ophiolite and its metamorphic sole during emplacement. Due to these factors, the BRO has remained mostly intact and was subjected only to typical seafloor deformation and alteration (Harris, 1998).

Previous studies suggest that the BRO is comprised of supra-subduction zone (SSZ) lithosphere associated with early development of the Koyukuk Arc, a fossil arc terrane situated today south of the Brooks range (Fig. 1) (Harris, 1998, e.g., 2004). Arc-continent collision between the Koyukuk Arc and the Arctic-Alaska continental margin probably led to obduction of the BRO (Harris, 1992, 1998; Moore et al., 2015).

$^{40}Ar/^{39}Ar$ plateau ages are interpreted to give overlapping cooling ages of 163-169 ± 5 Ma for both the BRO and its metamorphic sole (Wirth, 1991; Wirth et al., 1993; Harris, 2004). Such overlap is a common characteristic among SSZ ophiolites with a metamorphic sole (Harris, 1992). U-Pb zircon data from late-stage BRO melts yield an age of 170 ± 3 Ma (Moore et al., 1993). This age is within error of $^{40}Ar/^{39}Ar$ ages from BRO gabbro and the metamorphic sole (Harris, 2004). These geochronological constraints indicate that the BRO was obducted onto the Angayucham terrane shortly after formation. The BRO's quick obduction, combined with its structurally highest position in the Brooks Range, has allowed the ophiolite to remain only lightly serpentinized and avoid overprinting by post-obduction events that commonly affect other Cordilleran ophiolites.

2.2 Other Oceanic Rocks

Typically, all Mesozoic oceanic rocks within the Brooks Range are referred to as the Angayucham terrane (Silberling et al., 1994). This terrane grouping, however, is somewhat misleading. The BRO has a supra-subduction zone origin (Harris, 1995), while the structurally underlying basalts have an oceanic plateau/MORB affinity (Barker et al., 1988; Pallister et al., 1989; Harris, 1992; Karl, 1992). Some authors (e.g., Moore et al., 2015) have therefore divided the Angayucham terrane into the Misheguk Mountain Allochthon and the structurally underlying Copter Peak Allochthon. However, differences in age and geochemistry preclude any shared geologic history between these units prior to emplacement (Harris, 1998). Further complicating the issue, many oceanic rocks in interior Alaska are also referred to as the Angayucham terrane (Fig. 1) (Patton et al., 1994). Ideally, the Angayucham terrane would be split into an arc-related and MORB-related terrane to

reflect this. However, most areas of the Angayucham terrane lack sufficient geochemical and geochronological data for such a split to be viable, especially in the Alaskan interior.

For the purposes of this study, the Jurassic BRO and the rest of the Angayucham terrane are not the same, and therefore we will always refer to the green areas in Fig. 1b as 'Brooks Range Ophiolite (BRO)' and the structurally lower purple areas as 'Angayucham'. This distinction will be particularly relevant later in this paper.

Most of the initial mapping in the area was done via helicopter/aerial photography, and it is likely that large swaths of the BRO are incorrectly mapped as Angayucham, as discovered in the Siniktanneyak massif (Harris, 2004). The Angayucham terrane structurally underlies the BRO, but consists of similar lithologies (gabbro, pillow basalt, and chert). It locally makes up the BRO's metamorphic sole (Harris, 1992, 1998), and was emplaced synchronously with the BRO. In our estimation, the BRO *could* currently cover as much as 3600 km^2. This makes it one of the largest, best exposed, and most complete ophiolites in the Western Hemisphere, yet relatively understudied.

2.3 Tectonics of Northern Alaska

The tectonic evolution of northern Alaska remains controversial and a full review is beyond the scope of this work. A number of recent review papers cover the subject in detail (e.g., Pease, 2011; Shephard et al., 2013; Pease et al., 2014; Amato et al., 2015; Till, 2016). In brief, since the breakup of Pangea, the Arctic region has experienced a poorly constrained series of tectonic shifts, rotations, and subduction events. The end result is that the area is now surrounded by blocks of continental crust with similar pre-Mesozoic

histories, but divergent Mesozoic-Cenozoic histories (Kuznetsov, 2006; Dumoulin et al., 2011; Pease, 2011).

One of these lithospheric blocks contains the Brooks Range (Fig. 1). After initial mineral exploration in the 1960s and 1970s, little mapping has been done in the range, and it remains among the least studied areas in North America. This situation is primarily due to its remote location and short summers. The range has experienced a revival in research interest in the last 10 years or so. The Brooks Range itself is composed of several accreted terranes (Jones et al., 1987; Moore et al., 1994; Silberling et al., 1994), and is bordered by the Koyukuk Terrane to the south and the North Slope subterrane (Colville Basin) to the north (Fig. 1). Many of these terranes have experienced multiple metamorphic and deformational events, but it is clear that in the early Jurassic, the Brooks Range did not yet exist (Moore et al., 2015). Instead, northern Alaska was a south-facing (in present-day coordinates) passive continental margin (referred to as 'Arctic Alaska'), which transitioned into the Angayucham oceanic basin (Harris, 1992).

It is thought that an oceanic arc (likely the Koyukuk arc) collided with the passive continental margin to initiate the Brookian orogeny along a south dipping subduction zone (Harris, 1987, 1992; Moore et al., 1994, 2015; Till, 2016). This model is similar to the presently active collision of the Banda Arc with the passive continental margin of northern Australia (Harris, 1992, 2011). In this model, the arc is not related to the continental margin in any way before collision. Other interpretations suggest the Koyukuk arc was formed by northward subduction and was separated from Arctic Alaska by a (likely narrow) back-arc sea (Churkin et al., 1979; Miller and Hudson, 1991; Hoiland et al., 2018b; Miller et al., 2018). The narrow sea or back-arc model for the BRO purports that sometime in the

Jurassic or Cretaceous, the back-arc basin closed as the Koyukuk arc collided with Arctic Alaska.

Collision between the continental margin and the Koyukuk Arc marked the beginning of the Brookian orogeny (Moore et al., 1994; Nokleberg et al., 2000). This collision must have occurred sometime in the Early Cretaceous or Late Jurassic, based on geochronological studies of metamorphism in the Brooks Range (Till, 2016). Precisely dating the onset of Brookian orogenesis has been an elusive goal for decades. Metamorphic rocks associated with this event have been difficult to date due to extensive Cretaceous greenschist-facies overprinting of the original blueschist facies metamorphism (Till, 2016; Hoiland et al., 2018a). This metamorphic overprint is not unique to the Brooks Range. Many collisional belts yield metamorphic ages much younger than the early phases of associated ophiolite emplacement (e.g., Oman, Warren et al., 2005).

A foreland basin (Colville, Fig. 1) developed adjacent to the Brooks Range during orogenesis. Its lowest units consist of mélange with blocks of Angayucham terrane and Late Jurassic intermediate volcanics (Crane, 1987). Overlying the mélange are synorogenic deposits containing Jurassic detrital zircons (Cole et al., 1997; Moore et al., 2015) that likely originated from the BRO and underlying Angayucham terrane mafic rocks. This led Moore et al. (2015) to conclude that the BRO and portions of the underlying Angayucham terrane were emplaced within the Colville basin watershed during Late Jurassic arc-continent collision. The Yukon-Koyukuk Basin (YKB) (Fig. 1B) currently does not expose any deposits older than Albian (i.e., latest Early Cretaceous). These units contain mafic lithic fragments and detrital zircons from 160-260 Ma. Clasts from these units have variable island-arc affinities, and have led researchers to recently conclude that a Late

Triassic-Early Jurassic island arc was present in the area before the Albian (O'Brien et al., 2018). It is possible that these clasts are derived from pre-BRO arc terranes, which may not have been near the continental margin at the time they formed. It is clear that the lowermost clasts from Jurassic Brookian foreland strata were derived from a different source than the Albian sediments accumulated in the YKB (O'Brien et al., 2018).

Geochronological data from the Koyukuk Arc is sparse. The Koyukuk arc itself is dated via invertebrate fossils and the K-Ar method. On the basis of these fossil and isotopic ages, Box and Patton (1989) divided the history of the Koyukuk Arc into four stages. The oldest lithologies (Stage 1) consist of late Paleozoic-early Mesozoic pillow basalt, chert, serpentinite, and limestone. Stage 2 consists of middle-Jurassic plutonic rocks (intermediate-felsic). Stages 3 and 4 consist of intermediate-felsic volcanic rocks, volcaniclastic sedimentary rocks, and shallow-deep marine sedimentary rocks. Stages 3 and 4 sedimentary rocks are early Cretaceous in age (<145 Ma) (Harris et al., 1987; Box and Patton, 1989). Recent zircon ages from Koyukuk Arc plutonic rocks confirm that the arc was active during the Cretaceous (Hoiland et al., 2018a).

This study presents evidence that the BRO was created in a forearc setting, which is a refinement of its earlier classification as an SSZ ophiolite (Harris, 1995, 2004). We will use this finding to determine the age of onset of Brookian orogenesis and develop a coherent tectonic model of the orogeny (see discussion).

3. Methods

3.1 Fieldwork

Most samples used in this study were collected by R. A. Harris in 1986 and 1989 at Misheguk Massif (Fig. 1b). Field descriptions of all units, geologic maps of several massifs, and detailed cross sections can be found in Harris (2004) and will not be reiterated here. The most relevant field observations for this study are that sheeted dikes and pillow basalts associated with the BRO are relatively rare. Most of the ophiolite is composed of intrusive and mantle lithologies. The intrusive lithologies include layered gabbro, massive gabbro, and high-level intermediate intrusives. The mantle lithologies consist mostly of dunite with abundant chromite and blebs or screens of harzburgite. Out-of-sequence mafic/ultramafic intrusives and plagiogranites can be found in any part of the ophiolitic section.

Three samples were collected by Lyle Nelson and Betsy Friedlander of Teck Resources in 2017. These samples are all mantle rocks from the Iyokrok massif, which is a small and poorly exposed klippe of the BRO. The entire Iyokrok massif consists of mantle lithologies and appears to be folded in a similar fashion to other BRO massifs (Harris, 2004).

3.2 Whole-rock Geochemistry

New major oxide and minor element abundances were determined for 15 samples. Samples with minimal petrographic evidence of metamorphism or serpentinization and only minor seafloor alteration were chosen, representing the common rock types within the

BRO. All samples were analyzed using a Panalytical Zetium XRF system at the California Institute of Technology. Major and minor elements were analyzed using fused-glass beads. Following LOI determined at 1050 °C, samples were mixed with 9 times their weight in 66.67% $Li_2B_4O_7$-32.83% $LiBO_2$-0.50% LiI flux and fused at 1200 °C.

We also determined rare-earth element (REE) concentrations in 15 samples using an Agilent Technologies 8800 triple quadrupole ICP-MS. Chips (~25 mg) of the beads used for XRF analysis were dissolved in 50 mL polypropylene containers in 2 mL of hot (99 °C) 3:1 nitric and hydrofluoric acid for 8 hours and diluted to 30 mL total volume with distilled water. To control for quality, four USGS standards (AGV-2, BCR-2, RGM-2, and DTS-2b) were included as unknowns. Whole-rock geochemical data (including detection limits and standards run as unknowns) are available in the Supplemental Information (Table S2).

3.3 Mineral Chemistry

Mineralogy and mineral chemistry were characterized for 33 polished sections. These sections were selected using the same criteria as the whole-rock samples. We employed a combination of Scanning Electron Microscopy (SEM) with Energy Dispersive X-ray Spectroscopy (EDS) and Electron Microprobe (EMP) analysis. Compositional maps were generated using SEM/EDS (Zeiss 1550 VP SEM operated at 15 kV, Oxford X-MAX Si-drift detector, Oxford AZTec software) to determine sample mineralogy, degree of serpentinization, and degree of metamorphism. EMP analyses (JEOL 8200 five-spectrometer instrument operated at 15 kV and 25 nA; synthetic and natural mineral and oxide standards; CITZAF data reduction) were used to determine the major-element

chemistry of individual phases in each sample. High-precision analyses of olivine grains (JEOL 8200 five-spectrometer instrument operated at 20 kV and 300 nA; synthetic mineral and oxide standards; CITZAF data reduction, method of Sobolev et al. (2007)) were also performed. During high-precision analysis, a San Carlos olivine crystal was analyzed before and after every sample and used as a drift correction standard. Mineral chemistry data is provided in the Supplemental Information (Tables S3, S4, S5, and S6).

4. Results

4.1 Samples and context

We performed new analyses on 12 whole-rock samples collected by R. Harris at Misheguk massif (Fig. 1b). Note that the samples were chosen to represent the wide array of rock types found in the BRO, and this translates to a wide array of compositions. Only one sample (a sheeted dike) was taken from the extrusive layer. The remaining sample set is from the intrusive section of the BRO. Misheguk is the largest massif in the BRO. The mantle section contains dunite, peridotite, transitional ultramafics, and late-stage ultramafic intrusions. The large crustal section contains layered gabbro (4 km stratigraphic thickness), massive gabbro, and high-level intermediate intrusives. See Harris (2004) for more detailed descriptions. We also analyzed 3 new ultramafic samples (whole-rock and thick-section) from the Iyokrok massif (Fig. 1b). Whole-rock analyses of samples previously published from Siniktanneyak, Misheguk, and Avan massifs are also used in the study (Bickerstaff, 1994; Harris, 1995). In addition, 22 thin sections from Harris' 1986 and 1989 sample sets and 3 thick sections from Iyokrok were analyzed for mineral

chemistry. Finally, 8 thin sections from the IBM forearc, South Sandwich forearc, and Hess Deep were analyzed using the high-precision olivine protocol described in the previous section. All mineral chemistry presented in this study is new.

4.2 Major, Minor, and Trace Elements

All new whole-rock oxide and elemental abundance data are reported in Table S2. The majority of discrimination diagrams typically used to assign the tectonic environment of igneous samples were developed for extrusive rocks. However, Baziotis et al. (2014) showed that many of the relative trace element abundance characteristics of extrusive rocks are inherited from their parent liquids faithfully enough to apply tectonic discrimination diagrams, even though absolute concentrations of incompatible elements are lower in samples containing some cumulate component. Figure 2 shows new whole-rock data alongside published analyses by Harris (1995) and Bickerstaff (1994) in selected tectonic discrimination diagrams.

Samples from the crustal section of the BRO are shown in Figs. 2a and 2b. Samples that are clearly cumulates (layered gabbro, anorthosite, etc.) are excluded from these plots but reported in Table S2. Figure 2a makes use of two immobile elements for tectonic discrimination. All samples in this plot contain <55% SiO_2 to avoid evolved/cumulate samples. Many samples from Bickerstaff (1994) do not have SiO_2 data and are not plotted here. Results show a range from boninitic to MORB-affinity. Figure 2b also makes use of immobile elements and shows some boninitic samples in the dataset. The majority of crustal samples are not boninitic. Figures 2c & 2d show whole-rock geochemical results from the mantle section of the BRO. Fig. 2c shows that these samples can be divided into

two groups: cpx-poor (harzburgite, dunite) and cpx-bearing (wehrlite, pyroxenite, etc.). Finally, most harzburgites and dunites plot within the forearc peridotite field in Fig. 2d, though some samples may have a different tectonic affinity.

4.3 Rare-Earth Elements

New whole-rock trace element data are reported in Table S2. We analyzed a wide range of rock types from the BRO and so a wide range of trace-element patterns are reported (Fig. 3). Note that many ultramafic samples do not have sufficient trace element concentrations to be detected and therefore are not plotted here. Most samples have lower REE concentrations than N-MORB, regardless of rock type. Samples shown in Fig. 3a have LREE/HREE >1 or strong Eu-anomalies. Samples in Fig. 3b have LREE/HREE ≅ 1 or less. REE data from Harris (1995) are also reported. Any gaps in the data indicate an element that was below the detection limit or not measured.

Samples in Fig. 3a generally show negative REE slopes after N-MORB normalization. These consist mostly of plagioclase-bearing rocks. Samples with strong depletion of HREEs and positive Eu anomalies are probably plagioclase cumulates. This is certainly the case for sample 114 (anorthosite). The remaining samples in Fig. 3a show smooth and monotonic REE patterns without prominent Eu-anomalies. The three samples with LREE and LREE/HREE higher than MORB are plausibly liquid or near-liquid compositions derived from a source more enriched than the MORB source or by smaller degrees of melting than average N-MORB. The two hornblende gabbros with overall REE lower than MORB but LREE/HREE higher than MORB may be derived from similar

liquids, but likely contain abundant cumulate clinopyroxene that dilutes their overall REE concentrations.

Samples in Fig 3b show concave-down MORB-normalized REE patterns, with flat MREEs and small to significant depletion in LREE relative to N-MORB. The only volcanic sample of the series (117, sheeted dike) is part of this group, although it differs from the others in having MREE/HREE lower than MORB, whereas all the others have MREE/HREE greater than MORB. Note that the sheeted dike sample has similar REE concentrations to cumulates in the sample suite (pyroxenite, wehrlite, etc.), despite being a frozen liquid. The sheeted dike sample must be from a depleted source, a high degree of melting, or both.

Fig. 3c shows additional N-MORB normalized trace element abundances. Concentrations determined by ICP-MS are shown for all elements except for XRF determinations of K, P, and Ti. Notable features of the dataset include clear negative Nb-Ta anomalies, positive Pb anomalies, and highly variable Ba and Sr concentrations. A number of samples have negative Zr-Hf anomalies. The patterns clearly indicate a subduction influence in all of these samples (Pearce and Stern, 2006), though the strength of the subduction signal varies.

Sample 117, the sheeted dike, shows positive anomalies in Ba, K, Pb, and Sr; strong negative Nb-Ta anomaly; and MORB-normalized levels of Pr, Ce, and P similar to the HREEs. These signatures have all been associated with a subduction influence derived from a slab at relatively shallow levels (see Fig. 4 in Pearce & Stern (2006)). In contrast, sample 116 (gabbro) shows weaker subduction-input signals, despite being more enriched overall. This sample also shows higher levels of Pr, Ce, and P, compared to HREEs,

suggesting a mostly deep subduction component (Pearce and Stern, 2006). Its high concentrations of incompatible elements and smooth overall pattern indicates that 116 can be interpreted as a frozen liquid. The extended trace element pattern of sample 114 (anorthosite), with elevated Ba, confirms plagioclase accumulation in this sample. Other samples (106a, 104e, 118, and 139) show negative Ba anomalies; these are olivine-clinopyroxene cumulates that left Ba in the residual liquid. Finally, two likely cumulate samples (108b and 123c) presumably reflect a combination of plagioclase and mafic mineral accumulation.

Trace element data and petrography therefore indicate that two samples (sheeted dike 117 and gabbro 116) are likely frozen liquids whereas most other samples are (at least partially) cumulates. Of the frozen liquids, 117 shows evidence of a high extent of melting and a significant shallow subduction signal, while 116 shows evidence of a small degree of melting or enriched source and some deep subduction input. All remaining samples show some subduction signatures as well but are more difficult to interpret due to crystal accumulation. Finally, based on overlapping REE patterns, it is likely that the Harris (1995) samples also include a mixture of frozen liquids and cumulates. Harris (1995) did not report extended trace element data so this cannot be confirmed.

4.4 Mineral Chemistry

SEM/EDS compositional mapping shows that mantle rocks of the BRO contain olivine, chromite, clinopyroxene, orthopyroxene, and (in some samples) minor plagioclase. Large chromitite layers that include economically-viable abundances of platinum group elements can be found in the mantle section of the BRO (Foley et al., 1992). In the gabbro

and crustal rocks, plagioclase, clinopyroxene, minor orthopyroxene, minor amphibole, and minor olivine are present. Minor amounts of euhedral apatite are also present in some of the gabbro samples. See Table S1 for a partial list of observed phases in each sample.

Mineral Data collected via EMP are shown in Figs. 4, 5, 6, and 7. Clinopyroxene data from BRO mantle samples are shown in Fig. 4. There is considerable scatter in the data, probably due to a combination of fractional crystallization, partial melting, and other processes. This likely explains why several samples fall outside the fields of Pagé et al. (2008). Regardless, the data generally shows a mixture of forearc and abyssal affinities.

Spinel data from a variety of peridotites representing various tectonic settings are shown in Fig. 5. BRO spinel compositions vary widely, whereas most tectonic localities show more tightly clustered spinel compositions; only peridotite from oceanic arc settings show such a large range in a single locality (Fig. 5b, Aleutians, Lesser Antilles). Nevertheless, the overlap in spinel composition between the BRO and other settings (mid-ocean ridges, forearcs, back-arcs) makes it difficult to exclude any of these settings based on spinel compositions alone.

Combined spinel-olivine data is shown in Fig. 6. BRO samples with high spinel Cr# are similar to samples from forearc and arc settings (Fig. 6a, b). Mid-ocean ridge data also overlaps with some of the BRO data. BRO samples with low spinel Cr# do not significantly overlap with any of the tectonic settings presented here. These samples plot within the passive margin/abyssal peridotite field of Pearce et al. (2000). Some BRO samples plot outside the olivine-spinel mantle array, likely indicating that melt-rock reaction, fractional crystallization, or low-temperature re-equilibration may have lowered the Mg# of olivine and spinel in these samples (Zhang, 2005). One dunite outlier has

particularly low Cr# spinel. This sample is very spinel-rich and has a more complex origin than can be adequately captured by the plot.

High-current olivine data are presented in Fig. 7. These analyses make use of high EMP beam currents and long counting times to lower detection limits of trace elements (Al, Co, and Cr) and improve precision of minor elements (Ca, Mn, and Ni) in olivine. Fewer data from the literature are available due to the relative rarity of high-precision olivine analyses. Data for olivine from the BRO, Izu-Bonin forearc (Leg 125), South Sandwich forearc, and Hess Deep were gathered in this study. Other data in Fig. 7 are compiled from the literature (see figure caption). The four plots in Fig. 7 were chosen because, among chemical signatures in olivine, these elements offer the best discrimination among tectonic settings. Figs. 7a and 7b show that olivine in the BRO harzburgite samples and in one dunite overlaps with arc/forearc data. Olivine from the BRO wehrlite sample and the other two dunite samples differ in at least one of the plotted elements from olivine in peridotites from any other tectonic setting. These samples evidently have anomalous histories of fractionation or melt-rock reaction that make them inappropriate for comparison to residual peridotites. BRO olivine, especially from the harzburgite and the "normal" dunite, has notably low Cr and Al (Table S4). This distinct feature is shared by other forearc samples in this study (Figs. 7c and 7d) and is, based on the available data, a feature uniquely associated with forearc peridotite. All other samples, including Hess Deep samples analyzed in this study, show higher levels of Cr and Al. This may be explained by high degrees of melt extraction and the persistent presence of residual chromium-spinel. High Cr# spinel is a prominent accessory phase in mantle rocks of the BRO, IBM forearc, S. Sandwich forearc, and Bismarck forearc (Parkinson and Pearce, 1998; Pearce et al.,

2000; McInnes et al., 2001). Low Ca-contents might be best explained by elevated magmatic water in the subduction-influenced system compared to the MORB system; water activity acts to decrease the partition coefficient for Ca in olivine and promote efficient Ca extraction from these residual rocks (Gavrilenko et al., 2016).

5. Discussion

5.1 Tectonic Setting

Previous studies of the BRO have concluded that it was created in an SSZ environment (Harris, 1995, 2004). The data presented above clearly supports this conclusion. Other tectonic environments such as mid-ocean ridges can be immediately ruled out based on the arc-like trace-element patterns (Fig. 3), whole rock data from both the crust and mantle sections of the BRO (Fig. 2a, d), and the high-precision olivine data (Fig. 7c, d). The assignment of the BRO to a SSZ setting has very high confidence.

Distinguishing between different SSZ settings is more difficult. Arc, forearc, and back-arc geochemical signatures often overlap. Notably, arc settings with complex tectonic histories can have signatures of multiple SSZ environments in co-temporal rocks (e.g., Todd et al., 2012). This is likely due to inheritance of geochemical signals from previous tectonic settings in the same area.

Nevertheless, the available geochemical data suggests that the BRO was created in a forearc setting. High-precision olivine analyses from the BRO uniquely overlap with forearc peridotites (Fig. 7). Whole-rock data from the mantle section of the BRO also show a predominantly forearc signature (Fig. 2d). Much of the spinel and olivine chemistry (Figs.

5, 6) also agrees with a forearc setting. However, some whole-rock and mineral compositions lie outside the known range of forearc samples (Figs. 2d, 4, 6b, 7). These data are from complex plutonic rocks with possible histories of crystal accumulation, melt-rock reaction, or late re-equilibration. They do not consistently match residual or volcanic samples from any other tectonic setting either. These samples reveal the hazards of working with intrusive crustal samples and atypical mantle samples; they would likely have been excluded from a study of a more accessible and better-sampled locality. Given the small total number of samples available from the BRO, we analyzed these samples anyway and it is remarkable that the tectonic setting is evident in our overall dataset despite the complexity of these rocks. Given the strong subduction signals in the trace-element data (Fig. 3), we cannot rule out a history of arc or back-arc influence on the mantle samples that later become incorporated in the BRO. Another possibility is that the forearc setting of the BRO gradually evolved into an oceanic arc setting prior to obduction of the ophiolite.

5.2 Possible Subduction Initiation

The only extrusive sample in the new dataset, 117 (sheeted dike), has a boninitic composition (Fig. 2d, Table S2a). In the Phanerozoic, boninites are found predominantly in subduction-initiation (SI) settings, but have been found in intraplate settings as well (Pearce and Reagan, 2019). As outlined by previous authors (Whattam and Stern, 2011; Stern et al., 2012), a SI setting can be identified by a temporal evolution from initially MORB-like lavas to boninites to arc-like lavas. The BRO lacks a sufficiently thick and stratigraphically coherent extrusive section to make this identification. The trace-element composition of the sheeted dike (117) has a signature of a shallow subduction component

(Fig. 3c). This is a characteristic feature of trench-proximal magmas, while deeper subduction signals are found in magmas farther from the trench (arc and back-arc) (Pearce and Stern, 2006). The combination of a boninitic composition and shallow subduction component make it difficult to argue for any tectonic origin for 117 other than subduction initiation. Other samples have boninitic compositions, but we do not have accompanying trace-element data for these samples. However, a small number of boninitic samples are not diagnostic of the entire ophiolite, and more samples are needed to make a definitive case for subduction initiation. Another sample, 116 (gabbro), is likely a frozen liquid that preserves both deep and shallow subduction signatures. This is not unusual, given the mix of forearc and other arc signals seen in the mineral and whole-rock chemistry of the BRO. Conceivably sample 116 represents a later stage than sample 117 in the evolution of the subduction system.

Based on the geochemical data presented here, we conclude that the BRO was created in a forearc setting. Although there is some suggestion from the data that the BRO preserves a subduction initiation event, we cannot definitively rule out other formation scenarios such as slab rollback. Other geologic evidence that has already been collected on the BRO is consistent with either origin for these rocks and does not greatly affect the subsequent tectonic history (see below).

5.3 Genesis of the BRO

5.3.1 Existing Tectonic Constraints — The new data presented here suggest that the BRO formed in a forearc setting. This interpretation is in agreement with previous work that

classified the BRO as a supra-subduction zone ophiolite (Harris, 1995, 2004). The earlier classification was not precise enough to delineate between different supra-subduction zone settings for the BRO. Its new classification as a forearc ophiolite allows us to tie in the BRO's genesis with specific tectonic events.

The tectonic history of northern/interior Alaska is poorly constrained. This is partly due to difficult access and lack of exposure. Any tectonic history will inevitably involve simplifications of existing constraints. For the tectonic history of the BRO, the most important constraints from various studies are:

1. This study yields several lines of geochemical evidence documenting that the BRO formed in a forearc setting. A zircon age of 170 ± 3 Ma was determined from a late-stage plagiogranite in the BRO (Moore et al., 1993) and likely represents a minimum age for the BRO. Overlapping $^{40}Ar/^{39}Ar$ ages from BRO gabbro and the metamorphic sole (Harris, 2004), together with documented amphibolite facies metamorphism and partial melting of the sole (Harris, 1998), suggest that the BRO was still young and hot during emplacement at ~165 Ma.
2. Sparse geochronological data exists for the Koyukuk Arc (currently to the south of the BRO). On the basis of invertebrate fossils and K-Ar ages (Box and Patton, 1989) from igneous samples, the arc was active in the early-middle Jurassic. Voluminous felsic magmatism began around 150 Ma in the arc (Box and Patton, 1989; Hoiland et al., 2018a); the timing and extent of magmatism prior to this is not well constrained.
3. The lowermost units of the Brookian foreland (Colville) basin contain abundant BRO-age clasts and detrital zircons, suggesting that these units were partially sourced from the BRO (Moore et al., 2015).

4. The lowermost exposed units of the Yukon-Koyukuk basin (YKB) contain comparatively few BRO-age detrital zircons. Instead they contain abundant mafic clasts that mostly predate the BRO (early Jurassic to Triassic). This is interpreted as evidence for an arc terrane in this area during this time (O'Brien et al., 2018).

5.3.2 Mafic Detritus, relation to the BRO — A recent detrital zircon study of 112 Ma and younger units in the NW corner of the Yukon-Koyukuk basin (YKB, Fig. 1) found abundant mafic detritus and cobbles in the lowermost exposed sedimentary units (Type 1 of O'Brien et al. (2018)). These sediments have an arc-like signature and a prominent population of 160-240 Ma detrital zircons with juvenile εHf signatures. In addition, the sediments have abundant detrital Cr-spinel, some of which shows a forearc signature. This led O'Brien et al. (2018) to conclude that a Triassic-Jurassic juvenile arc terrane must have supplied this mafic-ultramafic material to the YKB. They further conclude that the Angayucham terrane (including the BRO) is the modern remnant of this arc. Finally, they exclude the Koyukuk Arc as a possible source of these sediments, due to a lack of exposed lithologies of the appropriate age.

While this interpretation is consistent with their data, it is not consistent with other geologic evidence from the BRO and Angayucham terrane. The eroding BRO was cut off from the YKB by a drainage divide at >113 Ma, and instead eroded into the Colville basin (Moore et al., 2015; O'Brien et al., 2018). Although the BRO's minimum age of 165-170 Ma is within the range of detrital zircons found by O'Brien (2018), the ophiolite was still young and hot during emplacement (Harris, 2004). Therefore, the ophiolite cannot account for most of the detrital zircon ages within the 160-240 Ma population of interest. The

structurally underlying Angayucham terrane is not an arc either. Basalts from this terrane (where it is exposed in the Brooks Range) primarily have an oceanic plateau/MORB affinity (Barker et al., 1988; Pallister et al., 1989; Karl, 1992; Harris, 1998). Given the >50 m.y. gap between the depositional age of the units samples by O'Brien et al. (2018) and the age of the 160-240 Ma detrital zircons, it is very difficult to determine where the zircons originally crystallized. It is possible that mafic detritus in the YKB was derived locally from somewhere in interior Alaska. For example, there is relatively little geochemical or geochronological data on areas mapped as Angayucham terrane outside of the Brooks Range (in interior Alaska); some of these may preserve an early Mesozoic arc. It is possible that, with more geochronological data from the BRO, material suitable to be the source of YKB sediments could be found. At the moment, however, more data are needed from possible source areas to determine the provenance of these sediments.

5.3.3 Onset of Brookian Orogenesis — Our model of genesis and emplacement of the BRO is illustrated in Figure 8. In the middle Jurassic, the only arc-related terranes in this area were the BRO and the Koyukuk Arc (Harris, 2004; Till, 2016). Given the BRO's forearc setting, it is most likely the preserved remnant of the Koyukuk forearc. This puts the BRO in-between the Koyukuk Arc and the Arctic-Alaska continental margin (Fig. 8b). The first part of the distal continental margin to encounter the BRO is the Angayucham terrane. The lithologies within the BRO metamorphic sole and underlying unmetamorphosed units match those in the Angayucham terrane and distal parts of the Etivluk group of the Arctic Alaska passive margin (Harris, 1998). The youngest passive margin units overlap in age (~163-169 Ma, (2004)) with ophiolite cooling and emplacement (Moore et al., 1994).

These lithologic and age relations constrain the onset age of age Koyukuk-Arctic Alaska collision (Brookian orogeny) to obduction of BRO (Fig. 8c).

Several authors have linked the onset of Brookian orogenesis and blueschist-facies metamorphism in the region to collision between the Koyukuk Arc and Arctic Alaska (Moore et al., 1994; Gottschalk, 1998; Nokleberg et al., 2000; Shephard et al., 2013). As discussed earlier, this event has been very difficult to date, due to greenschist overprinting of the original blueschist-facies metamorphism. However, collisional deformation and metamorphism of the Arctic Alaska passive margin must coincide with obduction of the BRO (Fig. 8b, c). Therefore we can conclude that Brookian orogenesis began around 169 Ma, which is the maximum age of BRO obduction (Harris, 2004). Later extension in the Brooks Range would separate the BRO from the Koyukuk Arc (Fig. 8d; Harris (2004); Law et al. (1994)). This separation is consistent with different detrital zircon populations seen in mafic material from the Brookian foreland and YKB (Moore et al., 2015; O'Brien et al., 2018).

The tectonic history outlined above and in Fig. 8 is a hybrid between several previously proposed models. However, it is consistent with the published detrital zircon record of surrounding basins, the BRO geochemistry and geochronology, and the geochronology of the Koyukuk Arc. Furthermore, it provides an upper age limit for the timing of blueschist metamorphism in the area (Gottschalk, 1998; Hoiland et al., 2018a) and provides a well constrained age of 163-169 Ma for the onset of Brookian orogenesis.

6. Conclusions

New geochemical data presented in this study shows that the Brooks Range ophiolite formed in a forearc setting. Some of this data suggests that subduction initiation played a role in the formation of the BRO, but more evidence is needed to support this hypothesis. It is likely that the BRO inherited some arc-like geochemical signatures from the neighboring Koyukuk arc or evolved to a more mature subduction state before obduction. The BRO's proximity to distal Arctic Alaska passive margin at the time it formed and was obducted (~169 Ma) constrains the onset of the Brookian orogen.

Acknowledgments

The authors of this study wish to thank Mike Dorais, Tober Dyorich, Chi Ma, and Nathan Dalleska for assistance with laboratory analyses. Betsy Friedlander, Lyle Nelson, and Teck Resources are greatly thanked for obtaining Iyokrok samples. We are grateful to Julian Pearce for sharing the IBM, South Sandwich, and Hess Deep thin sections. Early reviews by Sarah Roeske, Erin Todd, and Mark Reagan greatly improved the manuscript. Portions of this work were presented at the American Geophysical Union 2017 meeting under a similar title: "T23C-0619: Tectonochemistry of the Brooks Range Ophiolite, Alaska." This work is supported in part by the U.S. National Science Foundation, award EAR-1550934. The authors are not aware of any financial conflicts or any other conflicts of interest that would affect the content of this study.

Supplementary Materials

Supplemental Tables S1-S6, which contain all of the new geochemical data used in this study, are available with the online version of this thesis.

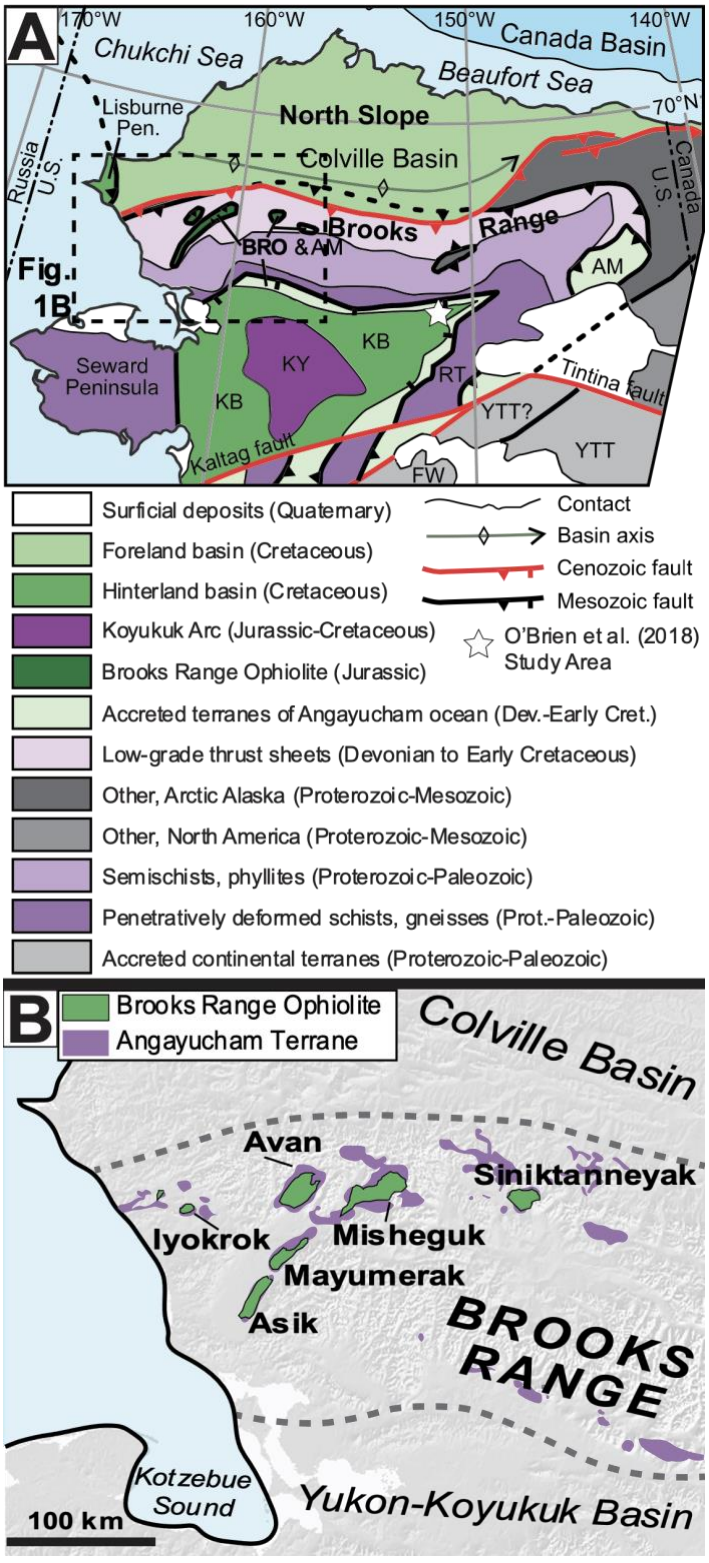

Figure 1 *– **A)** Overview map showing major areas discussed in the text. Lightly modified from (Hoiland et al., 2018b). Abbreviations: AM, Angayucham terrane; BRO, Brooks Range Ophiolite; KB, Yukon-Koyukuk Basin; KY, Koyukuk Arc; FW, Farewell terrane; RT, Ruby terrane; YTT, Yukon-Tanana terrane.* ***B)*** *Map of the western Brooks Range showing exposures of the Brooks Range ophiolite (green) and Angayucham terrane (purple). The dashed lines mark the approximate boundaries of the Brooks Range. Based on maps by Wilson et al. (2015) and Harris (2004).*

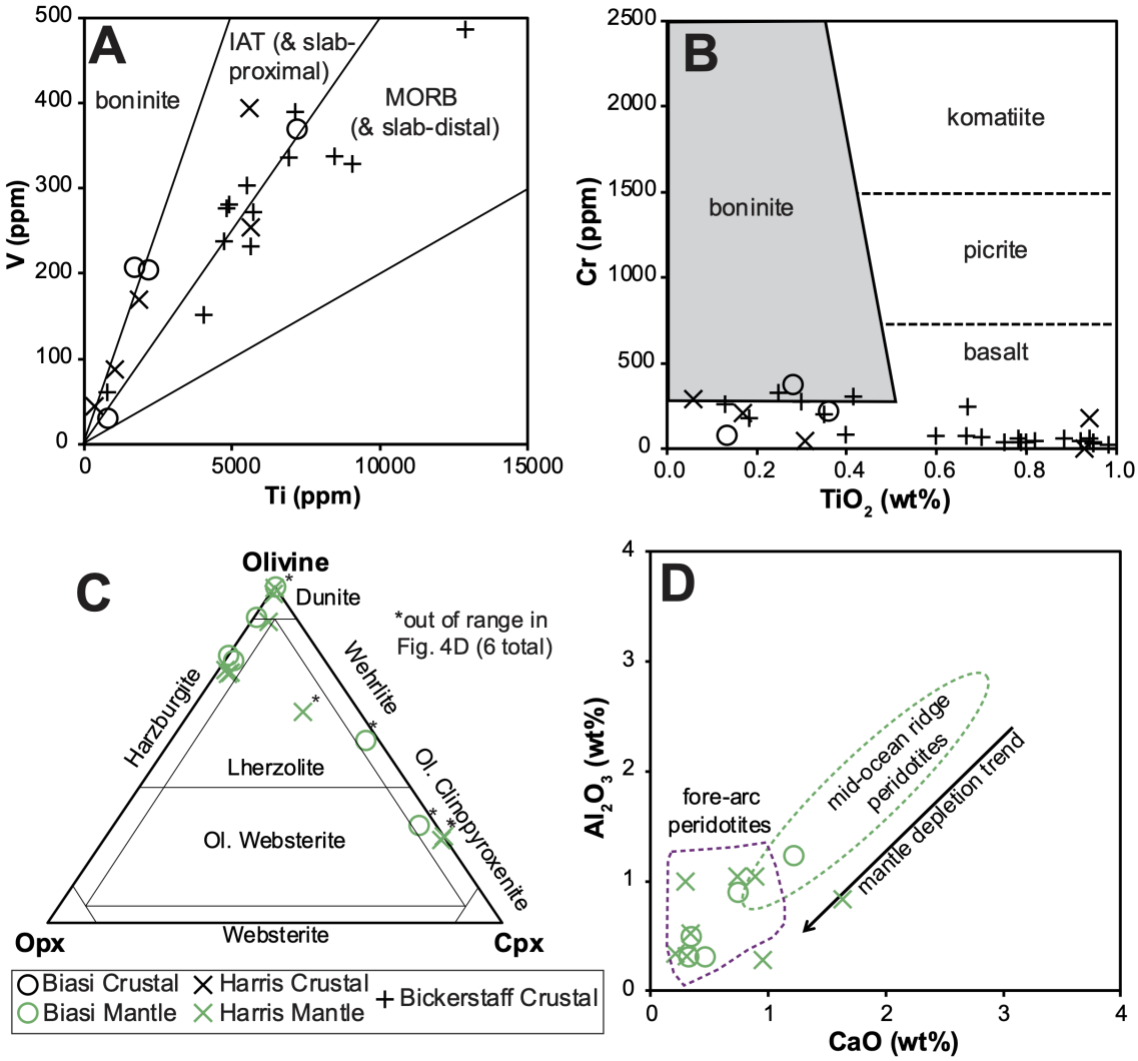
A
IAT (& slab-proximal)
boninite
MORB (& slab-distal)
V (ppm)
Ti (ppm)
B
komatiite
boninite
picrite
basalt
Cr (ppm)
TiO2 (wt%)
C
Olivine
Dunite
*out of range in Fig. 4D (6 total)
Harzburgite
Wehrlite
Ol. Clinopyroxenite
Lherzolite
Ol. Websterite
Websterite
Opx
Cpx
Biasi Crustal
Harris Crustal
Bickerstaff Crustal
Biasi Mantle
Harris Mantle
D
fore-arc peridotites
mid-ocean ridge peridotites
mantle depletion trend
Al2O3 (wt%)
CaO (wt%)

Figure 2 *– Major and trace element chemistry of the BRO. This is a compilation of new data (circles), and data from Harris (1995) (x) and Bickerstaff (1994) (+).* ***A & B)*** *Only samples from the crustal section of the BRO, with <55 wt% SiO_2, and no obvious cumulate textures (layered gabbro, anorthosite, etc.) are shown. Note that many samples from Bickerstaff (1994) do not have major element analyses, and thus are not plotted here.* ***A)*** *V vs. Ti diagram showing a range of affinities for BRO samples. Modified from Pearce (2014) and Shervais (1982).* ***B)*** *Boninite classification plot (immobile element version) showing boninitic compositions from some BRO crustal rocks. Modified from Pearce & Reagan (2019).* ***C)*** *CIPW-normative mineralogy for BRO mantle samples. Modified from Coleman (1977).* ***D)*** *BRO mantle samples have low Al_2O_3 and CaO, a common feature of forearc peridotites. Modified from Ishii et al. (1992) and Gahlan et al. (2020). See text for discussion.*

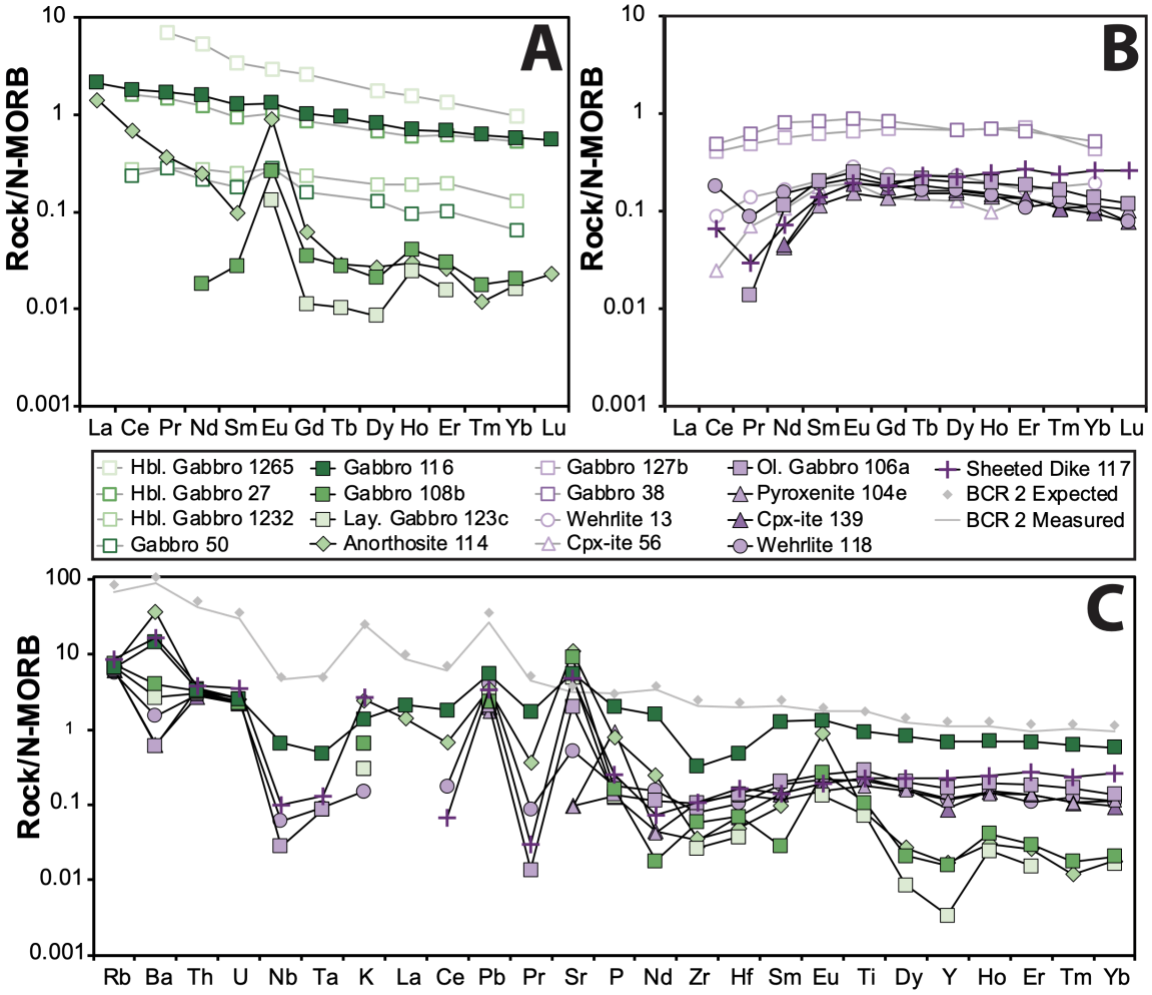

Figure 3 *– N-MORB-normalized trace-element plots. Filled symbols are new data, hollow symbols are data from Harris (1995).* ***A)*** *Subset of BRO samples that show HREE depletion (or LREE enrichment).* ***B)*** *BRO samples that show LREE depletion.* ***C)*** *Extended trace-element diagram. Only REE data exists for samples from Harris (1995), so those samples are not plotted here. An example standard (BCR-2, run as an unknown) is shown in grey. "BCR Expected" values from the U.S. Geological Survey. See text for discussion. N-MORB normalizing values from Sun and McDonough (1989).*

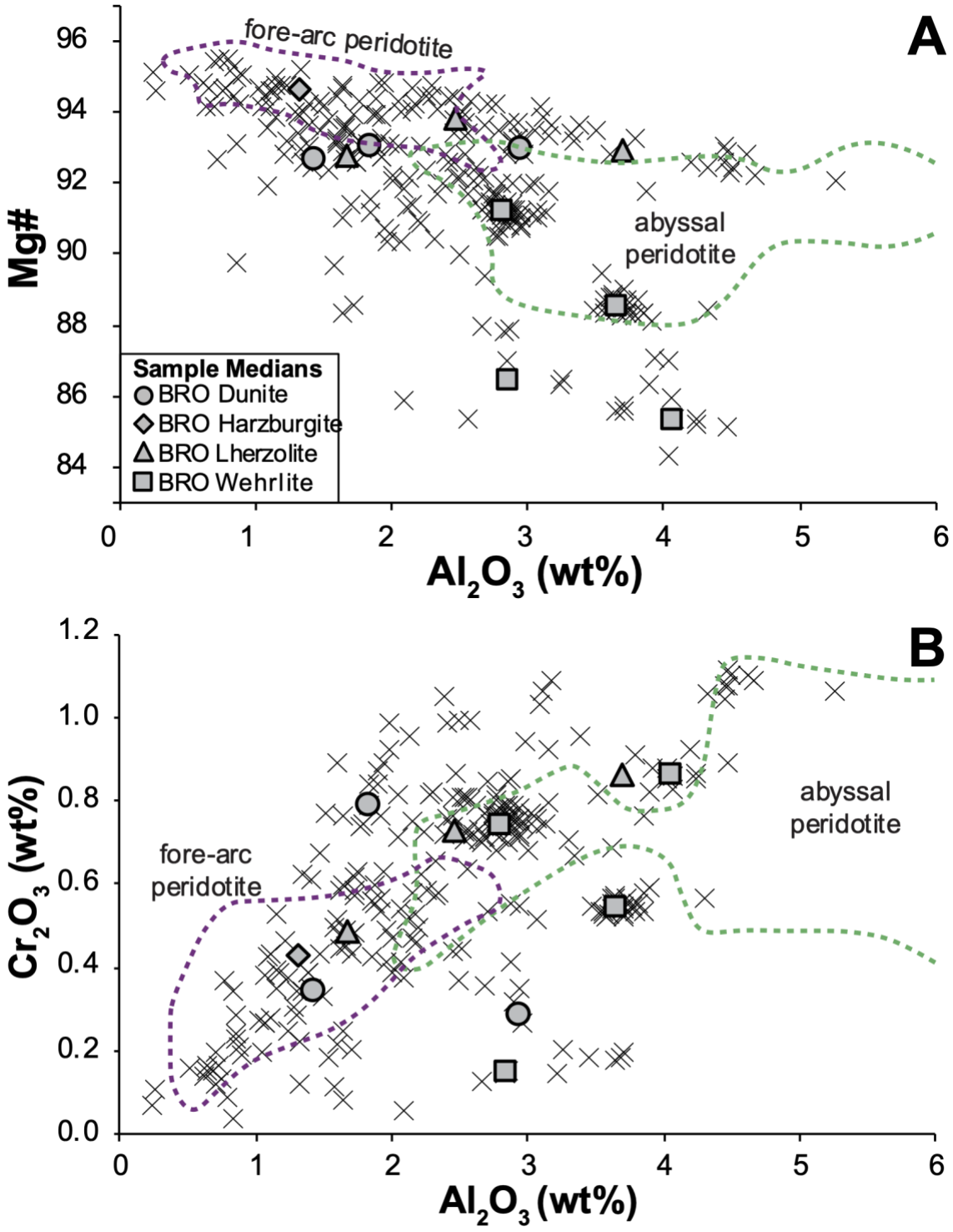

Figure 4 *– Clinopyroxene mineral chemistry of representative BRO mantle samples. Individual analyses are shown with 'x' symbols. Fields based on Pagé et al. (2008). See text for discussion.*

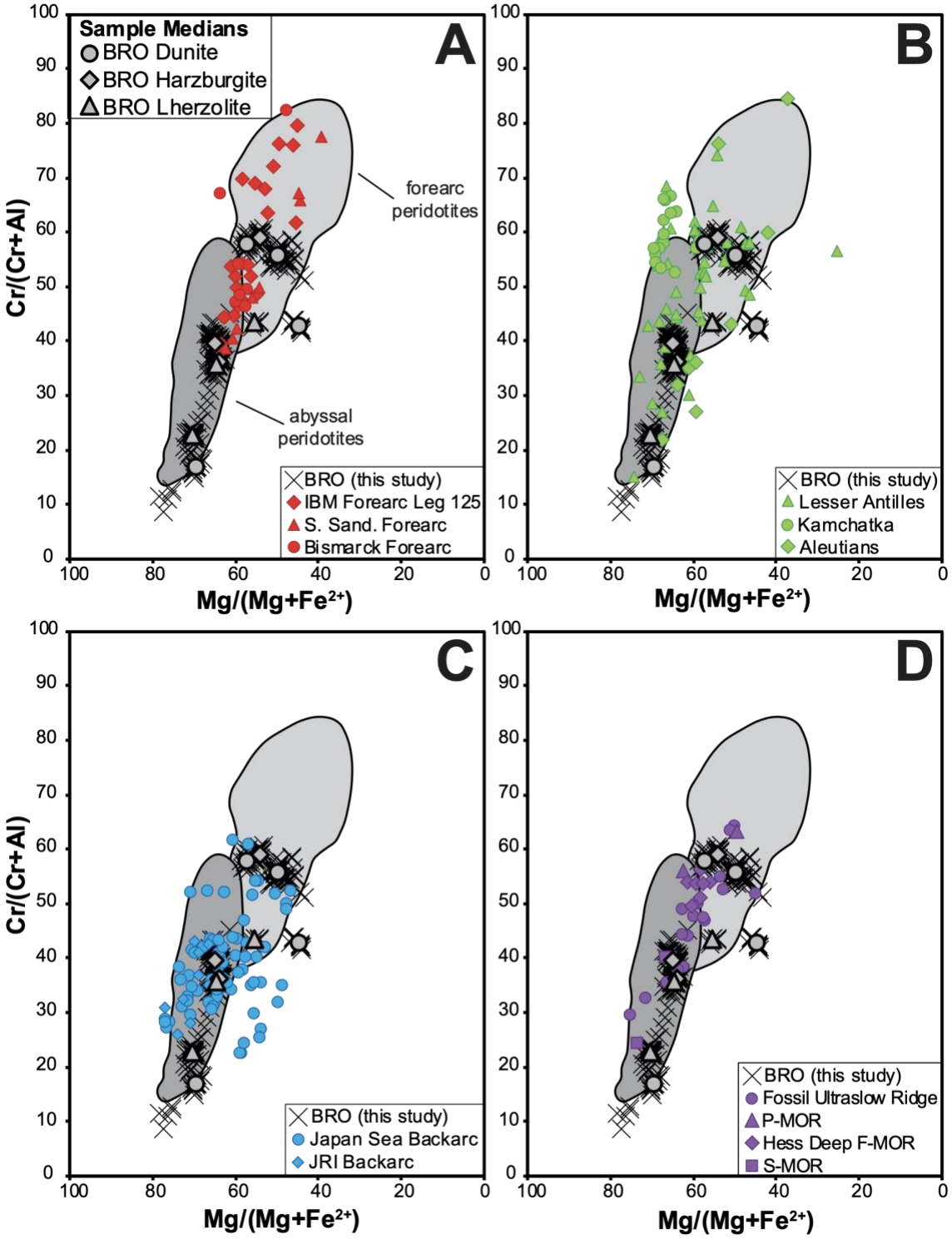
A
Sample Medians
BRO Dunite
BRO Harzburgite
BRO Lherzolite
forearc peridotites
abyssal peridotites
BRO (this study)
IBM Forearc Leg 125
S. Sand. Forearc
Bismarck Forearc
B
BRO (this study)
Lesser Antilles
Kamchatka
Aleutians
C
BRO (this study)
Japan Sea Backarc
JRI Backarc
D
BRO (this study)
Fossil Ultraslow Ridge
P-MOR
Hess Deep F-MOR
S-MOR
Cr/(Cr+Al)
Mg/(Mg+Fe2+)

Figure 5 *– Cr-spinel data from BRO mantle lithologies (Table S6) and a compilation of data from multiple tectonic settings. Compiled data is sourced from peridotite xenoliths and exposures of mantle peridotites. BRO data is shown with black 'x' symbols, BRO sample median values are shown with grey symbols.* ***A)*** *Comparison of BRO data (this study) with spinel from forearc settings. Data from Pearce et al. (2000), Parkinson and Pearce (1998), McInnes et al. (2001), and Gregoire et al. (2001).* ***B)*** *Compilation of spinel data from arcs. Data from Ionov (2010), Parkinson et al. (2003), Vannucci et al. (2007), Conrad and Kay (1984), and Debari et al. (1987).* ***C)*** *Comparison with back-arc spinel. JRI = James Ross Island, Antarctica. Data from Calabozo et al. (2014), Altunkaynak (2019), and Ichiyama et al. (2016).* ***D)*** *Comparison with Mid-Ocean Ridge (MOR) spinel data. P = slow-spreading plume related, S = slow-spreading ridge, F = fast-spreading ridge. Data from Sanfilippo et al. (2014) and Dare et al. (2009). Modified from Arai & Ishimaru (2008).*

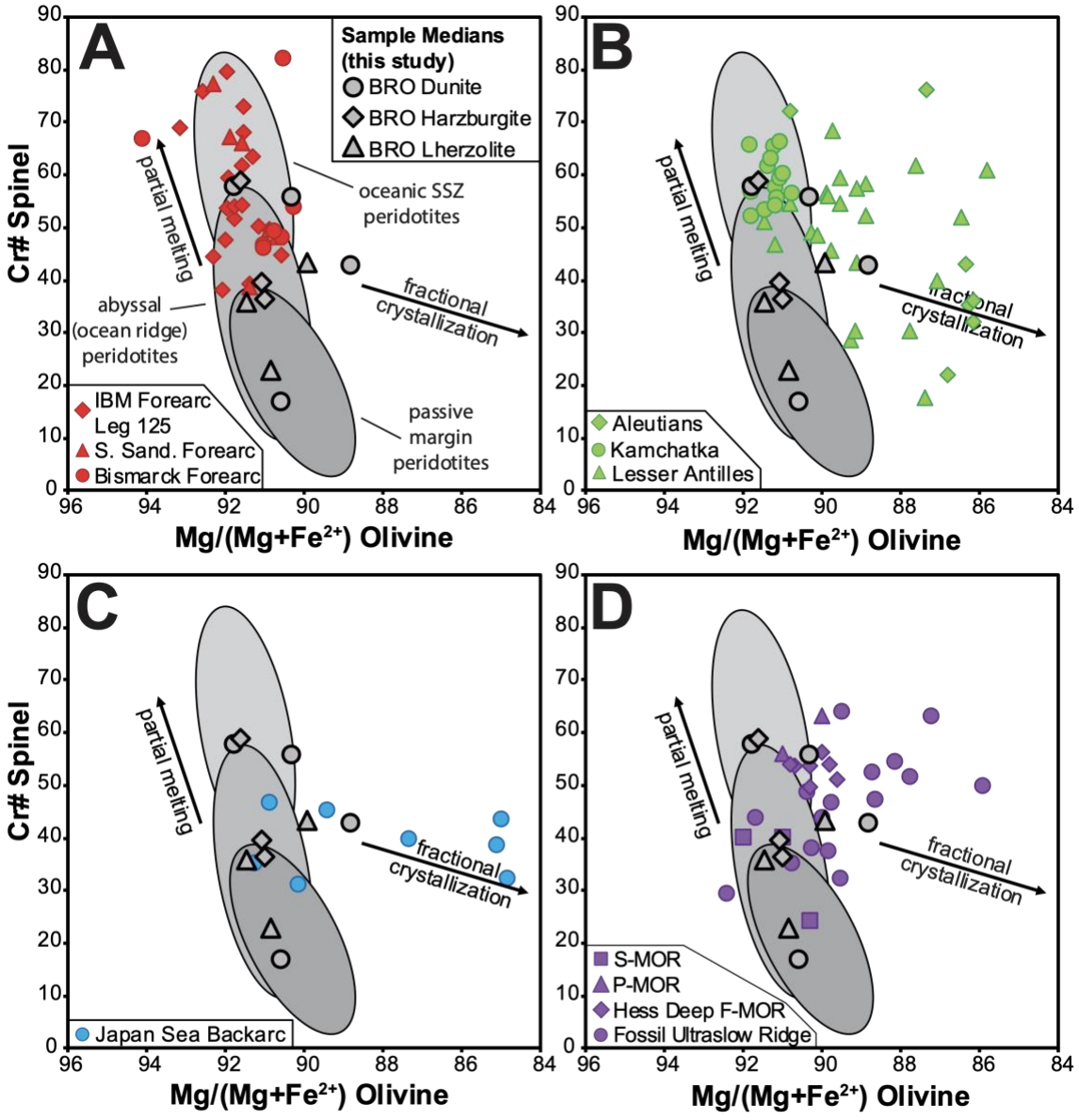

Figure 6 *– Cr-spinel and olivine data from BRO mantle lithologies (Table S3, S4, S6) and a compilation of data from various settings. Plotted on discrimination diagram of Pearce et al. (2000). Data sources and symbols as in Fig. 5. See text for discussion.*

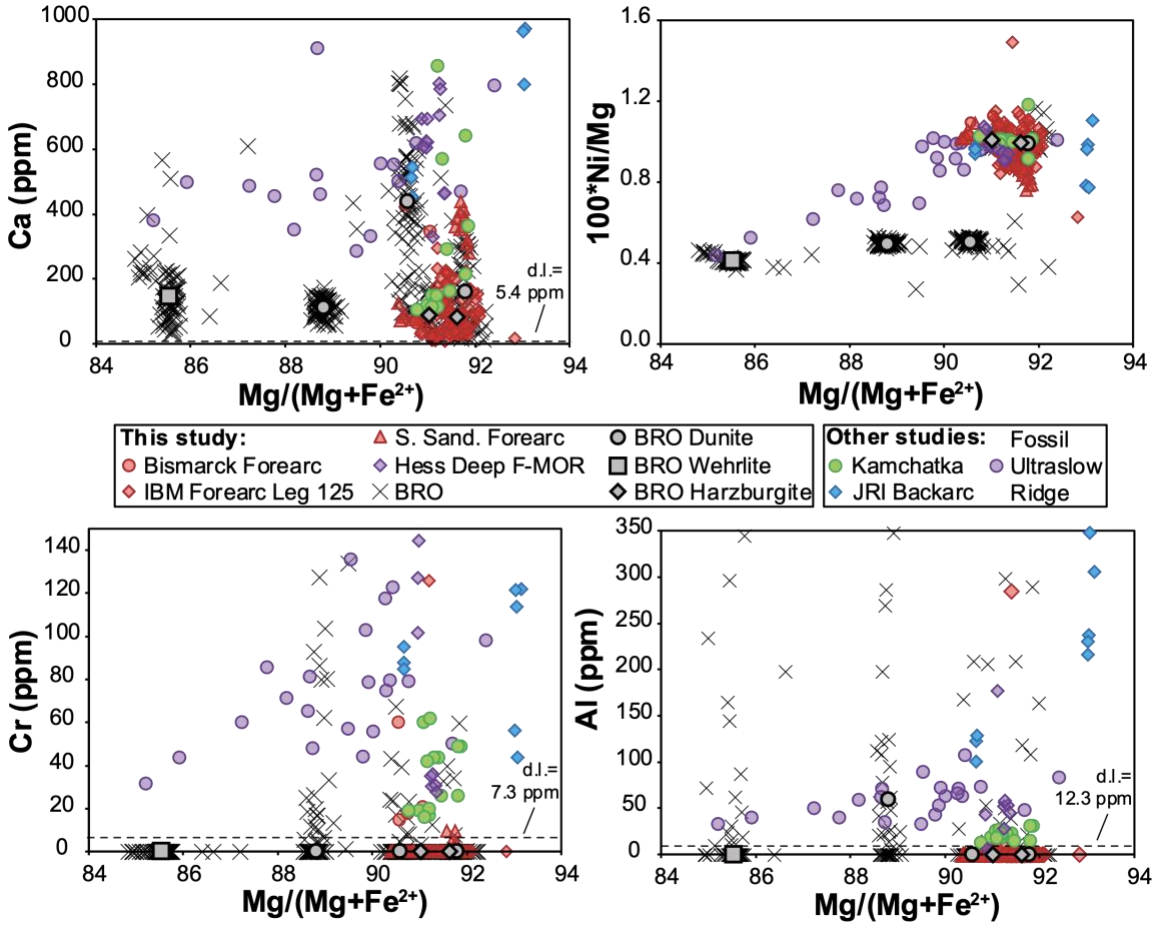

Figure 7 *– High-precision olivine analyses from BRO mantle lithologies (Table S4) and a compilation of data from various tectonic settings. Grey symbols are median values for BRO samples. Analyses with no detectable signal are plotted on the x-axis. Data from the BRO, IBM forearc Leg 125, S. Sandwich forearc, and Hess Deep are from this study. Other analyses are from Gregoire (2001), Ionov (2010), Altunkaynak et al. (2019), and Sanfilippo et al. (2014). Leg 125 samples are harzburgites from Conical and Torishima Seamounts in the IBM forearc. Hess Deep samples are harzburgites from ODP Leg 147 (site 895). Scotia samples are harbzurgites from the South Sandwich forearc. d.l. = detection limit. See Dare et al. (2009) and Pearce et al. (2000) for more sample details. See text for discussion.*

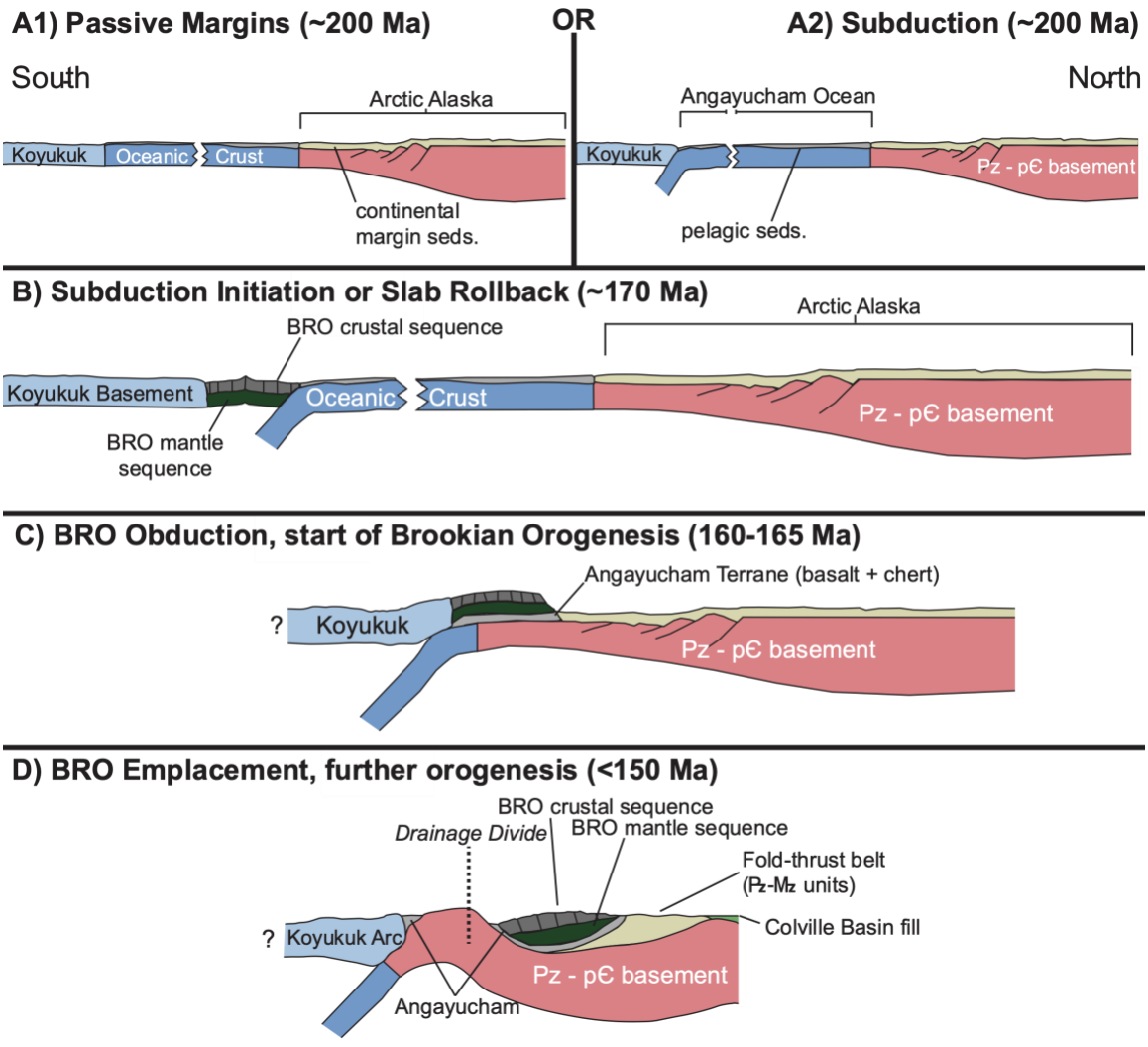
A1) Passive Margins (~200 Ma)
OR
A2) Subduction (~200 Ma)
South
North
Arctic Alaska
Angayucham Ocean
Koyukuk
Oceanic Crust
Koyukuk
Pz - pЄ basement
continental margin seds.
pelagic seds.
B) Subduction Initiation or Slab Rollback (~170 Ma)
Arctic Alaska
BRO crustal sequence
Koyukuk Basement
Oceanic Crust
Pz - pЄ basement
BRO mantle sequence
C) BRO Obduction, start of Brookian Orogenesis (160-165 Ma)
Angayucham Terrane (basalt + chert)
?
Koyukuk
Pz - pЄ basement
D) BRO Emplacement, further orogenesis (<150 Ma)
BRO crustal sequence
Drainage Divide
BRO mantle sequence
Fold-thrust belt
(Pz-Mz units)
Colville Basin fill
?
Koyukuk Arc
Pz - pЄ basement
Angayucham

Figure 8 *– Genesis and emplacement of the BRO. Two initial conditions are possible, depending on whether the BRO was formed via subduction initiation or slab rollback.* ***A1)*** *Both the Arctic Alaska and Koyukuk margins are passive, or* ***A2)*** *A subduction zone already exists along northern margin of the Koyukuk terrane (present day coordinates).* ***A1, A2)*** *A sea of unknown size (shown by a break in the section) separates the Arctic-Alaska passive margin from the oldest units of the Koyukuk terrane (Box and Patton, 1989).* ***B)*** *Either southward subduction or slab rollback begins at the northern Koyukuk margin. The BRO is created in the Koyukuk forearc during this event.* ***C)*** *Collision between the Koyukuk terrane and the continental margin causes the BRO to obduct over Angayucham basalts/sediments and onto Arctic-Alaska (Harris, 1987).* ***D)*** *Further orogenesis separates the BRO from the Koyukuk Arc (Law et al., 1994; Harris, 2004).*

References

Altunkaynak, Ş., Ünal, A., Howarth, G.H., Aldanmaz, E., and Nỳvlt, D., 2019, The origin of low-Ca olivine from ultramafic xenoliths and host basaltic lavas in a back-arc setting, James Ross Island, Antarctic Peninsula: Lithos, v. 342, p. 276–287.

Amato, J.M., Toro, J., Akinin, V.V., Hampton, B.A., Salnikov, A.S., and Tuchkova, M.I., 2015, Tectonic evolution of the Mesozoic South Anyui suture zone, eastern Russia: A critical component of paleogeographic reconstructions of the Arctic region: Geosphere, v. 11, p. 1530–1564, doi:10.1130/ges01165.1.

Arai, S., and Ishimaru, S., 2008, Insights into petrological characteristics of the lithosphere of mantle wedge beneath arcs through peridotite xenoliths: A review: Journal of Petrology, v. 49, p. 665–695.

Barker, F., Jones, D.L., Budahn, J.R., and Coney, P.J., 1988, Ocean plateau-seamount origin of basaltic rocks, Angayucham terrane, central Alaska: The Journal of Geology, p. 368–374.

Baziotis, I., Mposkos, E., and Asimow, P., 2014, Continental rift and oceanic protoliths of mafic–ultramafic rocks from the Kechros Complex, NE Rhodope (Greece): implications from petrography, major and trace-element systematics, and MELTS modeling: International Journal of Earth Sciences, v. 103, p. 981–1003.

Bickerstaff, D., 1994, The crustal section of the Siniktanneyak Mountain ophiolite, Brooks Range, Alaska: West Virginia University, 82 p.

Box, S.E., and Patton, W.W., 1989, Igneous history of the Koyukuk Terrane, western Alaska: Constraints on the origin, evolution, and ultimate collision of an accreted

island arc terrane: Journal of Geophysical Research: Solid Earth, v. 94, p. 15843–15867, doi:10.1029/JB094iB11p15843.

Calabozo, F., Strelin, J., Keller, R., Brod, J., and Fuentes-Iza, F., 2014, Mantle xenoliths from James Ross Island, Antarctic Peninsula: A preliminary whole-rock and mineral chemistry study: XIX Congreso Geológico Argentino, p. T8-11.

Churkin, M., Nokleberg, W.J., and Huie, C., 1979, Collision-deformed Paleozoic continental margin, western Brooks Range, Alaska: Geology, v. 7, p. 379–383.

Cole, F., Bird, K.J., Toro, J., Roure, F., O'Sullivan, P.B., Pawlewicz, M., and Howelll, D.G., 1997, An integrated model for the tectonic development of the frontal Brooks Range and Colville Basin 250 km west of the Trans-Alaska Crustal Transect: Journal of Geophysical Research: Solid Earth, v. 102, p. 20685–20708, doi:10.1029/96jb03670.

Coleman, R.G., 1977, Ophiolites: Ancient oceanic lithosphere? Springer Verlag, 229p.

Conrad, W.K., and Kay, R.W., 1984, Ultramafic and mafic inclusions from Adak Island: Crystallization history, and implications for the nature of primary magmas and crustal evolution in the Aleutian Arc: Journal of Petrology, v. 25, p. 88–125.

Crane, R., 1987, Cretaceous olistostrome model, Brooks Range, Alaska, *in* Alaskan North Slope Geology, Bakersfield, California, Pacific Section of Society of Economic Paleontologists and Mineralogists and the Alaska Geological Society, v. 50, p. 433–440.

Dare, S.A., Pearce, J.A., McDonald, I., and Styles, M.T., 2009, Tectonic discrimination of peridotites using fO2–Cr# and Ga–Ti–FeIII systematics in chrome–spinel: Chemical Geology, v. 261, p. 199–216.

Debari, S., Kay, S.M., and Kay, R., 1987, Ultramafic xenoliths from Adagdak volcano, Adak, Aleutian Islands, Alaska: Deformed igneous cumulates from the Moho of an island arc: The Journal of Geology, v. 95, p. 329–341.

Dumoulin, J., Till, A., and Bradley, D., 2011, Neoproterozoic–Paleozoic paleogeographic reconstruction of the Arctic Alaska–Chukotka terrane: Stone, DB, Clough, JG, and Thurston, DK, compilers, Geophysical Institute Report UAG, p. 51–53.

Foley, J., Dahlin, D.C., Mardock, C.L., and O'Connor, W.K., 1992, Reconnaissance investigations of chromite deposits and platinum-group metals in the western Brooks Range, northwestern Alaska: US Bur. Mines Rep, p. 80–92.

Gahlan, H.A., Azer, M.K., Asimow, P.D., and Al-Kahtany, K.M., 2020, Genesis and geodynamic evolution of serpentinized ultramafics and associated magnesite deposits in the Al-Wask ophiolite, Arabian Shield, Saudi Arabia: American Journal of Science, v. 320, p. 236–279.

Gavrilenko, M., Herzberg, C., Vidito, C., Carr, M.J., Tenner, T., and Ozerov, A., 2016, A calcium-in-olivine geohygrometer and its application to subduction zone magmatism: Journal of Petrology, v. 57, p. 1811–1832.

Gealey, W., 1980, Ophiolite obduction mechanism, *in* Ophiolites: Proceedings of the International Ophiolite Symposium, Nicosia, Cyprus Geological Survey Department, p. 228–243.

Gottschalk, R.R., 1998, Petrology of eclogite and associated high-pressure metamorphic rocks, south-central Brooks Range, Alaska: Special Papers-Geological Society of America, p. 141–162.

Grégoire, M., McInnes, B.I., and O'Reilly, S.Y., 2001, Hydrous metasomatism of oceanic sub-arc mantle, Lihir, Papua New Guinea: Part 2. Trace element characteristics of slab-derived fluids: Lithos, v. 59, p. 91–108.

Harris, R., 1995, Geochemistry and tectonomagmatic affinity of the Misheguk massif, Brooks Range ophiolite, Alaska: Lithos, v. 35, p. 1–25.

Harris, R., 1998, Origin and tectonic evolution of the metamorphic sole beneath the Brooks Range ophiolite, Alaska: Special Papers-Geological Society of America, p. 293–312.

Harris, R., 1992, Peri-collisional extension and the formation of Oman-type ophiolites in the Banda Arc and Brooks Range: Geological Society, London, Special Publications, v. 60, p. 301–325.

Harris, R., 1987, Structure and composition of sub-ophiolite metamorphic rocks, western Brooks Range ophiolite belt, Alaska, *in* v. 19, p. 387.

Harris, R., 2004, Tectonic evolution of the Brooks Range ophiolite, northern Alaska: Tectonophysics, v. 392, p. 143–163, doi:10.1016/j.tecto.2004.04.021.

Harris, R., 2011, The nature of the Banda Arc–continent collision in the Timor region, *in* Arc-Continent Collision, Springer, p. 163–211.

Harris, R., Stone, D., and Turner, D., 1987, Tectonic implications of paleomagnetic and geochronologic data from the Yukon-Koyukuk province, Alaska: Geological Society of America Bulletin, v. 99, p. 362–375.

Hoiland, C.W., Miller, E.L., and Pease, V., 2018a, Greenschist facies metamorphic zircon overgrowths as a constraint on exhumation of the Brooks Range metamorphic core, Alaska: Tectonics, v. 37, p. 3429–3455.

Hoiland, C.W., Miller, E.L., Pease, V., and Hourigan, J.K., 2018b, Detrital zircon U–Pb geochronology and Hf isotope geochemistry of metasedimentary strata in the southern Brooks Range: Constraints on Neoproterozoic–Cretaceous evolution of Arctic Alaska: Geological Society, London, Special Publications, v. 460, p. 121–158.

Ichiyama, Y., Morishita, T., Tamura, A., and Arai, S., 2016, Peridotite xenoliths from the Shiribeshi Seamount, Japan Sea: Insights into mantle processes in a back-arc basin: Contributions to Mineralogy and Petrology, v. 171, p. 86.

Ionov, D.A., 2010, Petrology of mantle wedge lithosphere: New data on supra-subduction zone peridotite xenoliths from the andesitic Avacha volcano, Kamchatka: Journal of Petrology, v. 51, p. 327–361.

Ishii, T., Robinson, P.T., Maekawa, H., Fiske, R., and others, 1992, Petrological studies of peridotites from diapiric serpentinite seamounts in the Izu-Ogasawara-Mariana forearc, Leg 125, *in* Proceedings of the ocean drilling program, scientific results, Ocean Drilling Program College Station, v. 125.

Jones, D., Silberling, N.J., Coney, P., and Plafker, G., 1987, Lithotectonic terrane map of Alaska (west of the 141st meridian): USGS Miscellaneous Field Studies Map, v. 1874-A, doi:https://doi.org/10.3133/mf1874A.

Karl, S.M., 1992, Arc and extensional basin geochemical and tectonic affinities for Maiyumerak basalts in the western Brooks Range, in Bradley, D.C., and Ford, A.B., eds., Geologic studies in Alaska by the U.S. Geological Survey, 1990: U.S. Geological Survey Bulletin 1999, p. 141-155.

Kuznetsov, N., 2006, The Cambrian Baltica-Arctida collision, pre-Uralide-Timanide orogen, and its erosion products in the Arctic, *in* Springer, v. 411, p. 1375–1380.

Law, R.D., Miller, E.L., Little, T.A., and Lee, J., 1994, Extensional origin of ductile fabrics in the Schist Belt, Central Brooks Range, Alaska—II. Microstructural and petrofabric evidence: Journal of Structural Geology, v. 16, p. 919–940.

Martin, A., 1970, Structure and Tectonic History of the Western Brooks Range, De Long Mountains and Lisburne Hills, Northern Alaska: Geological Society of America Bulletin, v. 81, p. 3605–3622.

Mayfield, C.F., Tailleur, I.L., Ellersieck, I., and Gryc, G., 1988, Stratigraphy, structure, and palinspastic synthesis of the western Brooks Range, northwestern Alaska: US Geological Survey Professional Paper, v. 1399, p. 143–186.

McInnes, B.I., Gregoire, M., Binns, R.A., Herzig, P.M., and Hannington, M.D., 2001, Hydrous metasomatism of oceanic sub-arc mantle, Lihir, Papua New Guinea: petrology and geochemistry of fluid-metasomatised mantle wedge xenoliths: Earth and Planetary Science Letters, v. 188, p. 169–183.

Miller, E.L., and Hudson, T.L., 1991, Mid-Cretaceous extensional fragmentation of a Jurassic-Early Cretaceous Compressional Orogen, Alaska: Tectonics, v. 10, p. 781–796.

Miller, E.L., Meisling, K.E., Akinin, V.V., Brumley, K., Coakley, B.J., Gottlieb, E.S., Hoiland, C.W., O'Brien, T.M., Soboleva, A., and Toro, J., 2018, Circum-Arctic Lithosphere Evolution (CALE) Transect C: Displacement of the Arctic Alaska–Chukotka microplate towards the Pacific during opening of the Amerasia Basin of

the Arctic: Geological Society, London, Special Publications, v. 460, p. 57–120, doi:10.1144/SP460.9.

Moore, T.E., Aleinikoff, J.N., and Walter, M., 1993, Middle Jurassic U-Pb crystallization age for Siniktanneyak Mountain ophiolite, Brooks Range, Alaska: Geological Society of America, Abstracts with Programs;(United States), v. 25.

Moore, T.E., O'Sullivan, P.B., Potter, C.J., and Donelick, R.A., 2015, Provenance and detrital zircon geochronologic evolution of lower Brookian foreland basin deposits of the western Brooks Range, Alaska, and implications for early Brookian tectonism: Geosphere, v. 11, p. 93–122, doi:10.1130/ges01043.1.

Moore, T.E., Wallace, W.K., Bird, K.J., Karl, S.M., Mull, C.G., and Dillon, J.T., 1994, Geology of Northern Alaska, *in* Geology of Alaska, Geological Society of America, p. 49–140, https://pubs.er.usgs.gov/publication/70186635.

Moores, E., 1982, Origin and emplacement of ophiolites: Reviews of Geophysics, v. 20, p. 735–760.

Nokleberg, W.J., Parfenov, L.M., Monger, J.W.H., Norton, I.O., Khanchuk, A.I., Stone, D.B., Scotese, C.R., Scholl, D.W., and Fujita, K., 2000, Phanerozoic tectonic evolution of the Circum-North Pacific: USGS Professional Paper, v. 1626.

O'Brien, T.M., Miller, E.L., Pease, V., Hayden, L.A., Fisher, C.M., Hourigan, J.K., and Vervoort, J.D., 2018, Provenance, U-Pb detrital zircon geochronology, Hf isotopic analyses, and Cr-spinel geochemistry of the northeast Yukon-Koyukuk Basin: Implications for interior basin development and sedimentation in Alaska: GSA Bulletin, v. 130, p. 825–847.

Pagé, P., Bédard, J.H., Schroetter, J.-M., and Tremblay, A., 2008, Mantle petrology and mineralogy of the Thetford Mines ophiolite complex: Lithos, v. 100, p. 255–292.

Pallister, J.S., Budahn, J.R., and Murchey, B.L., 1989, Pillow basalts of the Angayucham terrane: Oceanic plateau and island crust accreted to the Brooks Range: Journal of Geophysical Research: Solid Earth, v. 94, p. 15901–15923, doi:10.1029/JB094iB11p15901.

Parkinson, I., Arculus, R., and Eggins, S., 2003, Peridotite xenoliths from Grenada, Lesser Antilles island arc: Contributions to Mineralogy and Petrology, v. 146, p. 241–262.

Parkinson, I.J., and Pearce, J.A., 1998, Peridotites from the Izu–Bonin–Mariana forearc (ODP Leg 125): Evidence for mantle melting and melt–mantle interaction in a supra-subduction zone setting: Journal of Petrology, v. 39, p. 1577–1618.

Patton, Jr., William W., Box, Stephen.E., and Grybeck, D.J., 1994, Ophiolites and other mafic-ultramafic complexes in Alaska, *in* The Geology of Alaska, Geological Society of America, doi:10.1130/DNAG-GNA-G1.671.

Pearce, J.A., 2014, Immobile element fingerprinting of ophiolites: Elements, v. 10, p. 101–108.

Pearce, J.A., Barker, P., Edwards, S., Parkinson, I., and Leat, P., 2000, Geochemistry and tectonic significance of peridotites from the South Sandwich arc–basin system, South Atlantic: Contributions to Mineralogy and Petrology, v. 139, p. 36–53.

Pearce, J.A., and Reagan, M.K., 2019, Identification, classification, and interpretation of boninites from Anthropocene to Eoarchean using Si-Mg-Ti systematics: Geosphere, v. 15, p. 1008–1037.

Pearce, J.A., Reagan, M., Petronotis, K., Morgan, S., Almeev, R., Avery, A., Carvallo, C., Chapman, T., Christeson, G., and Ferre, E., 2015, International Ocean Discovery Program Expedition 352 Preliminary Report; Izu-Bonin-Mariana fore arc; testing subduction initiation and ophiolite models by drilling the outer Izu-Bonin-Mariana fore arc; 30 July-29 September 2014: Preliminary Reports (International Ocean Discovery Program), v. 352, p. 1–86.

Pearce, J.A., and Stern, R.J., 2006, Origin of back-arc basin magmas: Trace element and isotope perspectives: Geophysical Monograph-American Geophysical Union, v. 166, p. 63.

Pease, V., 2011, Eurasian orogens and Arctic tectonics: An overview: Geological Society, London, Memoirs, v. 35, p. 311–324.

Pease, V., Drachev, S., Stephenson, R., and Zhang, X., 2014, Arctic lithosphere — A review: Tectonophysics, v. 628, p. 1–25, doi:10.1016/j.tecto.2014.05.033.

Reagan, M.K. et al., 2017, Subduction initiation and ophiolite crust: New insights from IODP drilling: International Geology Review, v. 59, p. 1439–1450, doi:10.1080/00206814.2016.1276482.

Reagan, M.K., Ishizuka, O., Stern, R.J., Kelley, K.A., Ohara, Y., Blichert-Toft, J., Bloomer, S.H., Cash, J., Fryer, P., and Hanan, B.B., 2010, Fore-arc basalts and subduction initiation in the Izu-Bonin-Mariana system: Geochemistry, Geophysics, Geosystems, v. 11.

Roeder, D., and Mull, C.G., 1978, Tectonics of Brooks Range ophiolites, Alaska: Geologic Notes: AAPG Bulletin, v. 62, p. 1696–1702.

Sanfilippo, A., Tribuzio, R., and Tiepolo, M., 2014, Mantle–crust interactions in the oceanic lithosphere: Constraints from minor and trace elements in olivine: Geochimica et Cosmochimica Acta, v. 141, p. 423–439.

Shephard, G.E., Müller, R.D., and Seton, M., 2013, The tectonic evolution of the Arctic since Pangea breakup: Integrating constraints from surface geology and geophysics with mantle structure: Earth-Science Reviews, v. 124, p. 148–183, doi:10.1016/j.earscirev.2013.05.012.

Shervais, J.W., 1982, Ti-V plots and the petrogenesis of modern and ophiolitic lavas: Earth and Planetary Science Letters, v. 59, p. 101–118.

Silberling, N.J., Jones, D., Monger, J.W.H., Coney, P., Berg, H.C., and Plafker, G., 1994, Lithotectonic terrane map of Alaska and adjacent parts of Canada: Geological Society of America. The Geology of Alaska, 1 Sheet.

Sobolev, A.V., Hofmann, A.W., Kuzmin, D.V., Yaxley, G.M., Arndt, N.T., Chung, S.-L., Danyushevsky, L.V., Elliott, T., Frey, F.A., and Garcia, M.O., 2007, The amount of recycled crust in sources of mantle-derived melts: Science, v. 316, p. 412–417.

Stern, R.J., Reagan, M., Ishizuka, O., Ohara, Y., and Whattam, S., 2012, To understand subduction initiation, study forearc crust: To understand forearc crust, study ophiolites: Lithosphere, v. 4, p. 469–483, doi:10.1130/l183.1.

Sun, S.-S., and McDonough, W.F., 1989, Chemical and isotopic systematics of oceanic basalts: Implications for mantle composition and processes: Geological Society, London, Special Publications, v. 42, p. 313–345.

Tailleur, I., 1970, Structure and stratigraphy of western Arctic Alaska: Abstract: AAPG Bulletin, v. 54, p. 2508–2508.

Till, A.B., 2016, A synthesis of Jurassic and Early Cretaceous crustal evolution along the southern margin of the Arctic Alaska–Chukotka microplate and implications for defining tectonic boundaries active during opening of Arctic Ocean basins: Lithosphere, v. 8, p. 219–237, doi:10.1130/l471.1.

Todd, E., Gill, J.B., and Pearce, J.A., 2012, A variably enriched mantle wedge and contrasting melt types during arc stages following subduction initiation in Fiji and Tonga, southwest Pacific: Earth and Planetary Science Letters, v. 335, p. 180–194.

Vannucci, R., Tiepolo, M., Defant, M., and Kepezhinskas, P., 2007, The metasomatic record in the shallow peridotite mantle beneath Grenada (Lesser Antilles arc): Lithos, v. 99, p. 25–44.

Wakabayashi, J., and Dilek, Y., 2003, What constitutes 'emplacement'of an ophiolite?: Mechanisms and relationship to subduction initiation and formation of metamorphic soles: Geological Society, London, Special Publications, v. 218, p. 427–447.

Warren, C.J., Parrish, R.R., Waters, D.J., and Searle, M.P., 2005, Dating the geologic history of Oman's Semail ophiolite: Insights from U-Pb geochronology: Contributions to Mineralogy and Petrology, v. 150, p. 403–422.

Whattam, S.A., and Stern, R.J., 2011, The 'subduction initiation rule': A key for linking ophiolites, intra-oceanic forearcs, and subduction initiation: Contributions to Mineralogy and Petrology, v. 162, p. 1031–1045.

Wilson, F.H., Hults, C.P., Mull, C.G., and Karl, S.M., 2015, Geologic map of Alaska: US Geological Survey Scientific Investigations Map, v. 3340, p. 196.

Wirth, K.R., 1991, Processes of lithosphere evolution: Geochemistry and tectonics of mafic rocks in the Brooks Range and Yukon-Tanana Region, Alaska. [Ph.D.]: Cornell University, 367 p.

Wirth, K.R., and Bird, J.M., 1992, Chronology of ophiolite crystallization, detachment, and deeper parts of subduction zones. emplacement: Evidence from the Brooks Range, Alaska: Geology, v. 20, p. 75–78.

Wirth, K.R., Bird, J.M., Blythe, A.E., Harding, D.J., and Heizler, M.T., 1993, Age and evolution of western Brooks Range ophiolites, Alaska: Results from 40Ar/39Ar thermochronometry: Tectonics, v. 12, p. 410–432.

Zhang, H.-F., 2005, Transformation of lithospheric mantle through peridotite-melt reaction: A case of Sino-Korean craton: Earth and Planetary Science Letters, v. 237, p. 768–780.

Chapter 3

Timescales of Magma Transport in the Columbia River Flood Basalts, Determined by Paleomagnetic Data

Coauthors: Joseph Biasi, Caltech; Leif Karlstrom, University of Oregon

This manuscript is currently in review, and has been lightly reformatted for this thesis.

Abstract

Flood basalts represent major events in Earth History, in part because they are linked to large climate perturbations and mass extinctions. However, the durations of individual flood basalt eruptions, which directly impact potential environmental crises, are poorly constrained. Here we use a combination of paleomagnetic data and thermal modeling to create a magnetic geothermometer (MGT) that can constrain the active transport lifetime of magmatic conduits and igneous intrusions. We apply the MGT technique to eight feeder dike segments of the Columbia River basalts (CRB), demonstrating that some dike segments were actively heating host rocks for less than one month, while other segments may have been active for several years. Results suggest that eruption rates, localized spatially along strike of dike segments, were as high as 1–8 km^3 day^{-1}. These results help contextualize field evidence for contrasting CRB eruption durations and suggest a pathway for constraining the tempo of global flood basalt magmatism that is beyond the resolution of geochronology.

1. Introduction

Throughout Earth History, emplacement of flood basalts often coincided with mass extinctions or major climate disturbances (Clapham and Renne, 2019). Individual flood basalt eruptions can release large amounts of carbon, sulfur, chlorine, fluorine, and mercury directly into the atmosphere (Thordarson and Self, 1996). If these volatiles are released over thousands of years, then their effects may be significantly muted through biogeochemical sequestration. However, if most of these volatiles are released in short-duration high-intensity pulses, they can have a major impact on the climate (Schmidt et

al., 2016). Uncertainty in individual eruption durations is therefore a major barrier to understanding these events.

Current geochronological techniques can determine the amount of time that has passed between two discrete eruptions if they are not within error of each other (~10 kyr for the Columbia River Basalts or CRB; Kasbohm and Schoene, 2018) but cannot measure the duration of the eruptions themselves. Paleoclimate proxies in the sedimentary record commonly preserve the climatic or biological impact of these eruptions (e.g. Fendley et al., 2019), not the eruptions themselves, and sedimentation rates are too slow to capture such events in detail.

In this study, we use a combination of paleomagnetic data and thermal modeling to create a magnetic geothermometer (MGT) and show how it can be used to determine the duration of magma transport in dikes, sills, and other igneous intrusions. We apply the MGT technique to eight Columbia River flood basalt feeder dike segments to determine the duration of eruptions in this event.

2. Geologic Background

From ~16.7 to ~6.2 Ma, flood basalt activity in the northwestern United States resulted in the eruption of ~210,000 km^3 of basalt and basaltic andesite (Fig. 1a) (Reidel et al., 2013; Kasbohm and Schoene, 2018). The largest formation of the CRB, the Grande Ronde basalts (149,000 km^3), was erupted over a timespan of <400 kyr (Kasbohm and Schoene, 2018). This implies average eruption rates of ~0.37 km^3/year. In the CRB, mapping of flow fields suggest eruptions persist for more than a decade (e.g. Thordarson and Self, 1998). However, other studies, based on analysis of inter-mixing flows (e.g.

Reidel, 1998), have suggested that eruptions persist for only a few months. The lavas in the CRB are also crystal-poor (Reidel et al., 2013), so geospeedometry, geothermometry, and cosmogenic surface exposure techniques are difficult to apply here.

The highest density of exposed CRB dikes is found in the Cretaceous Wallowa Mountains (Fig. 1b). In particular, dikes near Maxwell Lake (Fig. 1c) have been the subject of previous studies (e.g. Petcovic and Grunder, 2003; Karlstrom et al., 2019; Bindeman et al., 2020). Much of the overlying CRB flows in the Wallowa Mountains have been eroded away so the true paleodepths of the dikes are not known, but Petcovic and Dufek (2005) argue that depths could be as great as 2.5 km. Perry-Houts et al. (2020), based on structure contour mapping of the CRB basal contact, refine the paleodepth of Maxwell Lake area (Fig. 1c) to at least ~400m, so we estimate a total paleodepth (including ~1 km of prior Imnaha basalts) of ~1.5 km. Dikes in the Grande Ronde river canyon (Fig. 1b) have basaltic wall-rock consisting of earlier CRB flows and generally represent <1 km paleodepths (Table 1).

3. Methods

3.1 Sample Collection

We attempted to sample the longest-lived dike segments by targeting feeder dikes to the Wapshilla Ridge member of the CRB, which is among the largest single volcanic units in the world (40,000 km^3, Reidel et al. (2013)). At least two of our dike segments feed this unit (Maxwell A and Jackson A, Table 1). These segments are rimmed by 2–5 m of partial melt on either side (Fig. 2a), a rarity in the Chief Joseph dike swarm (only ~3% of Chief Joseph dikes bear outcrop scale evidence for partial melting of host rocks;

Morriss et al. (2020)). The combination of these attributes suggest that these segments represent some of the longest total durations of magma transport that the CRB have to offer. We also targeted dikes with clear physical connections to surface flows (Fig. 2b, 2c), to constrain the range of variability in established feeders to surface eruptions.

We collected geochemical and paleomagnetic samples from eight dike segments of the Chief Joseph dike swarm (Tables 1, S1) (Taubeneck, 1970). Studied segments span a range of thicknesses from 2–20 m (the average thickness of Chief Joseph dikes is ~8 m; Morriss et al., 2020). At each site, one or more sampling transects were performed across the dike and surrounding wall-rock (Fig. 2a). Paleomagnetic cores were collected using a handheld electric drill at all of the Grande Ronde Canyon dike segments (Fig. 1b). These cores were oriented using a Pomeroy orientation device and sun compass measurements when possible. Oriented block samples were collected at the Maxwell Lake segments (Fig. 1c) due to their location in a wilderness area. Sun compass measurements were used to orient the blocks when possible. Any large gaps in block sampling profiles are likely due to a lack of sampleable outcrop. Each block was taken back to the lab and two or more cores (2.54 cm diameter) were drilled into each sample when large enough. Some samples were too small to drill multiple cores while still preserving the orientation markings (e.g. JKA 4, Table S3). Specimens were cut from each core, which were typically 0.5–1 cm in height and 2.54 cm in diameter. Declination corrections were calculated using sun compass measurements when available or using the NOAA geomagnetic field calculator.

3.2 Rock Magnetism

To determine the magnetic mineralogy of the samples, thermal-susceptibility curves were measured from representative samples. These data are also used to determine the Curie temperatures (T_c) of the samples, which are necessary for the thermal modeling (see Section 3.4.1). Measurements of thermal-susceptibility curves were performed using an AGICO Multi-Function Kappabridge instrument. The samples were heated from room temperature at a rate of 9 ºC/minute, at an operating frequency of 976 Hz, and field intensity of 200 A m^{-1}. Maximum temperatures reached were 700 ºC, and all experiments were run in an argon atmosphere to minimize oxidation effects. Background 'noise' was removed via the subtraction of a blank sample (run under identical conditions) using AGICO's *Cureval* software.

3.3 Demagnetization

All paleomagnetic samples were measured on a 2G Enterprises vertical SQUID magnetometer with RAPID automatic sample changer (Kirschvink et al., 2008). The magnetometer is housed in a shielded room with a background field of ~200 nT. Samples at some sites were subject to 20-step thermal demagnetization (100–600 °C), while other samples were subject to 20-step alternating field demagnetization (1.6–90 mT). Some samples were also subjected to two rounds of liquid nitrogen immersion after measurement of NRM in order to enhance the signal of finer (single domain) magnetite grains (Dunlop, 2003), followed by either AF or thermal demagnetization. Characteristic remanence directions were very similar regardless of demagnetization technique. Sample analysis was done using the DemagGUI program as part of the PmagPy software package

(Tauxe et al., 2016). Principal component analysis (floating best-fit lines, no origin) was used to determine best-fit directions (Kirschvink, 1980). Maximum angle of deviation (MAD) is reported to assess goodness of fit (Kirschvink, 1980). Best-fits with >16 MAD were excluded from further analysis. Detailed sample statistics are reported with each transect in Table S3.

3.4 Magnetic Geothermometer (MGT)

To estimate the total amount of time that each dike segment was transporting magma (hereafter called the intrusion 'lifetime'), we combine two established and complementary techniques described below.

3.4.1 Baked Contact Test

First, samples from an intrusion and surrounding wall-rock are used for a *baked contact test*. This paleomagnetic technique is used to identify thermal overprinting and resetting of paleomagnetic data in the wall-rock near an igneous intrusion (Graham, 1949; Collinson, 1983). The test can be used to determine which samples have exceeded their Curie temperature (T_c) or blocking temperature (T_b). Samples that are heated above T_c are magnetically 'reset' and the direction of their remanent magnetism will match that of the dike (Fig. 2a). Samples that remained below T_c and T_b will retain their original paleomagnetic direction, though a portion of their magnetization may be altered to match that of the dike (Dunlop and Özdemir, 1997). Crucially, the transfer of heat from dike to wall-rock is a time-dependent diffusive process; short-lived intrusions will reset a small volume of wall-rock compared to long-lived intrusions. Here we construct a conservative

upper limit to the duration of wall-rock heating by assuming that resetting occurs at 580 °C (T_c of pure elongate magnetite grains) for all samples. Our rock-magnetic data (Fig. S9) suggests that this is a reasonable assumption; see section 4.2 for further details.

3.4.2 Thermal Modeling

Next, we model the heating of wall-rock by a dike, in order to interpret the distance between a dike margin and effective T_c isotherm (hereafter called the Curie distance or D_c, Fig. 2a) in terms of active magma transport that provides a transient heat source. In this study, we use a one-dimensional multi-component thermal conduction and melting model implemented by Karlstrom et al., (2019) (Fig. 3), which simulates continuous magmatic flow through a dike followed by cooling in-place. Several simplifying assumptions are made in this model, some of which are discussed below. Additional model information may be found in Section S5 of the Supplementary Material.

Flow of magma is parameterized by a time-evolving dike/host rock contact temperature. While active, the interior temperature $T_d(t)$ of the dike up to the contact is assumed to be spatially uniform but unsteady in time t (up to a total active duration τ_f) according to

$$T_d\left(t < \tau_f\right) = \frac{T_l - T_{bdy}(t)}{2}\left(1 - \tanh\left[10\frac{(t-\tau_c)}{\tau_w}\right]\right) + T_{bdy}(t). \quad (1)$$

Here T_l is the liquidus of the basalt within the dike, and $T_{bdy}(t)$ is the temperature of the host rocks at the dike contact, which evolves in time as conduction proceeds and host rocks heat up. The vigor of actively flowing magma is modeled by two timescale parameters in Equation 1—the parameter τ_c is a measure of flow duration, while τ_w

models a monotonic decrease of dike boundary temperature as might occur during declining flow. The total duration of dike flow (the 'dike lifetime') τ_f is defined to be the time at which $(T_d(t) - T_{bdy}(0))/(T_l - T_{bdy}(0)) = 0.01$, and is a linear combination of τ_c and τ_w (Fig. 3).

The impact of these timescales on the dike-contact thermal history and subsequent wall-rock time-temperature paths is illustrated in Fig. 3, varying τ_w at constant τ_c. As demonstrated by detailed studies of advection and conduction within a dike (e.g. Petcovic and Dufek, 2005), progressive cooling and associated decline of flow within a dike involves the growth of thermal boundary layers within the dike (and eventually freezing of magma) that cause the hot and near-isothermal core of the dike to retreat from the dike margins in time. Our kinematic approach avoids explicit treatment of unsteady flow within the dike, and thus cannot uniquely resolve contributions to dike margin temperature from viscous dissipation versus driving pressure gradients in the flowing magma (e.g. Fialko and Rubin, 1999). However, with only two parameters, we can effectively explore both the overall timescale of dike flow and the role of flow transience to match thermal constraints from wall rocks that encompass a range of magma transport scenarios.

A grid search over model parameters constrains the range of possible dike segment lifetimes. Time-temperature histories recorded by D_c are sensitive to a range of parameters including background temperature of the crust, thermal conductivity, and composition-dependent melting of host and dike material (Karlstrom et al., 2019). However, given the large contrast between T_c and initial temperatures of near-surface wall-rocks and the relatively small thermal mass of dikes, the parameters that most

strongly affect D_c are those that control the duration of heating by the dike by magma flow. These parameters, τ_c and τ_w, trade off with thermal conductivity of host rocks (Fig. S29) to control D_c, while dike widths or paleodepths in the range of CRB dike exposures (2–10 m widths and 0–2 km depths; Table 1) are not significant. In the case of a flow fed by a single feeder dike, the lifetime of the dike corresponds to the total duration of the eruption itself. Conversely, if a dike exhibits non-monotonic flow the lifetime will be a time-integrated measure of the dike's thermal footprint on host rocks.

3.4.3 MGT Summary

To summarize, the MGT technique combines the baked contact test (Fig. 2a) with a thermal model of the intrusion (Fig. 3). Thermal models have previously been applied to baked contact tests (e.g. Buchan et al., 1980; Kristjansson, 1985), and to planetary thermoremanent magnetization (e.g., Lillis et al., 2009), but overall this approach has been under-utilized given its applicability to most igneous systems. MGT works equally well on young (< 1 Ma) and old (e.g., Ga) magmatic systems, as it relies on thermal effects as opposed to radioactive decay. In addition, MGT can also be applied to any host rock containing magnetic minerals that have not been significantly altered or reset since time of reheating.

3.5 Geochemistry

The link between dike segments and lava flows is established on the basis of composition, as physical connections between subsurface transport structures and eruptive deposits are rare in the CRB (Camp et al., 2017). Major oxide and minor element

abundances were determined for 15 samples by X-ray fluorescence spectrometry (Table S1). All samples were analyzed using a Panalytical Zetium XRF system at the California Institute of Technology. Major and minor elements were analyzed using fused-glass beads. Following loss on ignition (LOI) determined at 1050 °C, samples were mixed with 9 times their weight in 66.67% $Li_2B_4O_7$–32.83% $LiBO_2$–0.50% LiI flux and fused at 1200 °C.

Unit assignments are based on magnetic polarity (this study, Camp et al., 2017), geologic maps (e.g. Reidel et al., 1992), least-squares regressions to previously published average geochemical compositions of CRB members (Reidel et al., 1992, 2013; Hooper, 2000; Reidel and Tolan, 2013), and mapped extent of flow units (e.g. Reidel and Tolan, 2013). See Section S1 of the Supplementary Material for more information.

4. Results

4.1 Dike Observations and Chemistry

A brief summary of observations from each dike segment is below, and more detailed descriptions of each dike segment, including field photos, are available in Section S2 of the Supplementary Material. We note that four out of eight dike segments studied here are not found in the extensive Chief Joseph dike swarm maps generated by William H. Taubeneck (Morriss et al., 2020).

The Jackson A dike features a ~2.5 m wide partial melt zone in the wall-rock on either side, which is marked by weathering-resistant granitoid in Figure 2a and Figure S1. Geochemical data from this segment (Table S1) do not match any CRB flow, which may be due to assimilation of partially melted wall-rock. Two sampling transects were done

here, on either side of the dike (Figs. 2a, S1). Disconnected outcrops of this dike can be followed along-strike to the Maxwell A dike (Fig. 1c). These dike segments are thus likely part of the same structural dike system. The western margin of the Maxwell A dike segment features a 2–5 m thick partial melt zone in the wall-rock (granitoid, Fig. S2). The eastern margin is poorly exposed due to erosion. The composition of Maxwell A (Table S1) matches the Wapshilla Ridge member of the CRB, which is the largest member by volume (40,000 km^3).

The Maxwell B dike is ~250 m from the Maxwell A dike (Fig. 1c) and several other dikes are present in this hillside (all hosted in granitoid, Fig. S3). A composition reported in Table S1 suggests that this segment is associated with the Wapshilla Ridge member as well. Given the similarities in composition and the close proximity of the Maxwell A and B dikes, we hypothesize that they were part of the same magmatic event. Unlike the other two dikes in this area, this dike does not feature an obvious partial melt zone in the wall-rock at outcrop scale.

The Tunnel dike (Fig. 2b) is hosted in earlier CRB flows, and three sampling transects were done at this segment—one in a flow interior on the western side, one in a flow interior on the eastern side, and one in a vesicular flow top on the eastern side (Fig. S4). The composition of this segment matches the Umatilla Member of the CRB (720 km^3, Table S1) (Reidel et al., 2013).

The Powatka Bridge dike (Figs. 1b, 2c, S5) is hosted in earlier CRB flows, has several internal quenched margins, and is likely composite with an unknown number of events (Ross, 1983). Therefore, our results capture an integrated thermal history of the dike segment. This might represent the oldest portion if re-injections happened in the

middle of the dike, although there is no evidence that this temporal stratigraphy is robust (and indeed, asymmetries in D_c seen at other dikes could be explained by multiple injections that are not centered). We assume that the lifetime reported in Table 2 represents the duration of a single diking event. Although the vent that is fed by this dike is not preserved, the Elephant Mountain member immediately overlies the dike (Fig. 2c) and it can be assumed that this dike breached the paleosurface. The composition of this dike segment matches the Elephant Mountain member of the CRB (440 km^3) (Reidel et al., 2013).

The Rattlesnake A dike (Figs. 1b) is part of a swarm of subparallel dikes related to the Roza member of the CRB that outcrop over a lateral extent of ~500 m (Thordarson and Self, 1998). Roughly a dozen other Roza dikes (all hosted in earlier CRB flows) have been found within 0.5 km of this site (Fig. S6). The Rattlesnake A segment is only ~2 m wide, and probably not a major contributor of magma transport in this dike swarm.

The Eagle dike (Fig. 1b) appears to be a single-injection event with a jointed core and finely fractured (quenched) margins (Fig. S7). All compositions reported from the core and margins of this segment match the Buford member (Table S1) (Reidel et al., 1992). This dike is hosted in earlier CRB flows.

Finally, the Boggan's Oasis dike (Fig. 1b) also has a jointed core and finely fractured margins, with no internal quenched zones, suggesting a single injection event. This dike is hosted in earlier CRB flows (Fig. S8), and its chemistry suggests an association with the Museum flow of the Sentinel Bluffs member (2349 km^3, see Section S1).

4.2 Rock Magnetism

Thermal-susceptibility data show that most wall-rock samples have a T_c of 570–580 °C (Table S2). Some thermal-susceptibility curves show evidence for one pure magnetite phase (Fig. S9a), while others show evidence for multiple phases with multiple Curie temperatures (Fig. S9c). When applying the MGT technique, the highest T_c that is measured in the sample is of greatest importance. Previous studies have found that Curie temperatures can be affected by prior thermal histories such as heating by a dike (e.g. Bowles et al., 2013). However, samples typically have lower T_c *after* heating. This is evident in our dataset, where T_c is either unaffected by heating, or is higher during heating than during cooling (Table S2, Fig. S9). A double-heating experiment (Fig. S9d) shows the permanent effects of sample heating on the measured T_c. Since most of our samples still have a T_c near 580 °C, we conclude that these samples did not experience lowering of T_c due to dike heating, and therefore assume a T_c of 580 °C is reasonable for all sites in our thermal models. Sensitivity tests with T_c = 570 and 550 °C suggest that variable Curie temperatures will lead to estimated dike lifetime differences of <8% (Fig. S31).

4.3 Paleomagnetic Directions

The Jackson A dike and wall-rock within the resetting zone preserve a reversed magnetic polarity (Fig. 4a, 4b). We found a D_c of 3.7–5.4 m and 5.6–7.4 m from the hanging wall and footwall sides of the dike, respectively (Table 2). Wall-rock samples that are outside of the resetting zone are very poor recorders of paleomagnetic direction. We have plotted best-fit lines in Figure 4b when possible, but these are not primary

thermal remanent magnetization directions from the cooling of the granodiorite batholith. Instead, they are likely recording the modern paleomagnetic field direction via a weak viscous remanent magnetization (Yu and Tauxe, 2006).

The Maxwell A dike and wall-rock within the resetting zone also preserve a reversed magnetic polarity (Fig. 4c, 4d). We found a D_c of 5.8–8.5 m (Table 2), and only one wall-rock sample was not reset (MXA 5).

The Maxwell B dike preserves a reversed magnetic polarity, while the wall-rock samples only have a viscous remanent magnetization (Fig. 4e, 4f). In this case, the closest wall-rock sample (1.15 m from the dike margin) was not reset, so there is no firm lower bound on the MGT-determined lifetime at this exposure (Table 2). Primary remanence directions from the Maxwell A and B dikes are both reversed, but notably different (Fig. 4d, 4f). This suggests that the Maxwell B dike is associated with a different Wapshilla Ridge flow than Maxwell A or Jackson A, as this unit is composed of >18 flows that are geochemically similar (Reidel and Tolan, 2013).

At the Tunnel Dike (Fig. 1b), the dike and wall-rock within the resetting zone preserve a normal magnetic polarity (Figs. 4g, 4h, S16). Wall-rock samples that are outside of the resetting zone preserve a reversed magnetic polarity. On the western side, D_c is well constrained to 60–66 cm from the dike margin (Table 2). On the eastern (footwall) side D_c is 18–30 cm in the flow interior and 18–26 cm in the flow top. We expect fluid flow and circulation to be more prevalent in the vesicular flow top, but our results suggest that this did not have a significant impact on D_c.

The Powatka Bridge dike preserves a transitional magnetic polarity (Fig. 4i, 4j), which is in agreement with previous measurements from the Elephant Mountain member

(Choiniere and Swanson, 1979). Wall-rock samples preserve a normal magnetic polarity. None of the wall-rock samples were reset by the dike, so the MGT-determined lifetime reported in Table 2 does not have a firm lower bound.

The Rattlesnake A dike preserves a reversed direction, and wall-rock samples also preserve a reversed magnetic polarity (Fig. 5a, 5b). In this case it is not initially clear if any wall-rock samples have been reset by the dike, but several lines of evidence suggest that extensive resetting has not occurred here. The average dike direction is D=189.6, I=-56.9, $a95$=15.1, N=3, while the average wall-rock direction is D=168.8, I=-42.1, $a95$=5.3, N=12. The test of mean directions (Fisher et al., 1993) can be applied to these averages to determine their degree of similarity. Applying the test yields a 0.01% confidence that the dike and wall-rock mean directions are the same. See Section 4.5 for further discussion.

The magnetization preserved in the Eagle is complex (likely due to a nearby lightning strike, Fig. 5c, 5d), and a discussion of these results is included in Section S4.7 of the Supplementary Material. We conclude that both the dike and wall-rock samples preserve a reversed magnetic polarity. Again it is not initially clear if any wall-rock samples have been reset by the dike, but several lines of evidence suggest that extensive resetting has not occurred here either. The average (reversed) dike direction is D=218.8, I=-46.5, $a95$=11.8, N=5, while the average wall-rock direction is D=216.6, I=-55.3, $a95$=1.9, N=23. Applying the test of mean directions (Fisher et al., 1993) to these data yields a 8.3% confidence that the dike and wall-rock mean directions are the same. See Section 4.5 for further discussion.

Finally, at the Boggan's Oasis dike, the wall-rock and dike directions show significant scatter (Fig. 5e, 5f). Given the scattered nature of these data, we conclude that

the MGT technique cannot be applied in this instance. For example, the closest sample (BD2 6, Table S3) is 5 cm from the dike margin and would be reset regardless of dike lifetime. However, this resetting is not clearly evident in the highly scattered data from this dike (Fig. 5f).

4.4 Magnetic Geothermometer

After conducting baked contact tests, the thermal model can now be used to determine which range of dike lifetimes will produce the measured D_c (Figure 6 and Table 2). Where possible, we have defined D_c on both sides of a given dike segment. Dike segment lifetimes range from 0–6 years, but these lifetimes are not distributed evenly between the sites. All four dikes in the Grande Ronde Canyon (Fig. 1b) show relatively short lifetimes of $\lesssim$ 1 year (Fig. 6a). At four dike segments (Maxwell B, Powatka Bridge, Rattlesnake A, and Eagle) the closest samples to the dike were not reset, so there is no lower bound on the MGT-determined lifetimes (Fig. 6a; Table 2).

Two dike segments in the Maxwell lake area (Jackson A and Maxwell A; Fig. 1c) show relatively long lifetimes of 1–6 years (Fig. 6a; Table 2), which is expected given the zones of partially melted wall-rock surrounding these segments (Fig. 2a). This range of uncertainty is primarily controlled by the relative proportion of flow unsteadiness τ_w to active lifetime in the thermal model (Fig. 3, 6a). While flow duration and unsteadiness can vary between dike segments, the efficacy of heat transport through wall-rocks is not expected to vary greatly between nearby dike segments. The Maxwell A and Maxwell B segments are ~250 meters from each other (Figs. 1c, S3) and hosted in granodiorite with minimal macroscopic fracture density at the same paleodepth. This same logic applies to

the studied dike segments within basaltic host rock (Fig. 1b). Thermal conductivity and degree of fluid-mediated heat transport might in principle vary between sites, as articulated by an ongoing debate about the general role of meteoric fluids in alteration of CRB rocks (Sawlan, 2017; Baker et al., 2019). However, variations in active magma flow are the simplest and hence most plausible way to account for the high temperature variation seen in D_c from our data. The trade-offs between these variables are shown in Figure 3.

4.5 Non-Ideal Results

Two sites have a reversed magnetic polarity in both the wall rock and dike (Figs. 5b, 5d). This makes it more difficult to determine which wall-rock samples have been reset by the dike. At the Rattlesnake A dike (Fig. 5b), resetting of all wall-rock samples would require an unrealistic dike lifetime of 1–4.3 years, which is inconsistent with field observations of this dike segment (quenched margins, no partial melt in wall-rock). Given that the Rattlesnake A segment is one of dozens in the Roza dike swarm (Fig. S6; Thordarson and Self, 1998), this narrow dike segment was probably not a long-lived principal feeder segment to the Roza member. The inset portion of Figure 5b shows that wall-rock samples within 1 m of the dike margin (5, 6, 7, and 8) are not systematically similar in direction to the dike samples. Together, this evidence (along with the test of mean directions, Section 4.3) suggests that no samples were reset. Nevertheless, the MGT-determined lifetime reported in Table 2 is less certain than the lifetimes of other dikes. See the section S4.6 of the Supplementary Material for additional information.

At the Eagle dike (Fig. 5d), resetting of all wall-rock samples is effectively impossible as it would require a dike lifetime of >10 years, which is inconsistent with field observations of this dike segment (quenched margins, no partially melted wall-rock). The dike feeds one of the smallest CRB members (Buford, 20 km^3) (Reidel et al., 2013) and shows no field evidence for multiple injections. There appears to be no systematic variation in the wall-rock direction, as shown in the inset portion of Figure 5d, which highlights samples that are within 1 m of the dike margins. The closest wall-rock samples are not systematically similar in direction to the dike samples. This evidence (along with the test of mean directions, Section 4.5) again suggests that no samples were reset. We are less certain of this interpretation at this dike than at Rattlesnake A, and additional data could disprove this assumption, so the MGT-determined lifetime reported in Table 2 is less certain than the lifetimes of the dikes previously discussed.

5. Discussion

5.1 Agreement with Previous Studies

The MGT results presented in this study are in agreement with previously published results from other methods at our study sites (Fig. 7). Reidel (1998) suggested that the Tunnel dike, and its associated vent, were active for a few months or less based on flow mapping, geochemistry, and thermal modeling. Studies of the Maxwell A dike (Petcovic and Grunder, 2003; Petcovic and Dufek, 2005) used mineral chemistry from partially melted host rocks to estimate that the dike segment was active for 3–4 years. (U-Th)/He thermochronology of the Jackson A dike segment suggested an active lifetime of 1.4–5.4 years (at 68% confidence from a Bayesian inversion; Karlstrom et al., 2019),

which matches models for oxygen isotope depletion observed around that segment which accounts for advective fluid-mediated heat transport in wall-rocks (Bindeman et al., 2020). Consistency between MGT and other independent estimates provides confidence in the accuracy of this method when applied to sites that are not amenable to study with the techniques listed above.

5.2 Heterogeneity in dike thermal footprints

The CRB are associated with over four thousand mapped dike segments (Morriss et al., 2020), but it is an open question regarding how many of these segments actively fed flows and for how long. While the eight segments analyzed in this study are not a representative sample of the entire system, they provide an important baseline that illustrates the likely variability in shallow crustal magma transport for the flood basalt province.

Two nearby dikes (Maxwell A and Maxwell B, Fig. 1c) have the same composition (Wapshilla Ridge Member, Petcovic and Grunder (2003)). However, these dike segments have different D_c (Table 2), suggesting that dike segments feeding the same eruptive episode were not active for the same amount of time. A nearby dike (Jackson A) is likely another segment of the same dike as Maxwell A, as they are on-strike with each other and only ~1 km apart (Fig. 1c). Both segments exhibit evidence for prolonged transport and heating, but differences in the amount of partially melted wall rock suggest that they may not have been active for the same amount of time either. Based on these observations and our results, we conclude that flow localization resulted in variable durations of magma transport within CRB dikes. Table 2 shows that the

studied dike segments have a broad distribution of D_c, with consistent but sometimes asymmetric heating on either side of the dike segment. If multiple injections occurred (e.g. Thiele et al., 2021) they do not need to intrude along the dike centerline, so such non-monotonic thermal histories are one way to explain the slight asymmetries in D_c observed in our data.

5.3 Links to Eruption Style

MGT results suggest that some dike segments can be active for less than one month (Table 2). Given the large effusive volume of CRB eruptions, this implies a fissure-style eruption characterized by very high eruption rates if the segments with small D_c were active feeders to observed flows (e.g. Fig. 2b, c). However, it is also possible some segments of a given dike were actively erupting over months or years while other segments were essentially inactive. This is a plausible explanation for our variety of MGT results (e.g., the distributions of τ_w and τ_c) and the field evidence for long versus short eruption durations (e.g. Reidel, 1998; Thordarson and Self, 1998). The MGT evidence for closely separated portions of a dike system with dissimilar transport times suggests along-strike localization of flow during the eruption. This behavior, common to historic basaltic fissure eruptions (e.g. Thordarson and Self, 1993), has been explained through thermoviscous focusing (e.g. Wylie et al., 1999) or mechanical erosion associated with wall-rock fracturing (e.g. Delaney and Pollard, 1982).

5.4 Eruption Rates

Each dike can be linked to an associated CRB member (Table S1), and the volume and number of flows have been previously estimated for each member (Reidel et al., 2013; Reidel and Tolan, 2013). Assuming that our dike active lifetimes are representative of their associated eruptive units, we can calculate an *apparent* upper bound eruption rate per eruptive unit by dividing CRB member volume by the number of flows and MGT-determined dike lifetime. We use the full range of active lifetimes τ_f for each dike segment to provide rough estimates, with the understanding that variations in boundary temperature implied by variable τ_w reflect time variations in Q (Karlstrom et al., 2019).

The calculated eruption rates (Table 3, Figure 6b) are notably high in most cases. We assess their physical plausibility with a calculation of flow rates given known dike segment geometry: Assuming Poiseuille flow through a rectangular slot, flow rate Q is a function of segment width w and length L, with dynamic viscosity μ driven by pressure gradient $\frac{dP}{dz}$,

$$Q = \frac{w^3 L}{3\mu}\left|\frac{dP}{dz}\right|. \quad (2)$$

Assuming Q corresponds to the eruption rate determined by MGT, we can independently estimate parameters on the right-hand-side of Equation 3. Active length is poorly constrained, but historical basaltic fissure eruptions (Thordarson and Self, 1993), and rare exposures of CRB vent facies (Brown et al., 2014) suggest that lengths of ~1 km are likely appropriate. Measured whole rock compositions (Table S1) constrain liquidus viscosity (neglecting the effects of water) to be $\leq 10^3$ Pa s (e.g. Hui and Zhang, 2007), and buoyancy driven flow implies driving pressure gradients of perhaps several hundred

Pa m^{-1} (e.g. Rivalta et al., 2015). The greatest unknown, with cubic dependence in Equation 2, is width of active flow within the dike segment.

If the calculated eruption rate can be reasonably reconciled with the Poiseuille flow model using observed dike segment width (including uncertainty in width as a proxy for error in all parameters), then the segment is deemed a 'likely feeder segment' (Table 3, Fig. 6b). If the calculated eruption rate differs from the Poiseuille flow model, then the segment is deemed an 'unlikely feeder', indicating that our MGT transect happened to intersect a portion of the dike that did not significantly contribute to its associated eruption.

Two MGT profiles are self-consistent with preserved structures, implying volumetric eruption rates of 1.1–7.7 km^3 day^{-1} during eruption of the Wapshilla Ridge member (Fig. 6b, Table 3). This is >10 times the average Laki 1783 fissure eruption rate of ~0.09 km^3 day^{-1} (Thordarson and Self, 1993). Three segments are judged to be 'possible feeders', because some of the MGT-determined eruption rates are self-consistent with preserved structures. Finally, two segments are 'unlikely feeders' (Table 3, Fig. 6b) because their MGT-determined eruption rates are not physically possible according to our Poiseuille flow calculations (Fig. 6b)

5.5 Applicability to Other Flood Basalts

This study focuses on the CRB, which is the youngest and smallest flood basalt on Earth. Therefore, the applicability of these results to other flood basalt provinces that had larger total volumes and a larger impact on the global climate and biosphere is not immediately clear. Our maximum eruption rate estimates (1.1–7.7 km^3 day^{-1}) are several

orders of magnitude higher than long-term eruption rates calculated for the Deccan Traps (~0.002 km^3 day^{-1}; Schoene et al. (2019), Sprain et al. (2019)), Siberian Traps (~0.009 km^3 day^{-1}; Burgess et al. (2017)), and the CRB (~0.0009 km^3 day^{-1}; Kasbohm and Schoene (2018)). They are more comparable to (although still larger than) previous estimates of individual CRB units, such as the Roza (~0.55 km^3/day, Tolan et al., 1989). This is consistent with the notion that activity from both historic and LIP-related basaltic volcanism is highly unsteady in time even during prolonged eruptive episodes (Mather and Schmidt, 2021). Although the CRB are smaller than other flood basalts, the volumes of CRB main phase eruptions ($\gtrsim$1000 km^3; Reidel et al. (2013)) are similar to the volumes of Deccan eruptions (Self et al., 2008). The widths of CRB dikes (~8m on average; Morriss et al. (2020)) are similar to dikes in the Deccan Traps (Ray et al., 2006). Therefore, we hypothesize that other flood basalt eruptions operate on a similar range of timescales as described here.

6. Conclusions

We implemented a magnetic geothermometer for determining timescales of magma transport in igneous intrusions and applied this to eight CRB dike segments that likely fed known lava flows. We found a range of active transport lifetimes from several years to less than one month. Two dikes (Maxwell A and Jackson A) are rimmed by partially melted wall rock, and likely fed the largest member of the CRB at average rates of 1.1–7.7 km^3 day^{-1}. Our survey also finds segments that did not contribute significantly to associated eruptions, and evidence for composite structures. A resulting picture of the shallow (<2 km depths) CRB plumbing system emerges in which re-use of transport

structures that feed surface eruptions and along-strike localization of magma flow are commonplace. Transport durations can vary over short (<1 km) length scales along flood basalt dikes, which is consistent with transitions from fissure-style to conduit-fed eruptions. The implied shortening of individual eruption timescales compared to province-scale emplacement should have significant implications for short-term climatic effects of the CRB and other flood basalt provinces.

The MGT technique employed in this study complements other methods by providing thermal history constraints regardless of host rock composition and age. MGT results can be determined in the lab in a short amount of time and at a low cost. However, the single temperature constraint is somewhat limiting. As with other methods, MGT will provide better constraints when used in combination with other techniques. A clear theoretical advance would be to better understand the kinetics of partial magnetic resetting in titanomagnetites, which would increase the resolving power of MGT for time-temperature histories.

Acknowledgements

The authors wish to thank Samuel Piascik, Marcel Griffioen, and Sydney Acito for their assistance with the project. Matthew Morris is thanked for his digitization of CRB dike data and suggestions for where to sample. The University of Oregon field camp is acknowledged for logistical support. Anita Grunder is thanked for helpful discussions regarding previous work. Joseph Kirschvink is greatly thanked for helpful discussions and use of his paleomagnetic laboratory. This work was supported in part by NSF CAREER 1848554 to LK and a GSA AGeS2 award to JB.

Appendix A: Supplementary Material

Supplementary tables related to this chapter are available with the online version of this thesis. Additional supplementary material is included in this file, starting on page C-46.

Table 1

Summary of dike properties and geochemistry.

Dike name	Latitude	Longitude	Strike	Dip	Dike width (m)	Paleodepth (m)	Host rock	Partial melt?	Quenched zones?	Affiliation
Jackson A	45.25091	-117.40853	030	68 E	9.0	>1280	Granitoid	Yes	No	Wapshilla Ridge?
Maxwell A	45.25799	-117.40326	030	75 W	8.0	>1400	Granitoid	Yes	No	Wapshilla Ridge
Maxwell B	45.25896	-117.40026	332	80 E	9.5	>1425	Granitoid	No?	Margin	Wapshilla Ridge
Tunnel	46.02878	-117.16166	354	~ 90	19.5	940	CRB Lavas	No	Margin	Umatilla/Sillusi
Powatka Bridge	45.89931	-117.48303	345	~ 90	20.0	520	CRB Lavas	No	Margin & internal	Elephant Mountain
Rattlesnake A	46.05049	-117.23890	342	~ 90	2.0	300	CRB Lavas	No	Margin	Roza
Eagle	46.04171	-117.13275	345	~ 90	7.6	900	CRB Lavas	No	Margin	Buford
Boggan's Oasis	46.04456	-117.25452	336	~ 90	6.5	340	CRB Lavas	No	Margin & internal	Sentinel Bluffs - Museum

Table 2

Summary of paleomagnetic and MGT results from CRB Dikes. Distance is measured from the nearest dike margin, second transect is on the footwall side. 'Lifetime' refers to the total duration of magma transport in the dike.

Dike Name	Dike polarity	Wall polarity	D_c (m)[b]	D_c, 2nd transect (m)	MGT-determined lifetime
Jackson A	Reversed	Normal	3.7 - 5.4	5.6 - 7.4	0.8 - 5.0 years
Maxwell A	Reversed	Normal	5.8 - 8.5	--	0.9 - 5.6 years
Maxwell B	Reversed	Normal	0 - 1.15	--	< 0.5 years
Tunnel	Normal	Reversed	0.60 - 0.66	0.18 - 0.26	0.3 - 1.3 months
Powatka Bridge	Transitional	Normal	0 - 0.23	--	< 1.1 months
Rattlesnake A[a]	Reversed	Reversed	0 - 0.20	--	< 0.5 months[a]
Eagle[a]	Reversed	Reversed	0 - 0.65	0 - 0.28	< 1.4 months[a]
Boggan's Oasis[a]	Normal	Normal?	Unclear	--	--

[a]Both dike and wall-rock are the same polarity, see section 4.5.

[b]Distance between the dike margin and T_c 'isotherm'

Table 3

Eruption rates and Poiseuille flow calculations. Parameters are: μ = 1000 Pa s, L = 1000 m, $\partial P/\partial z$ = 300 Pa m^{-1}.

Dike name	Active width (m)	Total volume (km^3)	# of flows	Apparent eruption rate (km^3 day^{-1})	Poiseuille flow rate (km^3 day^{-1})	Conclusion
Jackson A	8 - 10	40250[a]	18	1.2 - 7.7	8.6 - 4.4	Likely feeder segment
Maxwell A	7 - 9	40250[a]	18	1.1 - 6.8	6.3 - 3	Likely feeder segment
Maxwell B	8.5 - 10.5	40250[a]	18	> 12.3	5.3 - 10	Unlikely feeder segment
Tunnel	8 - 20.5[c]	720[b]	2	9.9 - 33	4.4 - 74	Possible feeder segment
Powatka Bridge	8 - 21[c]	440[b]	1	> 12	4.4 - 80	Possible feeder segment
Rattlesnake A	1 - 3	1300[b]	5	> 18	0.01 - 0.2	Unlikely feeder segment[d]
Eagle	6.6 - 8.6	20[b]	1	> 0.5	2.5 - 5.5	Possible feeder segment[d]

Data from: Reidel & Tolan (2013)[a], Reidel et al. (2013)[b]

[c]Composite dikes are assumed to have a minimum width of 8 m, the CRB average (Morriss et al., 2020)

[d]Assuming no wall-rock samples are reset, see Section 4.5.

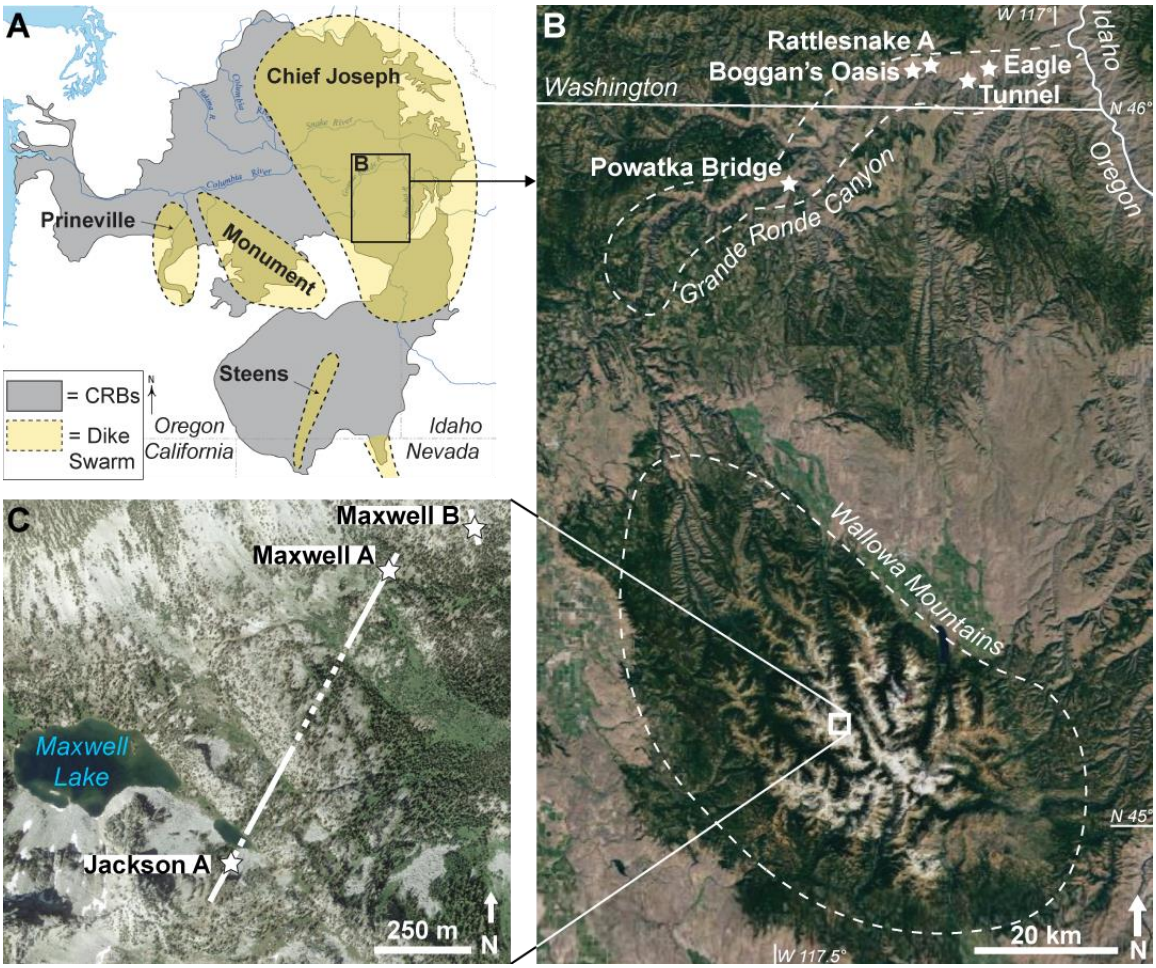

Figure 1 – ***A)*** *Map of the Columbia River Basalts and associated dike swarms. Lightly modified from Camp et al. (2017).* ***B)*** *Satellite image showing the locations of studied dikes in the Grande Ronde Canyon (hosted in earlier CRB flows) and the location of the Wallowa Mountains.* ***C)*** *Satellite image of the Maxwell Lake area, showing the locations of three dike segments (hosted in granitoid) that are likely related to the Wapshilla Ridge member of the CRB. Solid lines show where the dikes have been observed, dashed lines show where the dikes are covered. Imagery from Google Earth.*

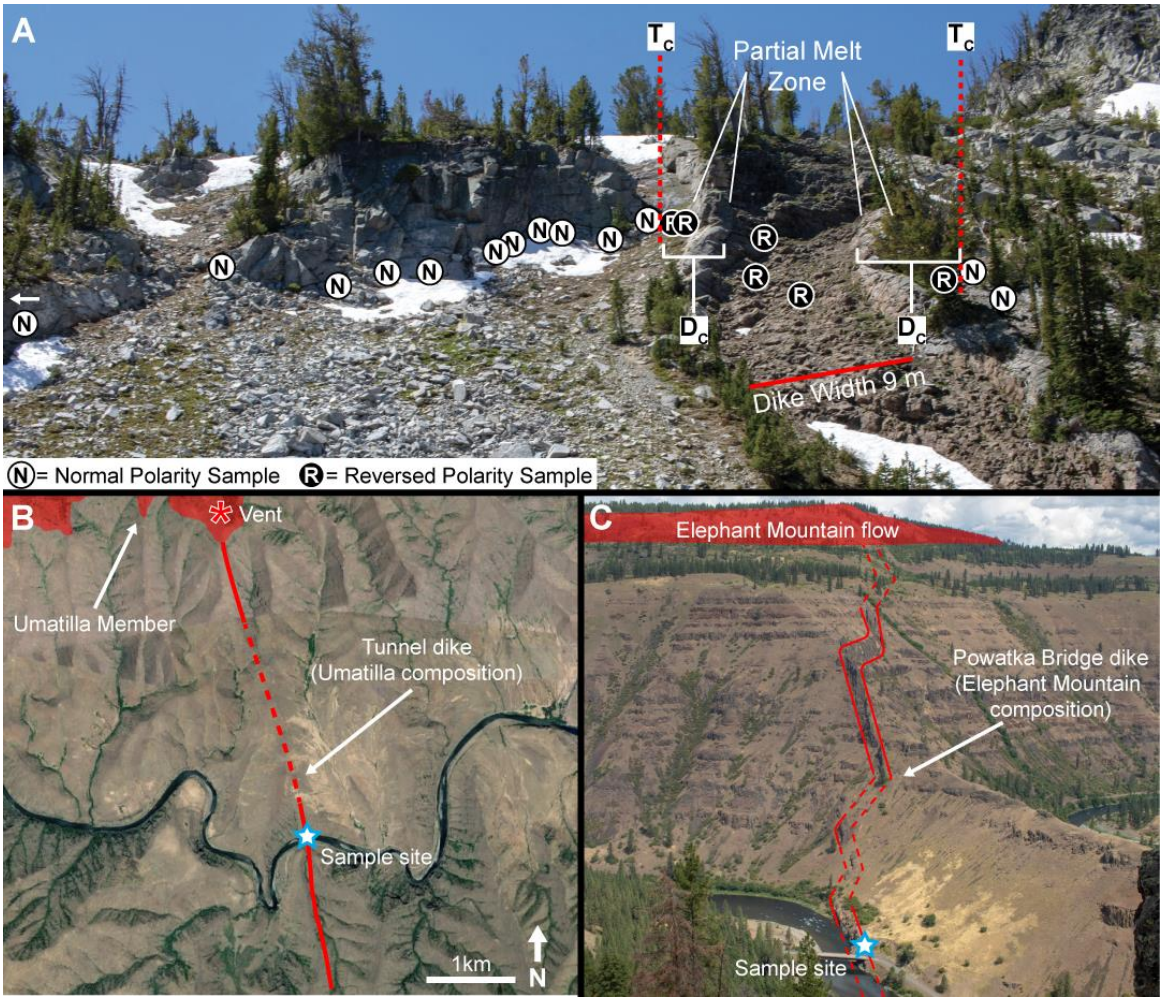

Figure 2 *– **A)** Sampling locations and results from the Jackson A Dike, looking southwest. T_c = location of Curie temperature isotherms, D_c = distance between Curie temperature isotherms and dike margins. Wall-rock samples outside the T_c isotherms retain some of their primary magnetic direction (normal), whereas those between the isotherms are thermally reset and their paleomagnetic direction now matches that of the dike (reversed).* **B)** *Map of the Tunnel dike (dashed where approximate) and associated vent. The dike has an identical composition to the Umatilla member of the CRB, which is shown in red. Imagery from Google Earth.* **C)** *Photo of the Powatka Bridge dike (outlined in red, dashed where approximate), looking northwest. The Elephant Mountain member of the CRB, which has an identical composition to the dike, is shown in red.*

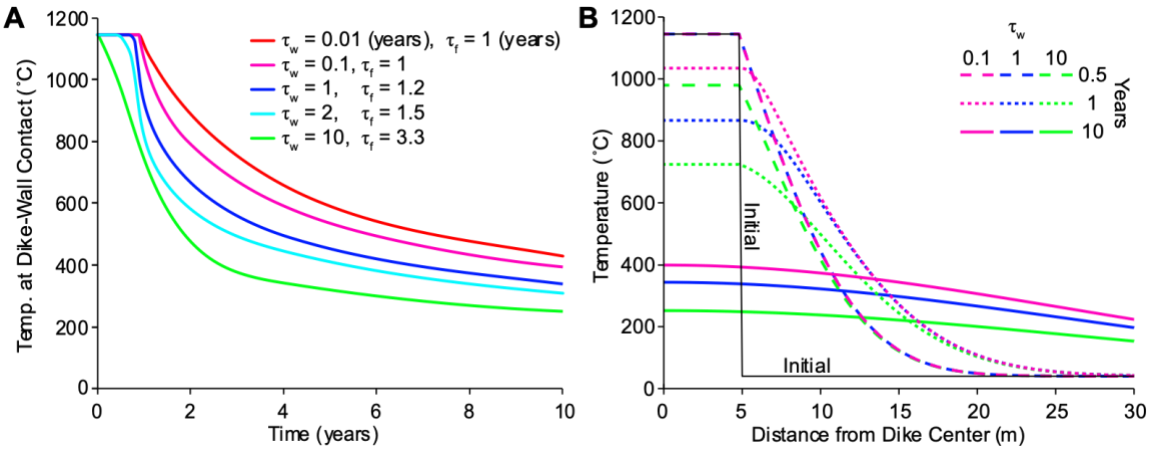

Figure 3 *– Effects of flow unsteadiness parameter* τ_w *on modeled thermal history for fixed flow duration parameter* τ_c *= 1 year.* ***A)*** *Temperature at the dike/wall-rock contact over time.* τ_f *= dike active lifetime. Note that the total dike lifetime* τ_f *increases with* τ_w *but the duration of high-temperature heating at the dike margin decreases.* ***B)*** *Temperature vs. distance from the center of the dike after 6 months, 1 year, and 10 years. Base conditions are: far-field background temperature = 40 °C, dike width = 10 m, thermal conductivity = 3 W* m^{-1} K^{-1}.

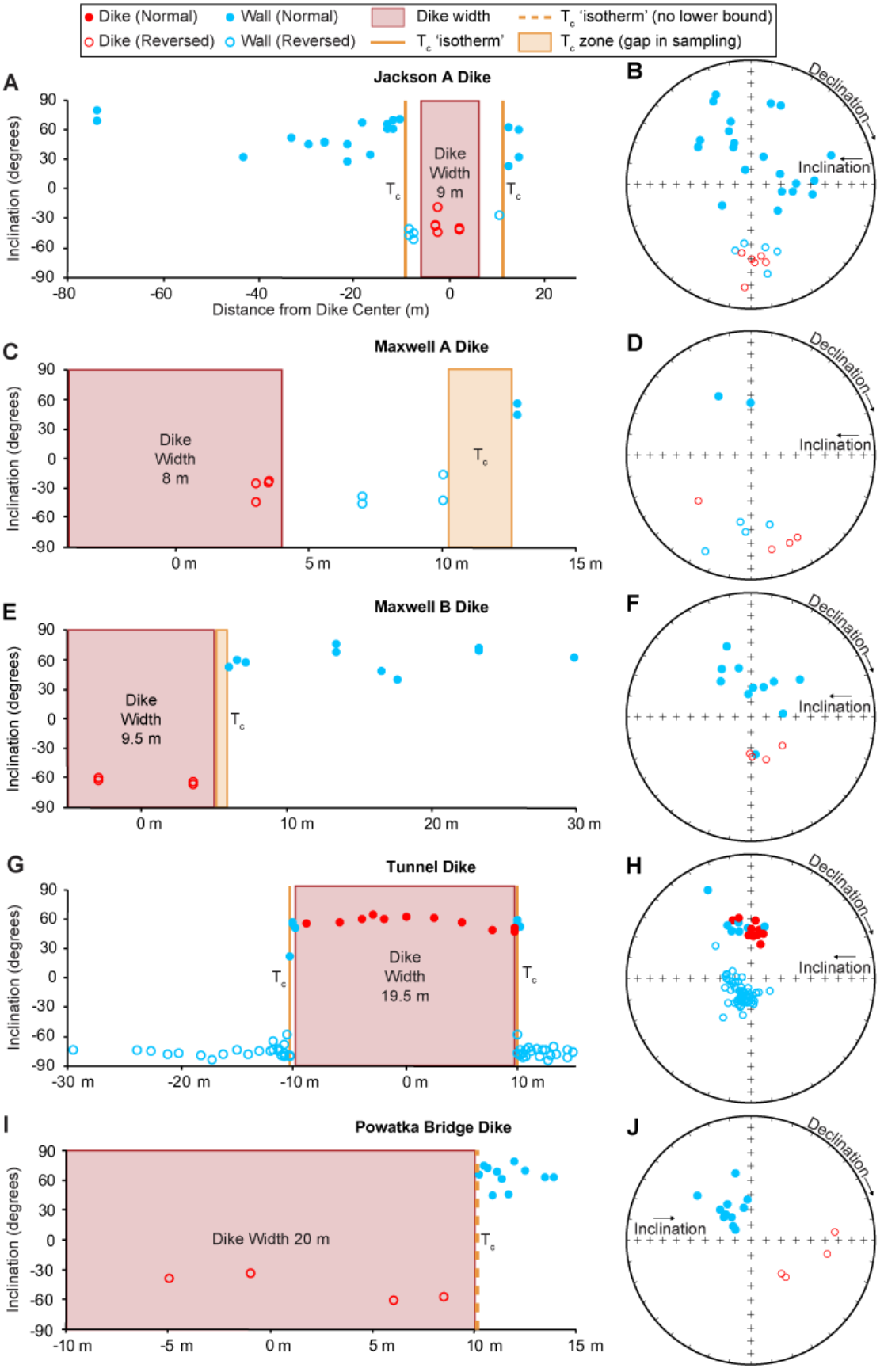
Dike (Normal)
Dike (Reversed)
Wall (Normal)
Wall (Reversed)
Dike width
T_c 'isotherm'
T_c 'isotherm' (no lower bound)
T_c zone (gap in sampling)
A
Jackson A Dike
Inclination (degrees)
Distance from Dike Center (m)
Dike Width 9 m
T_c
B
Declination
Inclination
C
Maxwell A Dike
Dike Width 8 m
0 m
5 m
10 m
15 m
D
E
Maxwell B Dike
Dike Width 9.5 m
0 m
10 m
20 m
30 m
F
G
Tunnel Dike
Dike Width 19.5 m
-30 m
-20 m
-10 m
0 m
10 m
H
I
Powatka Bridge Dike
Dike Width 20 m
-10 m
-5 m
0 m
5 m
10 m
15 m
J

Figure 4 *– Paleomagnetic results from five CRB dike segments where the dike and wall-rock have different polarities.* ***Left column)*** *Distance from the dike center (x-axis) vs. inclination of the primary paleomagnetic remanence (y-axis).* T_c *= Curie temperature 'isotherm'.* ***Right column)*** *Equal area projection showing primary remanence directions for each dike segment.*

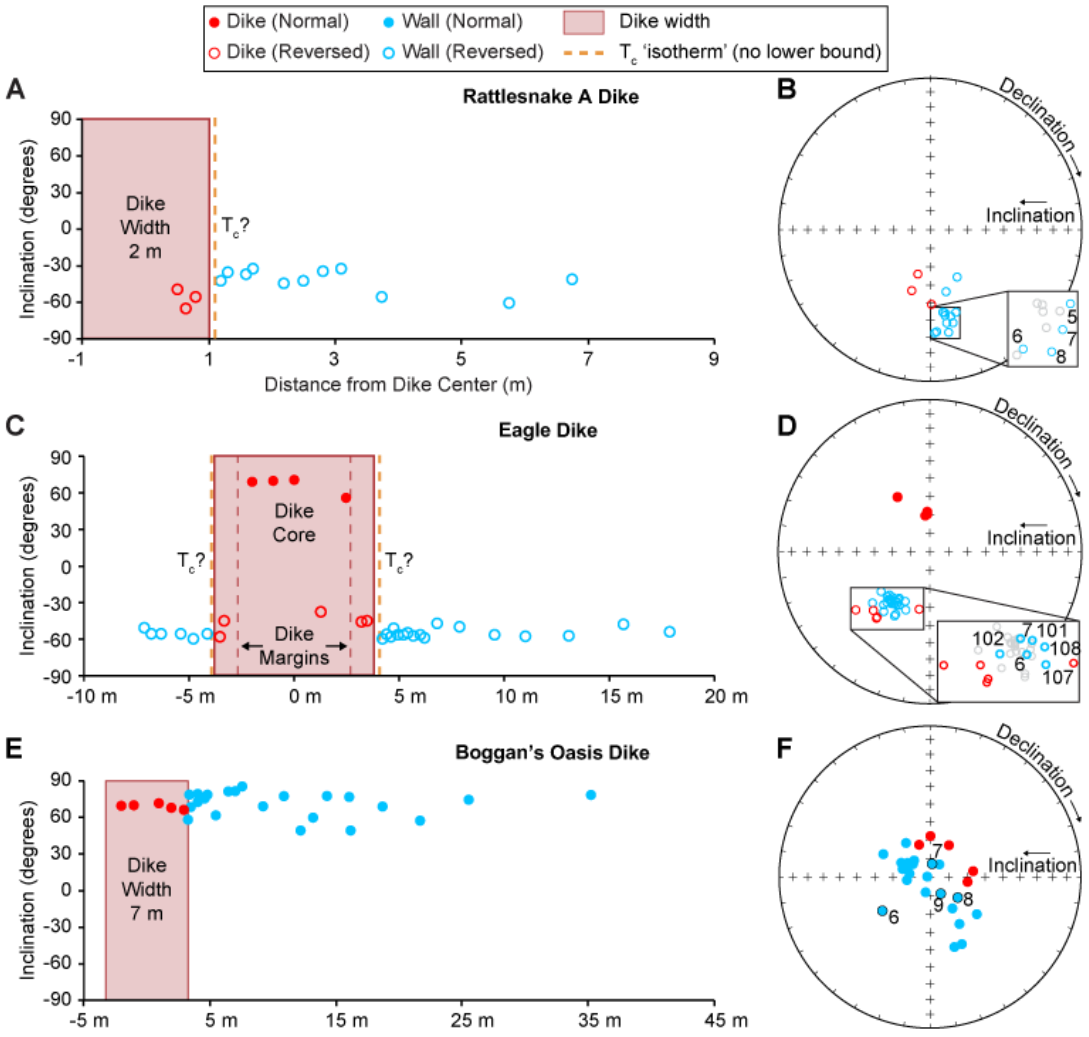

Figure 5 *– Paleomagnetic results from three CRB dike segments where the dike and wall-rock have the same polarity.* ***Left column)*** *Distance from the dike center (x-axis) vs. inclination of the primary paleomagnetic remanence (y-axis).* T_c *= Curie temperature 'isotherm'.* ***Right column)*** *Equal area projection showing primary remanence directions for each dike segment. Insets show wall-rock samples within 1 m of the dike in blue (with sample numbers, see Table S3), while more distant wall-rock samples are in grey. See Sections 4.3 and 4.5 for discussion.*

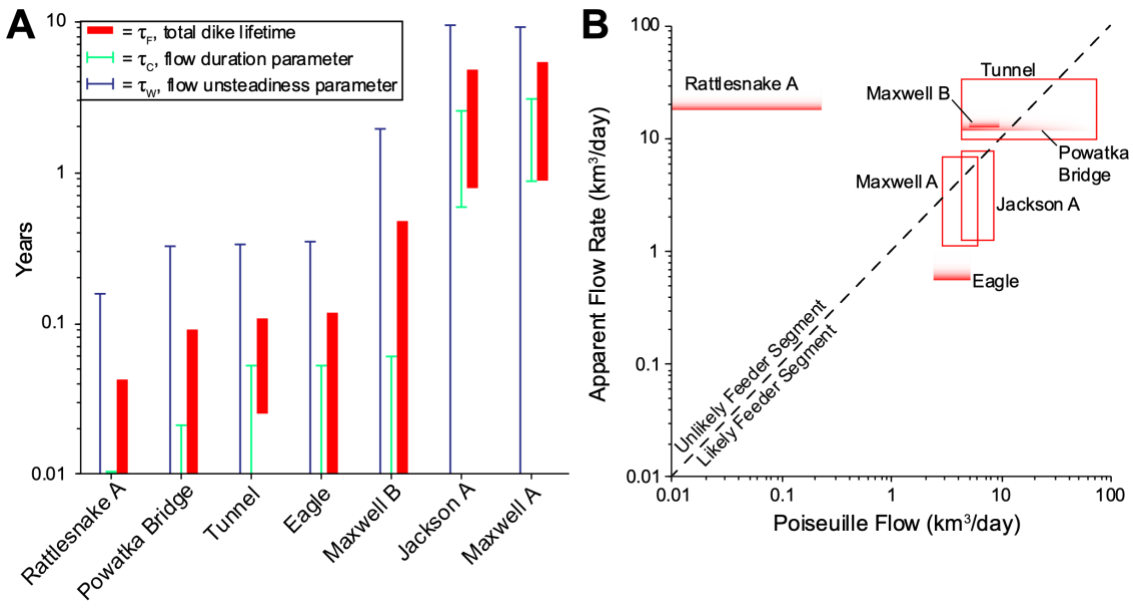

Figure 6 *– **A)** MGT results from seven dike segments in this study, showing a bimodal distribution of dike lifetimes (red bars). Blue and green lines indicate the range of uncertainty for each flow parameter in Equation 1 as determined by a grid search through* τ_c *and* τ_w *(Fig. S30). **B)** Results from flow rate calculations (y-axis, Table 3) plotted against the expected flow rates from Poiseuille flow calculations using outcrops to estimate dike width (x-axis). Horizontal width of symbol represents uncertainty in active width of the dike (see Table 3). Dike segments with only a minimum calculated flow rate are shown with a vertical gradient. See Section 5.4 for details.*

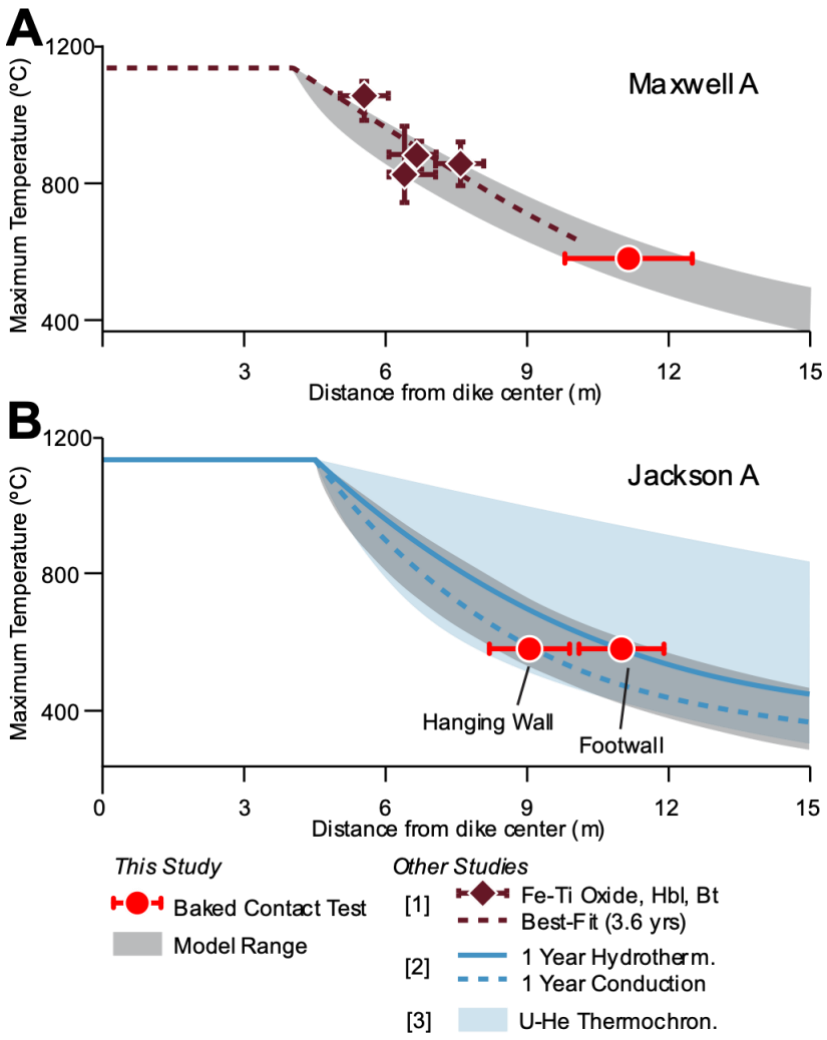

Figure 7 *– **A)** MGT results from the Maxwell A dike (red circles) compared to Fe-Ti oxide, hornblende, and biotite results from [1] Petcovic and Grunder (2003). The range of model solutions from this study that are in agreement paleomagnetic results is shown in grey.* ***B)*** *MGT results from the Jackson A dike (red circles). Greater D_c in the footwall side of the dike might arise from the non-planar dike geometry seen in Fig. 2a, or reflect asymmetric heat transport efficacy below versus above the dipping dike structure. [2] Hydrothermal convection and conduction simulations from Bindeman et al. (2020) matching $\delta^{18}O$ depletion profile around the dike. [3] (U-Th)/He thermochronology 68% confidence envelope of $>10^6$ simulations from Karlstrom et al. (2019).*

References

Baker, L.L., Camp, V.E., Reidel, S.P., Martin, B.S., Ross, M.E., and Tolan, T.L., 2019, Alteration, mass analysis, and magmatic compositions of the Sentinel Bluffs Member, Columbia River flood basalt province: Comment: Geosphere, v. 15, p. 1436–1447, doi:10.1130/GES02047.1.

Bindeman, I., Greber, N., Melnik, O., Artyomova, A., Utkin, I., Karlstrom, L., and Colón, D., 2020, Pervasive hydrothermal events associated with large igneous provinces documented by the Columbia River basaltic province: Scientific Reports, v. 10, p. 1–9, doi:10.1038/s41598-020-67226-9.

Bowles, J.A., Jackson, M.J., Berquó, T.S., Sølheid, P.A., and Gee, J.S., 2013, Inferred time-and temperature-dependent cation ordering in natural titanomagnetites: Nature Communications, v. 4, p. 1–9.

Brown, R.J., Blake, S., Thordarson, T., and Self, S., 2014, Pyroclastic edifices record vigorous lava fountains during the emplacement of a flood basalt flow field, Roza Member, Columbia River Basalt Province, USA: GSA Bulletin, v. 126, p. 875–891, doi:10.1130/B30857.1.

Buchan, K., Schwarz, E., Symons, D., and Stupavsky, M., 1980, Remanent magnetization in the contact zone between Columbia Plateau flows and feeder dikes: Evidence for groundwater layer at time of intrusion: Journal of Geophysical Research: Solid Earth, v. 85, p. 1888–1898, doi:10.1029/JB085iB04p01888.

Burgess, S.D., Muirhead, J.D., and Bowring, S.A., 2017, Initial pulse of Siberian Traps sills as the trigger of the end-Permian mass extinction: Nature Communications, v. 8, p. 1–6, doi:10.1038/s41467-017-00083-9.

Camp, V.E., Reidel, S.P., Ross, M.E., Brown, R.J., and Self, S., 2017, Field-trip guide to the vents, dikes, stratigraphy, and structure of the Columbia River Basalt Group, eastern Oregon and southeastern Washington: U.S. Geological Survey Scientific Investigations Report USGS Numbered Series 2017-5022-N, 104 p., https://doi.org/10.3133/sir20175022N.

Choiniere, S.R., and Swanson, D.A., 1979, Magnetostratigraphy and correlation of Miocene basalts of the northern Oregon coast and Columbia Plateau, southeast Washington: American Journal of Science, v. 279, p. 755–777, doi:10.2475/ajs.279.7.755.

Clapham, M.E., and Renne, P.R., 2019, Flood basalts and mass extinctions: Annual Review of Earth and Planetary Sciences, v. 47, p. 275–303, doi:10.1146/annurev-earth-053018-060136.

Collinson, D.W., 1983, Methods in rock magnetism and palaeomagnetism: Techniques and Instrumentation: London; New York, Chapman and Hall, 503 p., https://doi.org/10.1007/978-94-015-3979-1.

Delaney, P.T., and Pollard, D.D., 1982, Solidification of basaltic magma during flow in a dike: American Journal of Science, v. 282, p. 856–885, doi:10.2475/ajs.282.6.856.

Dunlop, D.J., 2003, Stepwise and continuous low-temperature demagnetization: Geophysical Research Letters, v. 30, doi:https://doi.org/10.1029/2003GL017268.

Dunlop, D.J., and Özdemir, Ö., 1997, Rock Magnetism: Fundamentals and Frontiers: Cambridge, Cambridge University Press, Cambridge Studies in Magnetism, 573 p., doi:10.1017/CBO9780511612794.

Fendley, I.M., Mittal, T., Sprain, C.J., Marvin-DiPasquale, M., Tobin, T.S., and Renne, P.R., 2019, Constraints on the volume and rate of Deccan Traps flood basalt eruptions using a combination of high-resolution terrestrial mercury records and geochemical box models: Earth and Planetary Science Letters, v. 524, p. 115721.

Fialko, Y.A., and Rubin, A.M., 1999, Thermal and mechanical aspects of magma emplacement in giant dike swarms: Journal of Geophysical Research: Solid Earth, v. 104, p. 23033–23049, doi:https://doi.org/10.1029/1999JB900213.

Fisher, N.I., Lewis, T., and Embleton, B.J., 1993, Statistical analysis of spherical data: Cambridge, UK, Cambridge University Press, 343 p.

Graham, J.W., 1949, The stability and significance of magnetism in sedimentary rocks: Journal of Geophysical Research, v. 54, p. 131–167, doi:10.1029/JZ054i002p00131.

Hooper, P.R., 2000, Chemical discrimination of Columbia River basalt flows: Geochemistry, Geophysics, Geosystems, v. 1, doi:10.1029/2000GC000040.

Hui, H., and Zhang, Y., 2007, Toward a general viscosity equation for natural anhydrous and hydrous silicate melts: Geochimica et Cosmochimica Acta, v. 71, p. 403–416, doi:10.1016/j.gca.2006.09.003.

Karlstrom, L., Murray, K.E., and Reiners, P.W., 2019, Bayesian Markov-chain Monte Carlo inversion of low-temperature thermochronology around two 8- 10 m wide Columbia River flood basalt dikes: Frontiers in Earth Science, v. 7, p. 90, doi:10.3389/feart.2019.00090.

Kasbohm, J., and Schoene, B., 2018, Rapid eruption of the Columbia River flood basalt and correlation with the mid-Miocene climate optimum: Science Advances, v. 4, doi:10.1126/sciadv.aat8223.

Kirschvink, J., 1980, The least-squares line and plane and the analysis of palaeomagnetic data: Geophysical Journal International, v. 62, p. 699–718, doi:10.1111/j.1365-246X.1980.tb02601.x.

Kirschvink, J.L., Kopp, R.E., Raub, T.D., Baumgartner, C.T., and Holt, J.W., 2008, Rapid, precise, and high-sensitivity acquisition of paleomagnetic and rock-magnetic data: Development of a low-noise automatic sample changing system for superconducting rock magnetometers: Geochemistry, Geophysics, Geosystems, v. 9, doi:10.1029/2007GC001856.

Kristjansson, L., 1985, Magnetic and thermal effects of dike intrusions in Iceland: Journal of Geophysical Research: Solid Earth, v. 90, p. 10129–10135, doi:10.1029/JB090iB12p10129.

Mather, T.A., and Schmidt, A., 2021, Environmental Effects of Volcanic Volatile Fluxes From Subaerial Large Igneous Provinces, *in* Large Igneous Provinces, American Geophysical Union (AGU), p. 103–116, doi:10.1002/9781119507444.ch4.

Morriss, M.C., Karlstrom, L., Nasholds, M.W., and Wolff, J.A., 2020, The Chief Joseph dike swarm of the Columbia River flood basalts, and the legacy data set of William H. Taubeneck: Geosphere, v. 16, p. 1082–1106, doi:10.1130/GES02173.1.

Perry-Houts, J., Schoettle-Greene, P., Humphreys, G., Klema, N., O'Hara, D., and Colón, A., 2020, The Columbia River Basalt as a record of Miocene topography and the deformation that followed, *in* AGU Fall Meeting 2020, AGU.

Petcovic, H.L., and Dufek, J.D., 2005, Modeling magma flow and cooling in dikes: Implications for emplacement of Columbia River flood basalts: Journal of Geophysical Research: Solid Earth, v. 110, doi:10.1029/2004JB003432.

Petcovic, H., and Grunder, A., 2003, Textural and thermal history of partial melting in tonalitic wallrock at the margin of a basalt dike, Wallowa Mountains, Oregon: Journal of Petrology, v. 44, p. 2287–2312, doi:10.1093/petrology/egg078.

Ray, R., Sheth, H.C., and Mallik, J., 2006, Structure and emplacement of the Nandurbar–Dhule mafic dyke swarm, Deccan Traps, and the tectonomagmatic evolution of flood basalts: Bulletin of Volcanology, v. 69, p. 537, doi:10.1007/s00445-006-0089-y.

Reidel, S.P., 1998, Emplacement of Columbia River flood basalt: Journal of Geophysical Research: Solid Earth, v. 103, p. 27393–27410, doi:10.1029/97JB03671.

Reidel, S.P., Camp, V.E., Tolan, T.L., and Martin, B.S., 2013, The Columbia River flood basalt province: Stratigraphy, areal extent, volume, and physical volcanology, *in* The Columbia River Flood Basalt Province, Geological Society of America, doi:10.1130/2013.2497(01).

Reidel, S.P., Hooper, P.R., Webster, G.D., and Camp, V.E., 1992, Geologic Map of Southeastern Asotin County, Washington: Washington Division of Geology and Earth Resources, Olympia, Washington Geologic Map 6M-40.

Reidel, S.P., and Tolan, T.L., 2013, The Grande Ronde Basalt, Columbia River Basalt Group, *in* Geological Society of America Special Paper, v. 497, p. 117–153, doi:10.1130/2013.2497(05).

Rivalta, E., Taisne, B., Bunger, A., and Katz, R., 2015, A review of mechanical models of dike propagation: Schools of thought, results and future directions: Tectonophysics, v. 638, p. 1–42, doi:10.1016/j.tecto.2014.10.003.

Ross, M.E., 1983, Chemical and mineralogic variations within four dikes of the Columbia River Basalt Group, southeastern Columbia Plateau: GSA Bulletin, v. 94, p. 1117–1126, doi:10.1130/0016-7606(1983)94<1117:CAMVWF>2.0.CO;2.

Sawlan, M.G., 2017, Alteration, mass analysis, and magmatic compositions of the Sentinel Bluffs Member, Columbia River flood basalt province: Geosphere, v. 14, p. 286–303, doi:10.1130/GES01188.1.

Schmidt, A., Skeffington, R.A., Thordarson, T., Self, S., Forster, P.M., Rap, A., Ridgwell, A., Fowler, D., Wilson, M., and Mann, G.W., 2016, Selective environmental stress from sulphur emitted by continental flood basalt eruptions: Nature Geoscience, v. 9, p. 77–82, doi:10.1038/ngeo2588.

Schoene, B., Eddy, M.P., Samperton, K.M., Keller, C.B., Keller, G., Adatte, T., and Khadri, S.F., 2019, U-Pb constraints on pulsed eruption of the Deccan Traps across the end-Cretaceous mass extinction: Science, v. 363, p. 862–866.

Self, S., Jay, A.E., Widdowson, M., and Keszthelyi, L.P., 2008, Correlation of the Deccan and Rajahmundry Trap lavas: Are these the longest and largest lava flows on Earth? Journal of Volcanology and Geothermal Research, v. 172, p. 3–19, doi:https://doi.org/10.1016/j.jvolgeores.2006.11.012.

Sprain, C.J., Renne, P.R., Vanderkluysen, L., Pande, K., Self, S., and Mittal, T., 2019, The eruptive tempo of Deccan volcanism in relation to the Cretaceous-Paleogene boundary: Science, v. 363, p. 866, doi:10.1126/science.aav1446.

Taubeneck, W.H., 1970, Dikes of Columbia River basalt in northeastern Oregon, western Idaho, and southeastern Washington, *in* Proc. 2nd Columbia River Basalt Symposium, Cheney, WA, Eastern Washington State College Press, p. 73–96.

Tauxe, L., Shaar, R., Jonestrask, L., Swanson-Hysell, N., Minnett, R., Koppers, A., Constable, C., Jarboe, N., Gaastra, K., and Fairchild, L., 2016, PmagPy: Software package for paleomagnetic data analysis and a bridge to the Magnetics Information Consortium (MagIC) Database: Geochemistry, Geophysics, Geosystems, v. 17, p. 2450–2463, doi:10.1002/2016GC006307.

Thiele, S.T., Cruden, A.R., Zhang, X., Micklethwaite, S., and Matchan, E.L., 2021, Reactivation of Magma Pathways: Insights From Field Observations, Geochronology, Geomechanical Tests, and Numerical Models: Journal of Geophysical Research: Solid Earth, v. 126, p. e2020JB021477, doi:https://doi.org/10.1029/2020JB021477.

Thordarson, T., and Self, S., 1996, Sulfur, chlorine and fluorine degassing and atmospheric loading by the Roza eruption, Columbia River Basalt Group, Washington, USA: Journal of Volcanology and Geothermal Research, v. 74, p. 49–73, doi:10.1016/S0377-0273(96)00054-6.

Thordarson, T., and Self, S., 1993, The Laki (Skaftár Fires) and Grímsvötn eruptions in 1783–1785: Bulletin of Volcanology, v. 55, p. 233–263, doi:10.1007/BF00624353.

Thordarson, T., and Self, S., 1998, The Roza Member, Columbia River Basalt Group: A gigantic pahoehoe lava flow field formed by endogenous processes? Journal of Geophysical Research: Solid Earth, v. 103, p. 27411–27445, doi:10.1029/98JB01355.

Wylie, J.J., Helfrich, K.R., Dade, B., Lister, J.R., and Salzig, J.F., 1999, Flow localization in fissure eruptions: Bulletin of Volcanology, v. 60, p. 432–440, doi:10.1007/s004450050243.

Yu, Y., and Tauxe, L., 2006, Acquisition of viscous remanent magnetization: Physics of the Earth and Planetary Interiors, v. 159, p. 32–42, doi:https://doi.org/10.1016/j.pepi.2006.05.002.

Chapter 3 Supplement

Timescales of Magma Transport in the Columbia River Flood Basalts, Determined by Paleomagnetic Data

Joseph Biasi[1] and Leif Karlstrom[2]

[1]*California Institute of Technology, Division of Geological and Planetary Sciences,*

biasi@caltech.edu

[2]*University of Oregon, Department of Earth Sciences*

This Supplemental Material contains:

(S1) Geochemical data and unit assignments

The XRF protocol was calibrated against 21 USGS standards: AGV-1, AGV-2, BCR-1, BCR-2, BHVO-2, BIR-1, DNC-1, DTS-2, G-2, GSP-2, MAG-1, NKT-1, NOD-A-1, QLO-1, RGM-2, SBC-1, SCO-1, SDC-1, SGR-1, STM-1, and W-2. USGS standards run as unknowns are: Guano Valley Andesite (AGV), Columbia River Basalt 2 (BCR), Hawaii Volcano Observatory Basalt 2 (BHVO), Silver Plume Granite (GSP), and Glass Mountain Rhyolite (RGM). **Table S1**, which includes whole-rock major and trace element compositions, is available as a separate excel file.

Individual Columbia River Basalt (CRB) members can vary in composition, so we compare our samples to *average* CRB member compositions (Reidel, 2005; Reidel et al., 2013; Reidel and Tolan, 2013). Geochemical similarities are assessed using a least-squares regression method applied to ten major oxides (SiO_2, Al_2O_3, TiO_2, Fe_2O_3, MnO, CaO, MgO, K_2O, Na_2O, and P_2O_5). If multiple CRB members are similar one of our

samples, additional weight was given to MgO, TiO_2, and P_2O_5 as suggested by (Hooper, 2000). Justifications for each assignment are as follows:

BD2 27 (Boggan's Oasis Wall) – Assigned to *China Creek* based on geochemical similarities to China Creek MgO, P_2O_5, and TiO_2 compositions, and to a lesser extent based on other major-element similarities (SiO_2, Al_2O_3, etc.) (Reidel and Tolan, 2013). The assignment to China Creek is in agreement with the geologic map of this wall rock, which is mapped as N1 Grande Ronde (Schuster, 1993), which is also in agreement with the measured polarity of the wall rock (Table 2). This assignment is also in agreement with the mapped extent of China Creek in (Reidel and Tolan, 2013).

BOD 2 (Boggan's Oasis Dike) – Assigned to *Sentinel Bluffs, basalt of Museum* based on geochemical similarities to Sentinel Bluffs MgO, P_2O_5, and TiO_2 compositions, and to a lesser extent based on other major-element similarities (SiO_2, Al_2O_3, etc.) (Reidel and Tolan, 2013). Trace element compositions rule out association with Wanapum or Saddle Mountains flows (Hooper, 2000). The composition of this dike has not been previously described. The polarity of this dike is normal (Table 2), which is in agreement with its assignment to Sentinel Bluffs (Reidel and Tolan, 2013) but disagrees with the map of Schuster (1993). This dike is not within the mapped extent of the Museum basalt, but other Museum dikes have been found in this area (Reidel, 2005).

FRE 1 to 5 (Eagle Dike) – Assigned to *Buford* based on geochemical similarities to Buford MgO, P_2O_5, and TiO_2 compositions, and to a lesser extent based on other major-element similarities (SiO_2, Al_2O_3, etc.) (Reidel et al., 2013). Trace element compositions (low Sr, high Zr) rule out association with Grande Ronde flows and match previous Buford analyses (Hooper, 2000). The composition of this dike was previously

described as Buford by Reidel et al. (1992). The polarity of this dike is reversed (Table 2), which is in agreement with its assignment to Buford (Reidel et al., 2013). This dike is also within the mapped extent of the Buford member (Reidel et al., 2013).

FRE 6, 19 (Eagle Dike Wall) – Assigned to *Teepee Butte – Pruitt Draw* based on geochemical similarities to Teepee Butte MgO, P_2O_5, and TiO_2 compositions, and to a lesser extent based on other major-element similarities (SiO_2, Al_2O_3, etc.) (Reidel and Tolan, 2013). The assignment to Teepee Butte is in agreement with the geologic map of this wall rock, which is mapped as R1 Grande Ronde (Reidel et al., 1992), which is also in agreement with the measured polarity of the wall rock (Table 2). This assignment is also in agreement with the mapped extent of the Teepee Butte member (Reidel and Tolan, 2013).

KD 2 (Jackson A Dike) – Assigned to *Wapshilla Ridge* based on its connection to the Maxwell A Dike, which is of Wapshilla Ridge composition (Petcovic and Grunder, 2003). Nearly continuous outcrop of this dike can be seen connecting these two dike segments (Fig. 1c). This segment is geochemically dissimilar to any other CRB flow of reversed polarity, perhaps due to fractional crystallization within the dike or incorporation of wall-rock material.

KD 5, 10 (Jackson A Wall) – Assigned to *Hurricane Divide Pluton* based on map of Žák et al. (2012).

PD 1 (Maxwell B Dike) – Assigned to *Wapshilla Ridge* based on geochemical similarities to Wapshilla Ridge MgO, P_2O_5, and TiO_2 compositions, and to a lesser extent based on other major-element similarities (SiO_2, Al_2O_3, etc.) (Reidel and Tolan, 2013). Trace element compositions rule out association with Wanapum or Saddle Mountains

flows (Hooper, 2000). The composition of this dike has not been previously described. The polarity of this dike is reversed (Table 2), which is in agreement with its assignment to Wapshilla Ridge (Reidel and Tolan, 2013). This dike is also within the mapped extent of the Wapshilla Ridge member (Reidel and Tolan, 2013).

PD 6 (Maxwell B Wall) – Assigned to *Hurricane Divide Pluton* based on map of Žák et al. (2012).

PBD 3 (Powatka Bridge Dike) – Assigned to *Elephant Mountain* based on geochemical similarities to Elephant Mountain MgO, P_2O_5, and TiO_2 compositions, and to a lesser extent based on other major-element similarities (SiO_2, Al_2O_3, etc.) (Reidel et al., 2013). Trace element compositions rule out association with Grande Ronde flows (Hooper, 2000). The composition of this dike has been previously described as Elephant Mountain by Ross (1983). The polarity of this dike is transitional (Table 2), which is in agreement with its assignment to Elephant Mountain (Choiniere and Swanson, 1979). This dike is within the mapped extent of the Elephant Mountain member (Reidel et al., 2013).

PD2 15 (Powatka Bridge Wall) – Assigned to *China Creek* based on geochemical similarities to China Creek MgO, P_2O_5, and TiO_2 compositions, and to a lesser extent based on other major-element similarities (SiO_2, Al_2O_3, etc.) (Reidel and Tolan, 2013). The assignment to China Creek is in agreement with the geologic map of this wall rock, which is mapped as N1 Grande Ronde (Swanson et al., 1981), which is also in agreement with the measured polarity of the wall rock (Table 2). This assignment is also in agreement with the mapped extent of the China Creek member (Reidel and Tolan, 2013).

GRV-18-1 (Rattlesnake A Dike) – Assigned to *Roza* based on geochemical similarities to Roza MgO, P_2O_5, and TiO_2 compositions, and to a lesser extent based on other major-element similarities (SiO_2, Al_2O_3, etc.) (Reidel et al., 2013). Trace element compositions rule out association with Grande Ronde flows (Hooper, 2000). The composition of this dike has been previously described as Roza by Reidel et al. (1992) and Thordarson and Self (1998). This dike is within the mapped extent of the Roza member (Reidel et al., 2013).

RDR 10 (Rattlesnake A Wall) – Assigned to *Wapshilla Ridge* based on geochemical similarities to Wapshilla Ridge MgO, P_2O_5, and TiO_2 compositions, and to a lesser extent based on other major-element similarities (SiO_2, Al_2O_3, etc.) (Reidel and Tolan, 2013). The assignment to Wapshilla is in agreement with the geologic map of this wall rock, which is mapped as R2 Grande Ronde (Reidel et al., 1992), which is also in agreement with the measured polarity of the wall rock (Table 2). This assignment is also in agreement with the mapped extent of Wapshilla Ridge (Reidel and Tolan, 2013).

SAD 21 (Tunnel Wall) – Assigned to *Rogersburg* based on geochemical similarities to Rogersburg MgO, P_2O_5, and TiO_2 compositions, and to a lesser extent based on other major-element similarities (SiO_2, Al_2O_3, etc.) (Reidel and Tolan, 2013). The assignment is in agreement with the geologic map of this wall rock, which is mapped as the Rogersburg member (Reidel et al., 1992), which is also in agreement with the measured polarity of the wall rock (Table 2).

SAD 4, 5 (Tunnel Dike) – Assigned to *Umatilla or Sillusi* based on geochemical similarities to Umatilla/Sillusi MgO, P_2O_5, and TiO_2 compositions, and due to its very high Ba content (Hooper, 2000). The composition of this dike has been previously

described by Reidel et al. (1992) and Reidel (1998) as Umatilla/Sillusi. The polarity of this dike is normal (Table 2), which is in agreement with this assignment (Reidel et al., 2013). This dike is also within the mapped extent of the Umatilla member (Reidel et al., 2013).

(S2) Additional dike descriptions and field observations

Additional figures and descriptions for each dike are included below. Any important information not presented here is included in the main text (Section 4.1).

(S2.1) Jackson A Dike

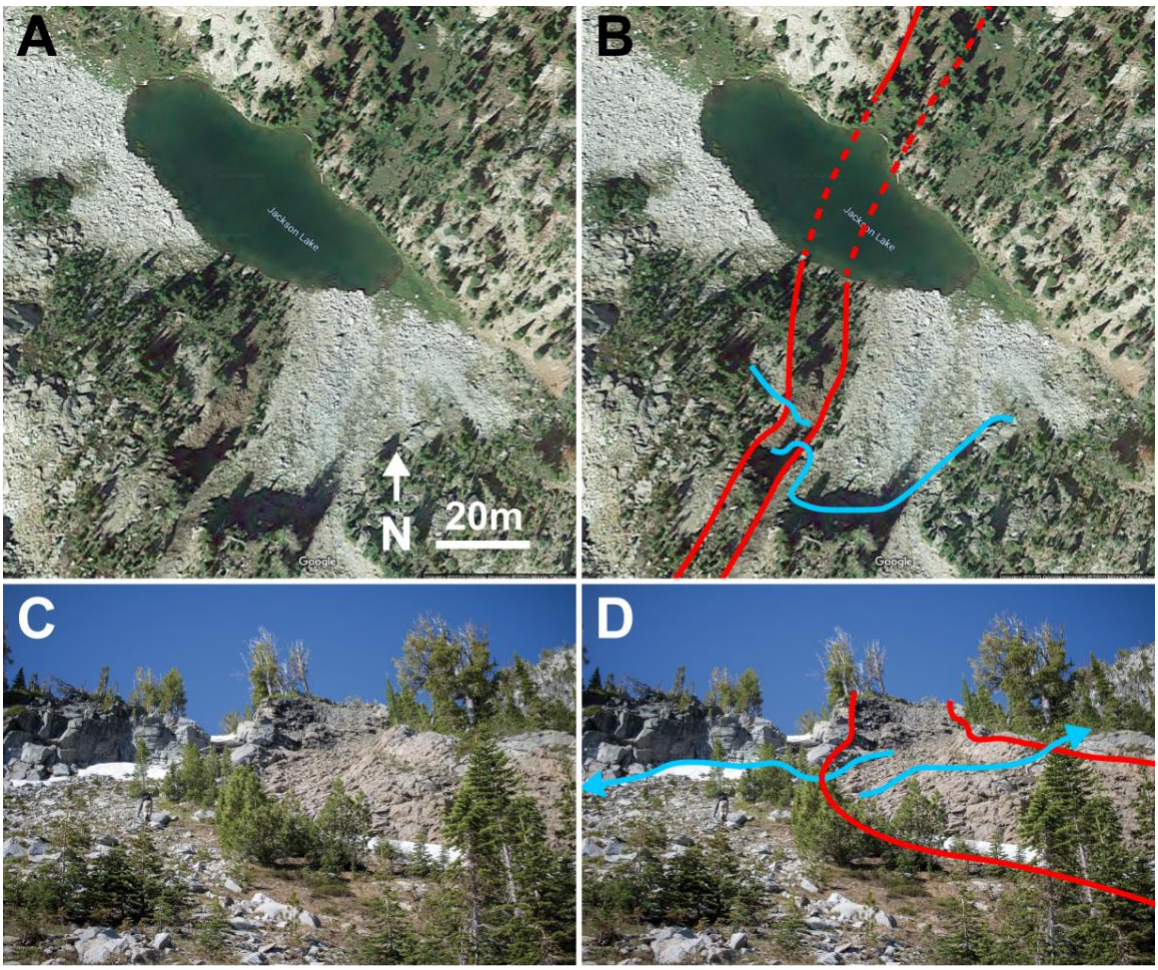

Figure S1. *A) Satellite image of the Jackson A dike, imagery from Google Earth. B) The dike is outlined in red (dashed where approximate), and the sampling transects are shown in blue. C) Outcrop photo of the Jackson A dike, looking southwest. D) The dike is outlined in red, the sampling transects are shown in blue.*

Dike Description

The Jackson A dike has a strike of 030º, variable dip around 68º E, and width of 8–10 m. The dike has sharp, undulatory contacts with the granitoid host rock, which is partially melted (Fig. 2a). Disconnected outcrops of this dike can be followed to the northeast to the Maxwell A dike (Fig. 1c), which is of Wapshilla Ridge composition. These two segments are likely part of the same dike system. This dike was studied by Karlstrom et al. (2019), who used low temperature (U-Th)/He thermochronology data from apatites and zircons in the wall-rock, along with a Bayesian Markov Chain Monte Carlo inversion for 6 parameters associated with diffusion of He and diffusion of heat, to constrain the lifetime of the dike (τ_c = 1.3–4.6 yr, τ_w = 0.1–3.8 yr, τ_f = 1.4–5.4 yr at 68% confidence). This dike was also studied by Bindeman et al. (2020) who measured depletion of oxygen isotopes surrounding the dike and matched this data with an advection-diffusion model of fluid circulation and heat conduction surrounding the dike. Best fitting models from Bindeman et al. (2020) match the family of curves from Karlstrom et al. (2019) that assume a larger-than-average conductivity (a proxy for fluid-enhanced heat transport). Our results are in agreement with the results of these studies, as demonstrated in Figure 7.

(S2.2) Maxwell A Dike

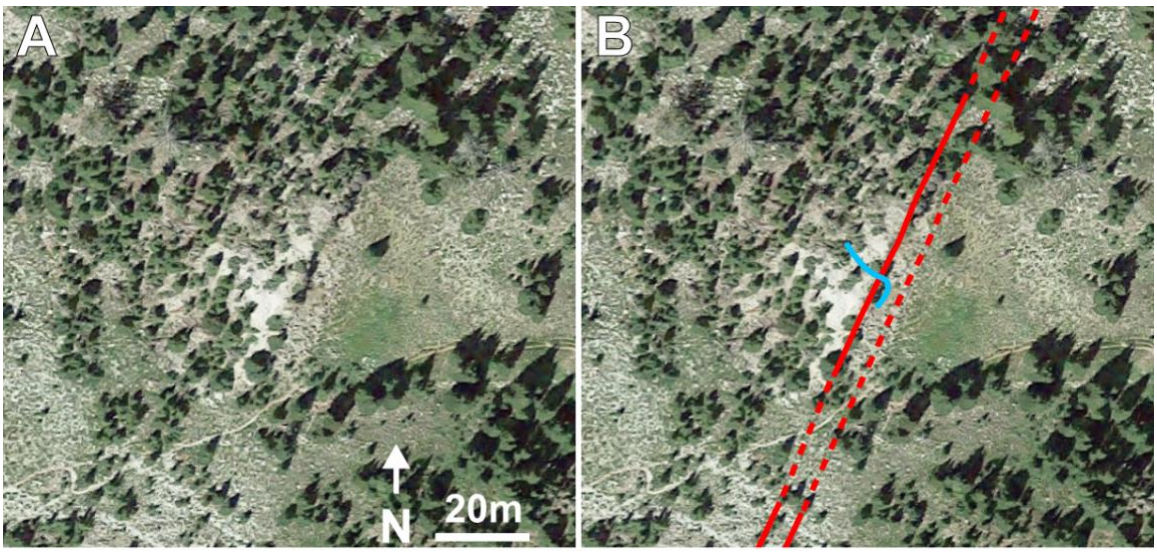

Figure S2*. A) Satellite image of the Maxwell A dike, imagery from Google Earth. B) The dike is outlined in red (dashed where approximate), and the sampling transect is shown in blue.*

Dike Description

The Maxwell A dike has a strike of ~210º, variable dip around 75º W, and width of ~8 m. The dike has sharp, meter-scale undulatory contacts with the granitoid host rock, which is partially melted. A detailed description of this dike and compositional data are reported in Petcovic and Grunder (2003), who proposed that the dike segment is associated with the Wapshilla Ridge member. This dike was studied by Petcovic and Grunder (2003) and Petcovic and Dufek (2005), who used mineral compositions from the wall-rock and thermal conduction models to constrain the lifetime of the dike (3–4 years). Our results are in general agreement with the results of those studies (Fig. 7). Wall-rock on the western side of the dike is partially exposed, but wall-rock on the eastern side is covered.

(S2.3) Maxwell B Dike

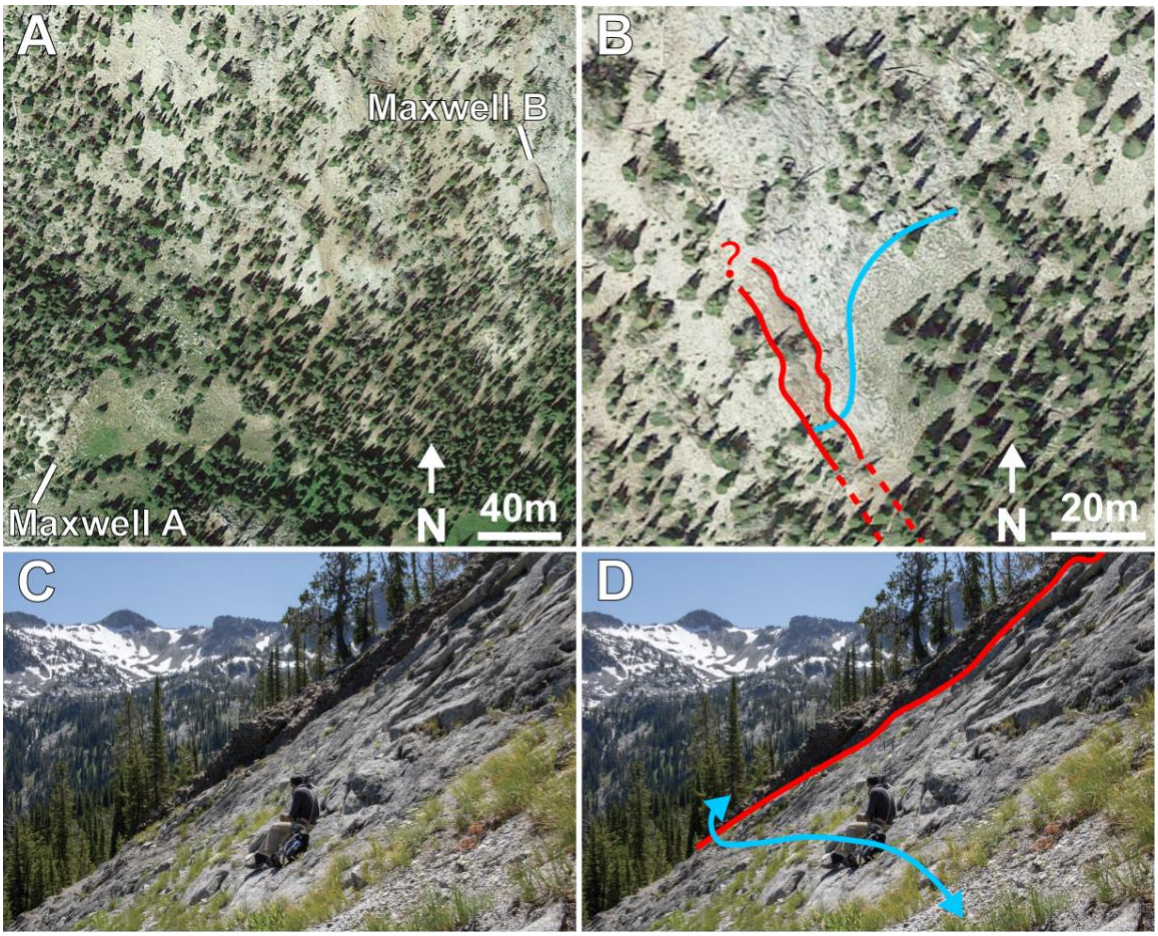

Figure S3*. A) The Maxwell B dike is 250 m to the ENE from the Maxwell A dike. B) The dike is outlined in red (dashed where approximate), and the sampling transect is shown in blue. C) Outcrop photo of the Maxwell B dike, looking southwest. D) The dike is outlined in red, the sampling transect is shown in blue.*

Dike Description

The Maxwell B dike has a strike of 332º, dip of 80º E, and width of 9.5 m. The dike has sharp, undulatory contacts with the granitoid host rock. Based on field observations, no textural evidence exists for internal differentiation or zonation, and there

is no obvious evidence for partially melted wall-rock. Several other dikes are exposed within ~300 m of this dike, most of which have not been studied. This dike might intersect with the Maxwell A dike to the northwest (Fig. S3a), but we did not attempt to confirm this in the field.

(S2.4) Tunnel Dike

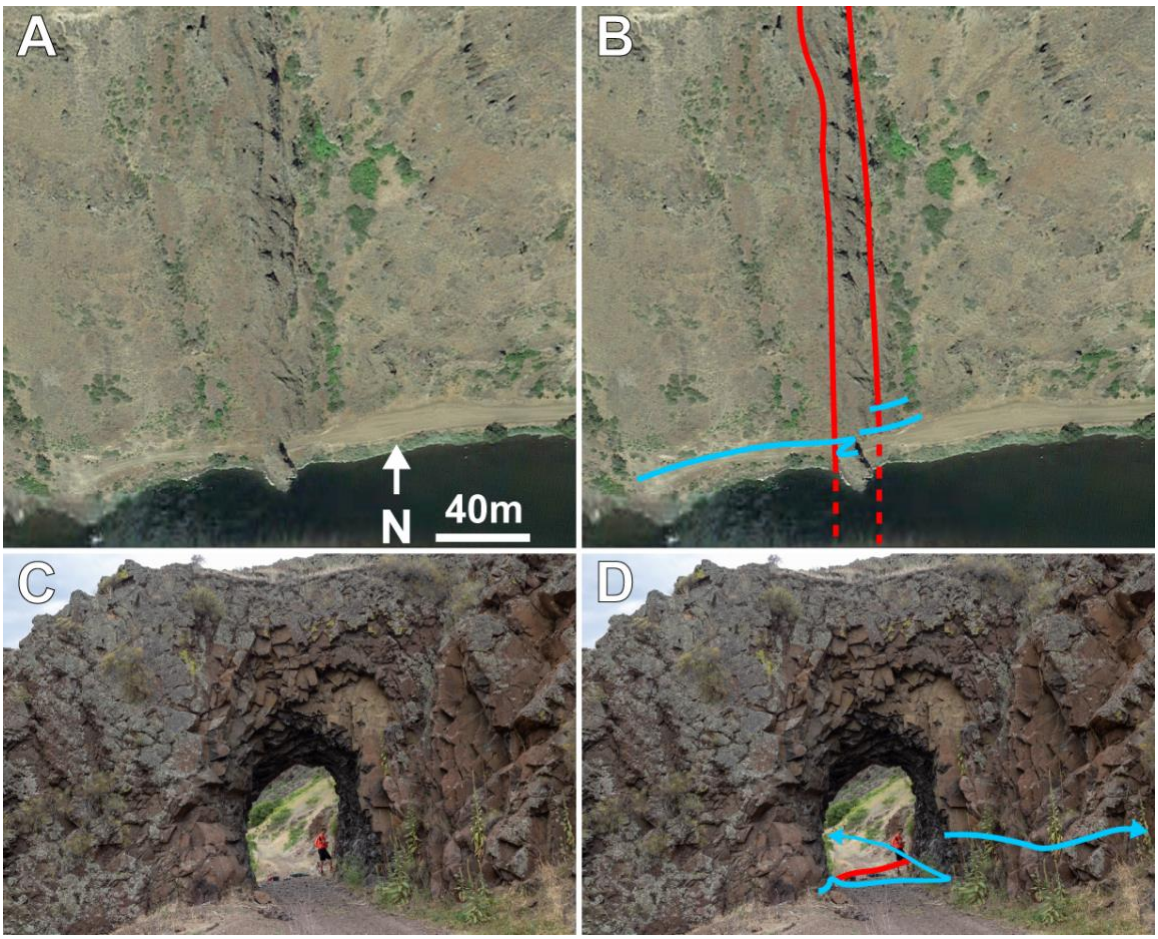

Figure S4*. A) Satellite image of the Tunnel dike, imagery from Google Earth. B) The dike is outlined in red (dashed where approximate), and the three sampling transects are shown in blue. C) Outcrop photo of the Tunnel dike, looking west. D) A portion of the*

dike outline is in red, two of the three sampling transects are shown in blue. The 'vesicular flow top' transect on the eastern side of the dike is out-of-frame.

Dike Description

The appropriately-named Tunnel dike has a strike of 354º, dip of ~90º, and width of 19.5 m at the sampling site. It has sharp, undulatory contacts with the basaltic host rock. The dike fed both the Umatilla and Sillusi flows (Fig. 2b), which Reidel (1998) determined were erupted within a few months or weeks of each other. The dike preserves both Umatilla and Sillusi compositions (Table S1), but there are no clear zones in the dike where only one of the compositions can be found. It is unclear if the Umatilla and Sillusi flows were erupted in separate events or if they were erupted in one continuous event with a change in composition during eruption. Some basaltic glass is preserved in the dike margins, but we found no glass in the dike interior. The vent that was fed by this dike is still preserved at Puffer Butte, which is 5 km to the north and 1 km higher in elevation (Fig. 2b).

(S2.5) Powatka Bridge Dike

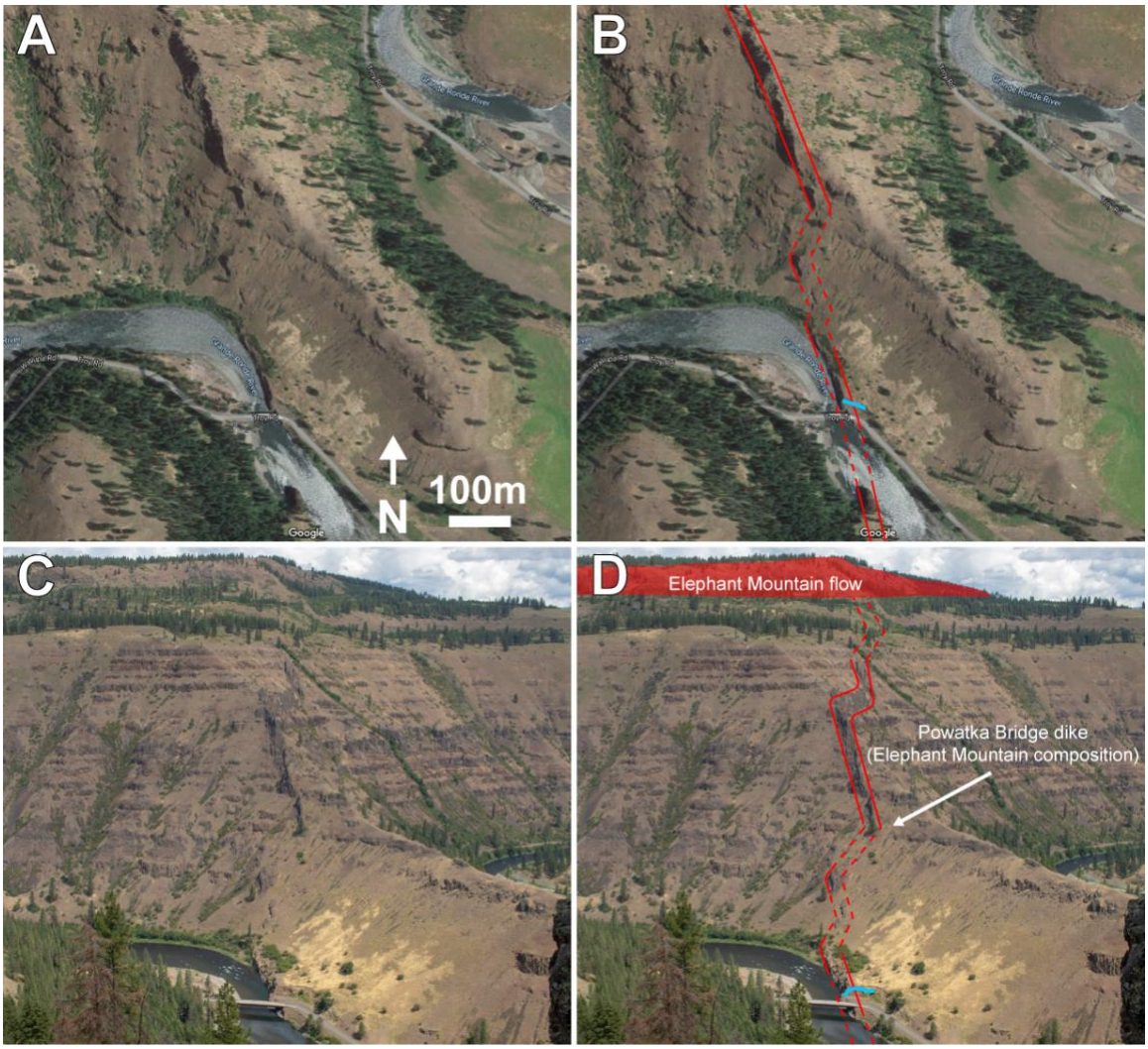

Figure S5*. A) Satellite image of the Powatka Bridge dike, imagery from Google Earth. B) The dike is outlined in red (dashed where approximate), and the sampling transect is shown in blue. C) Outcrop photo of the Powatka Bridge dike, looking northwest. This photo was taken while standing on another segment of the same dike. D) The dike is outlined in red, the sampling transect is shown in blue. The Elephant Mountain member of the CRB, which has an identical composition to the dike, is shown in red.*

Dike Description

The Powatka Bridge dike has a strike of 345º, dip of ~90º, and width of up to 57 m. At the studied exposure, the dike is only 20m wide but much of it has been eroded by a river (Fig. S5). The dike has sharp, undulatory contacts with the basaltic host rock. All compositions reported for this dike match the Elephant Mountain member (including the composition reported in Table S2) (Camp et al., 2017). This dike almost certainly breached the surface to feed the Elephant Mountain member (Fig. 5d).

(S2.6) Rattlesnake A Dike

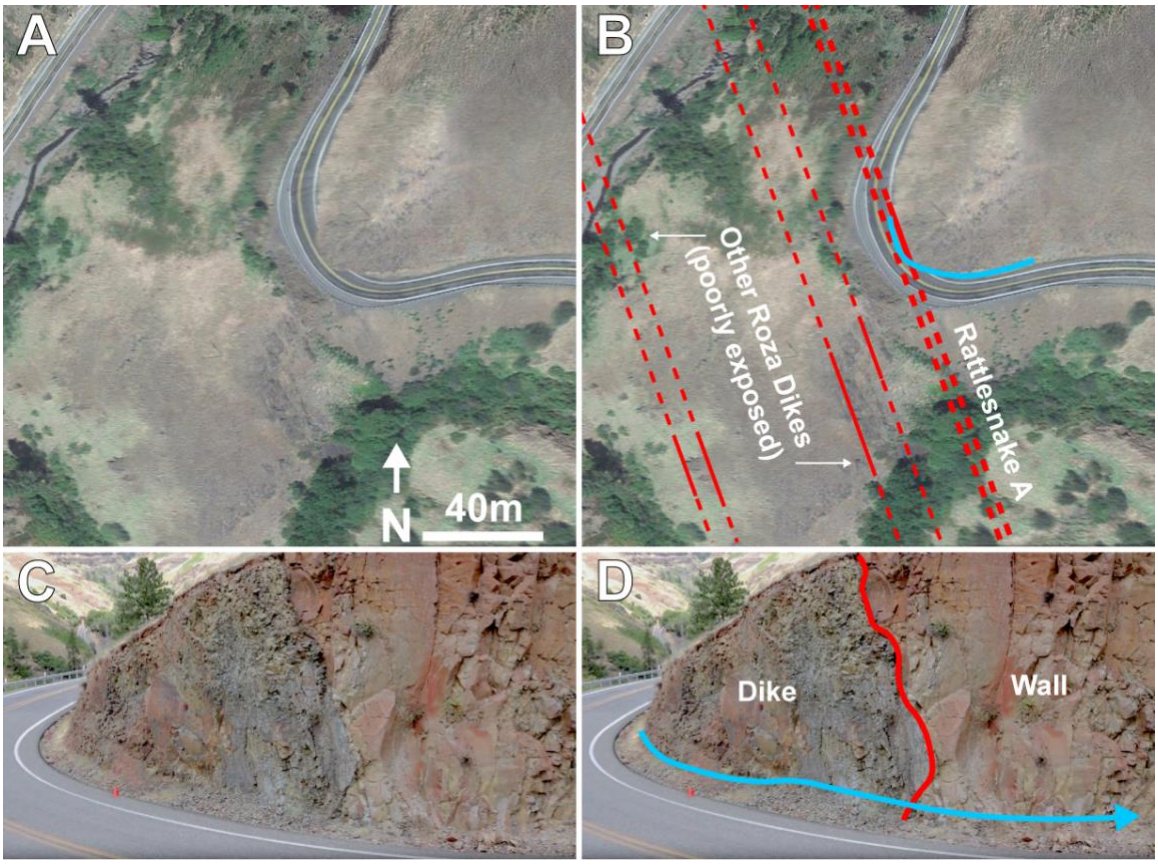

Figure S6*. A) Satellite image of the Rattlesnake A dike, imagery from Google Earth. B) The dike is outlined in red (dashed where approximate), and the sampling transect is*

shown in blue. Other poorly exposed Roza dikes are also shown. These were not sampled because the wall-rock surrounding these dikes is covered. C) Outcrop photo of the Rattlesnake A dike, looking north. D) The dike margin is outlined in red, the sampling transect is shown in blue.

Dike Description

The Rattlesnake A dike has a strike of 342º, dip of ~90º, and width of at least 1 m. The dike has sharp, angular contacts with the basaltic host rock. The core of the dike has been removed during road construction, leaving only the dike margin. The width of the dike at the sampling location is at least 1 m, but a nearby exposure of this dike segment is 2 m wide, so we assume a width of 2 m for this dike. This is part of a swarm of Roza dikes (Fig. S6b), and the entire Roza dike system extends for 150 km (Thordarson and Self, 1998).

(S2.7) Eagle Dike

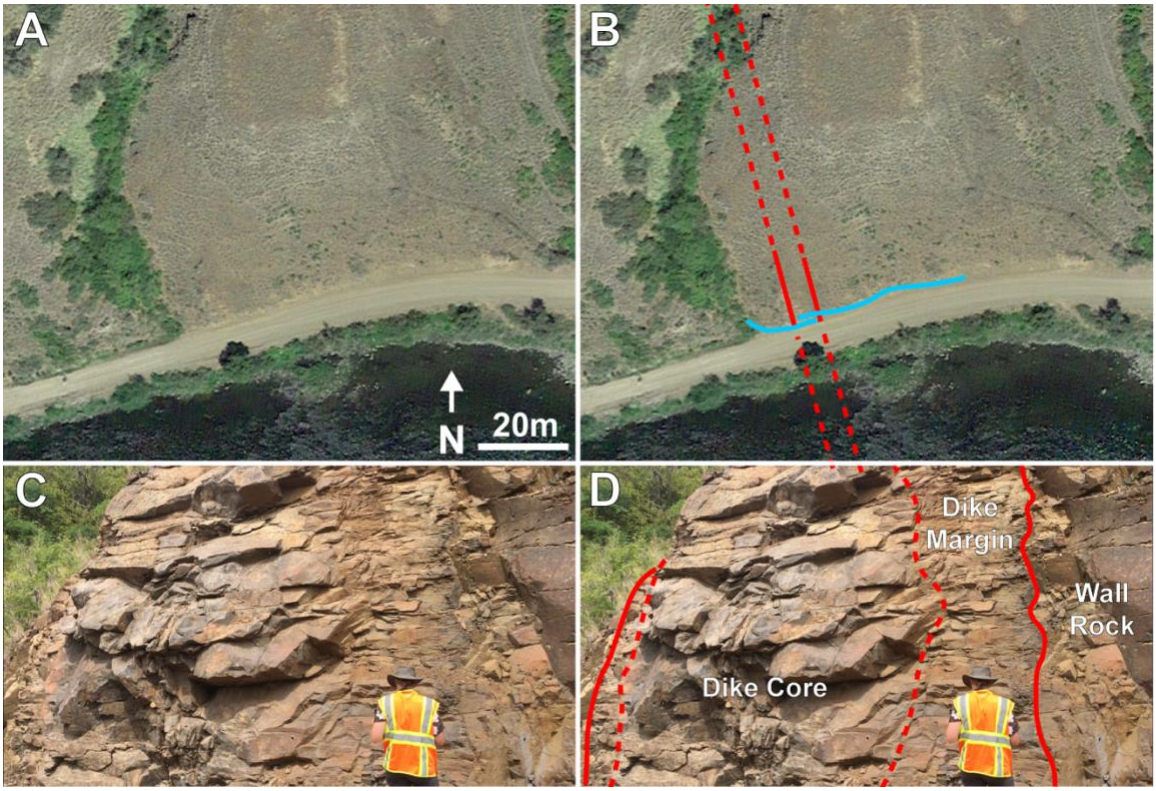

Figure S7*. A) Satellite image of the Eagle dike, imagery from Google Earth. The dike is generally not visible in satellite imagery. B) The dike is outlined in red (dashed where approximate), and the sampling transects are shown in blue. C) Outcrop photo of the Eagle dike, looking northwest. D) The sharp contact between dike and wall-rock is shown in solid red. The approximate contact between dike core and dike margin is shown in dashed red. See text for discussion.*

Dike Description

The Eagle dike has a strike of 345º, dip of ~90º, and width of 7.6 m. The dike has sharp, angular contacts with the basaltic host rock. No basaltic glass was preserved at the studied exposure. Although the vent that is fed by this dike is not preserved, the Buford

flow is exposed nearby (3.9 km to the northwest and 1 km higher in elevation) and it can be assumed that this dike breached the paleosurface. This dike is well-exposed in a roadcut, but natural exposures of the dike are very limited.

(S2.8) Boggan's Oasis Dike

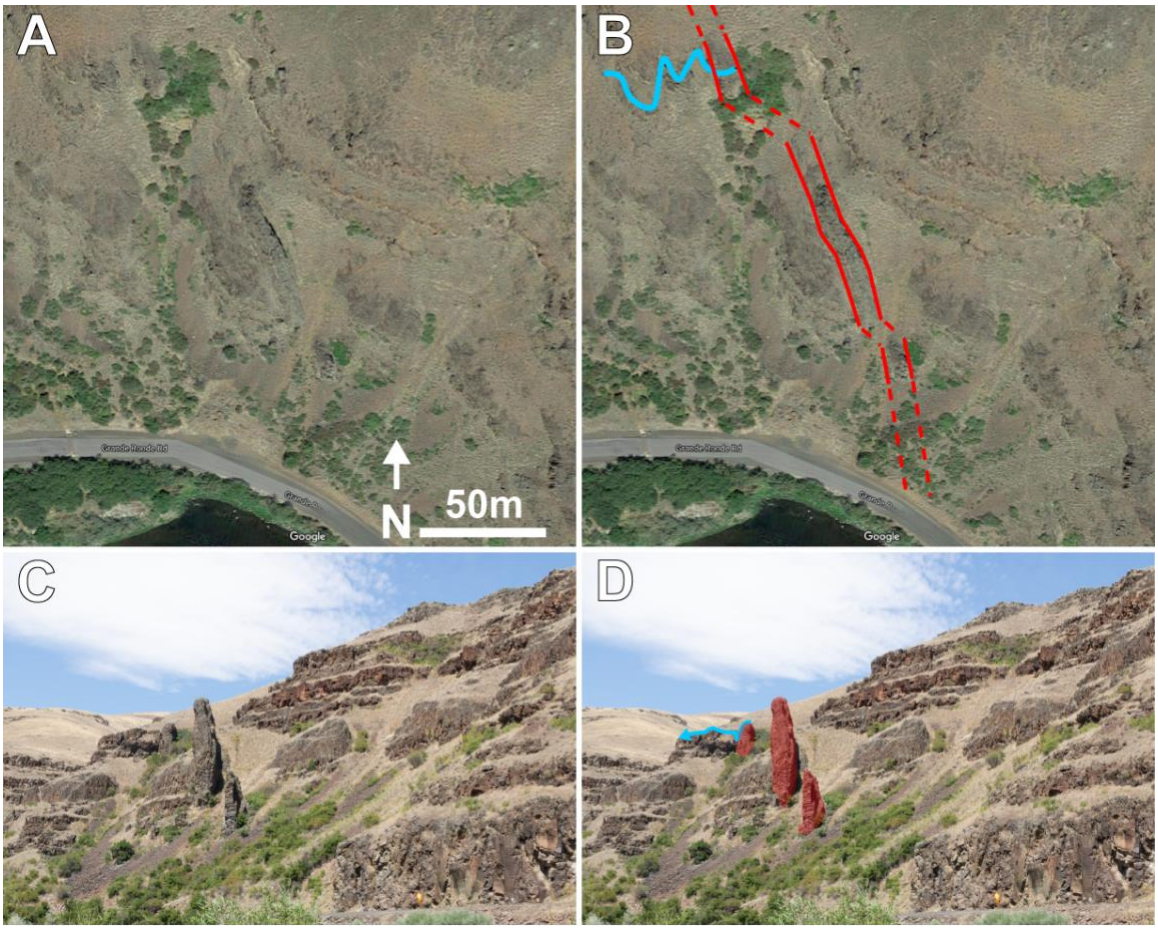

Figure S8*. A) Satellite image of the Boggan's Oasis dike, imagery from Google Earth. B) The dike is outlined in red (dashed where approximate), and the sampling transect is shown in blue. C) Outcrop photo of the Boggan's Oasis dike, looking northwest. D) The three dike segments are highlighted in red, the sampling transect is shown in blue.*

Dike Description

The Boggan's Oasis dike has a strike of 336º, dip of ~90º, and width of 6.5 m. The dike has sharp, planar contacts with the basaltic host rock where exposed. Natural exposures of the dike weather very high (Fig. S8c). The composition of the dike most closely matches the Sentinel Bluffs member (basalt of Museum, Table S1).

(S3) Thermal-susceptibility curves

Representative examples of thermal-susceptibility curves are given below. **Table S2**, which includes results from 28 samples, is available as a separate excel file.

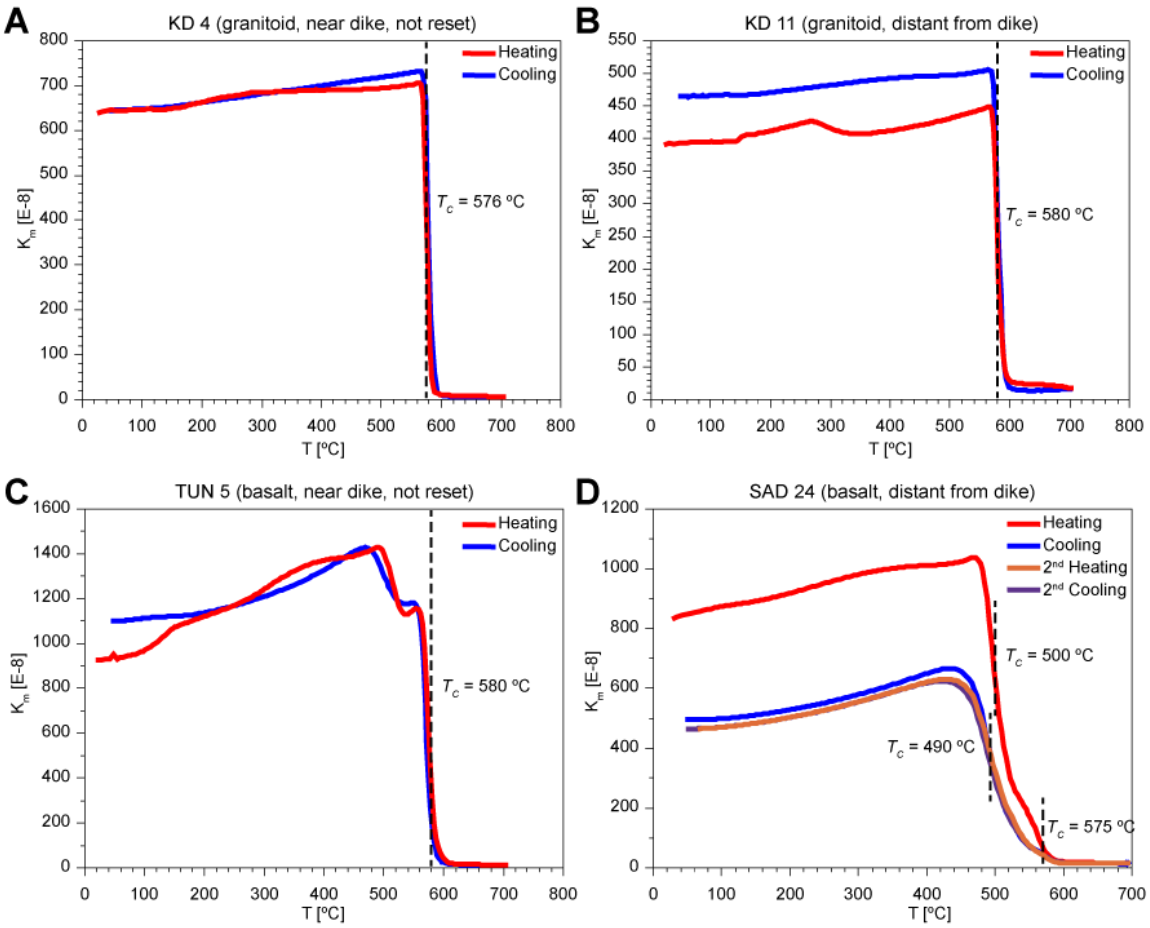

Figure S9*. Thermal-susceptibility curves from four representative samples. Mass susceptibility is shown on the y-axis, temperature is on the x-axis. A, B) The granitoid samples (KD 4, KD 11) show a simple curve with a sharp drop in susceptibility around 580 °C, indicating pure magnetite with no other significant magnetic phases. C) TUN 5 shows a more complex curve, suggesting that other phases such as titanomagnetite are present in addition to pure magnetite. D) SAD 24 underwent two rounds of heating to 700 °C, and also shows a mix of magnetite and titanomagnetite phases. Notably, the curve and T_c of this sample was irreversibly altered after the first heating event.*

(S4) Additional paleomagnetic results

Detailed paleomagnetic results for each site are given below, including overprint directions. **Table S3**, which includes all of the least-squares fits, is available as a separate excel file.

(S4.1) Jackson A Dike

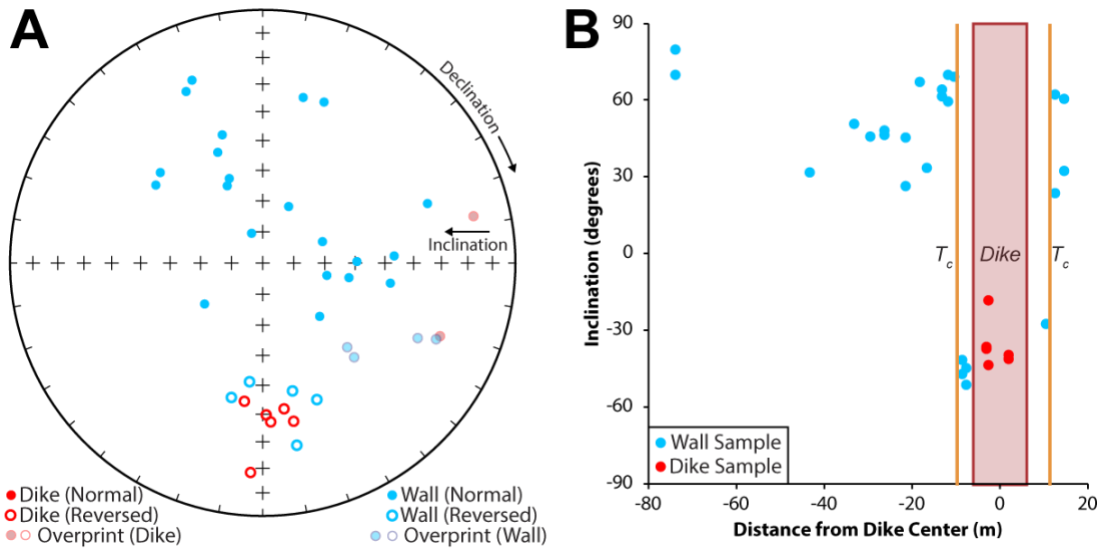

Figure S10. *Summary of paleomagnetic data from Jackson A dike. Wall-rock samples are blue, dike samples are red. A) Equal area projection. B) Distance vs. inclination plot. T_c = Curie temperature (as in Fig. 4).*

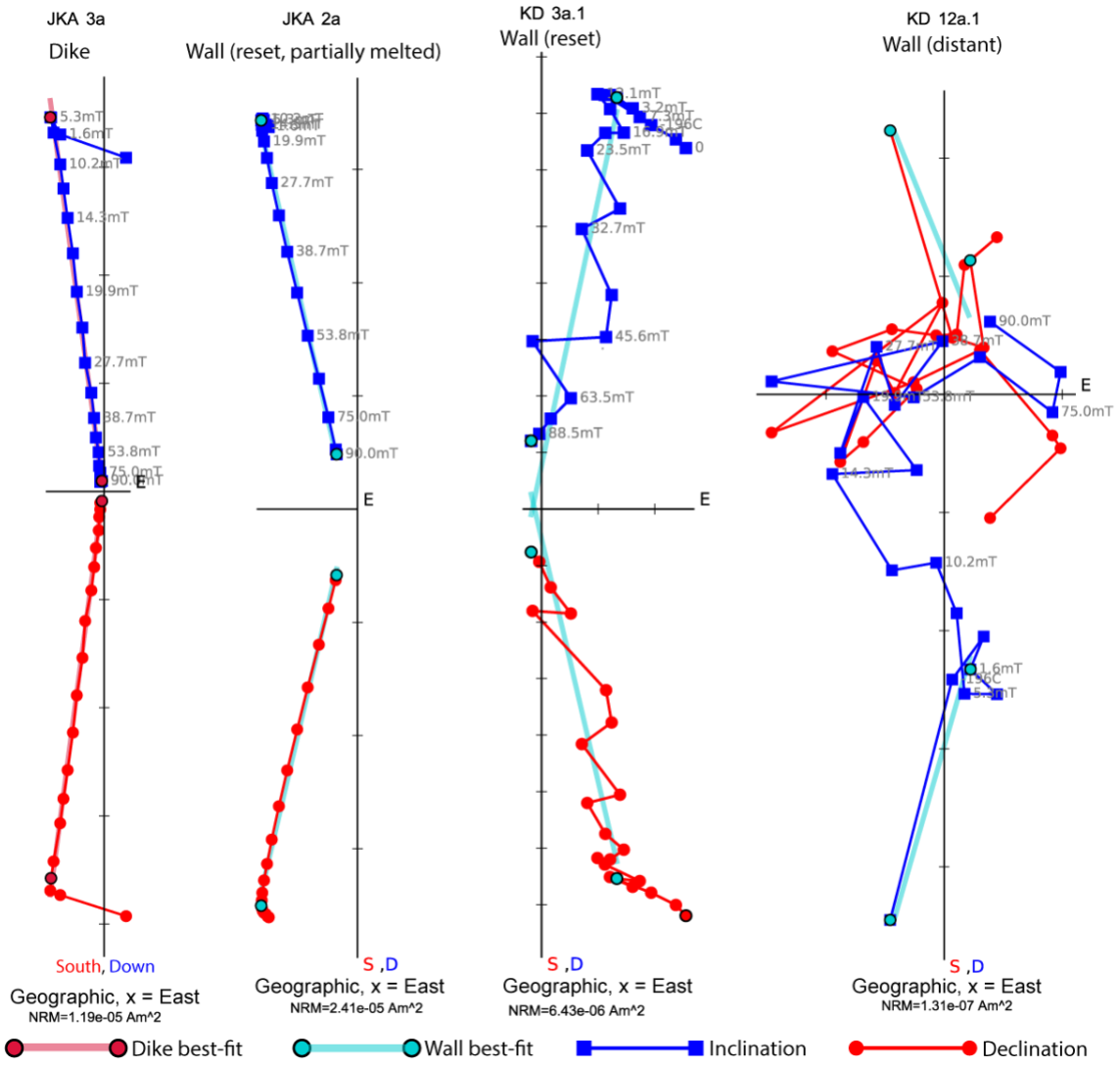

Figure S11*. Orthogonal projections showing representative demagnetization results from four Jackson A samples. All orthogonal projections in this manuscript are in the geographic reference frame. S = south, D = down, E = east.*

At the Jackson A site (Fig. 1c), granitoid samples are poor recorders of remanent magnetism unless fully reset by the dike (Fig. S11). Given that all of the non-reset directions from the wall-rock are of normal polarity, we conclude that these samples have a viscous remanent magnetism that is poorly preserving the modern field direction.

(S4.2) Maxwell A Dike

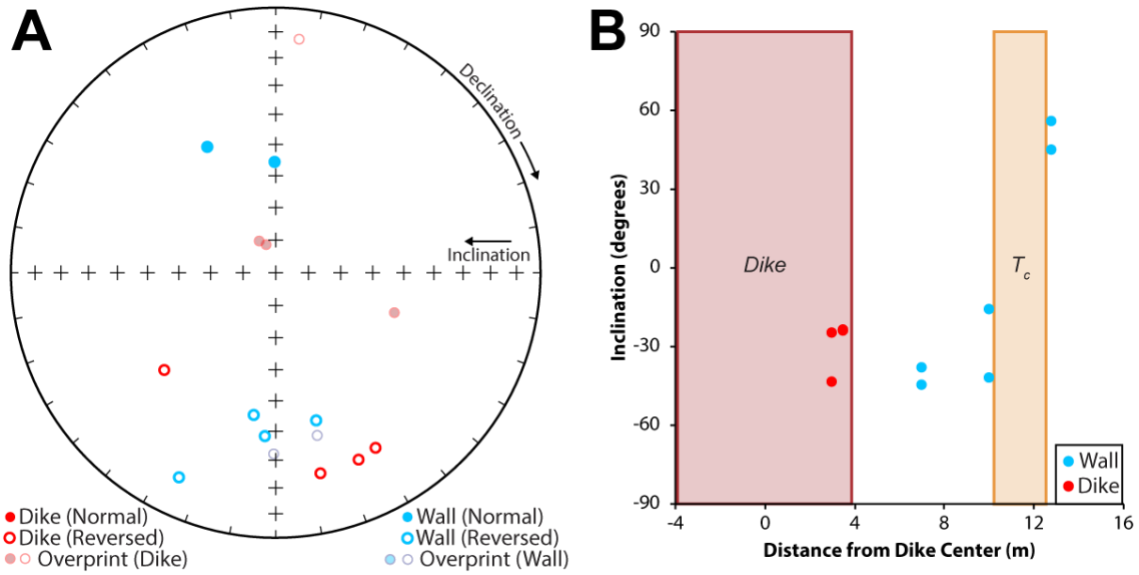

Figure S12. *Summary of paleomagnetic data from Maxwell A dike. Wall-rock samples are blue, dike samples are red. A) Equal area projection. B) Distance vs. inclination plot.* T_c *= Curie temperature zone (as in Fig. 4).*

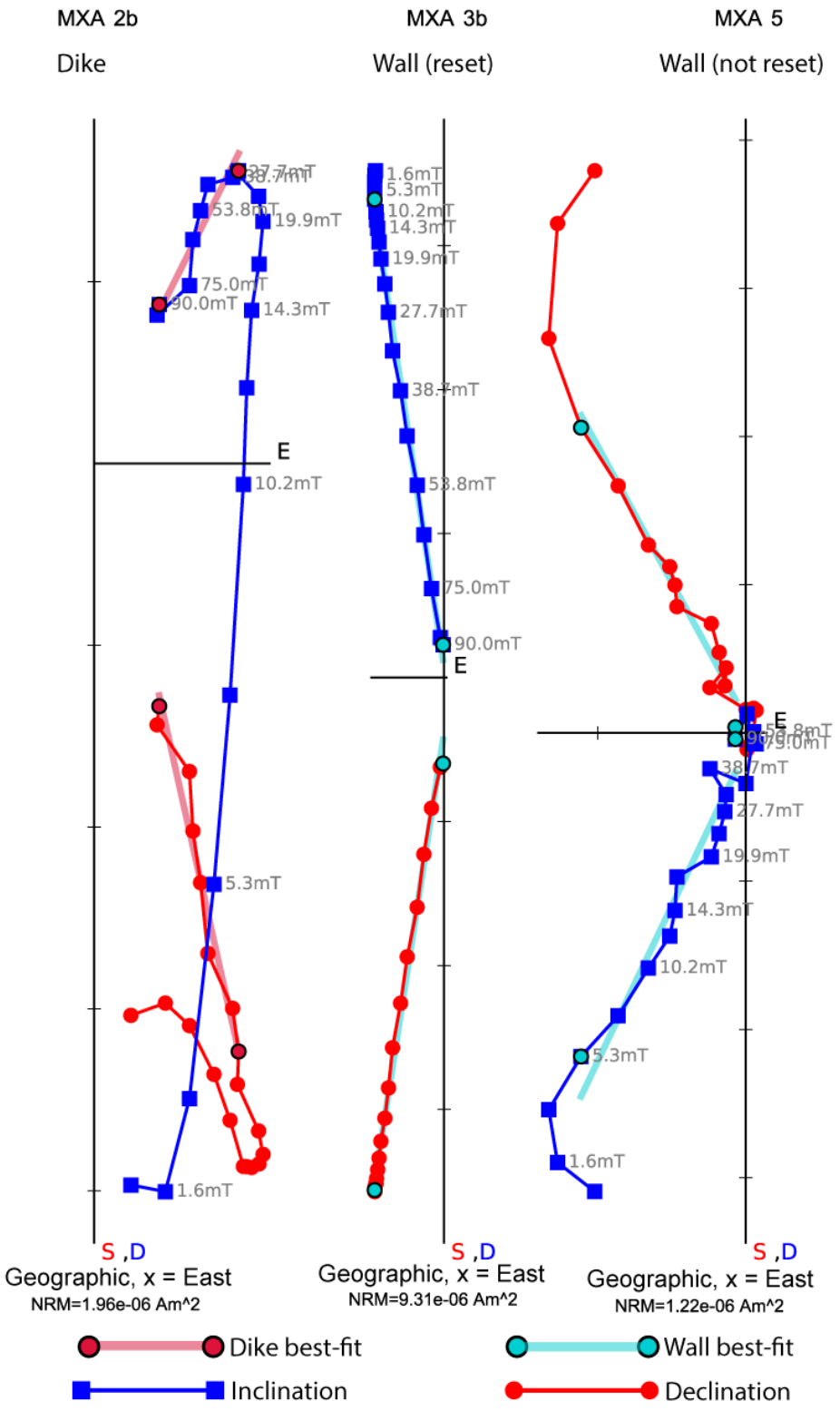

Figure S13*. Orthogonal projections showing representative demagnetization results from three Maxwell A samples. S = south, D = down, E = east.*

At the Maxwell A site (Fig. 1c), only one wall-rock sample is not reset by the dike (MXA 5). This sample has a much more consistent direction during demagnetization than granitoid samples from the Jackson A and Maxwell B site (Fig. S13). This may suggest that the granitoids in this area originally had a normal magnetic polarity.

(S4.3) Maxwell B Dike

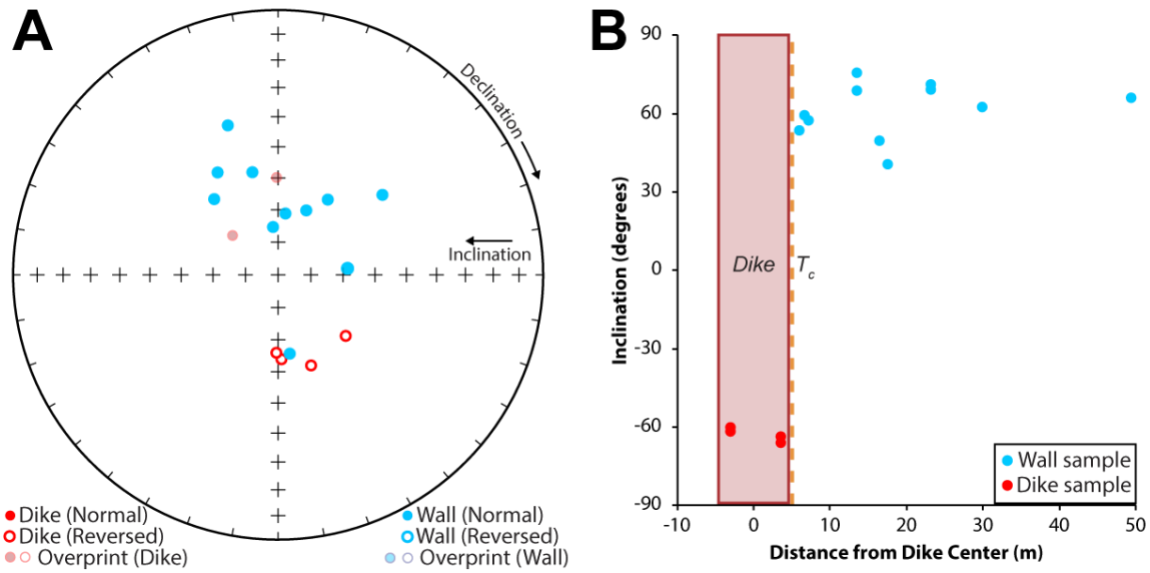

Figure S14. *Summary of paleomagnetic data from Maxwell B dike. Wall-rock samples are blue, dike samples are red. A) Equal area projections. B) Distance vs. inclination plot.* T_c *= Curie temperature (as in Fig. 4).*

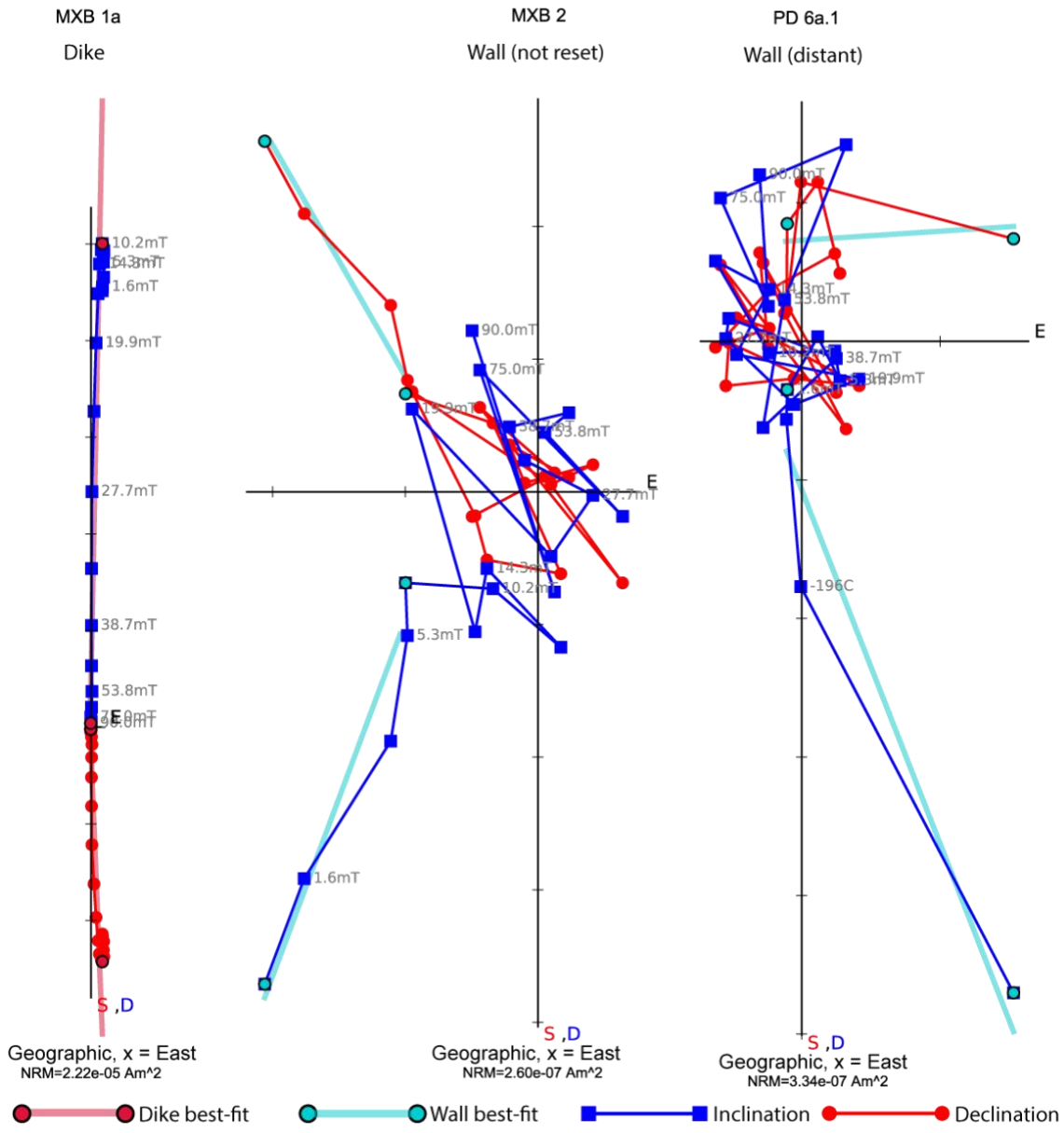

Figure S15*. Orthogonal projections showing representative demagnetization results from three Maxwell B samples. S = south, D = down, E = east.*

At the Maxwell B site (Fig. 1c), granitoid samples are poor recorders of remanent magnetism unless fully reset by the dike (Fig. S15). Given that all of the non-reset

directions from the wall-rock are of normal polarity, we conclude that these samples have a viscous remanent magnetism that is poorly preserving the modern field direction.

(S4.4) Tunnel Dike

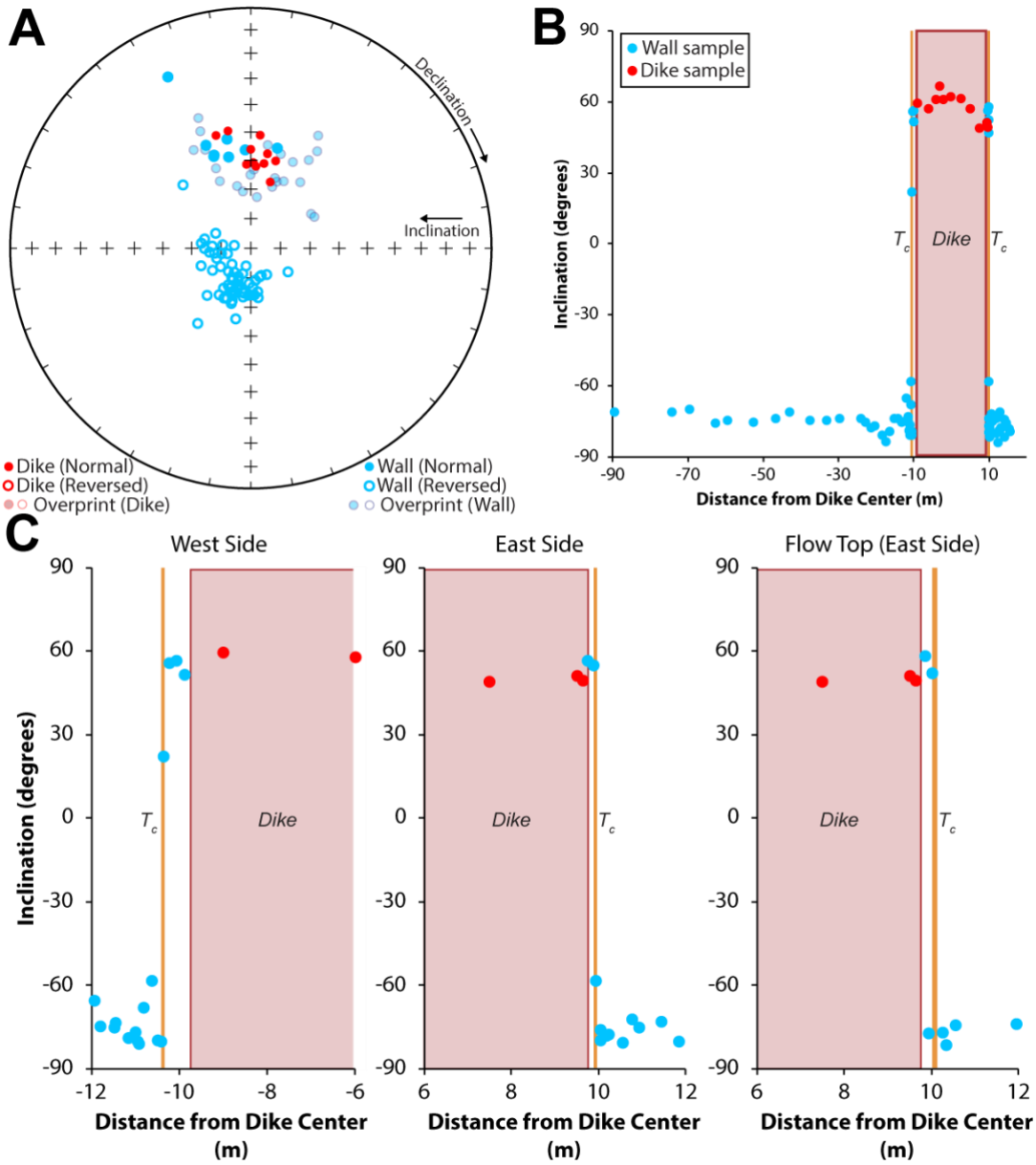

Figure S16. *Summary of paleomagnetic data from the Tunnel dike. Wall-rock samples are blue, dike samples are red. A) Equal area projection. B) Distance vs. inclination plot. T_c = Curie temperature (as in Fig. 4). C) Distance vs. inclination plots showing near-dike samples in greater detail. See text in this section for discussion.*

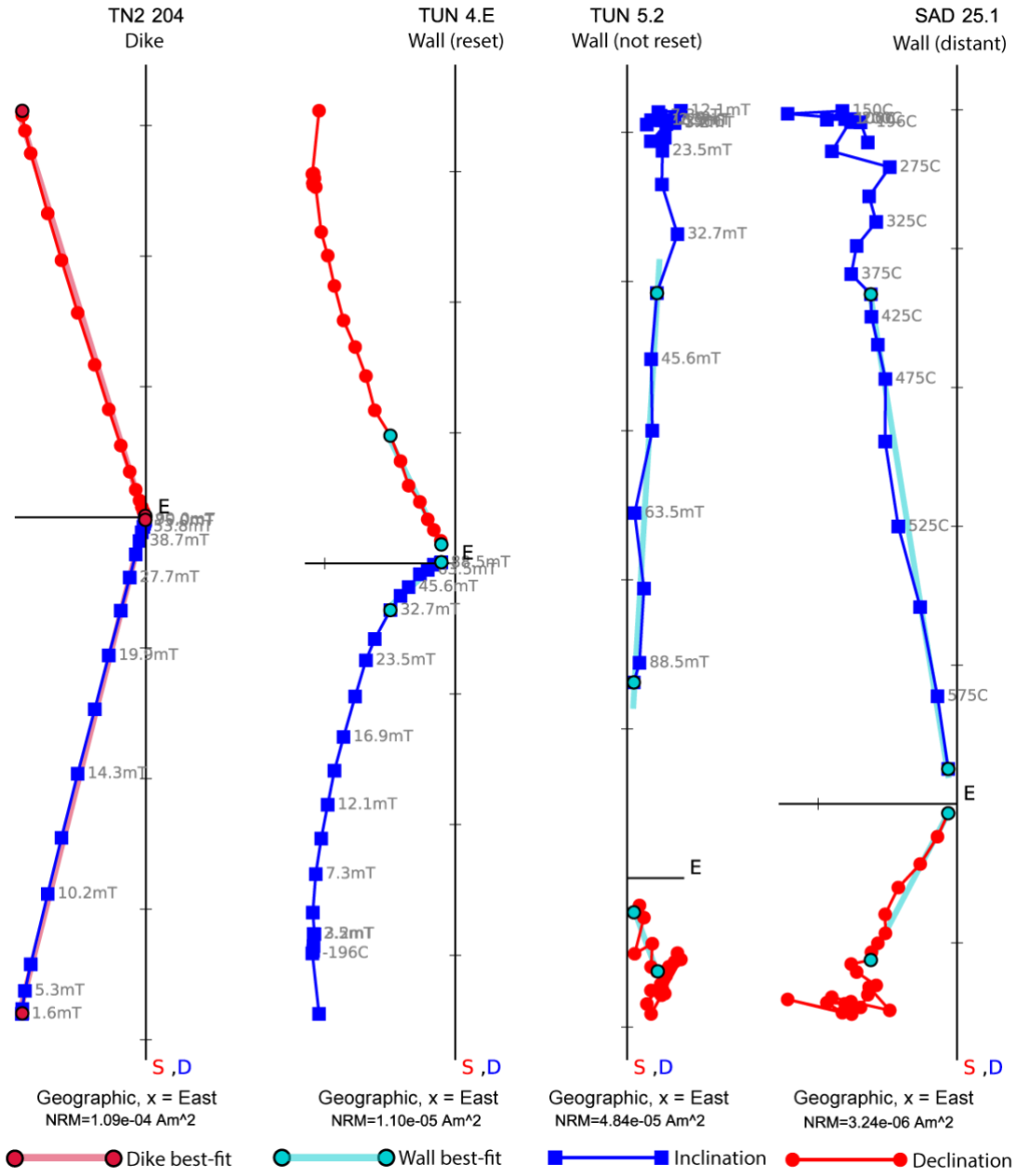

Figure S17. *Orthogonal projections showing representative demagnetization results from four Tunnel samples. S = south, D = down, E = east.*

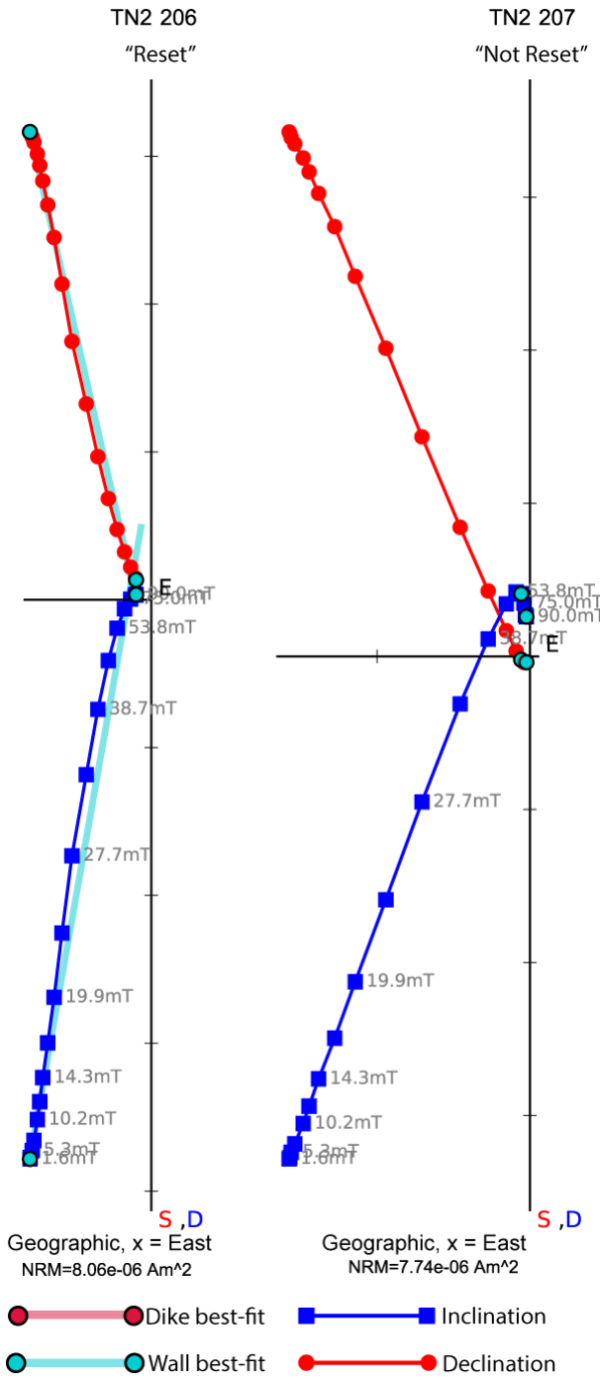

Figure S18. *Orthogonal projections showing demagnetization results from two Tunnel samples of interest. See text for discussion. S = south, D = down, E = east.*

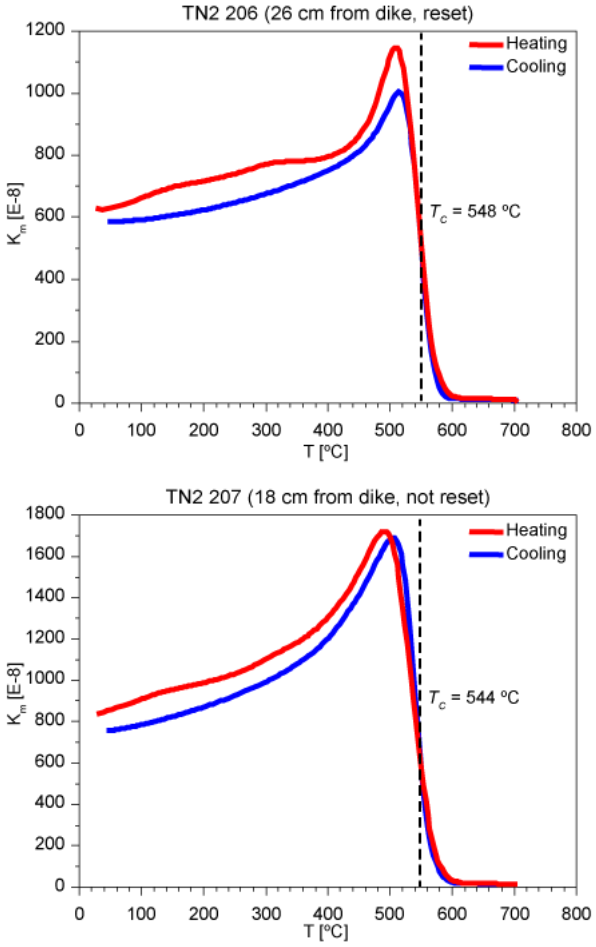

Figure S19. *Thermal-susceptibility curves showing results from two Tunnel samples of interest. See text for discussion.*

The dike and reset wall-rock preserve a normal polarity at this site, while the remaining wall-rock preserves a reversed polarity. Notably, numerous overprints from the non-reset wall-rock yield the same direction as the dike (Fig. S16a).

One disparity in the data concerns samples TN2 206 and TN2 207. Sample TN2 206 has a normal polarity (reset) and is 26 cm from the dike margin. Sample TN2 207 has a reversed polarity (not reset) and is nominally closer to the dike at 18 cm (Figs. S16c, S18). It is possible that mineralogical differences between these samples makes TN 206 more susceptible to magnetic resetting than TN 207. We assume a resetting temperature of 580 °C for all samples in this study, but the shape, size, and Fe/Ti ratio of magnetite in each sample will affect the resetting temperature. However, thermal-susceptibility data from these samples (Fig. S19) suggests that their resetting temperatures are very similar. The dike has a fairly sharp contact, but can locally undulate up to 50 cm, so it is possible that the distance between the dike margin and these samples was not correctly measured. This appears to be the most likely explanation. We assume that the resetting distance is 26 cm, in order to determine the maximum possible lifetime of magma transport in the dike.

(S4.5) Powatka Bridge Dike

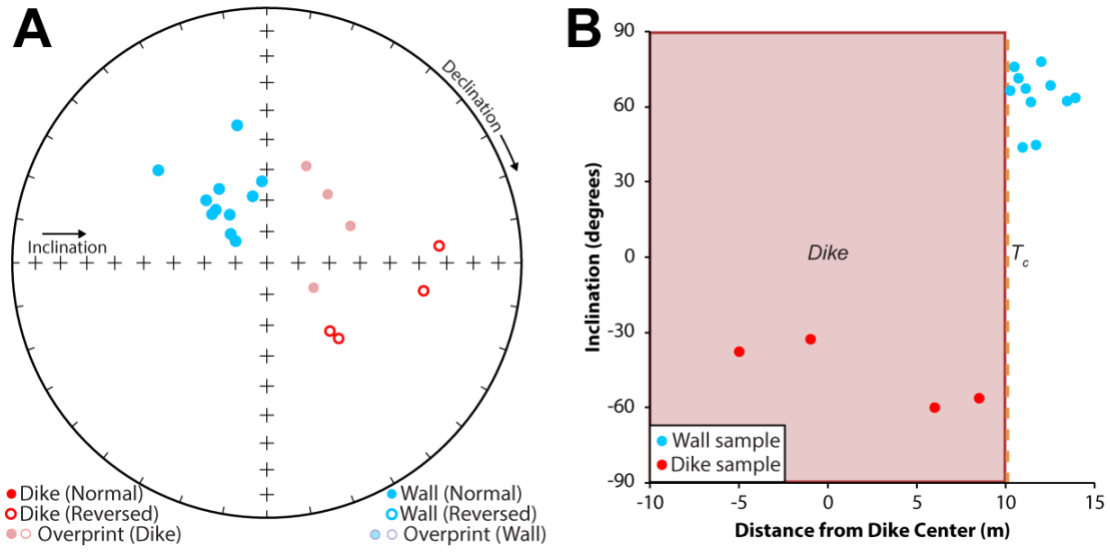

Figure S20. *Summary of paleomagnetic data from the Powatka Bridge dike. Wall-rock samples are blue, dike samples are red. A) Equal area projection. B) Distance vs. inclination plot. T_c = Curie temperature (as in Fig. 4).*

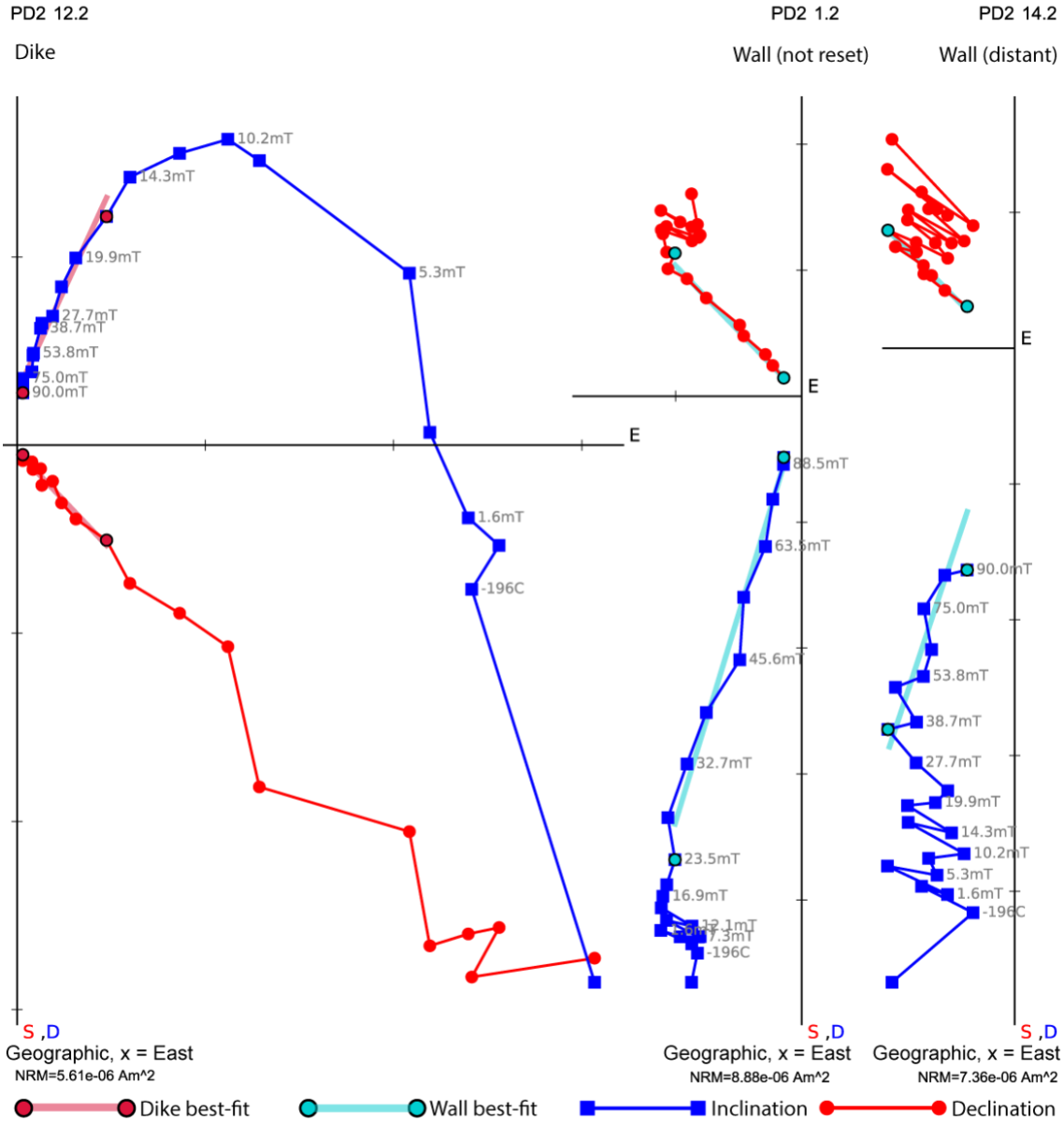

Figure S21*. Orthogonal projections showing representative demagnetization results from three Powatka Bridge samples. S = south, D = down, E = east.*

The wall-rock at this site has a normal polarity (Fig. S20a), while the dike has a transitional(?) magnetic polarity, in agreement with previous studies (Choiniere and Swanson, 1979). Several dike samples show a strong normal overprint (Fig. S21), which may be related to the modern field, but we are not sure of this.

(S4.6) Rattlesnake A Dike

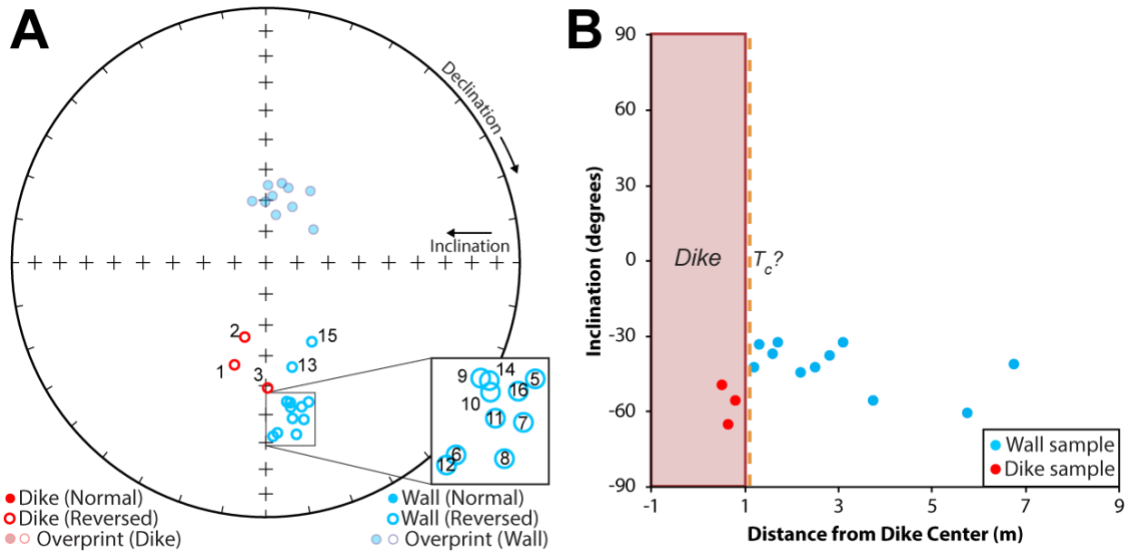

Figure S22. *Summary of paleomagnetic data from the Rattlesnake A dike. Wall-rock samples are blue, dike samples are red. A) Equal area projection. Inset shows sample numbers (see Table S3). B) Distance vs. inclination plot.* T_c *= Curie temperature (as in Fig. 4). See text for discussion.*

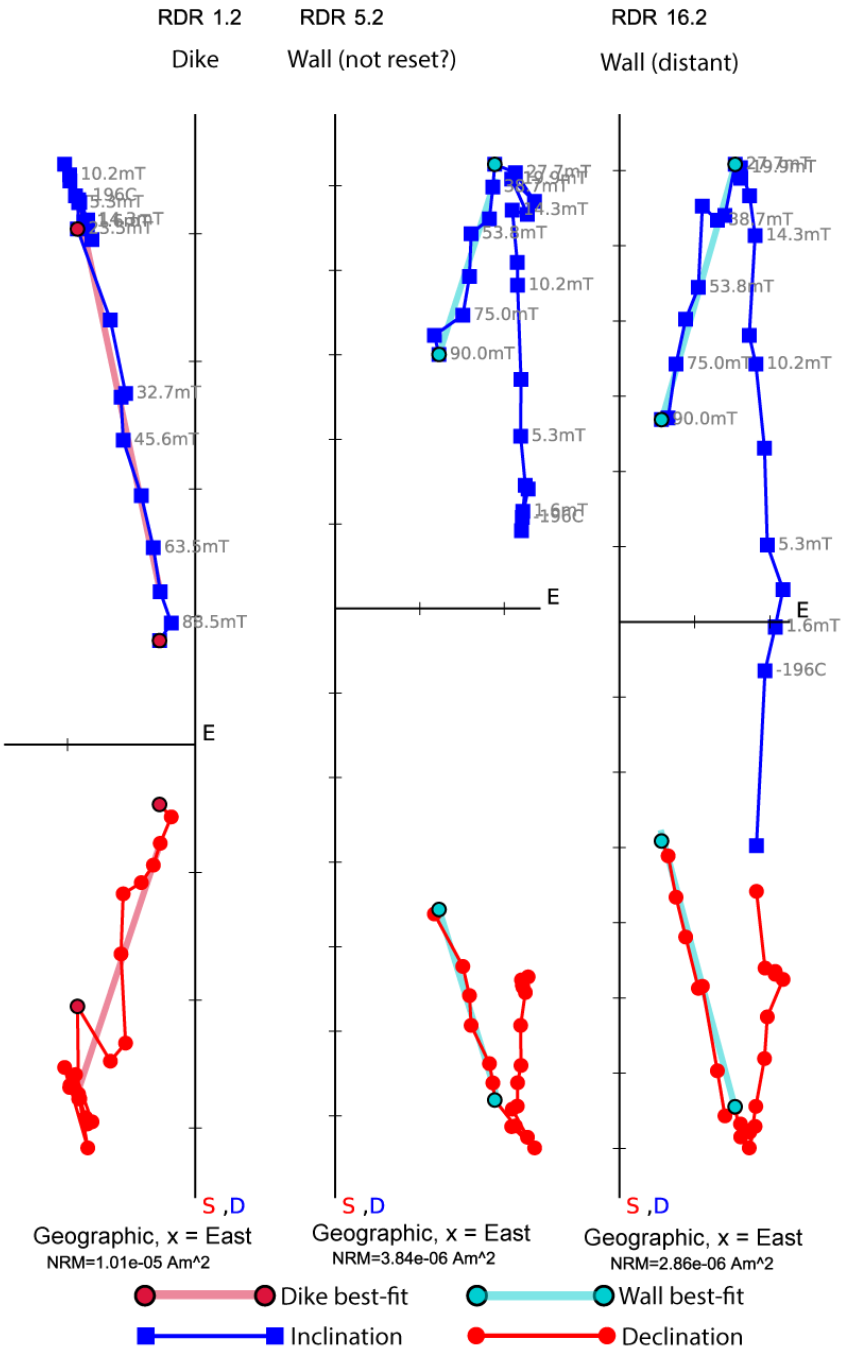

Figure S23*. Orthogonal projections showing representative demagnetization results from three Rattlesnake A samples. S = south, D = down, E = east.*

This dike preserves a reversed polarity, which is consistent with the transitional/reversed polarity determined for the Roza member (Choiniere and Swanson, 1979). The wall-rock also preserves a reversed polarity, in agreement with their assignment to the R2 magnetostratigraphic unit of the Grande Ronde basalts (Reidel et al., 1992). Several wall-rock samples, including samples closest to the dike, show a normal overprint (Fig. S23).

As discussed in the main text, the wall-rock and dike have the same magnetic polarity here. It is highly unlikely that that all of the wall-rock samples are reset (the furthest sample is 5.75 m from the dike margin, Table S3). According to our thermal model, this would require a dike lifetime of 1–4.3+ years, which is similar to the lifetimes of the Jackson A and Maxwell A segments that fed the most voluminous unit of the CRB (Wapshilla Ridge, 40000 km^3). The finely fractured margin of this dike and lack of partially melted wall-rock are also inconsistent with prolonged activity at this exposure. Dozens of other Roza dikes have been found in the immediate area (Fig. S6b), which also suggests that this narrow dike segment was probably not a principal feeder to the Roza member.

(S4.7) Eagle Dike

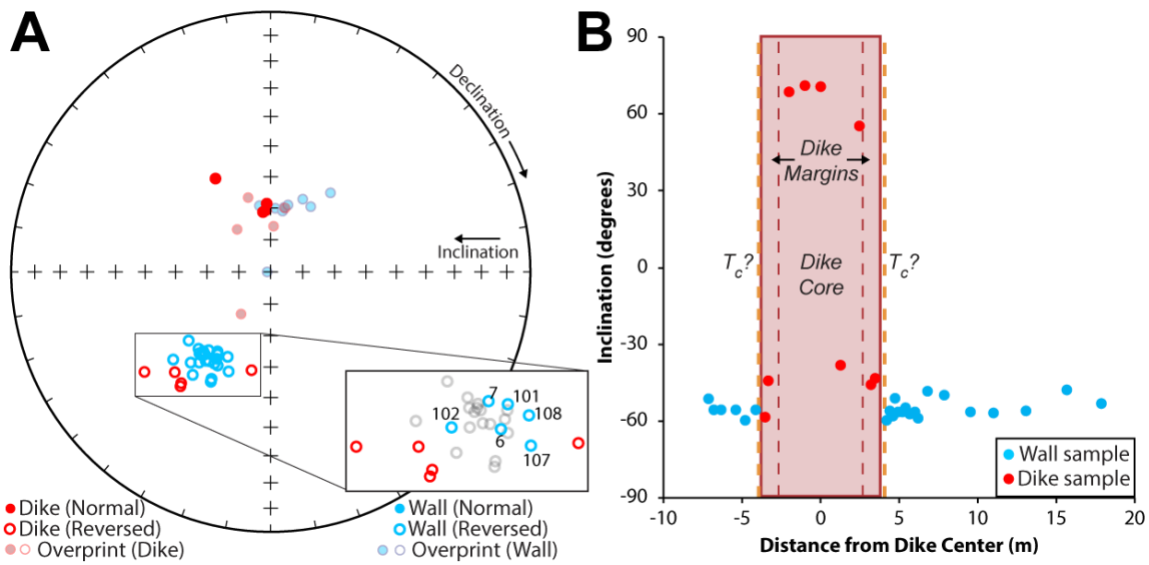

Figure S24. *Summary of paleomagnetic data from the Eagle dike. Wall-rock samples are blue, dike samples are red. A) Equal area projection. Inset shows wall-rock samples within 1 meter of the dike (blue symbols, see Table S3), samples further than 1 m from the dike are in grey. B) Distance vs. inclination plot.* T_c *= Curie temperature (as in Fig. 4). See text for discussion.*

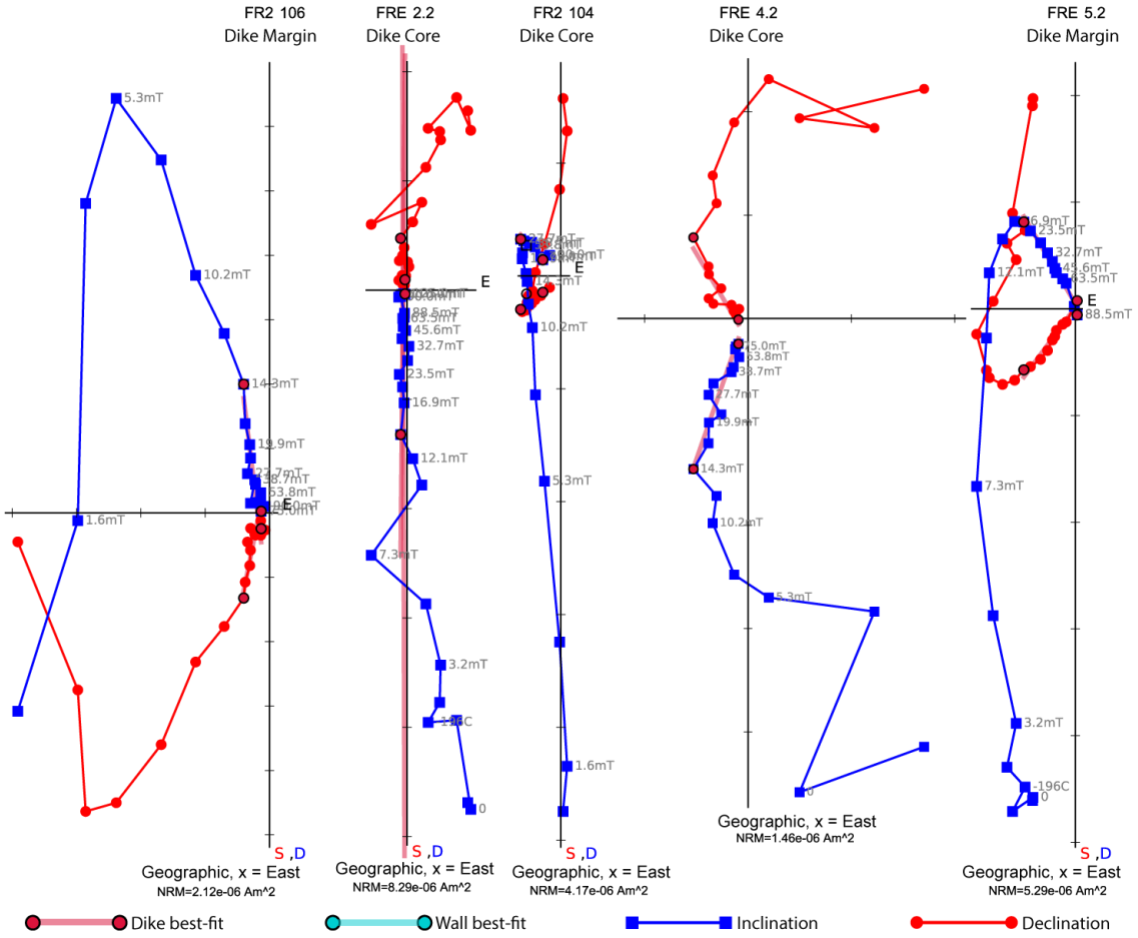

Figure S25*. Orthogonal projections showing representative demagnetization results (dike only) from four Eagle samples. See text for discussion. S = south, D = down, E = east.*

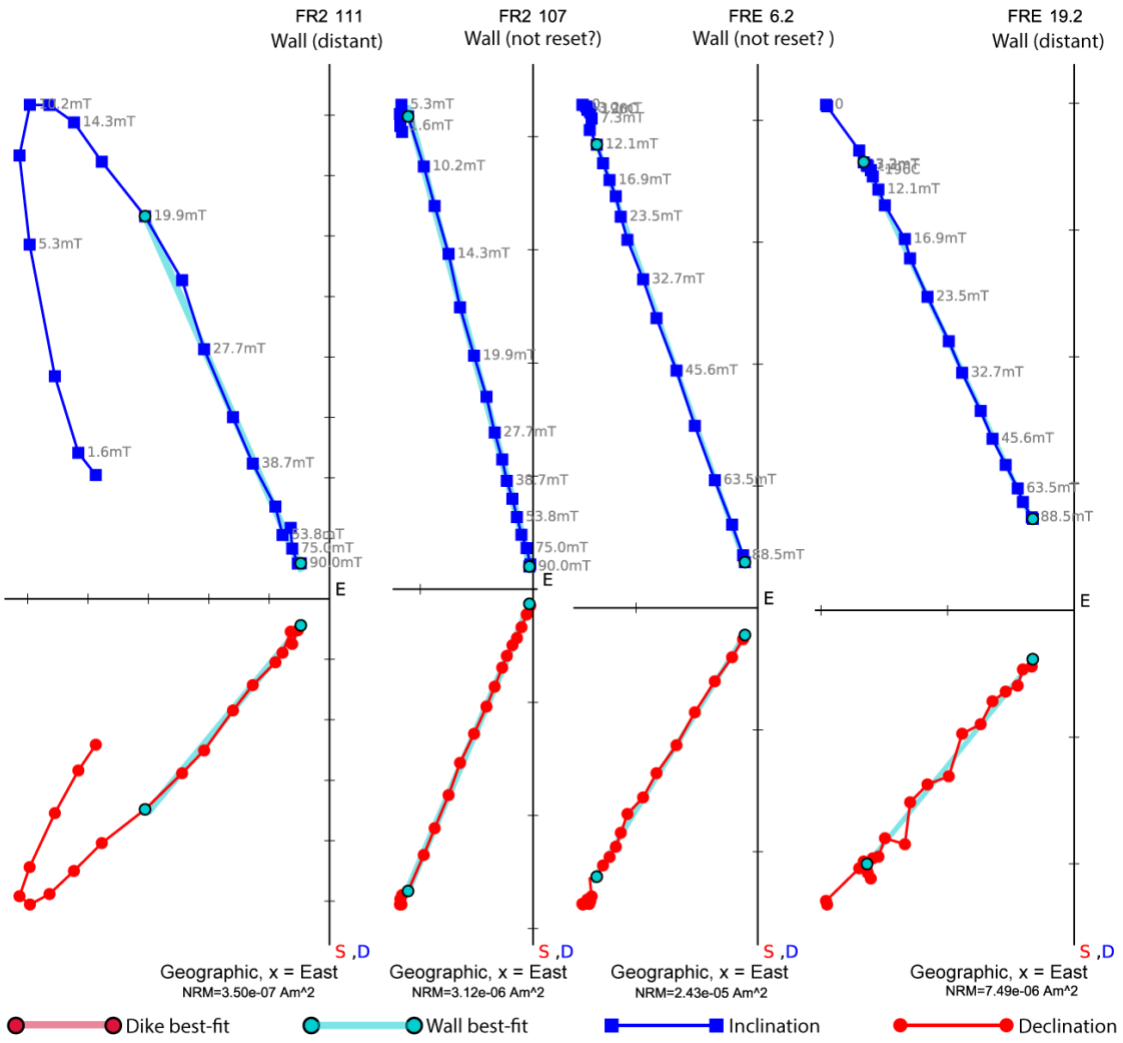

Figure S26*. Orthogonal projections showing representative demagnetization results (wall-rock only) from four Eagle samples. See text for discussion. S = south, D = down, E = east.*

This site has a complex magnetic profile. The dike margins preserve a clear reversed direction with a prominent normal overprint (Fig. S24a). Most samples from the core of the dike preserve a normal direction. Initially, this would imply that the dike is composite, with a margin that was emplaced during a reversed polarity period and a core that was emplaced during a normal polarity period. However, there is no clear evidence

for multiple injections at the outcrop, and the exposure is excellent (Fig. S7c). In addition, five dike samples have been analyzed for geochemical compositions, and both the margins and the core of the dike are nearly identical (Table S1). Finally, one core sample (FR2 104) preserves a reversed direction with a very strong normal overprint (Fig. S25). These combined factors rule out the multiple injection theory. Sample 104 may explain the results seen in Figs. S24 and S25. It appears that the original magnetization of the dike was reversed, and another event has remagnetized some of the samples from the core of the dike. For most of the core samples, this remagnetization event was strong enough to completely replace the primary reversed magnetization. However, one core sample (104) still preserves this original direction. The Buford flow that is fed by this dike has a reversed polarity (Price, 1977; Swanson et al., 1979; Ross, 1989), which also suggests that the primary remanence of the dike is reversed.

Several events can remagnetize a dike. Evidence is lacking for another diking event, as no other dikes are exposed in the roadcut and all of the Eagle dike compositions match the Buford flow (Table S1). Regional heating is ruled out because most of the wall-rock samples do not have a prominent normal overprint (Fig. S26). Thermal-susceptibility data from dike samples (Table S2) show no significant differences between the resetting temperatures of FR2 105 (normal) and FR2 104 (reversed).

Therefore, an isothermal source of remagnetization is probably involved. The most likely candidate for this is a lightning strike, which is localized enough to only remagnetize the core of the dike. This explanation is not ideal because this site is at the bottom of a steep 1000 m canyon, there are several trees that are taller than the outcrop, and the outcrop has only been exposed since the roadcut was made ~100? years ago.

However, we do not have a better explanation for the remagnetization, so we will assume that the core of the dike was struck by lightning.

The wall-rock samples preserve a reversed magnetic polarity, is in agreement with their assignment to the R1 magnetostratigraphic unit of the Grande Ronde basalts (Reidel et al., 1992). As discussed in the main text, it is highly unlikely that all of the wall-rock samples are reset (the furthest sample is 14.1 m from the dike margin, Table S3). According to our thermal model, this would require a dike lifetime of >10 years. The Jackson A and Maxwell A segments that fed the most voluminous unit of the CRB (Wapshilla Ridge, 40000 km^3) were active for a shorter period of time. The finely fractured margins of this dike and lack of partially melted wall-rock are also inconsistent with prolonged activity at this exposure.

(S4.8) Boggan's Oasis Dike

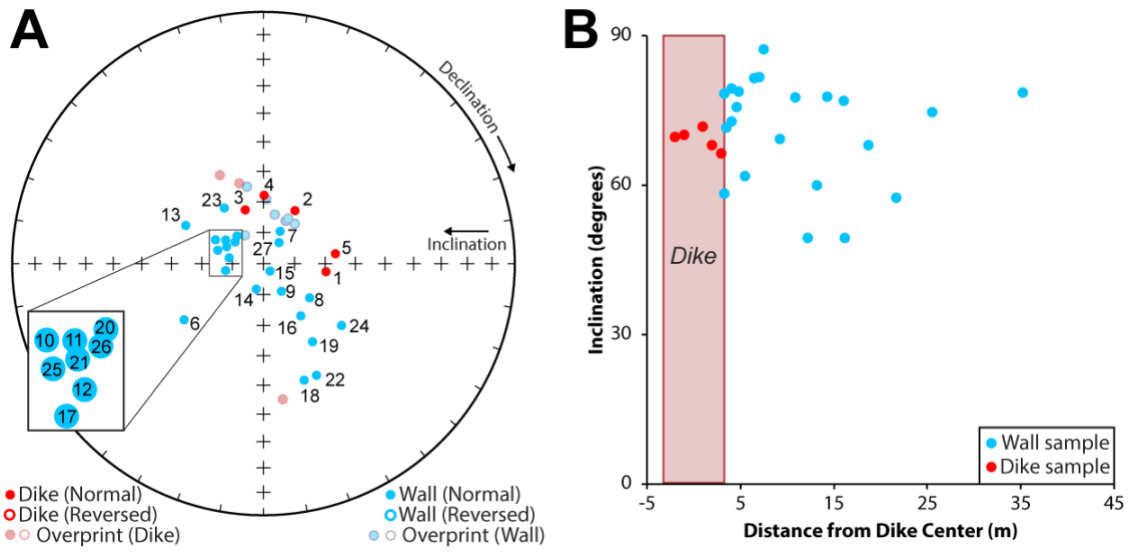

Figure S27. *Summary of paleomagnetic data from the Boggan's Oasis dike. Wall-rock samples are blue, dike samples are red. A) Equal area projection. Inset shows sample numbers (see Table S3). B) Distance vs. inclination plot. See text for discussion.*

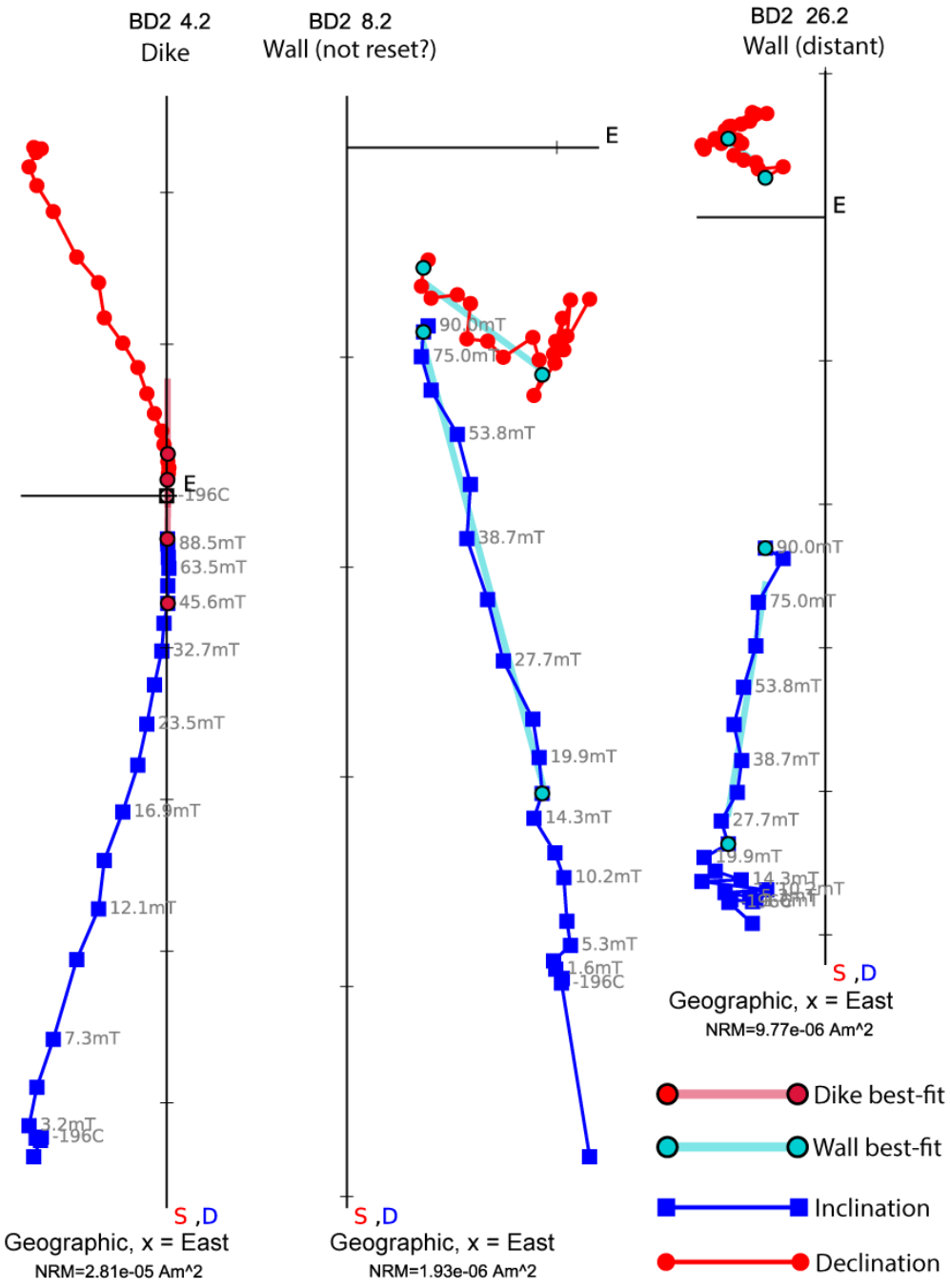

Figure S28*. Orthogonal projections showing representative demagnetization results from three Boggan's Oasis samples. S = south, D = down, E = east.*

The dike preserves a normal polarity (Fig. S27), while the associated Sentinel Bluffs member is transitional (Reidel, 2005). Wall-rock samples preserve a normal or transitional magnetic polarity, and are assigned to the N1 magnetostratigraphic unit of the Grande Ronde basalts (Schuster, 1993). Some wall-rock samples have overprints that are similar to the dike directions (Fig. S27a), but it is not clear if any of the wall-rock samples have been fully reset by the dike. For example, the closest sample (BD2 6) is 5 cm from the dike margin, and our thermal model requires that this sample be reset, regardless of dike lifetime. This resetting is not clearly evident in the highly scattered data from this dike. Therefore, we conclude that the MGT technique cannot be applied here given the ambiguity in our current dataset.

(S5) Additional information on the thermal model of Karlstrom et al. (2019)

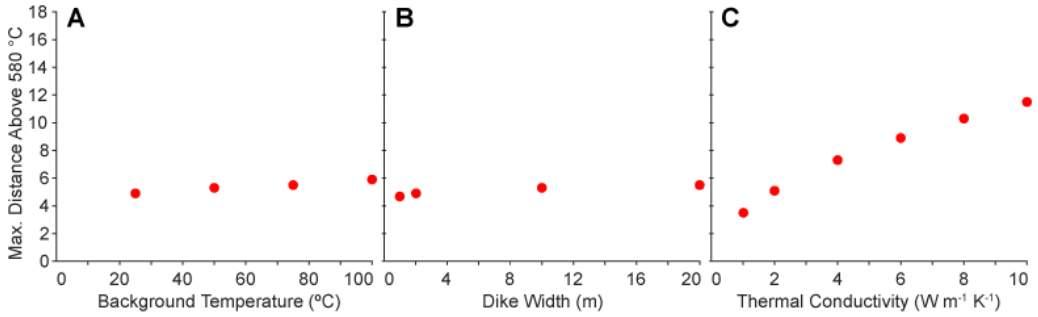

Figure S29. *Effect of other variables on distance from the dike margin to the T_c isotherm. The same conditions are used in each model run, with modifications shown on the x-axis of each plot. Base conditions are: background temperature = 40 °C, dike width = 10 m,*

flow unsteadiness (τ_w) = 0.01 year, thermal conductivity = 3 W m^{-1} K^{-1}, flow duration (τ_c) = 1 year.

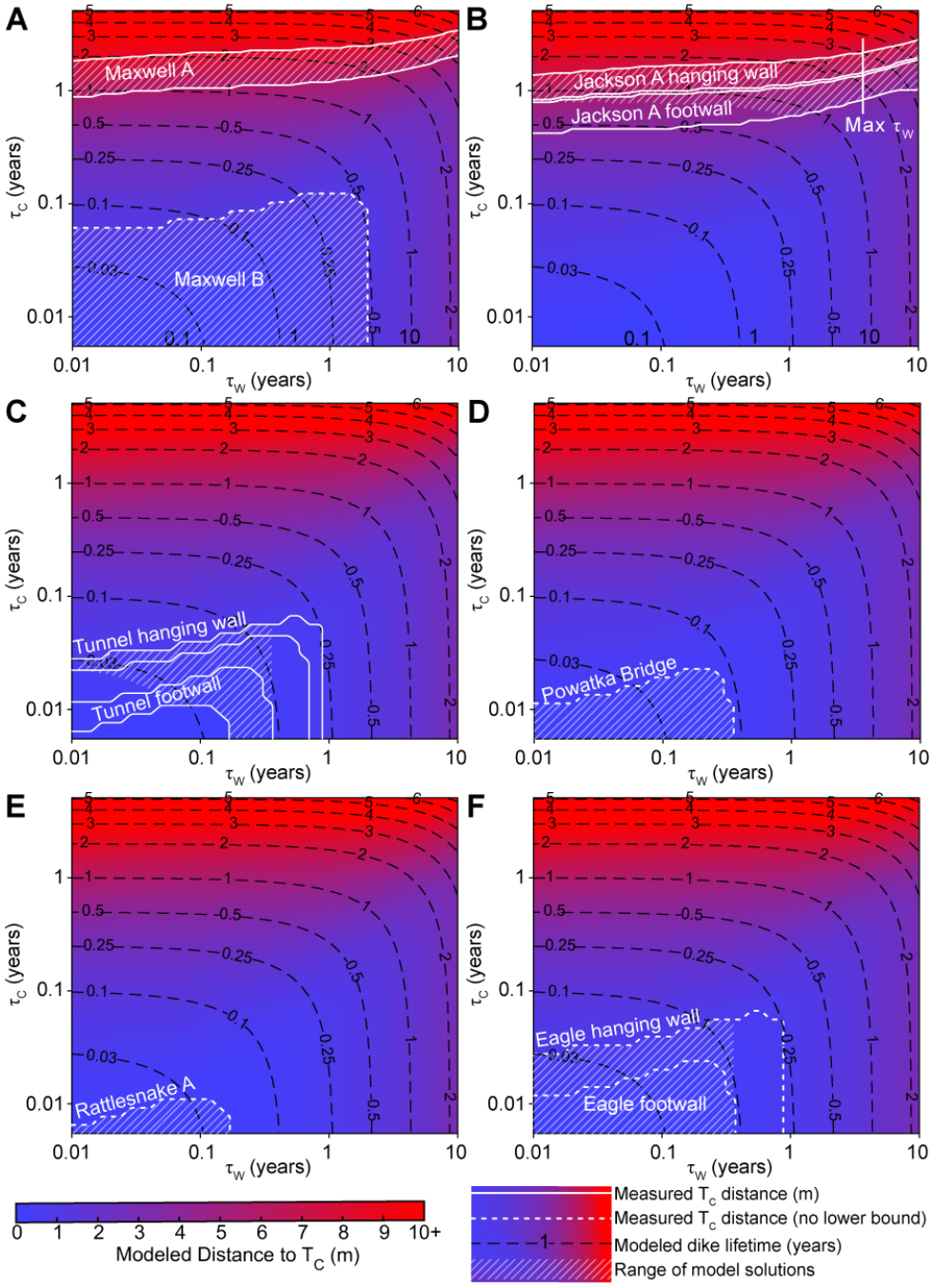

Figure S30. *Modeling results from this study, showing the dike lifetime (black contours), modeled distance to the T_c isotherm from the dike margin (color scale), and measured distance to the T_c isotherm for each dike (white). Maximum τ_w from Karlstrom et al.*

(2019). Background temperature = 40 ºC, thermal conductivity = 3 W m^{-1} K^{-1}, dike width = 10 m. See text for discussion.

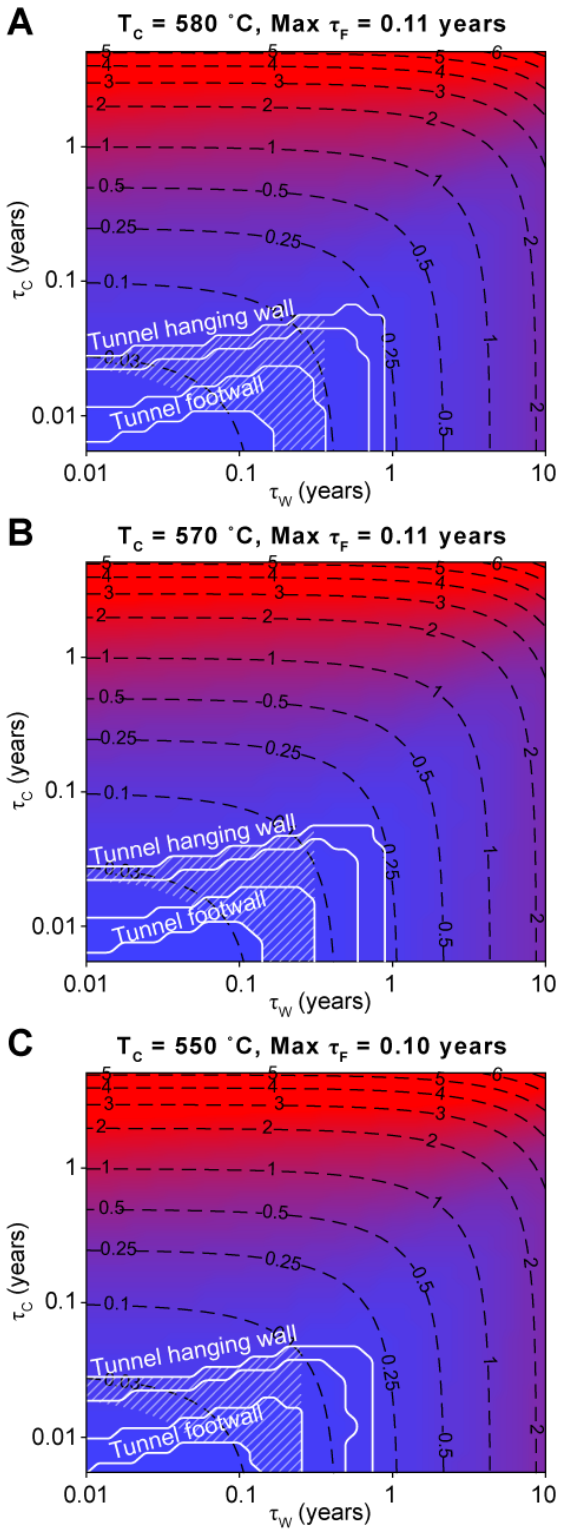

Figure S31. *Modeling results from this study, showing the effects of lower Curie temperatures. Symbols as in Fig. S30.*

We do not model the possible effects of non-monotonic time-temperature histories, such as would occur for pulsed magma flow or reinjection of the same dike structure by multiple intrusions. As noted by Petcovic (2004), such non-monotonic thermal histories may play an important role in the heating of host rocks and their assimilation by CRB magmas. Direct evidence of selvage zones in some dikes also points to this scenario. However, from the standpoint of MGT, the high temperatures required to remagnetize rocks simplify our problem. As argued in Connerney et al. (2005) in the context of lava flows, once a dike is emplaced subsequent injections have a significant thermal barrier to overcome in order to remagnetize host rocks due to the insulating effects of cool basalt.

Heat transport around magmatic intrusions in the shallow crust generally involves conduction as well as advection mediated by fluids present in wall-rocks (Delaney, 1982; Weis, 2015; Bindeman et al., 2020). However, the high temperatures associated with thermal remagnetization of host rocks around a dike, along with the relatively small thermal mass of the dike compared to host rocks, again results in a somewhat simpler thermal problem than the general case. For example, as demonstrated by Figure 5a of Bindeman et al. (2020), the maximum distance to ~580 °C from the dike margin is negligibly different between pure conduction models and advection-diffusion models. This is not true for lower temperatures: a maximum of 200 °C is for example reached

between 2–5 times farther away from the dike margin in simulations including fluid advection than pure conduction in Bindeman et al. (2020).

We therefore assume that conduction dominates heat transport for the magnetic geothermometer (MGT) technique. This idealized approach, also typical of other thermochronologic techniques (Fox and Carter, 2020), is sufficient given the lack of constraints on fluid transport. Fig. (S29) illustrates the variability in resetting distance (D_c) for parameter variation through background temperature, dike width, and host rock thermal conductivity. Although thermal conductivity is seen to cause significant variability in D_c, we use the advection-diffusion results of Bindeman et al., (2020) to argue that that our choice of k=$3\ W\ m^{-1}\ K^{-1}$ is appropriate in this initial study.

Of more direct relevance to MGT, we can also study the impacts of variable T_c on D_c. Based on the magnetic thermal-susceptibility results presented in Table S2, a Curie temperature of 550-580 ℃ reasonably spans the likely range of variability found in basaltic host rocks. We re-ran the Tunnel dike model using lower T_c and find that the maximum dike lifetime (τ_f) is reduced from 1.3 to 1.2 months when T_c is reduced from 580 ℃ to 550 ℃ (Fig. S31), which is an 8% change.

References

Bindeman, I., Greber, N., Melnik, O., Artyomova, A., Utkin, I., Karlstrom, L., and Colón, D., 2020, Pervasive hydrothermal events associated with large igneous provinces documented by the Columbia River basaltic province: Scientific Reports, v. 10, p. 1–9, doi:10.1038/s41598-020-67226-9.

Camp, V.E., Reidel, S.P., Ross, M.E., Brown, R.J., and Self, S., 2017, Field-trip guide to the vents, dikes, stratigraphy, and structure of the Columbia River Basalt Group, eastern Oregon and southeastern Washington: U.S. Geological Survey Scientific Investigations Report USGS Numbered Series 2017-5022-N, 104 p., https://doi.org/10.3133/sir20175022N.

Choiniere, S.R., and Swanson, D.A., 1979, Magnetostratigraphy and correlation of Miocene basalts of the northern Oregon coast and Columbia Plateau, southeast Washington: American Journal of Science, v. 279, p. 755–777, doi:10.2475/ajs.279.7.755.

Connerney, J., Acuña, M., Ness, N., Kletetschka, G., Mitchell, D., Lin, R., and Reme, H., 2005, Tectonic implications of Mars crustal magnetism: Proceedings of the National Academy of Sciences, v. 102, p. 14970–14975, doi:10.1073/pnas.0507469102.

Delaney, P.T., 1982, Rapid intrusion of magma into wet rock: groundwater flow due to pore pressure increases: Journal of Geophysical Research: Solid Earth, v. 87, p. 7739–7756, doi:10.1029/JB087iB09p07739.

Fox, M., and Carter, A., 2020, Heated topics in Thermochronology and paths towards resolution: Geosciences, v. 10, p. 375, doi:10.3390/geosciences10090375.

Hooper, P.R., 2000, Chemical discrimination of Columbia River basalt flows: Geochemistry, Geophysics, Geosystems, v. 1, doi:10.1029/2000GC000040.

Karlstrom, L., Murray, K.E., and Reiners, P.W., 2019, Bayesian Markov-chain Monte Carlo inversion of low-temperature thermochronology around two 8- 10 m wide

Columbia River flood basalt dikes: Frontiers in Earth Science, v. 7, p. 90, doi:10.3389/feart.2019.00090.

Kirschvink, J., 1980, The least-squares line and plane and the analysis of palaeomagnetic data: Geophysical Journal International, v. 62, p. 699–718, doi:10.1111/j.1365-246X.1980.tb02601.x.

Petcovic, H.L., 2004, Feeder dikes to the Columbia River flood basalts: underpinnings of a large igneous province [PhD Thesis]: Oregon State University, 240 p.

Petcovic, H.L., and Dufek, J.D., 2005, Modeling magma flow and cooling in dikes: Implications for emplacement of Columbia River flood basalts: Journal of Geophysical Research: Solid Earth, v. 110, doi:10.1029/2004JB003432.

Petcovic, H., and Grunder, A., 2003, Textural and thermal history of partial melting in tonalitic wallrock at the margin of a basalt dike, Wallowa Mountains, Oregon: Journal of Petrology, v. 44, p. 2287–2312, doi:10.1093/petrology/egg078.

Price, S.M., 1977, An evaluation of dike-flow correlations indicated by geochemistry, Chief Joseph swarm, Columbia River basalt [PhD Thesis]: University of Idaho, 320 p.

Reidel, S.P., 2005, A lava flow without a source: The Cohassett flow and its compositional components, Sentinel Bluffs Member, Columbia River Basalt Group: The Journal of Geology, v. 113, p. 1–21, doi:10.1086/425966.

Reidel, S.P., 1998, Emplacement of Columbia River flood basalt: Journal of Geophysical Research: Solid Earth, v. 103, p. 27393–27410, doi:10.1029/97JB03671.

Reidel, S.P., Camp, V.E., Tolan, T.L., and Martin, B.S., 2013, The Columbia River flood basalt province: Stratigraphy, areal extent, volume, and physical volcanology, *in*

The Columbia River Flood Basalt Province, Geological Society of America, doi:10.1130/2013.2497(01).

Reidel, S.P., Hooper, P.R., Webster, G.D., and Camp, V.E., 1992, Geologic Map of Southeastern Asotin County, Washington: Washington Division of Geology and Earth Resources, Olympia, Washington Geologic Map 6M-40.

Reidel, S.P., and Tolan, T.L., 2013, The Grande Ronde Basalt, Columbia River Basalt Group, *in* Geological Society of America Special Paper, v. 497, p. 117–153, doi:10.1130/2013.2497(05).

Ross, M.E., 1983, Chemical and mineralogic variations within four dikes of the Columbia River Basalt Group, southeastern Columbia Plateau: GSA Bulletin, v. 94, p. 1117–1126, doi:10.1130/0016-7606(1983)94<1117:CAMVWF>2.0.CO;2.

Ross, M.E., 1989, Stratigraphic relationships of subaerial, invasive, and intracanyon flows of Saddle Mountains Basalt: Volcanism and Tectonism in the Columbia River Flood-Basalt Province, v. 239, p. 131.

Schuster, J., 1993, Geologic map of the Clarkston 1:100,000 quadrangle, Washington–Idaho, and the Washington portion of the Orofino 1:100,000 quadrangle: Washington Division of Geology and Earth Resources Open File Report 93-4, 1 plate.

Swanson, D.A., Anderson, J., Camp, V., Hooper, P., Taubeneck, W., and Wright, T., 1981, Reconnaissance geologic map of the Columbia River basalt group, northern Oregon and western Idaho: US Geological Survey, Open-File Report 81–797, https://doi.org/10.3133/ofr81797.

Swanson, D.A., Wright, T., Hooper, P., and Bentley, R., 1979, Revisions in stratigraphic nomenclature of the Columbia River Basalt Group: Bulletin USGS Numbered Series 1457, https://doi.org/10.3133/b1457G.

Tauxe, L., and Staudigel, H., 2004, Strength of the geomagnetic field in the Cretaceous Normal Superchron: New data from submarine basaltic glass of the Troodos Ophiolite: Geochemistry, Geophysics, Geosystems, v. 5, doi:10.1029/2003GC000635.

Thordarson, T., and Self, S., 1998, The Roza Member, Columbia River Basalt Group: A gigantic pahoehoe lava flow field formed by endogenous processes? Journal of Geophysical Research: Solid Earth, v. 103, p. 27411–27445, doi:10.1029/98JB01355.

Weis, P., 2015, The dynamic interplay between saline fluid flow and rock permeability in magmatic-hydrothermal systems: Geofluids, v. 15, p. 350–371, doi:10.1111/gfl.12100.

Žák, J., Verner, K., Johnson, K., and Schwartz, J.J., 2012, Magma emplacement process zone preserved in the roof of a large Cordilleran batholith, Wallowa Mountains, northeastern Oregon: Journal of Volcanology and Geothermal Research, v. 227, p. 61–75, doi:10.1016/j.jvolgeores.2012.03.001.

Chapter 4

Eruption Rates, Tempo, and Stratigraphy of Paleocene Flood Basalts from Baffin Island, Canada

Coauthors: Joseph Biasi, Caltech; Paul Asimow, Caltech; Forrest Horton, Woods Hole Oceanographic Institution

Abstract

We present new stratigraphic and paleomagnetic data from Paleocene flood basalts on Baffin Island. These basalts and picrites are part of the North Atlantic igneous province and are well known among geochemists for their extremely primitive $^{3}He/^{4}He$ ratios. Despite extensive geochemical study, little is known about the stratigraphy, geochronology, and eruptive tempo of these lavas. We address these knowledge gaps by presenting the first measured stratigraphic sections of these deposits, seven in total. The locations of 158 paleomagnetic, geochemical, and geochronological samples are also given with stratigraphic context. This study focuses on new data from 38 paleomagnetic sites, representing 95 paleomagnetic samples and 111 paleomagnetic specimens. These sites include the Paleocene lavas as well as the underlying Cretaceous sediments (Quqaluit Fm.). Among the igneous sites, the average pole does not overlap with the expected pole for a stable North American site at 60 Ma, suggesting that the eruptive sequence at Baffin was emplaced in less time than needed to 'average out' paleosecular variation. Paleosecular variation paths generated by our data, combined with an expected rate of secular variation, are used to calculate the eruptive tempo of lava flow sequences. We find a total eruption duration of 1665^{+191}_{-143} years and average eruption interval of ~22 years per flow for the thickest sequence of exposed lavas. It appears that the entire package of volcanic deposits was emplaced in a relatively short 'burst' of activity, which has also been inferred at similar deposits in western Greenland. Finally, we use our stratigraphic data in combination with the mapped distribution of the lavas to estimate the total volume of Paleocene Baffin lavas to be 176 km^3. This is a conservative estimate as

it does not include any deposits that are submerged in Baffin Bay. When combined with the ~1665-year eruption duration estimate, this implies an average eruption rate of ~0.1 $km^3\ yr^{-1}$, which is greater than rates found in West Greenland but less than larger flood basalts that are associated with mass extinctions. This suggests that higher eruptive rates or eruptive tempos are necessary to cause significant global climate shifts than the rates and tempos observed in the Baffin and West Greenland flood basalts.

1. Introduction

Throughout Earth History, large shifts in climate and loss of biological diversity often coincide with voluminous igneous eruptions (Wignall, 2005). While some degree of volcanic activity has been constant for billions of years, the 'background' level of volcanic CO_2, H_2S, and SO_2 emissions do not lead to large climatic shifts, as various sequestration mechanisms are able to handle these volatile inputs (Wigley et al., 2005). In the case of large-scale igneous activity such as flood basalts, large igneous provinces (LIPs), or super-eruptions, the flux of volatiles and/or ash into the atmosphere overwhelms the available array of sequestration mechanisms. As a result, longer-term or more dramatic climatic shifts can occur, having profound effects on the biosphere in turn (Clapham and Renne, 2019).

For example, the Paleocene epoch (Fig. 1) began with the Cretaceous-Paleogene (K-Pg) mass extinction, the Chicxulub Impact, and eruption of the Deccan Traps LIP in India (Schoene et al., 2015). The epoch ended with the Paleocene-Eocene thermal maximum (PETM), a period of rapid global warming with temperatures rising by 5-8 ºC on average (Wing et al., 2005). The exact cause(s) of the PETM are not certain, but this

event correlates with eruption of flood basalts in eastern Greenland (Wilkinson et al., 2017). In addition, flood basalt eruptions were ongoing in western Greenland and Baffin Island during the mid-Paleocene (Fig. 1). These areas were once adjacent, but were separated by the opening of Baffin Bay (Larsen et al., 2016). The west Greenland and Baffin Island flood basalt activity has been associated with the 'End C27n event,' a short period of ~2 ºC global warming and hence a relatively moderate climate disturbance by flood basalt standards (Dinarès-Turell et al., 2012).

There is vigorous debate on the causes of major climate disturbances and the relative role of flood basalts in these events (Chenet et al., 2009; e.g. Schulte et al., 2010; Cox et al., 2016; Fischer et al., 2016; Schmidt et al., 2016; Macdonald and Wordsworth, 2017). Much of this uncertainty is due to poor constraints on flood basalt eruption *rates* and eruptive *tempo*. The previous chapter of this thesis addressed flood basalt eruption *rates* (of individual lava flows in the Columbia River basalts), so here we turn to the issue of eruptive *tempo* (defined as the amount of time between eruptions and the clustering of eruptive events).

In general, there are two main approaches to determining the eruptive tempo of flood basalt events. The most popular approach is to use geochronological methods such as whole-rock $^{40}Ar/^{39}Ar$ or Zircon U-Pb geochronology (e.g. Barry et al., 2013; Kasbohm and Schoene, 2018). By dating the oldest and youngest deposits in a flood basalt, the total duration of activity can be determined. This total duration can then be divided by the number of flows or the total eruptive volume to calculate the average eruptive frequency or the volumetric eruption rate, respectively. Early attempts to date flood basalt eruptions were hampered by high uncertainties, causing overlapping ages between clearly distinct

formations or members (e.g. Baksi, 1989). As geochronological methods advanced, the uncertainties were reduced but the issue of overlapping errors was not resolved. Instead, it was found that large portions of some flood basalt events were still within the error of single U-Pb and $^{40}Ar/^{39}Ar$ age determinations (Schoene et al., 2019; Sprain et al., 2019). This suggests that peak activity in flood basalts may be characterized by a very high eruptive tempo that is difficult to characterize geochronologically.

In order to determine the eruptive tempo at finer resolution than is currently possible with geochronological methods, a different approach based on *geomagnetic paleosecular variation* (PSV) may be most effective. This technique uses the fundamental properties of the Earth's magnetic field to reconstruct eruptive tempo and is briefly explained here. Despite secular variation in the geographic location of the magnetic north pole (Butler, 1992), the average position of magnetic north over the course of 10^4 to 10^5 years is equivalent to geographic north (Jackson and Finlay, 2007). Each lava flow in a sequence records the position of magnetic north at the time of its cooling (Tauxe et al., 2010); if a large package of lava flows (such as a flood basalt) erupts over 10^5 years, then the average of all paleomagnetic directions from all of the flows will correspond with the position of the geographic north pole. However, if the average paleomagnetic direction does not coincide with geographic north, then the entire eruptive package must have taken less than ~10^4 years to be emplaced, as there was not enough time to 'average out' secular variation (e.g. Chenet et al., 2009). In some cases, the amount of time between eruptions can be estimated to a resolution of a few decades, using an assumed rate of PSV (e.g. Champion and Donnelly-Nolan, 1994; Giorgis et al., 2019). This approach has been used with lava flow sequences in the Deccan Traps,

Columbia River Basalts, and west Greenland lavas (Bogue and Coe, 1981; Riisager et al., 2003a; Chenet et al., 2009). These studies generally show short periods of frequent eruptions followed by relatively long hiatuses, which are averaged out in most geochronological studies.

This study focuses on the Paleocene flood basalts of Baffin Island, which are not well studied geochronologically or paleomagnetically. As a result, the eruptive tempo is not well constrained. Furthermore, the absolute age of the basalts is not well known either, as only a whole-rock K-Ar age of 58 ± 2 Ma (Clarke and Upton, 1971) has been determined for these lavas, in part due to their low potassium content (Francis, 1985). Finally, the general stratigraphy of these basalts been described by Clarke (1968), but not described for specific sites.

This study aims to determine the eruptive tempo of the Paleocene basalts and picrites of Baffin Island. To accomplish this, geomagnetic PSV data from paleomagnetic samples are combined with a refined stratigraphy and age estimation of these lavas. Finally, the results from Baffin Island will be compared to other flood basalt provinces, including the related west Greenland lavas.

2. Geologic Background and Previous Work

2.1 Regional Geology

As a part of the Canadian Shield, Baffin Island hosts lavas, dikes, and intrusions from numerous mafic igneous events spanning billions of years of geologic history (de Kemp et al., 2006). The Paleocene flood basalts are the latest igneous activity in the area

and will hereafter be referred to as the Paleocene Baffin Lavas or 'PBL', to avoid confusion with earlier events. The PBL are part of the much larger North Atlantic Igneous Province (NAIP) (Fig. 2a) (Horni et al., 2017). Most of the igneous activity has been attributed to the Iceland Plume in some form. and the entire province was active from ~64 Ma to 13 Ma (not including modern activity in Iceland) (Kent et al., 2004; Storey et al., 2007; Wilkinson et al., 2017; Steinberger et al., 2019). However, a contingent of researchers argue that some portions of the NAIP are not plume related and attribute the igneous activity to other processes (e.g. Day, 2016; Clarke and Beutel, 2020; Hole and Natland, 2020). What is not in dispute, however, is that the emplacement of flood basalts on the eastern portion of Baffin Island and western Greenland coincides with the opening of the Davis Strait and Baffin Bay (Chauvet et al., 2019), as part of the larger opening of the North Atlantic and breakup of Pangea (Peace et al., 2020).

The Paleocene/Eocene west Greenland lavas (WGL) have been studied intensively by the Danish Geological Survey and other researchers (e.g. Storey et al., 2007; Larsen et al., 2009; Agranier et al., 2019), and have well-documented stratigraphy (Dam et al., 2009), geochemistry (Pedersen et al., 2017, 2018), paleomagnetism (Riisager and Abrahamsen, 1999; Riisager et al., 1999, 2003b, 2003a; Pedersen et al., 2002), and geochronology (Larsen et al., 2016 and references therein). The lowest member of the WGL, the Anaanaa member, consists of picrites similar in geochemistry and magnetic polarity to the PBL. The Anaanaa member erupted around 62 Ma during Chron C27n (Larsen et al., 2016), and it is therefore generally assumed that the PBL also erupted at that time (Kent et al., 2004). However, some Baffin lavas are more isotopically primitive

than any Anaanaa samples (Horton et al., 2021), suggesting that some of the PBL may predate the oldest Anaanaa member lavas.

2.2 Baffin Island

Descriptions of the physical volcanology, field relations, and structural relations of the PBL are given in a PhD thesis by Clarke (1968) and in two subsequent papers (Clarke, 1970; Clarke and Upton, 1971). The oldest units in the area are Archean tonalite and granodiorite gneisses, which are ubiquitous on the Cumberland Peninsula (Fig. 2b) (Sanborn-Barrie and Young, 2013; Sanborn-Barrie et al., 2013). Overlying this are Cretaceous to Paleogene sediments, consisting of white sands, siltstones, and coal beds. These units have been studied by Burden and Langille (1990, 1991), who concluded that the youngest deposits are the product of early extension prior to full opening of the Davis Strait and Baffin Bay. The uppermost sedimentary units are occasionally interbedded with the PBL (Clarke, 1968). Where the base of the PBL sequence is exposed, it rests directly on either the sediments or on the Archean gneisses (Clarke and Upton, 1971). The PBL consists of a lower subaqueous section mostly composed of palagonite breccias, and an upper subaerial section consisting of lava flows (Fig. 3a, b). Occasionally a transition zone is present between the subaqueous and subaerial deposits, consisting of interbedded flows and palagonite breccias (Fig. 3c). Prior studies (Clarke, 1968; Clarke and Upton, 1971) contain accurate and detailed descriptions of the PBL stratigraphy, but do not include specific stratigraphic sections or detailed measurements of stratigraphic sequences. In this study we present seven new stratigraphic sections, encompassing both the PBL and underlying sediments, with accompanying paleomagnetic data.

The PBL are occasionally cut by normal faults (Fig. 3d), which dip to the northeast (towards Baffin Bay) (Clarke, 1968). In addition, it is highly likely that the majority of PBL are below sea level in Baffin Bay and not exposed. Therefore, a 'complete' stratigraphic section of PBL is not available. In general, the thickest PBL deposits are near the northeast coastlines, and the stratigraphic sections thin substantially as one moves southwest towards the interior of Baffin Island (Clarke and Upton, 1971).

Perhaps the most distinctive feature of the PBL are their extremely primitive geochemistry and isotopic compositions. They are highly magnesian olivine tholeiites and picrites (up to 22 wt% MgO) whose petrological evolution is dominated by olivine fractionation and accumulation (Francis, 1985), though some component of crustal contamination is present in PBL lavas as well (Yaxley et al., 2004; Harlou et al., 2006). Notably, the PBL shows the highest $^{3}He/^{4}He$ ratios recorded in any terrestrial lavas, suggesting that they are sourced from a unique mantle reservoir or that they sample a common undegassed reservoir with greater purity than any other province (Starkey et al., 2009; de Leeuw et al., 2017, p. 333; Willhite et al., 2019; Horton et al., 2021). This isotopic distinction has led to extensive geochemical study of these lavas as a window into mantle geochemistry and processes (Clarke, 1970; Francis, 1985; Kent et al., 2004; McCoy-West et al., 2018).

Paleomagnetic data from the PBL come from only one study by Deutsch et al. (1971). Their analyses of six PBL flows on Cape Searle (Fig. 2b) found normal polarities and steep inclinations, as expected from a site of this latitude. They also determined that remanence resides in a single titanomagnetite component. Some anomalous samples

show a reversed polarity, and they concluded that these samples must have been remagnetized during a reversed polarity period.

Despite the numerous prior studies of PBL, several gaps exist in our knowledge that this study aims to fill. Most notably, we greatly expand the paleomagnetic data, including 38 new sites in total. Five of these sites are from the Cretaceous Quqaluit Formation, which has not received any prior paleomagnetic study. This research also expands upon the stratigraphic work of Clarke (1968), including presentation of seven new stratigraphic sections with sampling information. Finally, the stratigraphic and paleomagnetic data are combined to determine the eruptive tempo of the PBL, and its implications for paleoclimate disturbances around 62 Ma.

3. Methods

3.1 Sample Collection

All samples were collected during a one-week period in August of 2018. Paleomagnetic samples were collected by Joseph Biasi (Caltech), while geochemical samples were collected by Paul Asimow (Caltech) and Forrest Horton (Woods Hole Oceanographic Institute). Helicopter support was crucial to reaching most of the samples. For paleomagnetic sampling, a combination of drilling and oriented block sampling was used. Paleomagnetic cores (2.54 cm diameter) were drilled using a battery powered Pomeroy DE-T3 electric drill, and oriented using a brass core-plate orientation tool. Block samples were oriented using a homemade tool designed for block sampling. Sun compass measurements were used to orient each core or block sample when available, as

the steep magnetic inclination caused high scatter in magnetic compass readings. Samples from Durban Island (Fig. 2d) were declination-corrected using sighting to five local landmarks due to low cloud cover. No paleomagnetic samples were taken from the Mainland section due to the lack of available sunlight and a thick fog that prevented their orientation by sighting to landmarks. After collection, two cores were drilled into each block sample to make any orientation errors easier to identify. Most lava flows were sampled twice, but in some cases only one sample could be collected or only one core could be drilled into a block sample. Each core was cut into specimens with 2.54 cm diameter and 0.5–1 cm height.

3.2 Stratigraphy

Stratigraphic and structural data were collected in the field and via extensive photography taken from the ground and from the helicopter. The elevations of most samples were determined using a combination of GPS coordinates, the Arctic DEM (Porter et al., 2018), photogrammetry, a tape measure, triangulation, and projection in some cases. Most features do not have names on topographic maps of the area, so we have assigned generic names to most of the stratigraphic sections. Also note that the names of several islands in the area have recently been changed. Padloping Island is now known as Paallavvik, Durban Island is now Aggijjat, and Cape Searle is now Qaqaluit. To maintain consistency with earlier studies we will continue to use the legacy names for each island in this manuscript, but list the modern names on maps and field photos as well.

3.3 Rock/Paleomagnetism

All samples were measured on a 2G Enterprises vertical SQUID magnetometer with RAPID automatic sample changer (Kirschvink et al., 2008). Samples were demagnetized using a 20-step alternating field demagnetization protocol (1.6-90 mT). The magnetometer is housed in a shielded room with a background field of ~200 nT. Sample analysis was done using the DemagGUI program as part of the PmagPy software package (Tauxe et al., 2016). Principal component analysis (floating best-fit lines, no origin) was used to determine best-fit directions (Kirschvink, 1980). Maximum angle of deviation (MAD) and deviation angle (DANG) statistics are reported to assess goodness of fit (Kirschvink, 1980; Tauxe and Staudigel, 2004) (Table S1).

Thermal-susceptibility curves were measured on an AGICO Multi-Function Kappabridge instrument. The samples were heated from room temperature at a rate of 9 ºC/minute, at an operating frequency of 976 Hz, and field intensity of 200 A m^{-1}. Maximum temperatures reached are 700 ºC, and all experiments were run in an Argon atmosphere to minimize oxidation effects. Background 'noise' was removed via the subtraction of a blank sample (run under identical conditions) using AGICO's Cureval software.

4. Results

4.1 Stratigraphy

The PBL consist of a lower subaqueous section containing abundant palagonite breccias and pillow basalts, with rare subaqueous sheet flows (Clarke and Upton, 1971;

this study). The subaqueous deposits range from 0-200 m in thickness (Fig. 4), and can preserve large foresets (Fig. 3b), which are a common feature of palagonite breccias (Nayudu, 1964). The thickest subaqueous section was found at Durban Island (Fig. 5). Two sections (Upper Padloping and Eastern Peak, Figs. 6 and 7) do not contain subaqueous deposits that we could identify. For the Eastern Peak section, this is likely due to fault motion at the subaerial-subaqueous contact (Fig. 3d). The Upper Padloping flows were most likely deposited directly on Archean basement rock. Large foresets are easily identified in the Cape Searle deposits (Fig. 3b) but are not obvious in any of our measured sections. In most cases the subaqueous deposits are poorly exposed and more susceptible to weathering processes than their subaerial counterparts (Figs. 5b, 8a). Therefore the lower bounds on subaqueous deposit thickness in most measured sections are approximate to within ±10% in our estimation. As noted in Clarke (1968), these deposits are typically orange in color (Fig. 3a, 8b) but occasionally black when extensive oxidation has not occurred. We did not find any exposed contact between the underlying Cretaceous sediments (Fig. 9) and the subaqueous igneous deposits.

Above the subaqueous deposits are ~30–225 m of subaerial lava flows (Fig. 4). These flows range in thickness from 0.5–35 m but are ~3 m thick on average (Clarke, 1968; this study). The flows tend to be horizontal, but are occasionally tilted due to fault motion (Clarke and Upton, 1971). The thickest subaerial section was found at Western Peak, though we did not explore most of this section (Fig. 8a). All sections contain some subaerial flows, with the thinnest section being at Upper Padloping (Fig. 7), containing probably two flows. The lower subaerial flows tend to be medium-grey in color and become progressively more red up-section (Fig. 6). This is likely due to longer exposure

times above sea level and greater levels of oxidative weathering. The subaerial deposits are most commonly exposed in steep, rapidly retreating cliffsides (Figs. 5b, 6b, 6c). During our August field season, sampling the subaerial flows was often dangerous due to constantly falling rock debris from overlying flows and poor footing at the top of scree aprons. The flows are typically vesicular near flow tops (Fig. 6d), and occasionally these vesicles are filled with zeolite minerals. Otherwise, the flows appear to be fresh in outcrop and hand sample, and do not show signs of post-emplacement deformation or metamorphism such as secondary mineralization or chloritization. Paleosols and volcaniclastic sediments between flows are extremely rare. One baked mud (~3 cm in thickness) was identified above sample PING18-B16 in the Eastern Peak section, and a volcanic conglomerate with ~10 cm granitoid clasts is located between samples B4 and H7 in the Eastern Peak section. The Durban Island section contains one volcaniclastic sedimentary layer, though the exposure was poor, and it is possibly a very thin palagonite breccia (samples DI1 8 to DI1 11, DURB18-H5).

Overall, the thickest section that we examined was at Western Peak (Fig. 4), which is 450 m in stratigraphic thickness, while the thinnest section was Upper Padloping, exposing ~30m of section. This is consistent with a source region to the northeast (currently submerged), with thinning of the volcanic section to the southwest towards the interior of Baffin Island and away from the coast (Clarke and Upton, 1971). Only one dike was found, in the Northeast Ridge section (Fig. 10). This dike was clearly intruding through Archean gneisses, with a strike of 064 and subvertical dip. No flows were exposed in the immediate vicinity, but it is assumed that this dike must have cut through overlying flows as well (see section 4.3). One small sill was identified in the

Mainland section, based on mineral textures and the body's intrusive relation to nearby flows (Fig. 11).

4.2 Rock Magnetism

Magnetic mineralogy was assessed, in part, based on thermal-susceptibility curves shown in Fig. 12. Panels A and B show samples from the Eastern Peak section. PB1-6 shows a typical (titano)magnetite curve with a curie temperature of ~570 ºC, indicating nearly titanium-free magnetite (Dunlop and Özdemir, 1997). Sample PB1-17a shows a titanomagnetite component with a range of Curie temperatures from ~450-580 ºC. This sample also appears to contain a high-susceptibility phase with a Curie or Néel temperature of ~150 ºC, most likely goethite or a similar Fe-oxyhydroxide (Liu et al., 2006). The heating and cooling curves are similar, but not identical in shape, suggesting that irreversible dewatering of a hydrous phase and/or annealing of some grains occurred during the heating process. Overall this sample appears to be only moderately altered post-emplacement. Figure 12c shows PAD 24 (from the Northeast ridge section), which displays Curie temperatures above 500 ºC, suggesting titanomagnetite. The cooling curve is not identical, again suggesting that some degree of annealing, cation reordering, or possibly exsolution has occurred during heating to granulite-grade temperatures (Dunlop, 2014).

Figure 12d shows data from PAD 11 (from the Northeast Ridge section), which was chosen because it produced a very anomalous paleomagnetic direction (see section 4.3) and showed evidence for significant alteration in the outcrop (along with nearby samples PAD 8, 9, and 10). The results in Fig. 12d confirm this, showing creation of new

magnetic components around ~250 ºC ((titano)maghemite? (Özdemir and Dunlop, 2010)) and ~500 ºC (titanomagnetite). The cooling curve shows a significant drop in susceptibility below 500 ºC, suggesting that the titanomagnetite created during heating is not a stable phase. Overall this sample has a complex magnetic mineralogy clearly affected by some degree of hydrous alteration, as evidenced by the lack of similarity between the heating and cooling curves.

Sample DI1 28 from Durban Island (Fig. 12e) shows a steady decline in susceptibility over most of its temperature range, suggesting that magnetites with a wide range of titanium content are present within the sample (Dunlop and Özdemir, 1997). The similarity between heating and cooling curves suggests that this mineralogy is stable at high temperatures, and no hydrous phases (such as goethite) are present within the sample. Finally, PIB 11 (a sandstone from the Beach section, Fig. 12f) shows initially low susceptibility, followed by the apparent creation of pure magnetite around 400-500 ºC. The cooling curve remains at high susceptibility below 580 ºC, suggesting that this new magnetite phase is stable in the sample. Overall, this suggests that most of the magnetic minerals in this sample were initially a low-susceptibility hydrous phase such as lepidocrocite that dewatered to form magnetite during heating.

4.3 Paleomagnetism

Paleomagnetic results for each section, including representative orthogonal projections, diagrams, are shown in Figs. 13 - 18 and summarized in Tables 1 and 2. Overall the lavas show remarkably consistent behavior and directions during demagnetization. MAD and DANG values are typically <1º. The majority of site-mean

directions have precision parameter (k) values of >100, some have k values over 1000 (Table 1). The high k values indicate that errors inherently associated with paleomagnetic sample collection, demagnetization, and analysis (orientation errors, uncertainties in fits) have had a minimal effect on the average directions that are determined for each site. In addition, only flat-lying sites have been sampled and Baffin Island has not rotated relative to stable North America since emplacement of these units, so errors from tectonic motion should be minimal. Therefore, while some igneous sites have large $\alpha 95$ values (Table 1), and the mean paleomagnetic poles often have high $\alpha 95$, this is almost exclusively due to low numbers of samples, not due to uncertainty in the least-squares fits. Most samples show steep inclinations, which replicates the results of Deutsch et al. (1971). The sedimentary layer in the Durban section shows one anomalous reversed direction (Fig. 13), so this layer will be excluded from further calculations. Another flow in the Northeast Ridge section (samples PAD 8-12) shows signs of significant alteration and also shows anomalous directions that deviate from both overlying and underlying flow directions (Fig. 18). In the field, the flow top that these samples were derived from had extensive secondary zeolite crystallization in all vesicles, and the flow was notably crumblier than any flows above or below it. There is no evidence to suggest that significant time passed between eruption of the flows in this sequence, so we conclude that localized fluid flow and alteration within this flow top (ne5, Table 1) is to blame for the anomalous directions, and this flow will also be excluded from further calculations.

We also sampled a dike in the Northeast ridge section, which showed a reversed/transitional polarity (Fig. 18b, d). Though we only see the dike intruding through Archean basement, the nearest PBL flows are ~180 m from the dike and at the

same elevation. Presumably the dike also intruded through these flows as well, but that contact-relation was lost due to differential weathering (Fig. 10b). When combined with the reversed paleomagnetic direction, this suggests that the dike is younger than the surrounding flows, probably intruding during the C26r polarity period. This also suggests that overlying reversed flows may have been present on Baffin Island at some point but have since been lost due to erosion. The dike site, due to its anomalous direction and likely younger age, will also be excluded in further calculations. This leaves 30 igneous sites that will contribute to the paleomagnetic pole position for the PBL (see section 5.4).

Paleomagnetic data from the Beach sediments is not of high quality and cannot be interpreted with much confidence. We attempted to sample fine-grained units in this section, but they were not receptive to drilling. Most fine-grained shales and siltstones were barely lithified, and the water-cooled drill could not produce cohesive cores. Even the sandstones were barely lithified, and the majority of drilling attempts were not successful in this section. Any future researcher attempting to sample the Quqaluit formation for paleomagnetic data should bring water-resistant epoxy in order to extract oriented block-samples. Fig. 17a shows one of the best samples from this section in terms of directional consistency during demagnetization. Fig. 17b shows one of the worst samples that could still be fitted. Two samples (PIB 10, 12) had data of such high scatter that no fit could be applied. The equal area projection in Fig. 17c shows high scatter in the best-fit directions, but the majority of samples seem to be of normal polarity, as expected for an Albian-age sediment (Burden and Langille, 1990; Gradstein et al., 2012). No stability tests were done here, and it is not clear if tests such as the fold, conglomerate, or reversal test would be possible during another sampling campaign. It is

entirely possible that these sediments are preserving a viscous remanence, recording only modern-field directions (or no coherent directions at all). Any future paleomagnetic work on these units should focus on fine-grained beds to maximize the potential to find more consistent directional data.

5. Discussion

5.1 Igneous Stratigraphy

Seven new stratigraphic sections of the PBL are shown in Fig. 4. We have plotted each section independently as a function of modern elevation, and not attempted to compile a 'complete' stratigraphic section. Based on the highly variable elevations of the subaqueous/subaerial transition (a range of 500 m), it appears that most stratigraphic sections are separated by faults of unknown magnitude. Therefore, it is difficult to assign the relative age of samples in different sections, because fault motion may have displaced some sections (such as Eastern Peak). We expect flows near the source region (Baffin Bay) and at the bottom of stratigraphic sections to be older than flows farther inland (Clarke and Upton, 1971). Given the unknown magnitude of fault displacements, we do not make any relative age determinations between different sections. For example, we cannot determine if sample H7 from the Durban section is older or younger than sample H4 from the Western Peak section, even though they both sit just above the subaqueous/subaerial transition. However, it is appropriate to assign relative ages to samples within a single section. For example, sample PING18-B4 is unambiguously older than PING18-B17 (both in the Eastern Peak section, Fig. 4). The subaqueous

deposits are typically – but not always – older than subaerial flows in the same section (see Clarke & Upton (1971) for an illustration of this). All seven stratigraphic sections are most likely offset from each other by normal or strike slip fault motion, with the possible exception of Upper Padloping, which may be a continuation of the Eastern Peak section (Fig. 2c, 4). Finally, we found that the extent of the PBL is underestimated on local geologic maps (Fig. 2b) (Sanborn-Barrie and Young, 2013; Sanborn-Barrie et al., 2013).

5.2 Sediments

Cretaceous sedimentary units on Padloping Island are also pervasively faulted. The section that we measured was within one fault block, because the throw of the (typically normal) faults is often hard to determine. The typical lithologies (sandstone, shale, mudstone, coal) and sedimentary features (such as cross bedding) that we observed are consistent with the Cretaceous Quqaluit Formation described by Burden & Langille (1990, 1991), but it is not clear if our section is within the upper or lower member of the Quqaluit Fm. The paleomagnetic data tentatively suggest that these sediments have a normal polarity, but the poor quality of the data leave no room for further interpretation beyond polarity.

5.3 Magnetostratigraphy

The inclination (*I*) and declination (*D*) of samples from four sections is shown in Fig. 19 as a function of elevation (stratigraphic height). Large changes in *D* are expected for a high-latitude site due to close proximity to the geomagnetic north pole. Overall the

PBL directions show remarkable consistency between flows, suggesting little PSV over the eruptive duration (panels A, B, and C). Fig. 19a shows consistent *I* through most of the Durban section, with the notable exception of one sedimentary sample (DI1-10, Table S1). It is possible that this sample is a conglomerate or breccia fragment, which is expected to produce a random direction in this case. However, the bed was poorly exposed, and it is not possible to determine definitively if this was the case. The sample appears to be oriented correctly based on the data gathered in the field. Fig. 19b shows remarkably consistent *I* throughout the entire 37-flow sequence at the Eastern Peak section (only 13 flows were sampled). The statistical likelihood that these flows would maintain such directional consistency while erupting at random intervals is very low. Instead it is far more likely that all of the flows in this section erupted over a short period of time and thus recorded very little PSV in the geomagnetic field. Fig. 19c, showing results from the Northeast Ridge section, are broadly similar to the Eastern Peak section. Finally, Fig. 19d shows the highly variable remanence directions from the Cretaceous Quqaluit Fm. As discussed earlier, these results should be interpreted with caution.

5.4 Paleosecular Variation

Two sections contain sufficient paleomagnetic data to reconstruct a PSV path (Fig. 20). The Eastern Peak path is composed of 13 virtual geomagnetic poles (VGPs), that overall show 2-3 loops to the east of the expected pole for stable north America at 60 Ma. Accounting for plate movements, these loops would be south of the geographic north pole during the time of eruption (Torsvik et al., 2012). The paleomagnetic pole for this section (calculated by averaging all VGPs) does not overlap with the expected pole

(shown in Green in Fig. 20a), suggesting that the entire eruptive sequence at Eastern Peak took less than ~10^4 years to erupt. When the test of mean directions is applied (Fisher et al., 1993), we find that there is less than a ~1% probability that the Eastern Peak pole and the Stable North American pole are the same. The Northeast Ridge PSV path is composed of 10 VGPs, that again show ~3 loops to the east of the expected pole for this time period (Fig. 20b). Again, Fisher's test of mean directions indicates that there is only a 0.003% probability that the paleomagnetic pole for the Northeast Ridge is the same as the expected north American pole. The Durban section only contains three igneous sites, so very little information can be gathered from their PSV path (Fig. 20c), but again the mean direction does not overlap the expected north American pole at 95% confidence. The other igneous sections (Mainland, Beach, Western Peak, and Upper Padloping) contain 0-2 sites and are plotted along with all other VGPs in Fig. 20d. The mean paleomagnetic pole for all Baffin sites is ~2200 km NNE of the expected pole for a North American site at 60 Ma (in present day coordinates). This implies that the entire PBL sequence took less time to erupt than the typical timescale of secular variation (10^4-10^5 years (Tauxe et al., 2010)). Applying Fisher's test of mean directions for a final time, we find that there is only a ~0.0001% probability that the PBL pole is the same as the stable north American pole. To simulate this pole offset by wholesale tilting of the entire PBL sequence would require 20° of post-eruptive dip, which is not consistent with the observed orientations of the nearly flat-lying subaerial lava flows.

5.5 Eruptive Tempo

PSV paths shown in Fig. 20 give the opportunity to place constraints on the amount of time elapsed between flows. By combining an assumed rate of PSV with the change in paleomagnetic direction between adjacent flows, a time between eruptions can be estimated (e.g. Champion and Donnelly-Nolan, 1994). In the geologic record, PSV is systematically underestimated or under-sampled, because sedimentary deposits will 'average out' some PSV due to the long-term nature of remanence acquisition in sedimentary deposits (Roberts and Winklhofer, 2004). Igneous rocks only capture discrete 'snapshots' of the field during lava cooling and therefore cannot record all variation that may take place over a given time period either. Therefore, we will use the maximum rate of PSV that is available as our assumed rate here, thereby providing a model-based minimum time estimate between flows.

However, determining this maximum rate is not straightforward, as very little information exists on PSV at this latitude. A local PSV curve has yet to be constructed for Iceland, for example (Pinton et al., 2017). Even less information is available on PSV at this latitude at ~62 Ma. Given the dearth of available PSV data, a reasonable path forward will be to find the maximum *historically observed* rate of travel of the geomagnetic north pole and use this as our assumed maximum PSV rate. Such records only span the last few thousand years, with a maximum travel speed of 60 km $year^{-1}$ of the geomagnetic north pole (Pavón-Carrasco et al., 2014; Livermore et al., 2020).

Now that we have determined the PSV rate, we must determine which VGPs to include in the calculations. VGPs from adjacent flows may be separated due to PSV, or due to errors that are inherent to paleomagnetic data collection and interpretation. For

example, the three flows in the Durban section have partially overlapping *A95* error envelopes, so it is not clear if the angular difference between these three directions is entirely due to PSV. To address this issue we have simulated *n=1000* secular variation paths using the errors of our VGP estimates to either lump adjacent flows together or keep them separate. These paths are then used to quantify the uncertainty in our eruption interval estimates using a bootstrap resampling method. *Appendix A* contains a detailed explanation of our eruption interval and error estimate procedure.

Distances between each Eastern Peak VGP are ~2700 km on average and ~36,000 km in total over the 37 flows in the section. At a rate of 60 km year^{-1}, this is equivalent to $\gtrsim 558^{+30}_{-54}$ years of PSV (95% confidence limits; using the bootstrap uncertainty method discussed above). At the Northeast Ridge section, distances between VGPs are 2700 km on average and 25,000 km in total over 11 flows in the section, equating to $\gtrsim 332^{+70}_{-164}$ years of PSV. Therefore, the eruptive tempo can be modeled as one eruption every $\gtrsim 15.1^{+0.8}_{-1.5}$ years in the Eastern Peak section and once every $\gtrsim 30.2^{+6.4}_{-14.9}$ years in the Northeast Ridge section. The thickest subaerial section is at Western Peak, with 225 m of subaerial flows that average 3 m in thickness, totaling roughly 75 flows. Using the distribution of eruption intervals at the Eastern Peak and Northeast Ridge sections, the entire subaerial sequence at the thickest section that we measured would have been emplaced in $\gtrsim 1665^{+191}_{-143}$ years (Appendix A).

5.6 Eruption Rates

With data generated in this study, we can also calculate volumetric eruption rates in order to compare the PBL to other flood basalt events. To do so, we need to calculate

the volume of Baffin lavas. This is not straightforward, because much of these lavas are submerged (Clarke, 1968; Chauvet et al., 2019), and most of the subaerially exposed sections have been eroded via extensive glaciation. Therefore, some simplifying assumptions will be made. The lavas are exposed over a distance of 83 km, from Cape Searle to Cape Dyer (Fig. 2b). The thickest section that we measured was 425 m, with thinning of all PBL flows progressively inland to a maximum distance of 10 km from the northeastern coast. Therefore, we can assume that the PBL initially comprised a wedge shape with a volume of 83000 m * 425 m * 10000 m / 2, or 1.76×10^{11} m^3, or 176 km^3. This is a very conservative estimate because it does not include any of the lavas below sea level in Baffin Bay, where the thickest deposits of PBL are likely to be found. To determine the eruption rate, we must divide this calculated volume by the total time of eruption. The most conservative estimate is derived from the length of the C27n chron (Gradstein et al., 2012) during which all the lavas erupted, 296 kyr, yielding an eruption rate of ~0.0006 km^3/year. However, the PBL most likely do not encompass the entire C27n chron, because younger lavas in west Greenland record the C27n/C26r reversal (Riisager and Abrahamsen, 1999; Riisager et al., 2003b), and the PSV path calculations in Ssection 5.5 suggest a minimum total eruption duration of ~1.7 kyr. If we use the minimum duration instead, then the eruption rate becomes ~0.1 km^3 $year^{-1}$, which is slightly higher than eruption rates calculated for west Greenland (Fig. 21).

5.7 Comparison to Other Studies

Overall, our results are in agreement with paleomagnetic results from the Vaigat Fm. of the WGL (Fig. 21), the likely equivalent to the PBL in Greenland (Riisager and

Abrahamsen, 1999). A 125 m package of picritic flows there erupted within a 5 kyr polarity transition period (Pedersen et al., 2002) and overall the WGL data suggests that volcanism is characterized by short bursts of volcanism followed by long hiatuses with little eruptive activity (Riisager and Abrahamsen, 1999; Riisager et al., 1999, 2003b, 2003a; Pedersen et al., 2002). It seems likely that our data on the PBL is capturing one of these short bursts, and that longer hiatuses are not represented in the sections that we sampled. Two poles from the Anaanaa Member (Fig. 20d) are technically within the range of VGPs that we measured in the PBL but are on the outer edge of this range. The Anaanaa member most likely erupted during a different 'burst' of activity than the PBL. Our paleomagnetic directions are also similar to those measured by Deutsch et al. (1971) at Cape Dyer. The VGP position that they calculate is within error of our paleomagnetic pole for the PBL, and their lavas generally show the steep inclination seen in our dataset as well. This result suggests that at least the northern flows of the PBL erupted during a single 'burst' of volcanic activity.

5.8 Effect on Paleoclimate

The WGL and PBL have been associated with the 'End C27n event' (Fig. 1) which was marked by a notable carbon isotope spike in some sediment cores and a global warming of ~2 ºC (Dinarès-Turell et al., 2012). This event occurred at the very beginning of the C26r chron, but as we established the Baffin Lavas erupted sometime earlier in the C27n chron. From the magnetostratigraphic record in west Greenland, it appears that several 'bursts' and hiatuses of volcanism occurred prior to this event, without significant global climatic changes (Pedersen et al., 2002). This suggests that even the elevated rates

of volcanism that occurred during the 'burst' at Baffin was not alone sufficient to significantly alter global climate. It appears, therefore, that such bursts either need to be of greater intensity, longer duration, or with a shorter hiatus between them in order to affect climate on a global scale (Fig. 1). This is in line with observations at other flood basalt provinces; Global climate shifts are associated with the peak of activity in the Deccan Traps and Columbia River basalts, while earlier volcanism of less intensity seemed to have a much smaller effect on the geological record (Kasbohm and Schoene, 2018; Schoene et al., 2019). Alternatively, several 'bursts' of activity in Baffin and West Greenland may have been necessary to create prerequisite atmospheric conditions for the 'End C27n event.'

6. Conclusions

Based on new stratigraphic and paleomagnetic data, we have found that the sequence of Paleocene Baffin Lavas most likely took ~1.7 kyr to erupt during the C27n chron at ~62.2 Ma. Using conservative estimates of the total volume of erupted magma, we also found that the average volumetric eruption rate during this time was ~0.1 km^3/year. These results are in agreement with previously determined eruptive tempos and rates from the cotemporal west Greenland lavas. It is important to note that volumetric eruption rates calculated here are likely underestimates because we did not account for volcanic material that is currently below sea level in Baffin Bay. Overall, the rates calculated here are less than those of larger and more climatically impactful flood basalt provinces (Fig. 21). This suggests that higher eruptive rates, eruptive tempos, or both are

necessary to cause significant global climate shifts than the rates and tempos observed in the PBL and WGL.

Going forward, additional paleomagnetic study of the PBL will refine the timing and tempo of this event. We estimate that only ~40% of the flows on Padloping Island were sampled in this study, and none of the PBL flows on the Cumberland Peninsula have been studied paleomagnetically. Additional research may lead to high-fidelity records of reversals or paleosecular variation in the Paleocene, which would greatly benefit long-term models of the geomagnetic field and better-inform rifting models of Baffin Bay and the Davis Strait.

Acknowledgements

Maryse Mahy of the Parks Canada Nunavut Field Unit, the Qikiqtani Inuit Association, and the Nunavut Research Institute are thanked for their assistance with permitting and logistics. Morris Kuniliusee is thanked for his vigilant bear monitoring and keen eye for local wildlife. Stephane Caron and Iqaluit Helicopters are thanked for transportation support. Arctic Kingdom Inc. is thanked for logistical support. Paul Asimow, Forrest Horton, and Xenia Boyes are greatly thanked for their help with the project and fruitful discussions. Joseph Kirschvink is greatly thanked for use of his paleomagnetics laboratory and for productive discussions of sample statistics. This work was supported by National Science Foundation (award #1911699), Woods Hole Oceanographic Institution (WHOI) Andrew W. Mellon Foundation Endowed Fund for Innovative Research, a National Geographic Society grant (#CP4-144R-18), and internal funding from the Caltech Geological and Planetary Sciences Division.

Supplementary Material

Table S1, which contains least-squares fit directions and associated statistics, is available with the online version of this thesis.

Appendix A: Paleosecular Variation Error Estimates

This study uses paleosecular variation (PSV) paths to estimate eruption intervals between adjacent lava flows. However, a change in average paleomagnetic direction between flows could be attributed to various sources of error in addition to PSV. For example, the variation in paleomagnetic directions between the Beach sediment layers (Fig. 17, 19d) can be entirely accounted for via random error, and does not require changes in the geomagnetic field between deposition of the layers.

Therefore, it is important to determine the uncertainty of the PSV paths, using the associated uncertainty of the VGP directions from the sites in the path (Table 1). This uncertainty in the PSV path-length can then be used to estimate the uncertainty in the eruption interval or total eruption duration, using an assumed rate of PSV (60 km yr^{-1} in this case). This is done in a five-step process:

1. Use the test of mean directions (Fisher et al., 1993) to determine our confidence that adjacent flows have distinct mean directions that cannot be explained by error alone (Table 1).

2. Use these confidence estimates to randomly construct *n=1000* new PSV paths using the existing dataset (a.k.a. bootstrapping). For example, if we have a 90% confidence that Flow 2 has a distinct mean direction from Flow 1, then the Flow 2 direction will appear in ~900 of the generated PSV paths. The Flow 2 direction is randomly included in any given path, but it's overall probability of appearing is 90%.
3. Calculate the distance between adjacent VGPs for all 1000 paths.
4. Divide the distance by the assumed secular variation rate (60 km yr^{-1}) to determine the total amount of time represented by each path. Calculate median time and 95% confidence limits using the distribution of times (Fig. A1a).
5. Divide each path by the number of flows in the section to determine the eruption interval (years/flow). Calculate median interval and the 95% confidence limits using the distribution of eruption intervals (Fig. A1b, c).

Note that a few sites in the Eastern Peak and Northeast Ridge section have only one sample (Table 1), but multiple samples are needed to conduct the test of mean directions in step 1 (Fisher et al., 1993). Therefore, we calculated the median precision parameter (k) and vector sum (R) of each section, and use these values at sites where N=1. Without doing this, sites with N=1 would be excluded from the paleosecular variation paths, producing an artificially short eruptive duration.

As discussed in Section 5.5, the Western Peak section contains the thickest package of subaerial lavas (~75 in total). To calculate the total eruption duration of this sequence, we can again apply the bootstrapping method, this time using the n=2000 eruption interval estimates from the Eastern Peak and Northeast Ridge sections:

1. Randomly assign each of the 75 flows with one of the 2000 eruption intervals.
2. Calculate the total eruption duration of the 75-flow Western Peak section.
3. Repeat 1000 times.
4. Calculate the median duration and the 95% confidence limits using the distribution of eruption durations (Fig. A1d).

Table 1: Site-mean Virtual Geomagnetic Poles (VGPs)

Section	Flow/Layer	N	D	I	a95	K	R	VGP Latitude	VGP Longitude	VGP dm	VGP dp	Confidence†
Eastern Peak	1	2	294	77.4	18.1	191	1.99	65	235.8	33.9	31.7	
Eastern Peak	2	1	310	80.9	--	--	--	72.6	246.4	--	--	38.45
Eastern Peak	4	1	353	76.4	--	--	--	85.8	164.9	--	--	80.79
Eastern Peak	5	2	341	75.1	3.1	6522	2.00	80.4	183.5	5.7	5.2	32.31
Eastern Peak	6	2	154	78.2	30.1	71	1.99	45.8	311.6	56.7	53.5	100.00
Eastern Peak	7	2	56.3	76.7	43.5	35	1.97	67.7	7.3	80.8	75.1	91.81
Eastern Peak	10	2	36.4	75.9	10.7	552	2.00	74.5	24.8	19.7	18.2	20.03
Eastern Peak	11	2	323	77.1	15	280	2.00	75.4	217.7	28	26.1	100.00
Eastern Peak	12	2	47.2	86.4	8.5	871	2.00	71.4	314.3	16.9	16.8	100.00
Eastern Peak	13	2	284	63.3	48.4	29	1.97	45.6	217.3	76.4	60.3	99.90
Eastern Peak	14	2	358	78.9	3.9	4048	2.00	88.5	273.4	7.4	7	99.65
Eastern Peak	23	1	338	68.3	--	--	--	70.9	163.1	--	--	99.46
Eastern Peak	31	1	330	65.5	--	--	--	65.1	171.3	--	--	28.72
Eastern Peak	37	2	313	77	7.8	1040	2.00	71.2	223.9	14.5	13.5	99.56
Northeast Ridge	Dike*	2	104	-40	13.3	355	2.00	-26.5	24	16.1	9.7	--
Northeast Ridge	1	2	309	70.8	23.5	115	1.99	63.7	205.6	40.8	35.5	
Northeast Ridge	2	2	4.7	84.8	5.7	1932	2.00	77.5	301.5	11.3	11.1	99.99
Northeast Ridge	3	3	82.4	76	35.5	13	2.85	58	354.1	65.5	60.4	65.54
Northeast Ridge	4	3	43.8	81.8	11	126	2.98	74.4	343.1	21.4	20.7	34.76
Northeast Ridge	5*	3	141	-20	180	1	0.98	-27.4	341.7	188.3	98.5	--
Northeast Ridge	6	4	8.5	69.4	22	18	3.84	75.3	97.1	37.6	32.1	85.11
Northeast Ridge	7	4	33.3	71.5	16.1	33	3.91	71.1	46.8	28.2	24.7	39.00
Northeast Ridge	8	6	23.4	82.1	4.5	220	5.98	79.5	333.4	8.8	8.5	87.54
Northeast Ridge	9	2	328	82.5	49	28	1.96	77.2	260	95.6	93.2	33.62
Northeast Ridge	10	2	223	79.3	15.3	267	2.00	49.7	275.6	29.1	27.7	79.77
Northeast Ridge	11	2	23.2	75.6	28.2	80	1.99	79.3	40.8	51.8	47.6	100.00
Durban	Pillow	4	29.4	86.3	11	71	3.96	73.1	310.3	21.9	21.7	
Durban	Sediment*	4	104	70.8	180	2	2.21	44.7	349.1	312.8	271.8	--
Durban	Flow A	6	4.3	79.4	5.1	176	5.97	87.1	329.3	9.7	9.3	84.38
Durban	Flow B	11	330	79.3	6.9	45	10.78	78.8	232.1	13.1	12.5	86.09
Upper	1	2	358	77.3	7.8	1028	2.00	88.4	143.2	14.6	13.6	
Upper	2	2	340	44	29.4	74	1.99	46.7	144.9	36.8	23	100.00
Western Peak	1	2	199	83.1	12.6	396	2.00	54.1	290	24.7	24.2	
Beach*	1	1	341	8.9	--	--	--	26	263.3	181.6	91.6	--
Beach*	8	2	227	14.7	180	1	0.43	-8.1	15	184.5	94.6	--
Beach*	13	3	23.1	68.2	180	2	2.10	70.5	195.3	302.8	254.6	--
Beach*	16	1	334	11.2	--	--	--	26	271.2	182.6	92.6	--
Beach*	21	9	158	44.9	180	1	2.73	5.1	82.3	227.4	143.7	--

N = number of measurements, D = declination, I = Inclination, a95 = 95% confidence interval, K = precision parameter, R = vector sum (ideally R=N)

*Site excluded from paleomagnetic pole calculations. See text for discussion.

†Confidence that this VGP is different than the previous VGP in the section, based on the test of mean directions (Fisher 1993).

Table 2: Mean Paleomagnetic Pole Positions

Pole Name	Latitude	Longitude	N	A95	R	K
All Lavas	**83.18**	**265.85**	**30**	**7.44**	**27.85**	**13.46**
All lavas*	82.20	281.97	26	8.20	24.07	12.94
Eastern Peak	80.57	242.33	14	11.13	13.05	13.72
Eastern Peak*	78.81	267.56	10	14.57	9.25	11.96
Northeast Ridge	81.83	320.04	10	12.96	9.39	14.86
Durban	81.92	285.48	3	16.20	2.97	58.93
Beach (sedimentary)	62.21	192.28	5	132.29	2.00	1.33

*pole excludes sites with only one sample

N = number of measurements, a95 = 95% confidence interval, K = precision parameter,
R = vector sum (ideally R=N)

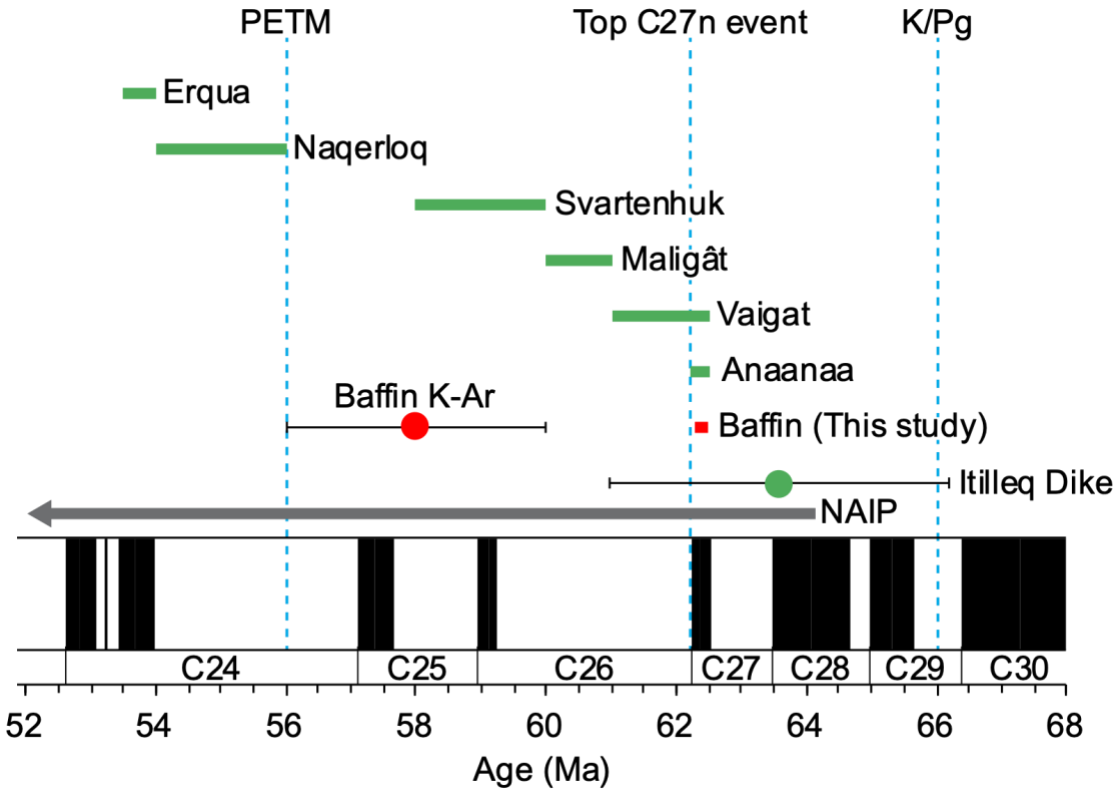

Figure 1 *– Compilation of geochronological data from the Paleocene Baffin lavas (PBL, red), west Greenland lavas (WGL, green), and North Atlantic Igneous Province (NAIP). Magnetic polarity timescale from Gradstein et al. (2012), Baffin K-Ar age from Clarke and Upton (1971), WGL data from Larsen et al. (2016) and references therein, Paleocene-Eocene Thermal Maximum (PETM) age from Gradstein et al. (2012), Top C27n age from Dinarès-Turell et al. (2012), Cretaceous-Paleogene boundary age from Gradstein et al. (2012).*

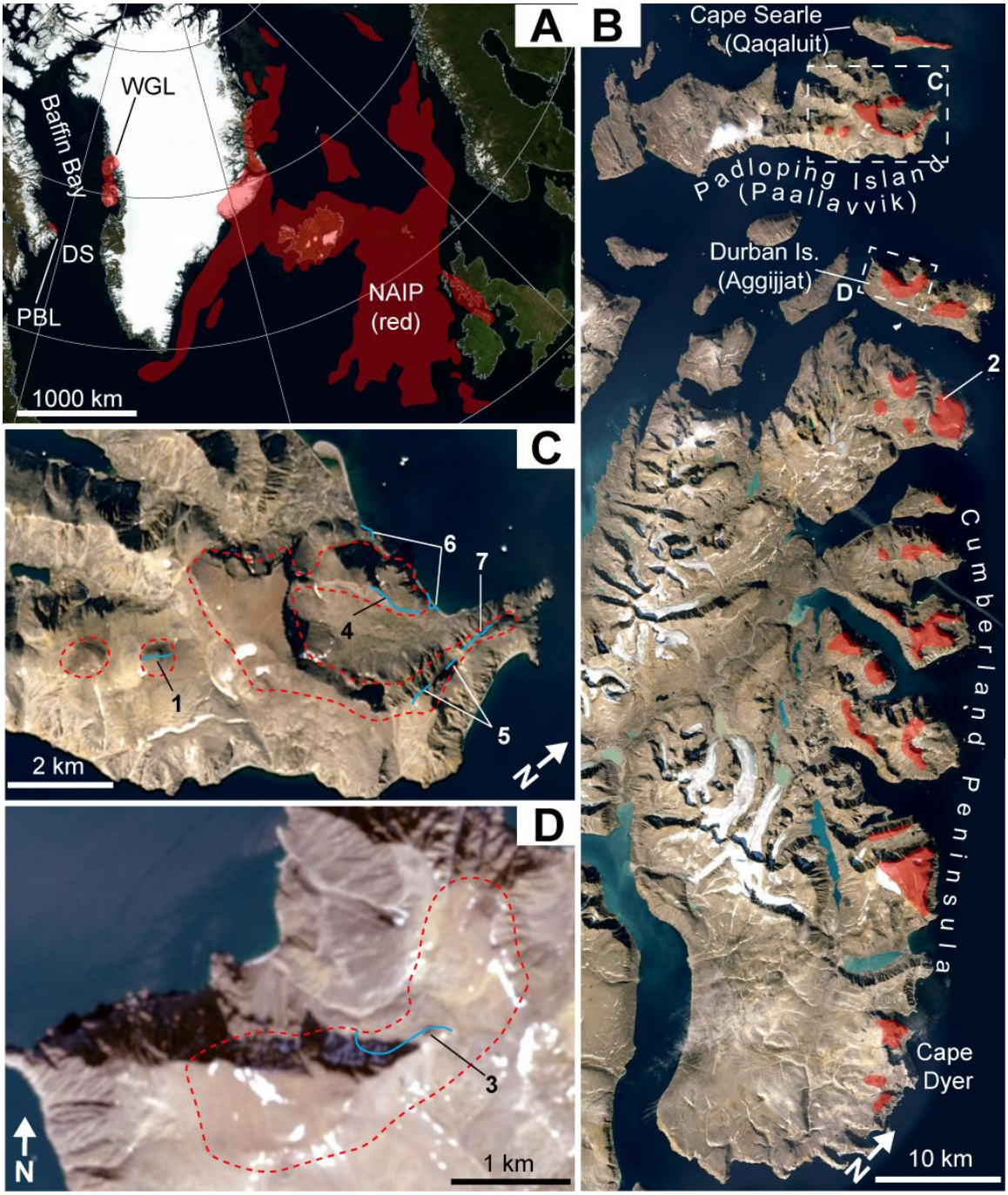
A
WGL
Baffin Bay
DS
PBL
NAIP
(red)
1000 km
B
Cape Searle
(Qaqaluit)
C
Padloping Island
(Paallavvik)
Durban Is.
(Aggijjat)
D
2
Cumberland Peninsula
Cape
Dyer
N
10 km
C
6
7
4
1
5
2 km
N
D
3
N
1 km

Figure 2 *– **A)** Overview map of the North Atlantic Igneous Province (NAIP), modified from Horni et al. (2017); PBL = Paleocene Baffin Lavas, WGL = west Greenland lavas, DS = Davis Strait. **B)** Regional satellite image showing the distribution of Paleocene Baffin Lavas (PBL, red), and the location of panels C and D on Padloping and Durban Island, respectively; 2 = Mainland section (Fig. 11). Based on maps by Sanborn-Barrie and Young (2013) and Sanborn-Barrie et al. (2013). **C)** Satellite image of northeastern Padloping Island, showing the approximate distribution of PBL in red and sampling transects in blue; 1 = Upper Padloping (Figs. 7, 15), 4 = Western Peak (Figs. 8, 16), 5 = Eastern Peak (Figs. 3c, 6, 14, 19b, 20b), 6 = Beach (two exposures) (Figs. 9, 17, 19d), 7 = Northeast Ridge (Figs. 10, 18, 19c, 20c). **D)** Satellite image of western Durban Island, showing the approximate distribution of PBL in red and sampling transect in blue; 4 = Durban section (Figs. 3d, 5, 13, 19a, 20a). All imagery from Google Earth or the Arctic DEM explorer (Porter et al., 2018).*

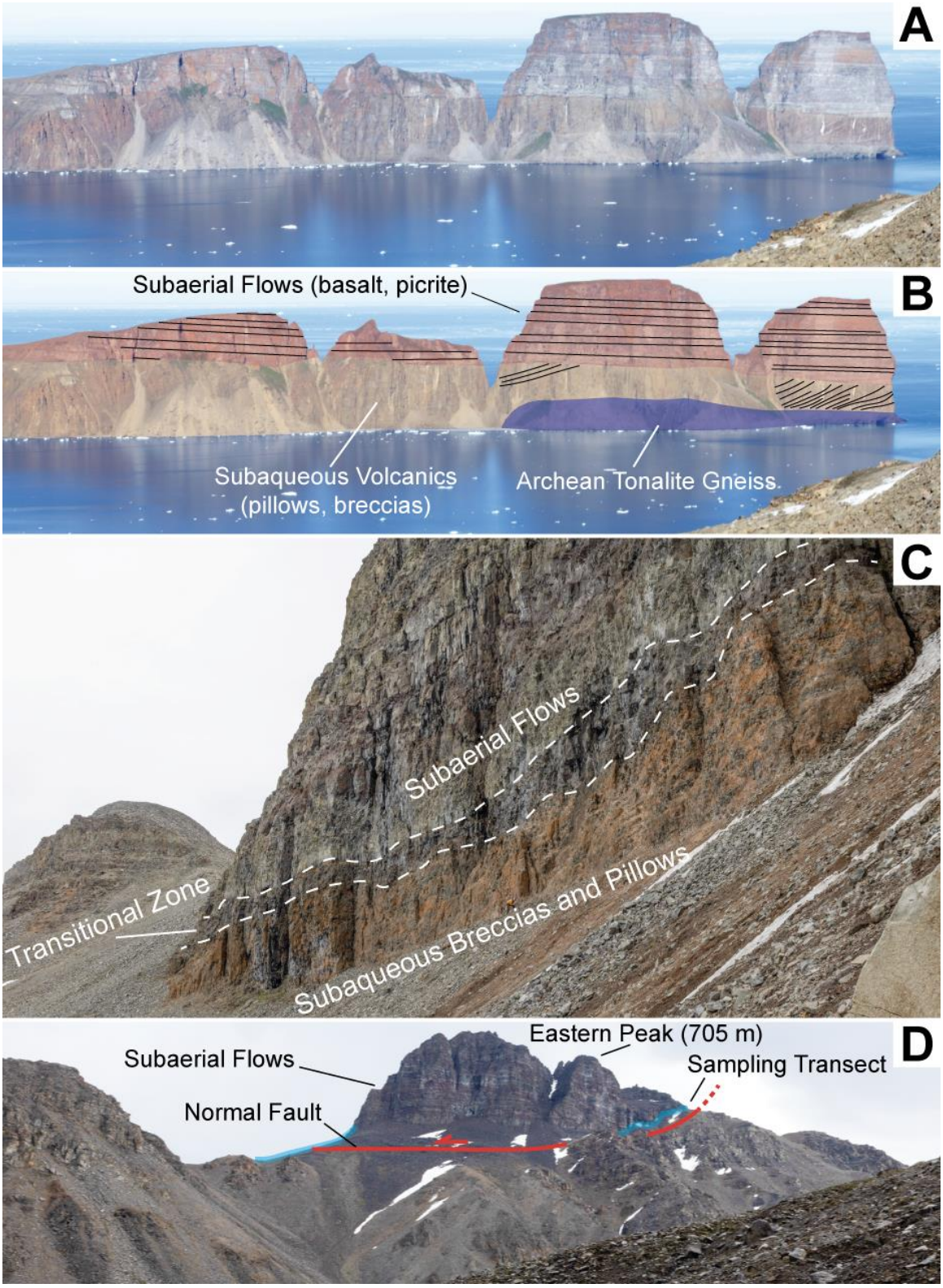
A
Subaerial Flows (basalt, picrite)
B
Subaqueous Volcanics
(pillows, breccias)
Archean Tonalite Gneiss
C
Subaerial Flows
Transitional Zone
Subaqueous Breccias and Pillows
Eastern Peak (705 m)
D
Subaerial Flows
Sampling Transect
Normal Fault

Figure 3 *– Field photos illustrating typical field relations in the PBL.* ***A)*** *Photo of Cape Searle (Qaqaluit), looking northwest and taken from the Western Peak section; the width of the field of view is 2.8 km and the highest point visible is 190 m above sea level.* ***B)*** *Interpreted version of panel A. Some of the subaerial flows are shown with horizonal lines. Occasional foresets can be seen in the subaqueous section, which are also highlighted.* ***C)*** *Photo of the subaerial/subaqueous transition zone on Durban Island, looking east. A geologist at lower center provides a scale reference.* ***D)*** *Photo of the entire Eastern Peak section, taken from the Western peak section and looking southeast; the width of the field of view is 2.2 km. Sampling transects are shown in blue, a prominent normal fault is highlighted in red.*

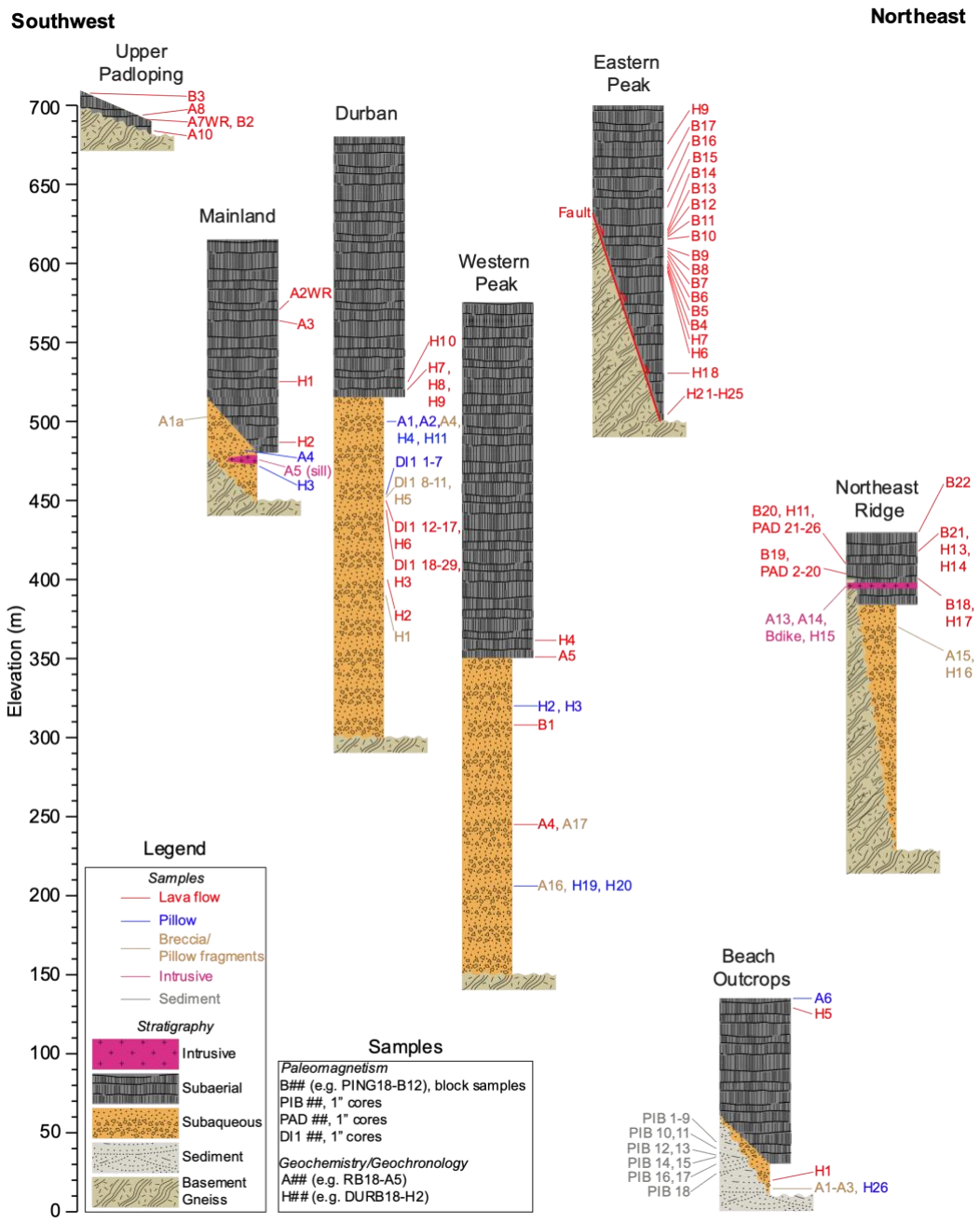

Figure 4 *– Overview of the seven stratigraphic sections, including positions of geochemical samples that were collected during the same field season but not discussed in this thesis. Flows from the top of the Eastern Peak section are possibly cotemporal with flows from the Upper Padloping section, but all other sections are separated by some degree of fault motion. See Section 4.1 for discussion.*

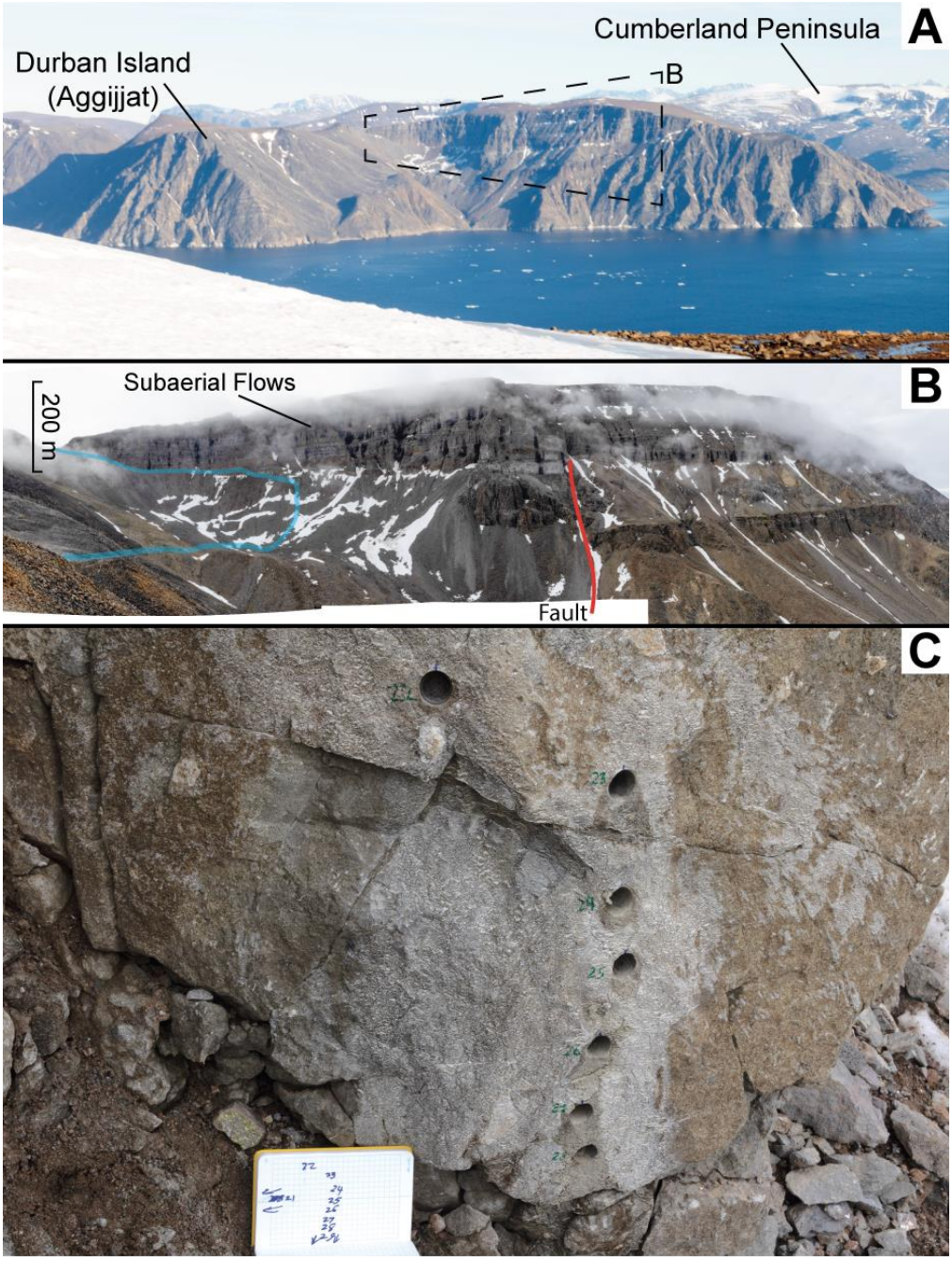

Figure 5 *– Field photos of the Durban section* ***A)*** *Photo taken from the top of the Eastern Peak section, looking southeast toward Durban Island; the field of view of Durban Island is 6 km wide.* ***B)*** *Panorama of the Durban section. The sampling transect is shown in blue, a probable fault is shown in red. Most of the section is exposed in vertical cliffs (see Fig. 3c).* ***C)*** *Photo of several drill cores from this section (Flow B, Table S1).*

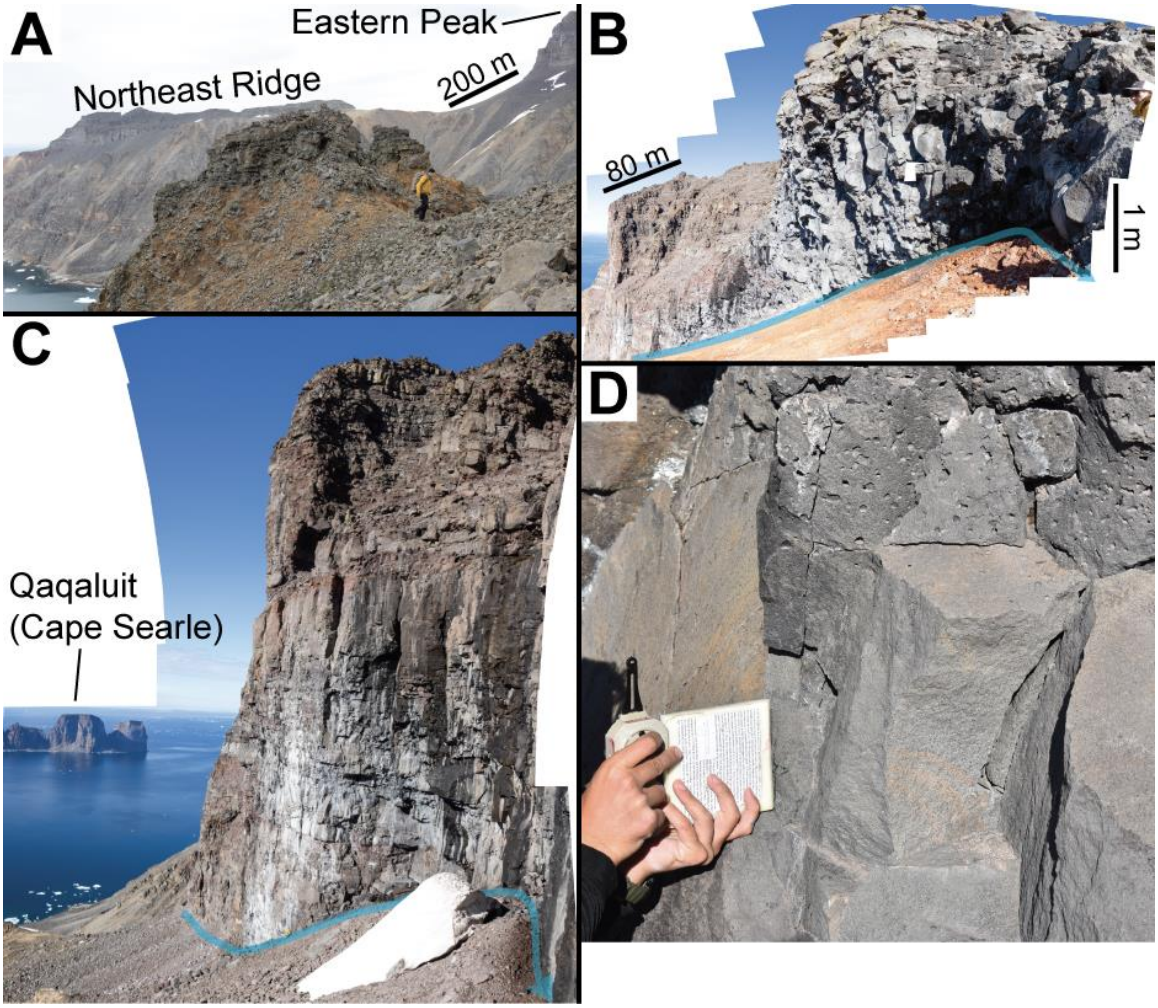

Figure 6 *– Field photos of the Eastern Peak section.* ***A)*** *Photo showing the relationship between the Eastern Peak and Northeast Ridge sections. This photo was taken from the Western Peak section, looking east.* ***B)*** *Photo of a series of flows in the upper Eastern Peak section, looking northeast.* ***C)*** *Photo of lower flows in the Eastern Peak section, looking northeast. The top of this photo can be seen in the lower left on Panel B.* ***D)*** *Close-up photo of the PING18-B7 sampling site, showing a typical flow top and interior. Photo credit Paul Asimow.*

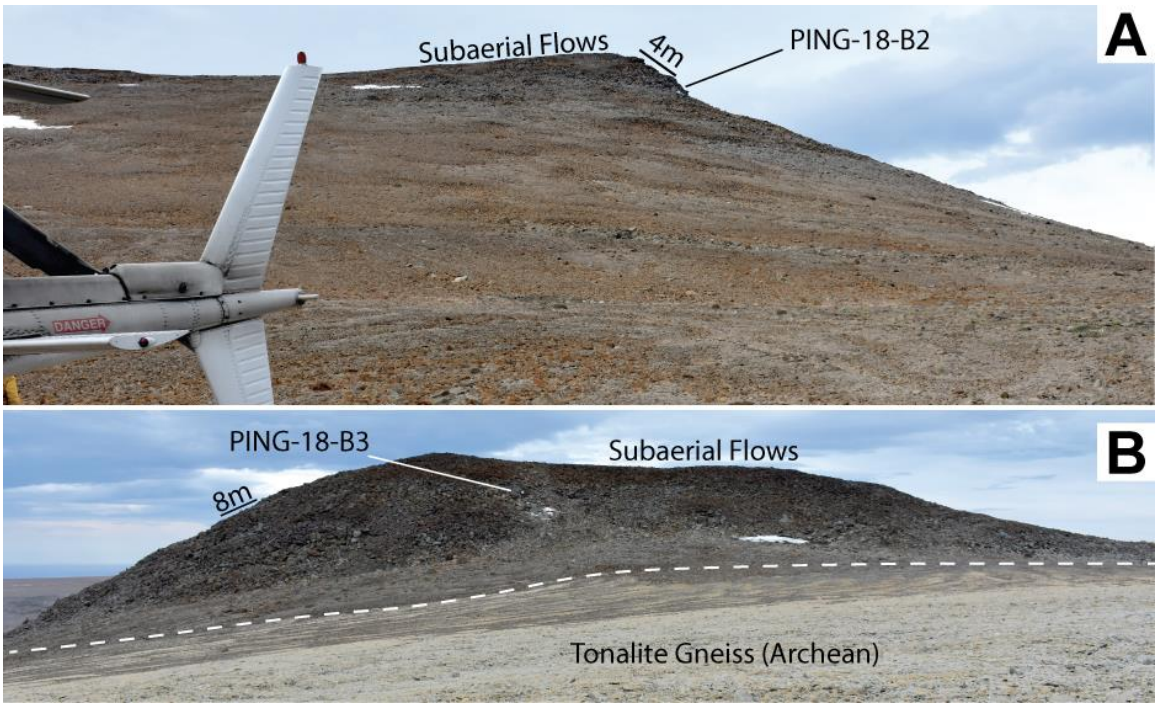

Figure 7 *– Field photos from the unimpressive Upper Padloping section.* ***A)*** *Photo (looking northwest) of the northern side of the section.* ***B)*** *Photo (looking north) of the southern side of the section.*

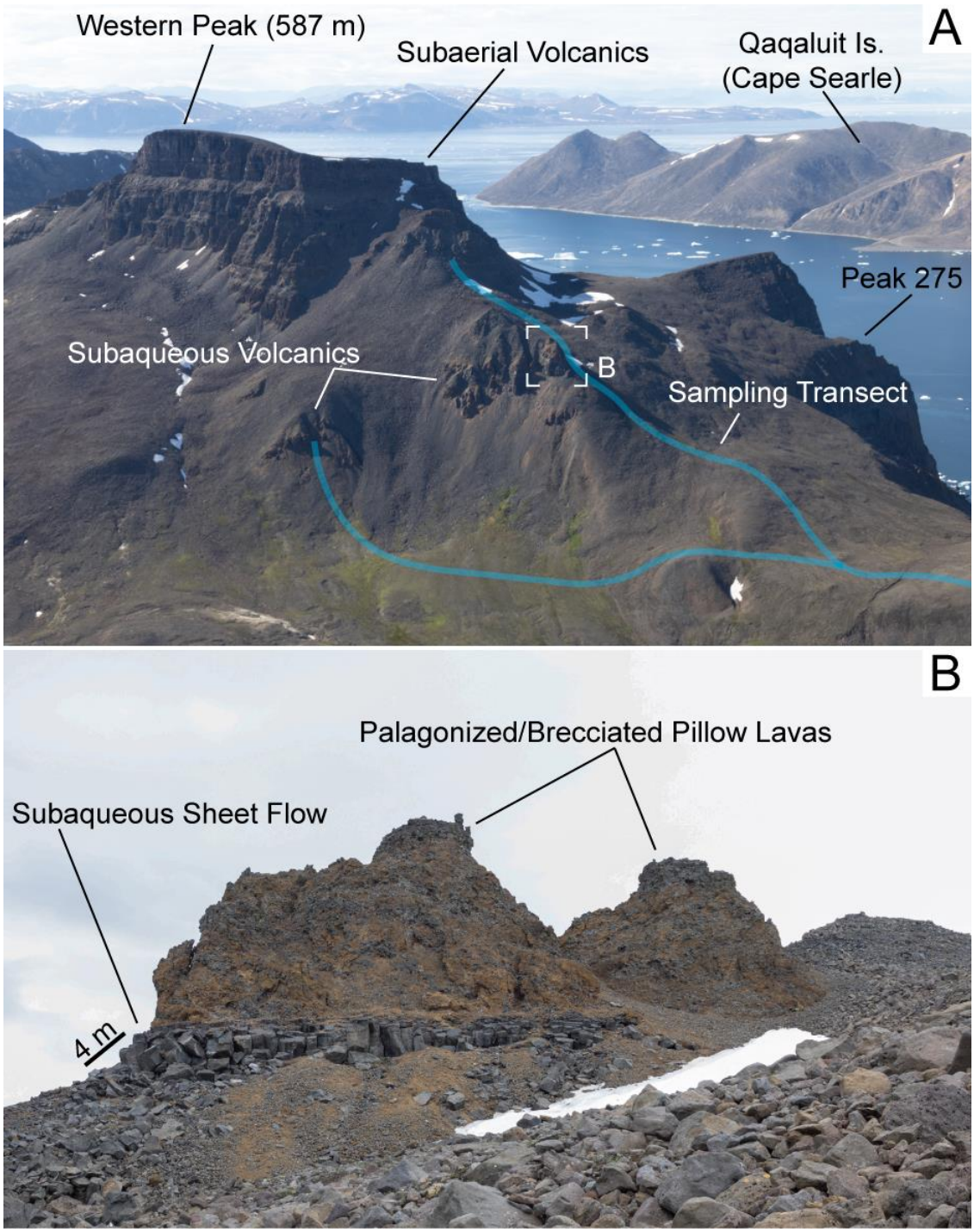

Figure 8 *– Field photos of the Western Peak section.* ***A)*** *Photo of the Western Peak, looking west. Sampling transects are shown in blue, the location of the photo in Panel B is also shown.* ***B)*** *Photo of a subaqueous sheet flow underneath palagonite breccias, which show their typical orange color here. This is the site of sample PING18-B1.*

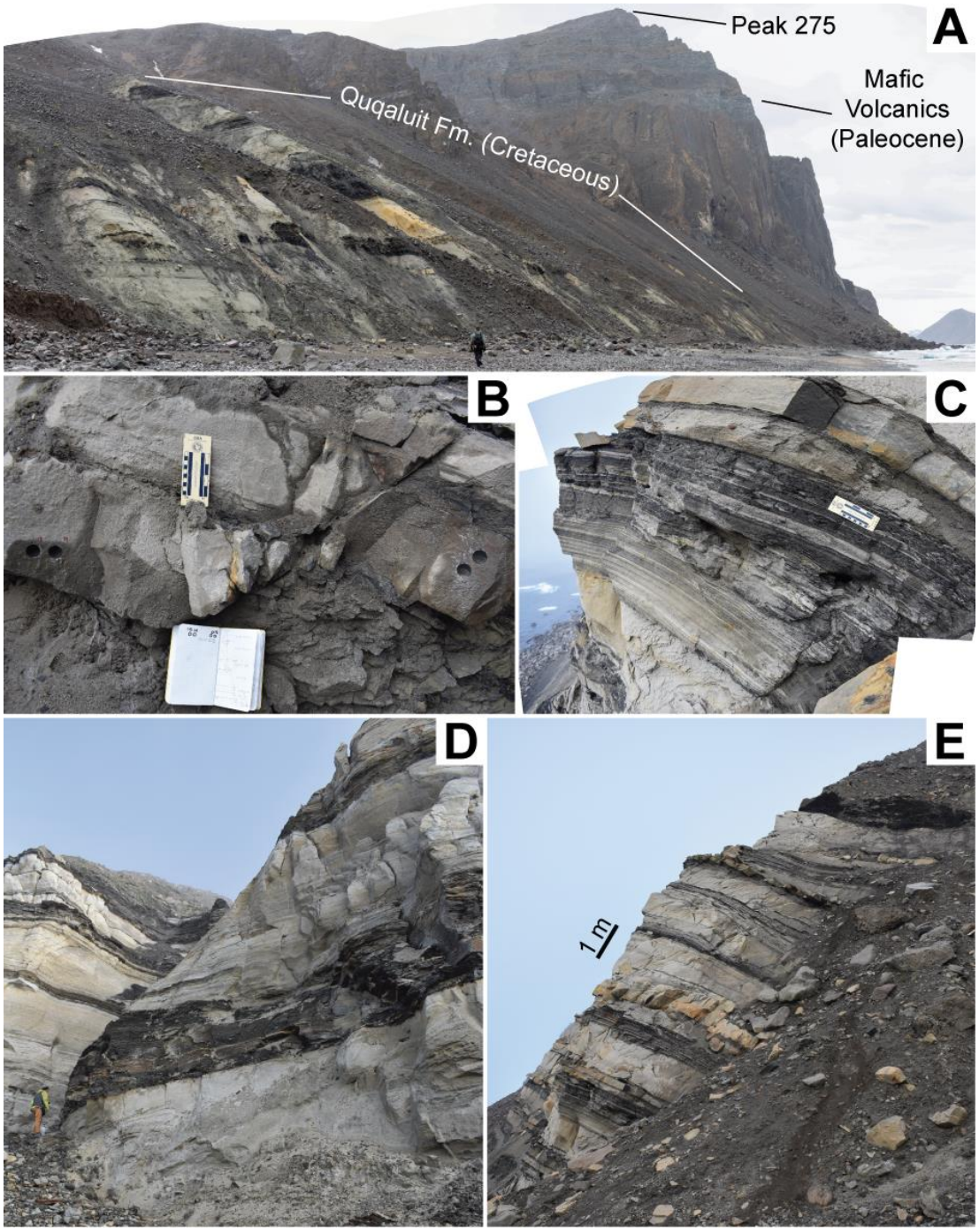

Figure 9 *– Field photos from the Beach section.* ***A)*** *Photo from the eastern portion of the section, looking west.* ***B-D)*** *Photos from the western portion of the section, where the paleomagnetic samples were collected. Note the frequent alternation between white sandstones and dark siltstones. Images courtesy of Paul Asimow.*

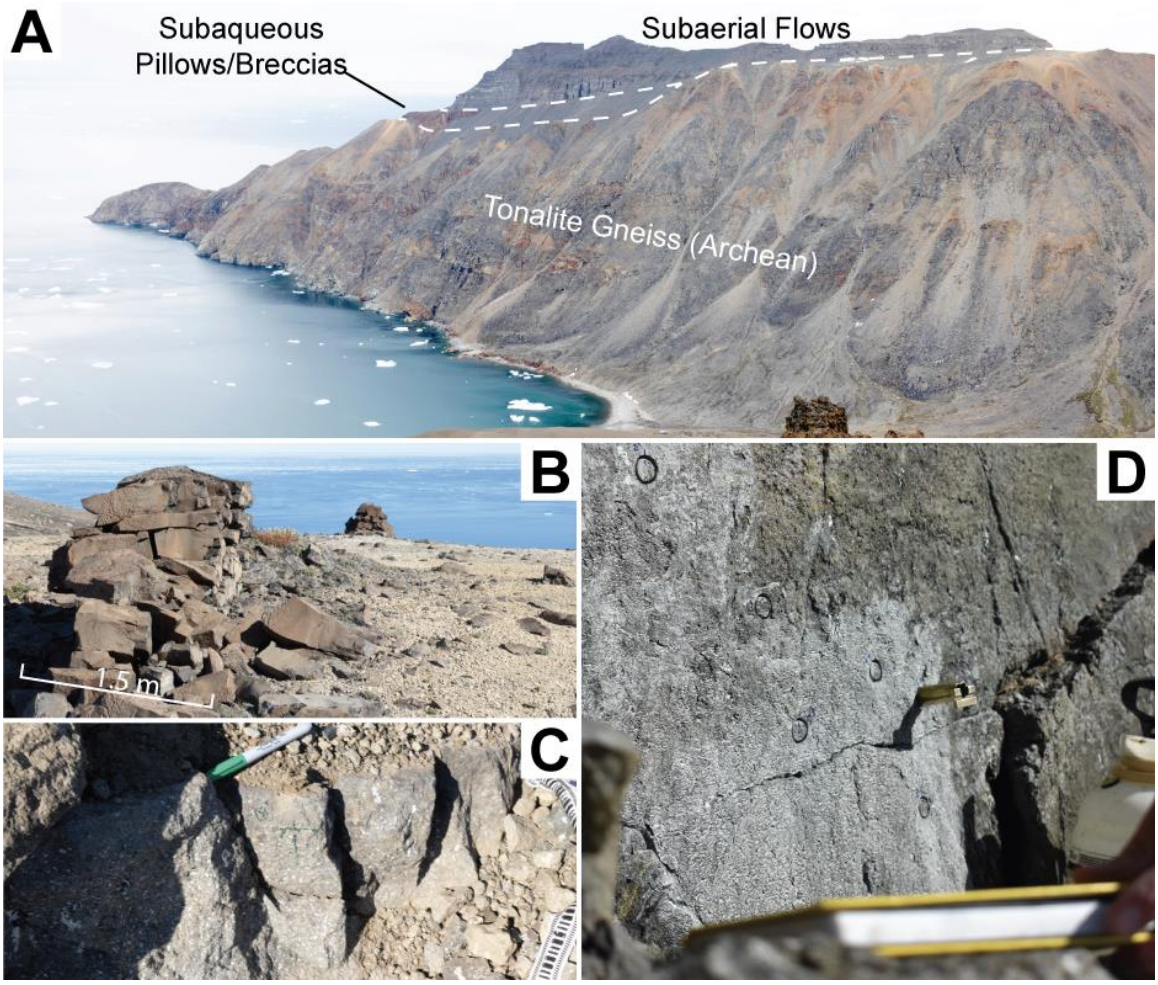

Figure 10 *– Field photos of the Northeast Ridge section.* ***A)*** *Photo (looking northeast) of the entire section, with approximate boundaries between the subaqueous and subaerial units. Photo was taken from the Western Peak section; field of view is 2.5 km wide.* ***B)*** *Photo of the only dike found in this study, looking northeast.* ***C)*** *Example of a block sample (PING18-B18) taken from this section.* ***D)*** *Photo of several cores, after drilling and before extraction, taken from this section (flow ne8).*

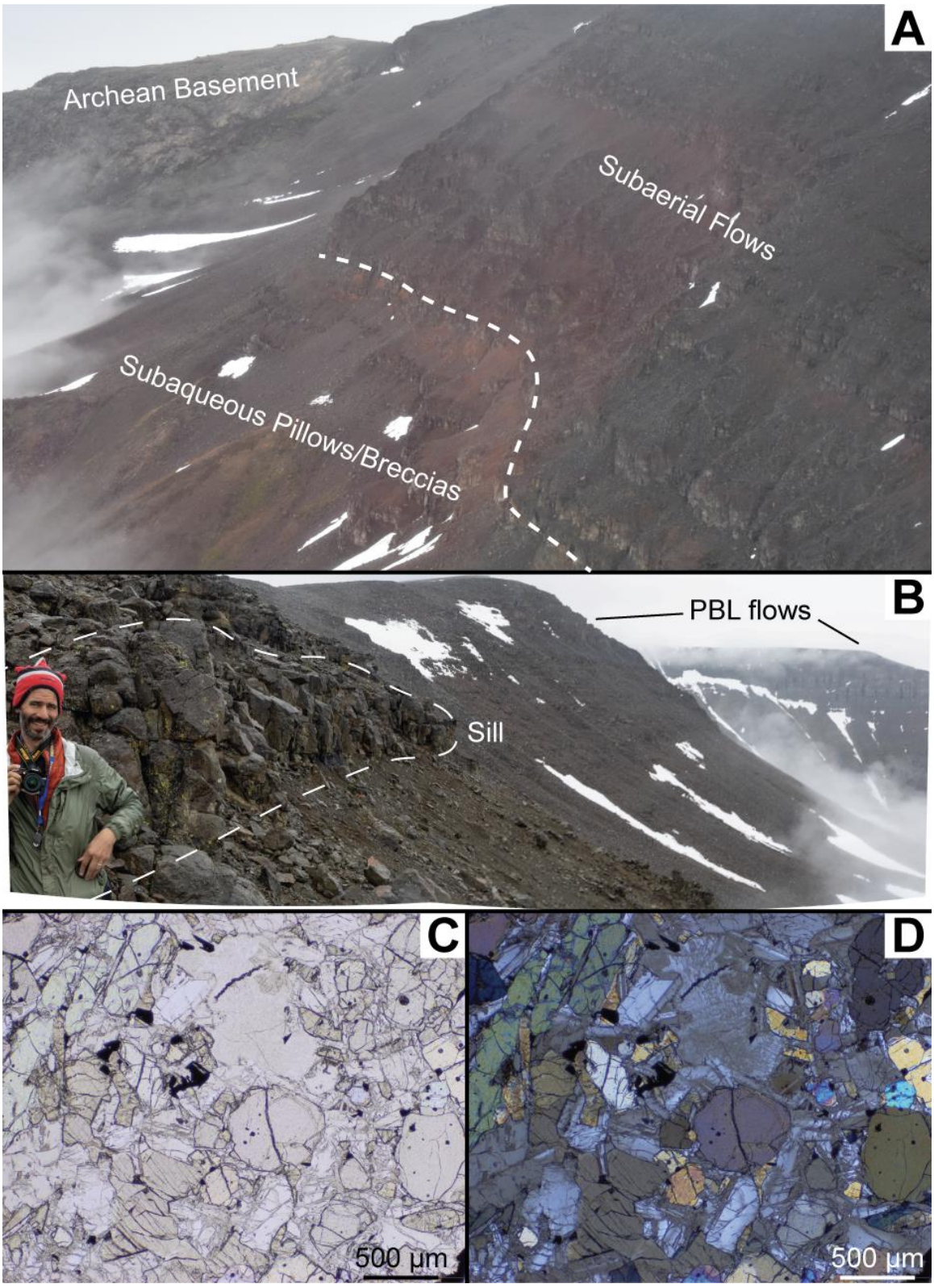
A
Archean Basement
Subaerial Flows
Subaqueous Pillows/Breccias
B
PBL flows
Sill
C
500 µm
D
500 µm

Figure 11 *– Field photos from the Mainland (Cumberland Peninsula) section.* ***A)*** *Photo taken from a helicopter (looking north), showing the subaqueous/subaerial transition and nearby Archean basement. It is not clear if the PBL unconformably lie on the basement, or if they are in fault contact here. Red coloration in the subaerial flows is from glare on the helicopter window, the flows themselves are grey in color here. Field of view is ~1 km wide. Image credit Paul Asimow.* ***B)*** *Photo looking south, showing intrusive sill and additional flows in the area.* ***C, D)*** *Photomicrograph of sample RB18-A5 in plane and cross-polarized light, showing above-average mineral grain diameters (~0.5 mm), consistent with our interpretation of a sill. Minerals in this sample include olivine, plagioclase, chromite, and orthopyroxene, and possibly clinopyroxene. Image credit Xenia Boyes.*

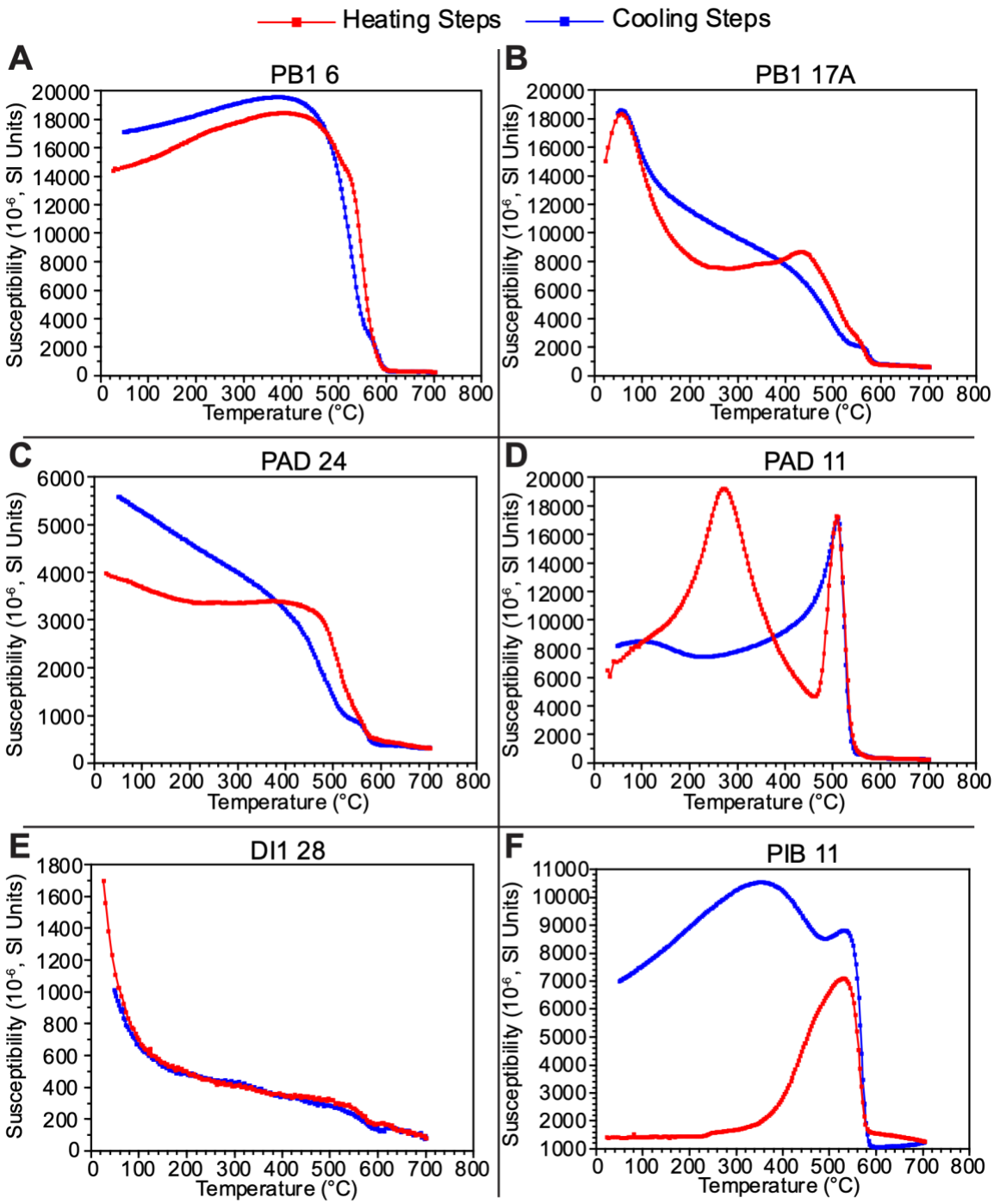

Figure 12 *– Plots of six representative thermal-susceptibility curves from the Eastern Peak section (**A, B**), Northeast Ridge section (**C, D**), Durban section (**E**), and Beach sediments (**F**). See Section 4.2 for discussion.*

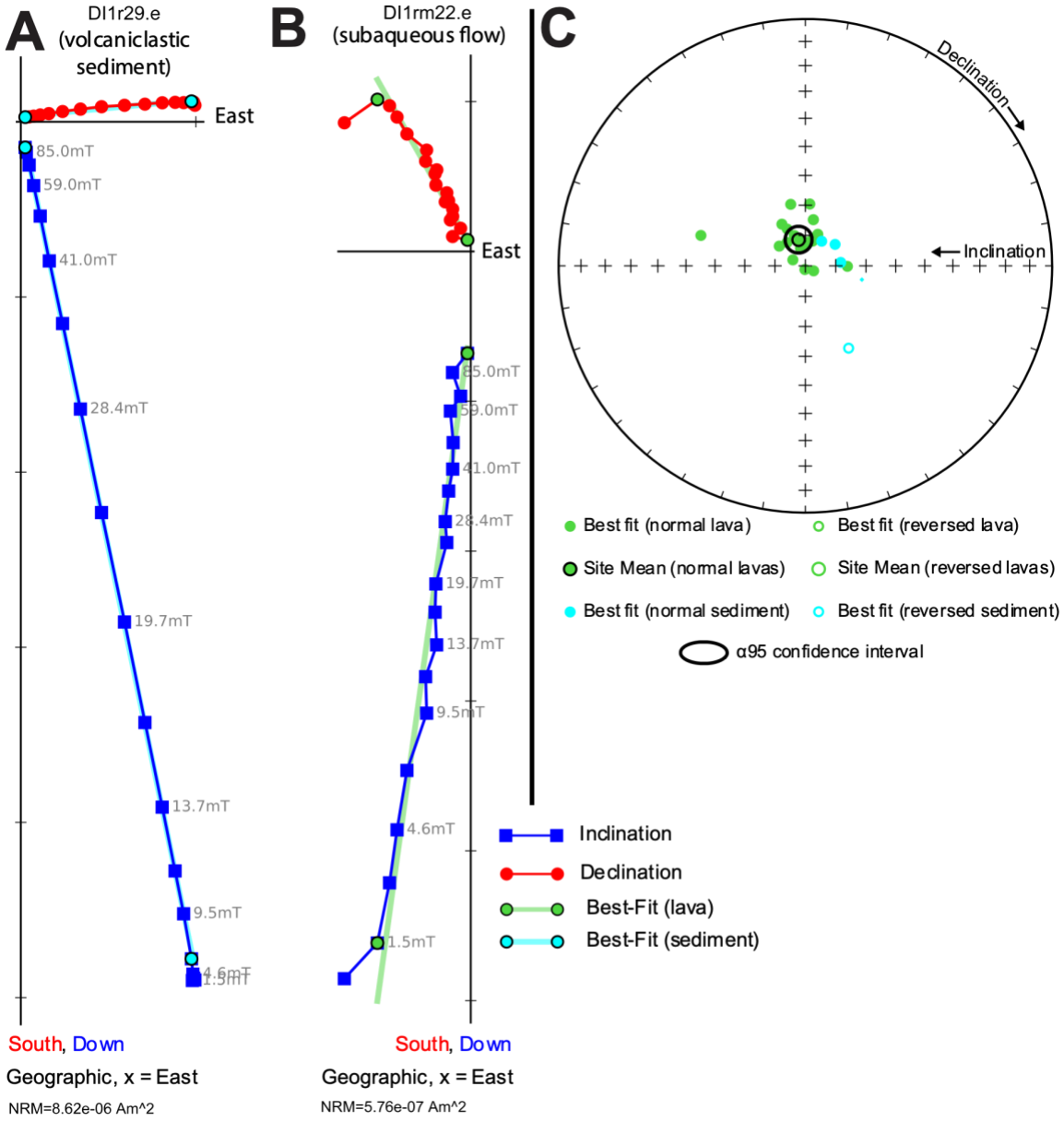

Figure 13 *– Results from the Durban section.* ***A)*** *Orthogonal projection showing one result from the volcaniclastic sediment layer.* ***B)*** *Similar plot showing a typical result from a lava flow.* ***C)*** *Equal area projection showing least-squares best fit directions for all samples in the section. Lavas are shown with green symbols, sediments are shown with blue symbols.*

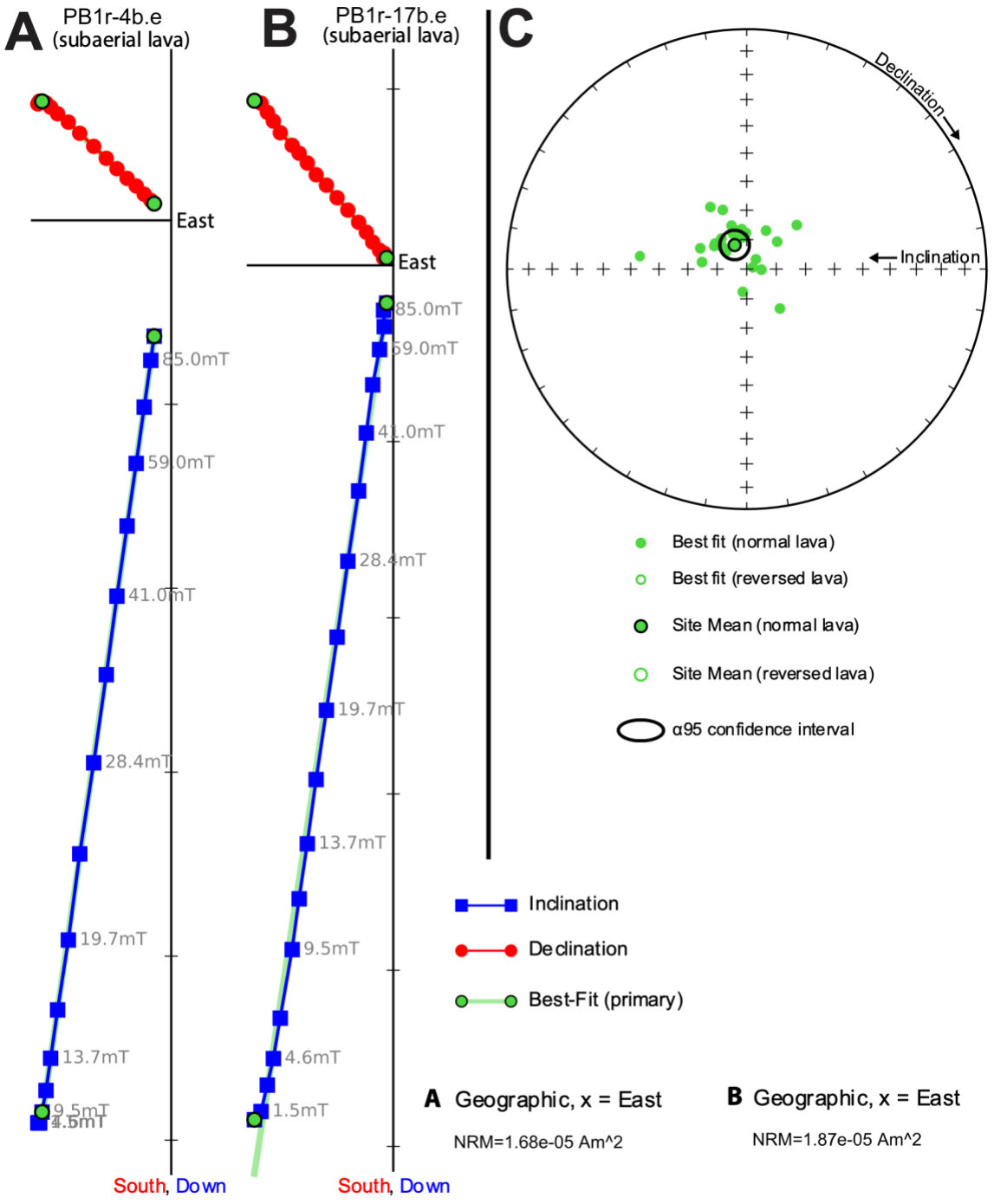

Figure 14 *– Results from the Eastern Peak section.* ***A, B)*** *Orthogonal projections showing results from the lower and upper parts of the section respectively.* ***C)*** *Equal area projection showing least-squares best fit directions for all samples in the section.*

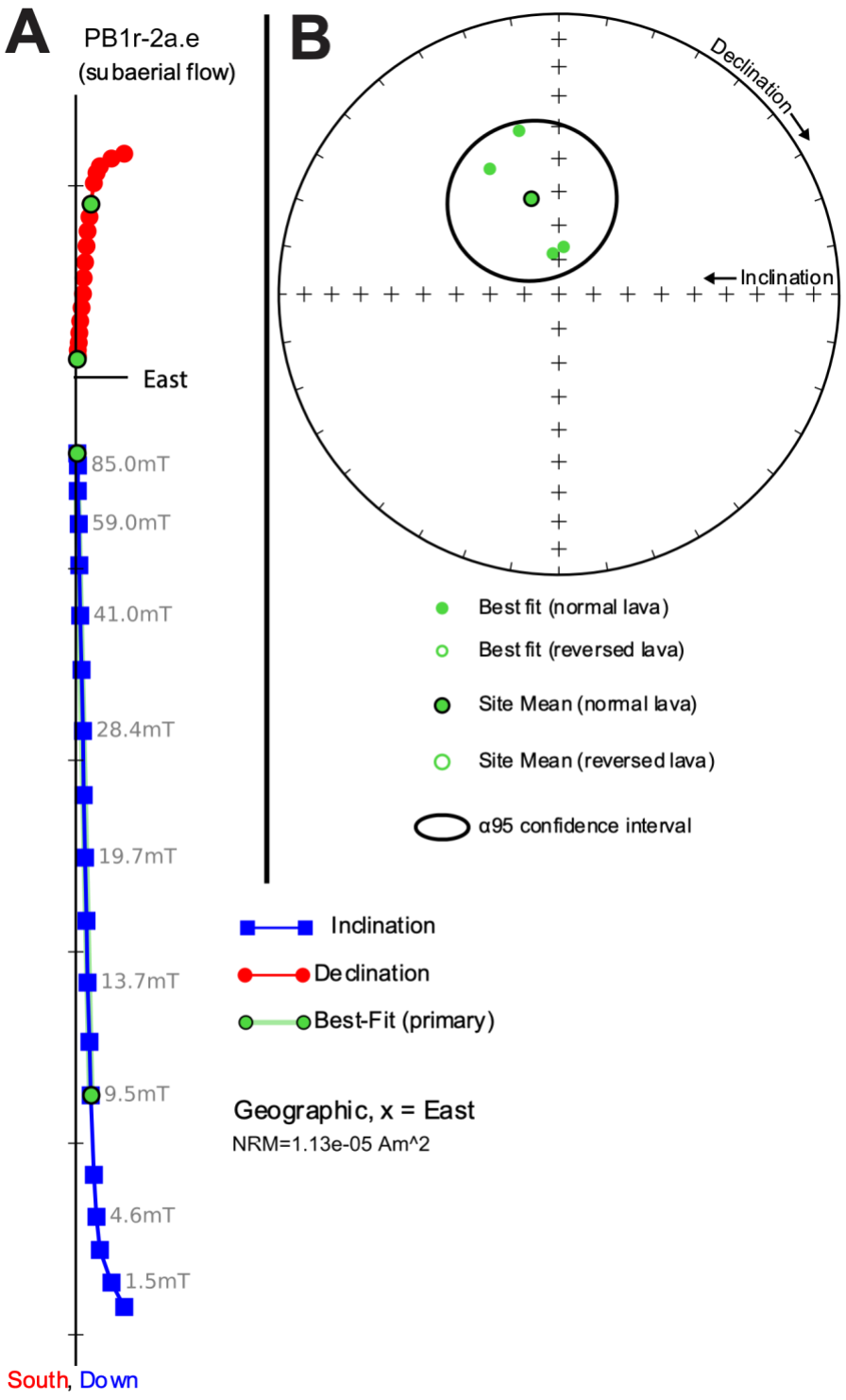

Figure 15 *– Results from the Upper Padloping section.* ***A)*** *Representative orthogonal projection.* ***B)*** *Equal area projection showing least-squares best fit directions for all samples in the section.*

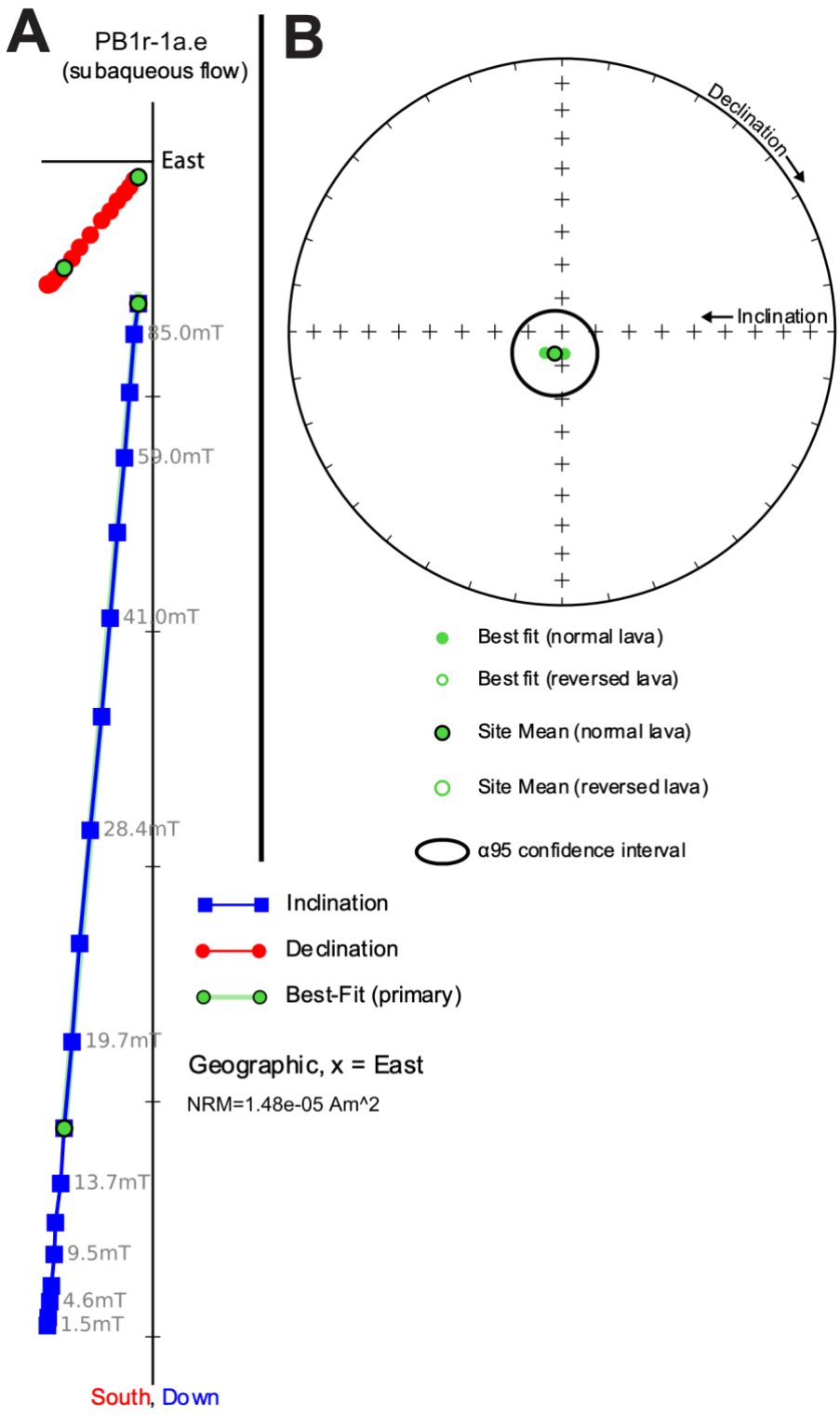

Figure 16 *– Results from the Western Peak section.* ***A)*** *Representative orthogonal projection.* ***B)*** *Equal area projection showing least-squares best fit directions for the only sample in the section.*

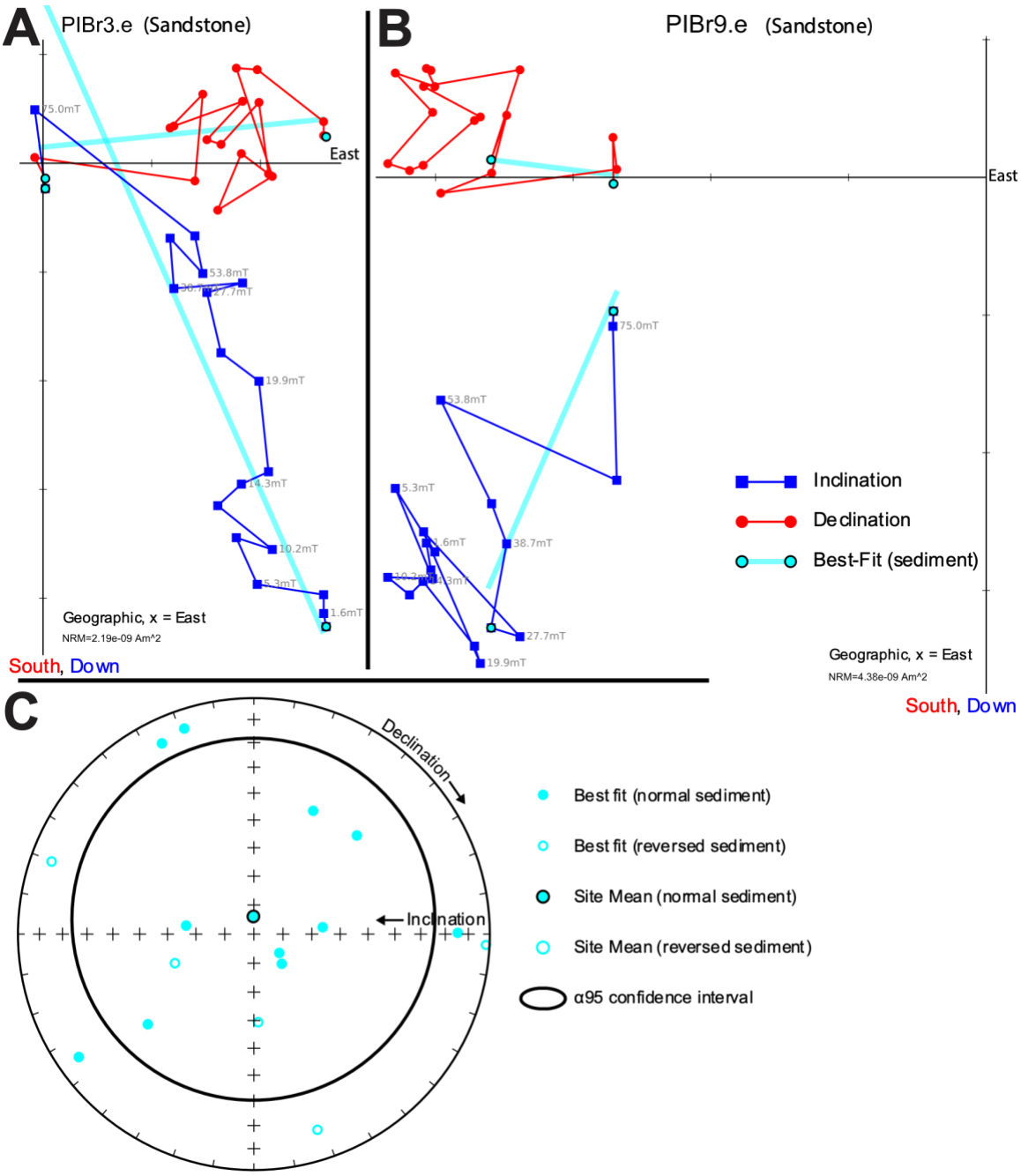

Figure 17 *– Results from the Beach section.* ***A)*** *Orthogonal projection showing one of the best samples from the section.* ***B)*** *Orthogonal projection showing one of the worst samples from the section.* ***C)*** *Equal area projection showing least-squares best fit directions for all samples in the section, with the exception of PIB 10 and 12 which did not yield an acceptable fit.*

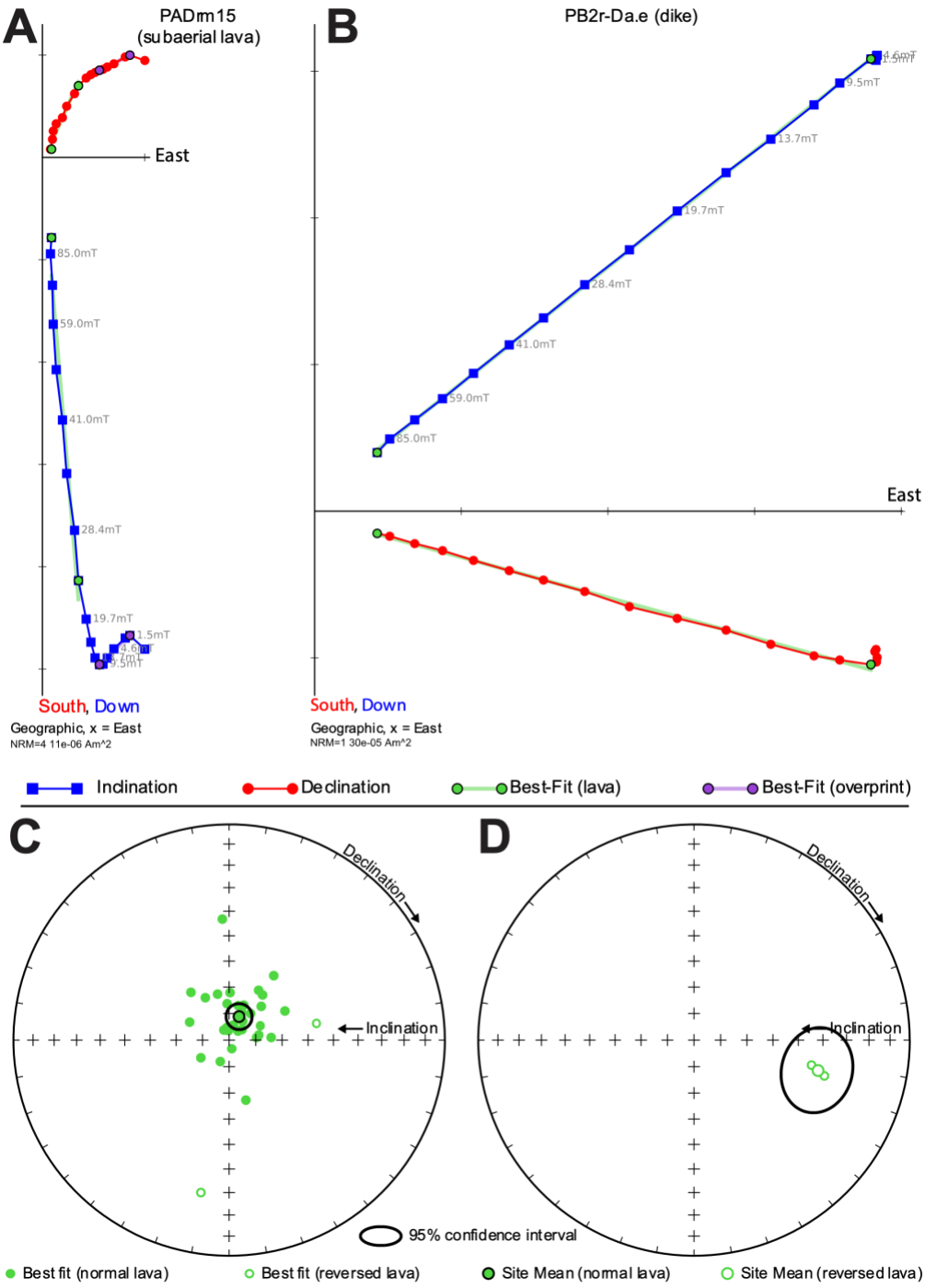

Figure 18 *– Results from the Northeast Ridge section.* ***A)*** *Orthogonal projection showing a flow with an overprint direction, which is uncommon in the PBL.* ***B)*** *Orthogonal projection showing a result from a dike sample.* ***C)*** *Equal area projection showing least-squares best fit directions for all lavas in the section.* ***D)*** *Equal area projection showing the reversed/transitional direction of the dike.*

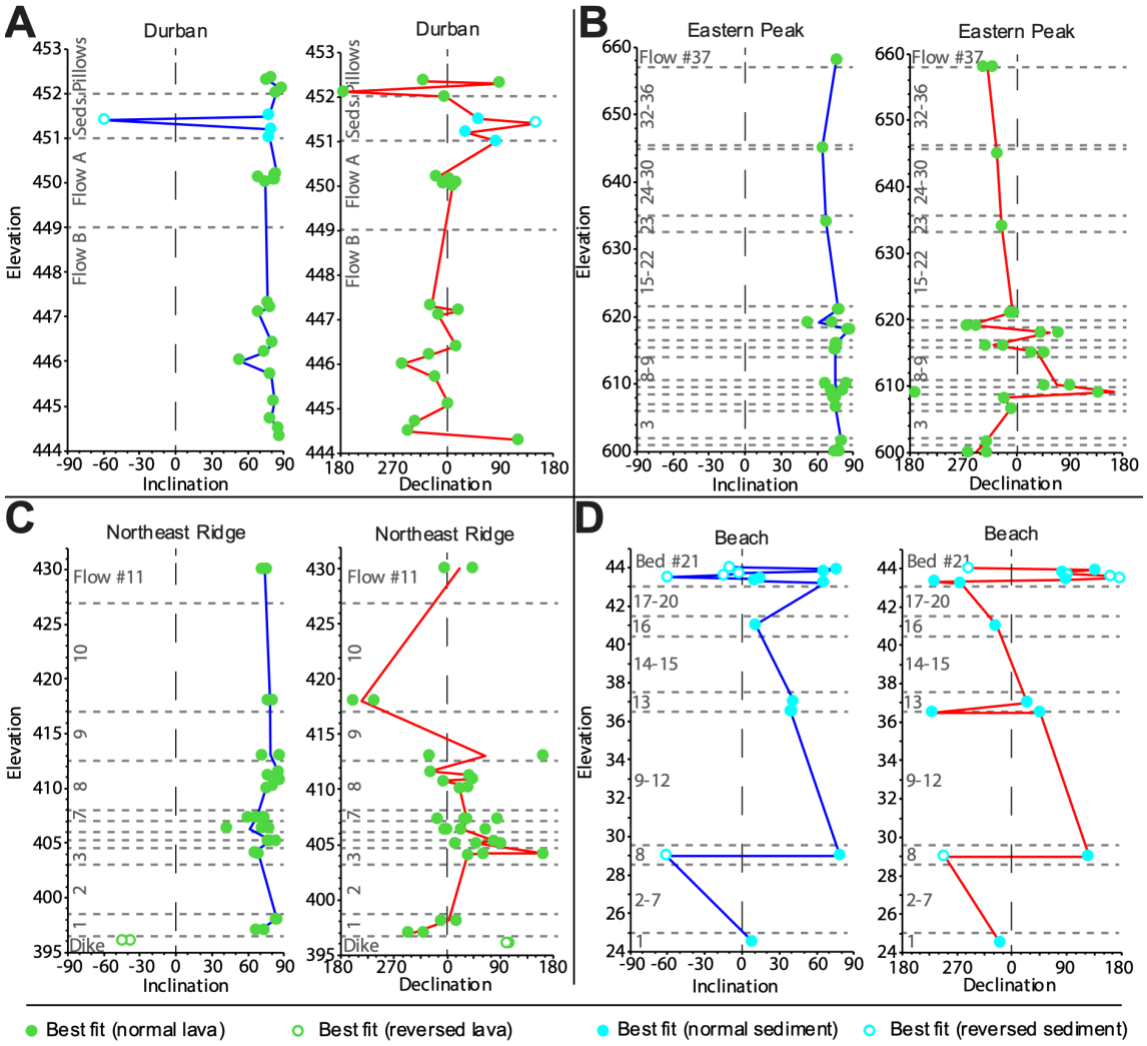

Figure 19 *– Plots of Inclination (I) and Declination (D) as a function of stratigraphic height at four sections. Colored lines show the average paleomagnetic direction at a given stratigraphic height.*

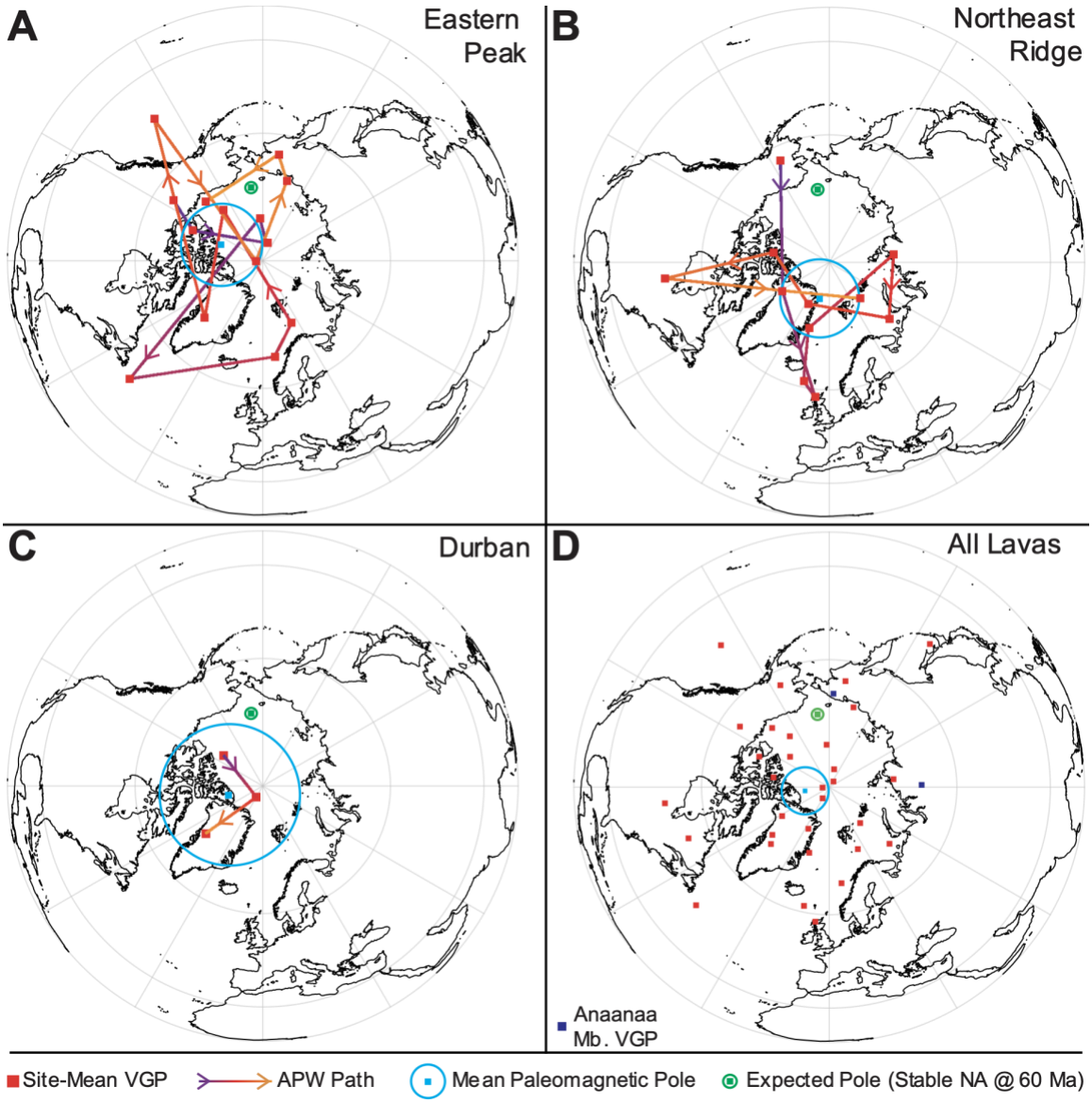

Figure 20 *– Paleosecular variation paths for three sections (**A-C**), and a compilation of all virtual geomagnetic poles (VGPs, panel **D**). Mean paleomagnetic poles in each panel are shown in blue, the expected pole for a North American site at ~60 Ma is shown in green (Torsvik et al., 2012). See Section 5.4 for discussion.*

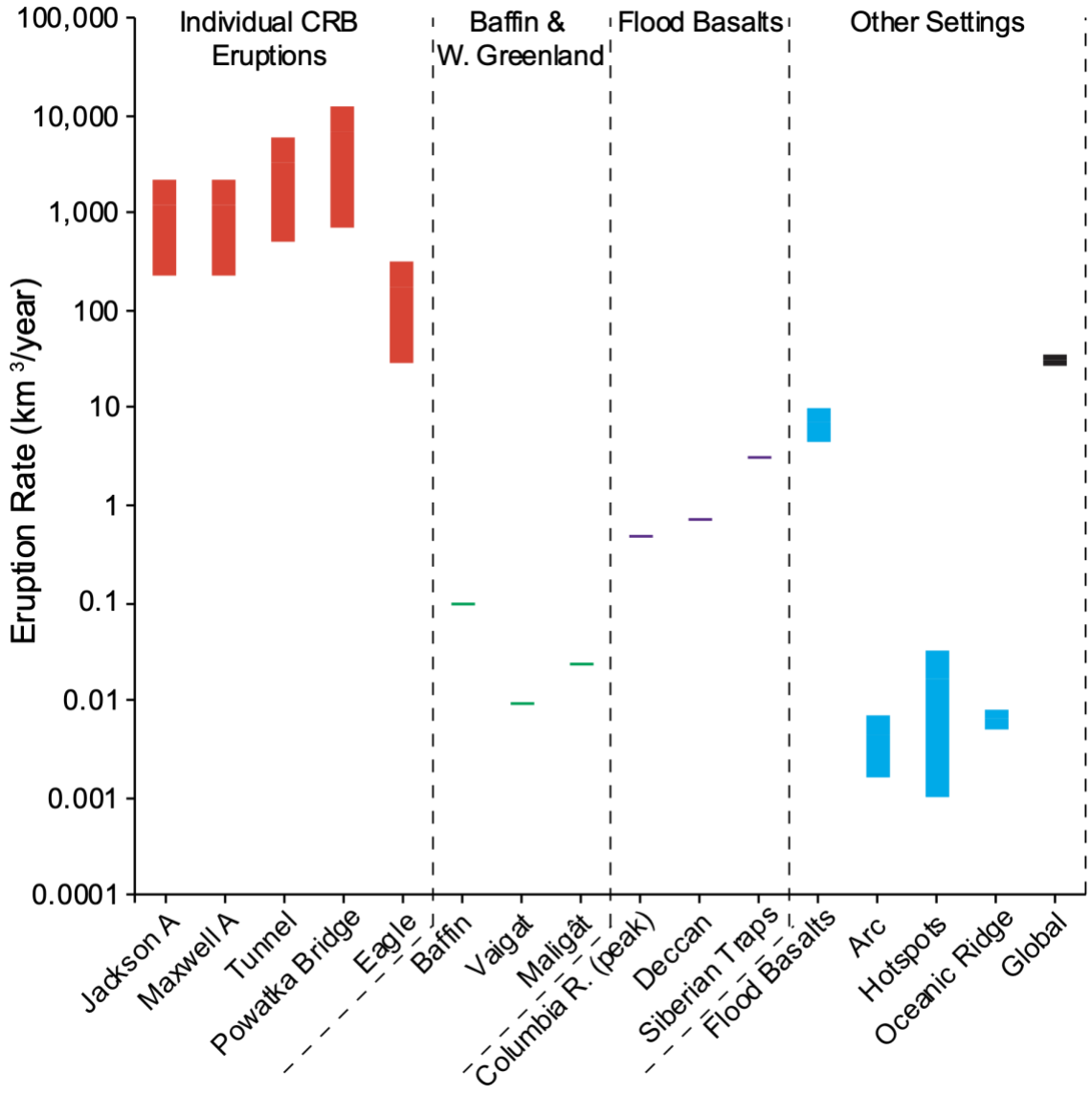

Figure 21 *– Compilation of eruption rates from various flood basalts and other tectonic settings. Data sources: Individual CRB eruptions – Chapter 2 of this thesis; Baffin – this study, west Greenland – (Larsen et al., 2016; Pedersen et al., 2017, 2018), Columbia River Basalts – (Kasbohm and Schoene, 2018), Deccan – (Schoene et al., 2019), Siberian Traps – (Burgess et al., 2017), Other Settings – (Crisp, 1984; White et al., 2006).*

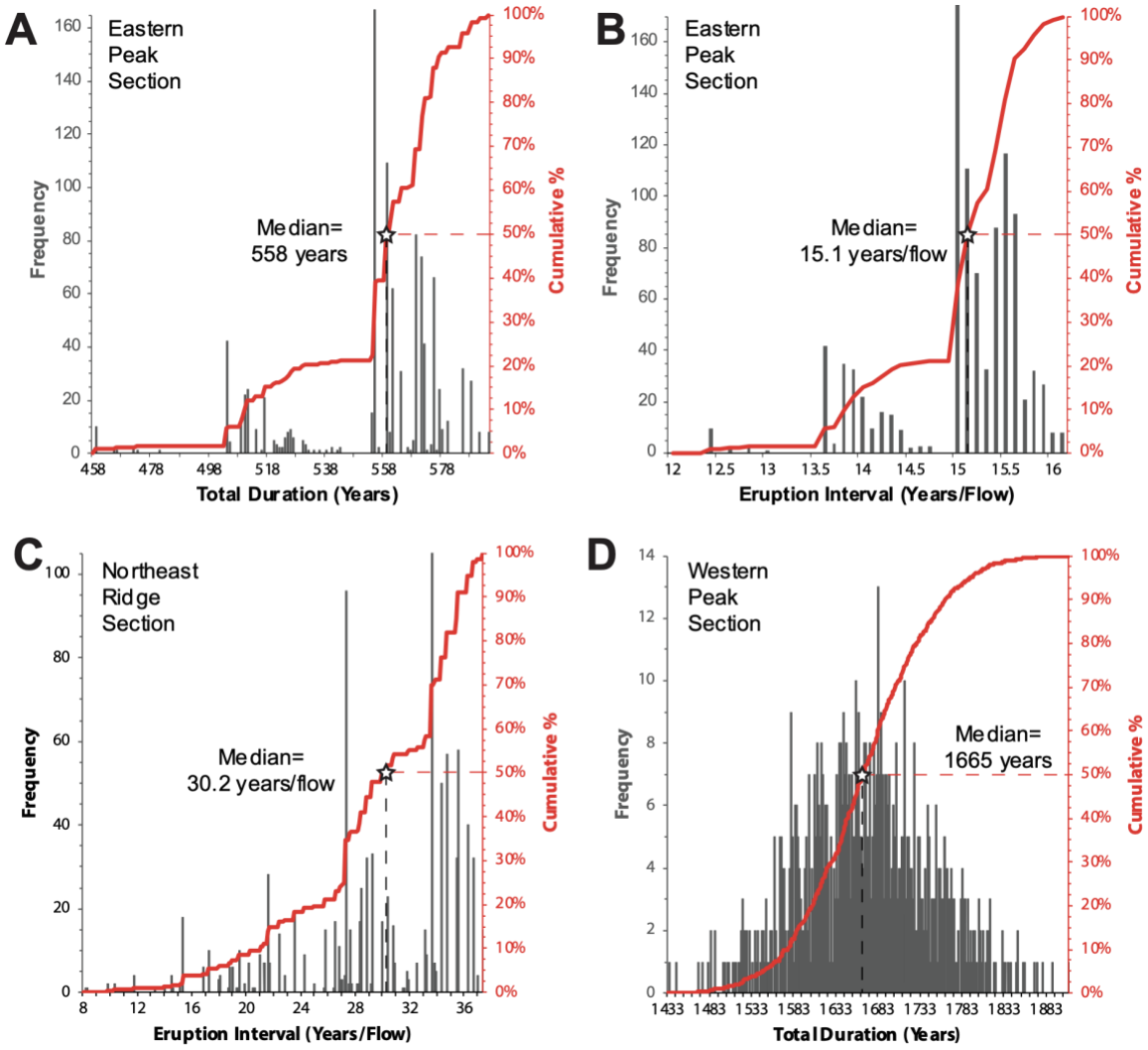

Figure A1 *– **A)** Estimates of total eruption duration at the Eastern Peak section, based on bootstrap simulations of paleosecular variation paths. **B)** Estimates of the eruption interval at the Eastern Peak section. **C)** Estimates of the eruption interval at the Northeast Ridge section, again using bootstrap simulations of paleosecular variation paths from this section. **D)** Estimates of total eruption duration at the Western Peak section, based on bootstrap resampling of the eruption intervals at the Eastern Peak and Northeast Ridge sections. See Appendix A for discussion.*

References

Agranier, A., Maury, R.C., Geoffroy, L., Chauvet, F., Le Gall, B., and Viana, A.R., 2019, Volcanic record of continental thinning in Baffin Bay margins: Insights from Svartenhuk Halvø Peninsula basalts, West Greenland: Lithos, v. 334, p. 117–140.

Baksi, A.K., 1989, Reevaluation of the timing and duration of extrusion of the Imnaha, Picture Gorge, and Grande Ronde Basalts, Columbia River Basalt Group, *in* Volcanism and Tectonism in the Columbia River Flood-Basalt Province, Geological Society of America, doi:10.1130/SPE239-p105.

Barry, T.L., Kelley, S.P., Reidel, S.P., Camp, V.E., Self, S., Jarboe, N.A., Duncan, R.A., and Renne, P.R., 2013, Eruption chronology of the Columbia River Basalt Group, *in* Geological Society of America Special Papers, Geological Society of America, v. 497, p. 45–66, doi:10.1130/2013.2497(02).

Bogue, S.W., and Coe, R.S., 1981, Paleomagnetic correlation of Columbia River Basalt flows using secular variation: Journal of Geophysical Research: Solid Earth, v. 86, p. 11883–11897.

Burden, E.T., and Langille, A.B., 1991, Palynology of Cretaceous and Tertiary strata, northeast Baffin Island, Northwest Territories, Canada: Implications for the history of rifting in Baffin Bay: Palynology, v. 15, p. 91–114.

Burden, E.T., and Langille, A., 1990, Stratigraphy and sedimentology of Cretaceous and Paleocene strata in half-grabens on the southeast coast of Baffin Island, Northwest Territories: Bulletin of Canadian Petroleum Geology, v. 38, p. 185–196.

Burgess, S.D., Muirhead, J.D., and Bowring, S.A., 2017, Initial pulse of Siberian Traps sills as the trigger of the end-Permian mass extinction: Nature Communications, v. 8, p. 1–6, doi:10.1038/s41467-017-00083-9.

Butler, R.F., 1992, Paleomagnetism: Magnetic domains to geologic terranes: Boston, MA, Blackwell Scientific Publications, v. 319, 319 p.

Champion, D.E., and Donnelly-Nolan, J.M., 1994, Duration of eruption at the Giant Crater lava field, Medicine Lake volcano, California, based on paleomagnetic secular variation: Journal of Geophysical Research: Solid Earth, v. 99, p. 15595–15604.

Chauvet, F., Geoffroy, L., Guillou, H., Maury, R.C., Le Gall, B., Agranier, A., and Viana, A., 2019, Eocene continental breakup in Baffin Bay: Tectonophysics, v. 757, p. 170–186.

Chenet, A.-L., Courtillot, V., Fluteau, F., Gérard, M., Quidelleur, X., Khadri, S., Subbarao, K., and Thordarson, T., 2009, Determination of rapid Deccan eruptions across the Cretaceous-Tertiary boundary using paleomagnetic secular variation: 2. Constraints from analysis of eight new sections and synthesis for a 3500-m-thick composite section: Journal of Geophysical Research: Solid Earth, v. 114, doi:10.1029/2008JB005644.

Clapham, M.E., and Renne, P.R., 2019, Flood basalts and mass extinctions: Annual Review of Earth and Planetary Sciences, v. 47, p. 275–303, doi:10.1146/annurev-earth-053018-060136.

Clarke, D.B., 1970, Tertiary basalts of Baffin Bay: Possible primary magma from the mantle: Contributions to Mineralogy and Petrology, v. 25, p. 203–224.

Clarke, D.B., 1968, Tertiary basalts of the Baffin Bay area [PhD Thesis]: University of Edinburgh, http://hdl.handle.net/1842/13421.

Clarke, D.B., and Beutel, E.K., 2020, Davis Strait Paleocene picrites: Products of a plume or plates? Earth-Science Reviews, v. 206, p. 102770, doi:https://doi.org/10.1016/j.earscirev.2019.01.012.

Clarke, D., and Upton, B., 1971, Tertiary basalts of Baffin Island: Field relations and tectonic setting: Canadian Journal of Earth Sciences, v. 8, p. 248–258.

Cox, G.M., Halverson, G.P., Stevenson, R.K., Vokaty, M., Poirier, A., Kunzmann, M., Li, Z.-X., Denyszyn, S.W., Strauss, J.V., and Macdonald, F.A., 2016, Continental flood basalt weathering as a trigger for Neoproterozoic Snowball Earth: Earth and Planetary Science Letters, v. 446, p. 89–99.

Crisp, J.A., 1984, Rates of magma emplacement and volcanic output: Journal of Volcanology and Geothermal Research, v. 20, p. 177–211.

Dam, G., Pedersen, G.K., Sønderholm, M., Midtgaard, H.H., Larsen, L.M., Nøhr-Hansen, H., and Pedersen, A.K., 2009, Lithostratigraphy of the Cretaceous–Paleocene Nuussuaq Group, Nuussuaq Basin, West Greenland: Geological Survey of Denmark and Greenland (GEUS) Bulletin, v. 19, p. 1–171.

Day, J.M., 2016, Evidence against an ancient non-chondritic mantle source for North Atlantic Igneous Province lavas: Chemical Geology, v. 440, p. 91–100.

Deutsch, E., Kristjansson, L., and May, B., 1971, Remanent magnetism of lower Tertiary lavas on Baffin Island: Canadian Journal of Earth Sciences, v. 8, p. 1542–1552.

Dinarès-Turell, J., Pujalte, V., Stoykova, K., Baceta, J.I., and Ivanov, M., 2012, The Palaeocene “top chron C27n” transient greenhouse episode: Evidence from marine pelagic Atlantic and peri-Tethyan sections: Terra Nova, v. 24, p. 477–486.

Dunlop, D.J., 2014, High-temperature susceptibility of magnetite: A new pseudo-single-domain effect: Geophysical Journal International, v. 199, p. 707–716, doi:10.1093/gji/ggu247.

Dunlop, D.J., and Özdemir, Ö., 1997, Rock Magnetism: Fundamentals and Frontiers: Cambridge, Cambridge University Press, Cambridge Studies in Magnetism, 573 p., doi:10.1017/CBO9780511612794.

Fischer, W.W., Hemp, J., and Johnson, J.E., 2016, Evolution of oxygenic photosynthesis: Annual Review of Earth and Planetary Sciences, v. 44, p. 647–683.

Fisher, N.I., Lewis, T., and Embleton, B.J., 1993, Statistical analysis of spherical data: Cambridge, UK, Cambridge University Press, 343 p.

Francis, D., 1985, The Baffin Bay lavas and the value of picrites as analogues of primary magmas: Contributions to Mineralogy and Petrology, v. 89, p. 144–154.

Giorgis, S., Horsman, E., Burmeister, K.C., Rost, R., Herbert, L.A., Pivarunas, A., and Braunagel, M., 2019, Constraints on emplacement rates of intrusions in the shallow crust based on paleomagnetic secular variation: Geophysical Research Letters, v. 46, p. 12815–12822.

Gradstein, F.M., Ogg, J.G., Schmitz, M.D., and Ogg, G.M., 2012, The geologic time scale 2012: Elsevier BV, 1176 p., https://doi.org/10.1016/C2011-1-08249-8.

Harlou, R., Pearson, D., Davidson, J., Kamenetsky, V., and Yaxley, G., 2006, Source variability and crustal contamination of the Baffin Island picrites—coupled Sr

isotope and trace element study of individual melt inclusions: Geochimica et Cosmochimica Acta, v. 70, p. A231.

Hole, M.J., and Natland, J.H., 2020, Magmatism in the North Atlantic Igneous Province; mantle temperatures, rifting and geodynamics: Earth-Science Reviews, v. 206, p. 102794, doi:https://doi.org/10.1016/j.earscirev.2019.02.011.

Horni, J.Á., Hopper, J.R., Blischke, A., Geisler, W.H., Stewart, M., McDermott, K., Judge, M., Erlendsson, Ö., and Árting, U., 2017, Regional distribution of volcanism within the North Atlantic Igneous Province: Geological Society, London, Special Publications, v. 447, p. 105–125.

Horton, F., Curtice, J., Farley, K., Kurz, M., Asimow, P., Treffkorn, J., and Boyes, X., 2021, Primordial neon in high-3He/4He Baffin Island olivines: Earth and Planetary Science Letters, v. 558, p. 116762.

Jackson, A., and Finlay, C., 2007, Geomagnetic secular variation and its applications to the core: Treatise on Geophysics, v. 5, p. 147–193.

Kasbohm, J., and Schoene, B., 2018, Rapid eruption of the Columbia River flood basalt and correlation with the mid-Miocene climate optimum: Science Advances, v. 4, doi:10.1126/sciadv.aat8223.

de Kemp, E.A., Gilbert, C., and James, D.T., 2006, Geology of Nunavut: Geological Survey of Canada, https://geoscan.nrcan.gc.ca/starweb/geoscan/servlet.starweb?path=geoscan/fulle.web&search1=R=223684.

Kent, A., Stolper, E., Francis, D., Woodhead, J., Frei, R., and Eiler, J., 2004, Mantle heterogeneity during the formation of the North Atlantic igneous province:

Constraints from trace element and Sr-Nd-Os-O isotope systematics of Baffin Island picrites: Geochemistry, Geophysics, Geosystems, v. 5.

Kirschvink, J., 1980, The least-squares line and plane and the analysis of palaeomagnetic data: Geophysical Journal International, v. 62, p. 699–718, doi:10.1111/j.1365-246X.1980.tb02601.x.

Kirschvink, J.L., Kopp, R.E., Raub, T.D., Baumgartner, C.T., and Holt, J.W., 2008, Rapid, precise, and high-sensitivity acquisition of paleomagnetic and rock-magnetic data: Development of a low-noise automatic sample changing system for superconducting rock magnetometers: Geochemistry, Geophysics, Geosystems, v. 9, doi:10.1029/2007GC001856.

Korte, M., Constable, C., Donadini, F., and Holme, R., 2011, Reconstructing the Holocene geomagnetic field: Earth and Planetary Science Letters, v. 312, p. 497–505.

Korte, M., Donadini, F., and Constable, C., 2009, Geomagnetic field for 0–3 ka: 2. A new series of time-varying global models: Geochemistry, Geophysics, Geosystems, v. 10.

Larsen, L.M., Heaman, L.M., Creaser, R.A., Duncan, R.A., Frei, R., and Hutchison, M., 2009, Tectonomagmatic events during stretching and basin formation in the Labrador Sea and the Davis Strait: Evidence from age and composition of Mesozoic to Palaeogene dyke swarms in West Greenland: Journal of the Geological Society, v. 166, p. 999–1012.

Larsen, L.M., Pedersen, A.K., Tegner, C., Duncan, R.A., Hald, N., and Larsen, J.G., 2016, Age of Tertiary volcanic rocks on the West Greenland continental margin:

volcanic evolution and event correlation to other parts of the North Atlantic Igneous Province: Geological Magazine, v. 153, p. 487–511.

de Leeuw, G., Ellam, R., Stuart, F., and Carlson, R., 2017, 142Nd/144Nd inferences on the nature and origin of the source of high 3He/4He magmas: Earth and Planetary Science Letters, v. 472, p. 62–68.

Liu, Q., Yu, Y., Torrent, J., Roberts, A.P., Pan, Y., and Zhu, R., 2006, Characteristic low-temperature magnetic properties of aluminous goethite [α-(Fe, Al) OOH] explained: Journal of Geophysical Research: Solid Earth, v. 111.

Livermore, P.W., Finlay, C.C., and Bayliff, M., 2020, Recent north magnetic pole acceleration towards Siberia caused by flux lobe elongation: Nature Geoscience, v. 13, p. 387–391, doi:10.1038/s41561-020-0570-9.

Macdonald, F.A., and Wordsworth, R., 2017, Initiation of Snowball Earth with volcanic sulfur aerosol emissions: Geophysical Research Letters, v. 44, p. 1938–1946.

McCoy-West, A.J., Fitton, J.G., Pons, M.-L., Inglis, E.C., and Williams, H.M., 2018, The Fe and Zn isotope composition of deep mantle source regions: Insights from Baffin Island picrites: Geochimica et Cosmochimica Acta, v. 238, p. 542–562.

Nayudu, Y.R., 1964, Palagonite tuffs (hyaloclastites) and the products of post-eruptive processes: Bulletin Volcanologique, v. 27, p. 391–410.

Özdemir, Ö., and Dunlop, D.J., 2010, Hallmarks of maghemitization in low-temperature remanence cycling of partially oxidized magnetite nanoparticles: Journal of Geophysical Research: Solid Earth, v. 115.

Pavón-Carrasco, F.J., Osete, M.L., Torta, J.M., and Santis, A.D., 2014, A geomagnetic field model for the Holocene based on archaeomagnetic and lava flow data: Earth

and Planetary Science Letters, v. 388, p. 98–109, doi: https://doi.org/10.1016/j.epsl.2013.11.046.

Peace, A.L., Phethean, J.J., Franke, D., Foulger, G.R., Schiffer, C., Welford, J.K., McHone, G., Rocchi, S., Schnabel, M., and Doré, A.G., 2020, A review of Pangaea dispersal and Large Igneous Provinces–In search of a causative mechanism: Earth-Science Reviews, v. 206, p. 102902.

Pedersen, A.K., Larsen, L.M., and Pedersen, G.K., 2018, Lithostratigraphy, geology and geochemistry of the volcanic rocks of the Maligât Formation and associated intrusions on Disko and Nuussuaq, Paleocene of West Greenland: GEUS Bulletin, v. 40, p. 1–239.

Pedersen, A.K., Larsen, L.M., and Pedersen, G.K., 2017, Lithostratigraphy, geology and geochemistry of the volcanic rocks of the Vaigat Formation on Disko and Nuussuaq, Paleocene of West Greenland: GEUS Bulletin, v. 39, p. 1–244.

Pedersen, A.K., Larsen, L.M., Riisager, P., and Dueholm, K.S., 2002, Rates of volcanic deposition, facies changes and movements in a dynamic basin: The Nuussuaq Basin, West Greenland, around the C27n-C26r transition: Geological Society, London, Special Publications, v. 197, p. 157–181.

Pinton, A., Giordano, G., Speranza, F., and Þórðarson, Þ., 2017, Paleomagnetism of Holocene lava flows from the Reykjanes Peninsula and the Tungnaá lava sequence (Iceland): Implications for flow correlation and ages: Bulletin of Volcanology, v. 80, p. 10, doi:10.1007/s00445-017-1187-8.

Porter, C. et al., 2018, Arctic DEM: Harvard Dataverse, v. 1, doi:https://doi.org/10.7910/DVN/OHHUKH.

Riisager, P., and Abrahamsen, N., 1999, Magnetostratigraphy of Palaeocene basalts from the Vaigat formation of West Greenland: Geophysical Journal International, v. 137, p. 774–782.

Riisager, J., Riisager, P., and Pedersen, A.K., 2003a, Paleomagnetism of large igneous provinces: Case-study from West Greenland, North Atlantic igneous province: Earth and Planetary Science Letters, v. 214, p. 409–425.

Riisager, J., Riisager, P., and Pedersen, A.K., 2003b, The C27n-C26r geomagnetic polarity reversal recorded in the west Greenland flood basalt province: How complex is the transitional field? Journal of Geophysical Research: Solid Earth, v. 108.

Riisager, J., Riisager, P., and Perrin, M., 1999, Palaeodirectional and palaeointensity results of Paleocene and Eocene basalts from West Greenland: Bulletin Geological Society of Denmark, v. 46, p. 69–78.

Roberts, A.P., and Winklhofer, M., 2004, Why are geomagnetic excursions not always recorded in sediments? Constraints from post-depositional remanent magnetization lock-in modelling: Earth and Planetary Science Letters, v. 227, p. 345–359.

Sanborn-Barrie, M., and Young, M., 2013, Geology, Durban Harbour, Baffin Island, Nunavut: Geological Survey of Canada Canadian Geoscience Map, https://doi.org/10.4095/292015.

Sanborn-Barrie, M., Young, M., Keim, R., and Hamilton, B., 2013, Geology, Sunneshine Fiord, Baffin Island, Nunavut: Geological Survey of Canada Canadian Geoscience Map, https://doi.org/10.4095/288931.

Schmidt, A., Skeffington, R.A., Thordarson, T., Self, S., Forster, P.M., Rap, A., Ridgwell, A., Fowler, D., Wilson, M., and Mann, G.W., 2016, Selective environmental stress from sulphur emitted by continental flood basalt eruptions: Nature Geoscience, v. 9, p. 77–82, doi:10.1038/ngeo2588.

Schoene, B., Eddy, M.P., Samperton, K.M., Keller, C.B., Keller, G., Adatte, T., and Khadri, S.F., 2019, U-Pb constraints on pulsed eruption of the Deccan Traps across the end-Cretaceous mass extinction: Science, v. 363, p. 862–866.

Schoene, B., Samperton, K.M., Eddy, M.P., Keller, G., Adatte, T., Bowring, S.A., Khadri, S.F., and Gertsch, B., 2015, U-Pb geochronology of the Deccan Traps and relation to the end-Cretaceous mass extinction: Science, v. 347, p. 182–184.

Schulte, P. et al., 2010, The Chicxulub asteroid impact and mass extinction at the Cretaceous-Paleogene boundary: Science, v. 327, p. 1214–1218, doi:10.1126/science.1177265.

Sprain, C.J., Renne, P.R., Vanderkluysen, L., Pande, K., Self, S., and Mittal, T., 2019, The eruptive tempo of Deccan volcanism in relation to the Cretaceous-Paleogene boundary: Science, v. 363, p. 866–870.

Starkey, N.A., Stuart, F.M., Ellam, R.M., Fitton, J.G., Basu, S., and Larsen, L.M., 2009, Helium isotopes in early Iceland plume picrites: Constraints on the composition of high 3He/4He mantle: Earth and Planetary Science Letters, v. 277, p. 91–100.

Steinberger, B., Bredow, E., Lebedev, S., Schaeffer, A., and Torsvik, T.H., 2019, Widespread volcanism in the Greenland–North Atlantic region explained by the Iceland plume: Nature Geoscience, v. 12, p. 61–68.

Storey, M., Duncan, R.A., and Tegner, C., 2007, Timing and duration of volcanism in the North Atlantic Igneous Province: Implications for geodynamics and links to the Iceland hotspot: Chemical Geology, v. 241, p. 264–281.

Tauxe, L., Butler, R.F., Van der Voo, R., and Banerjee, S.K., 2010, Essentials of paleomagnetism: Univ of California Press, 512 p.

Tauxe, L., Shaar, R., Jonestrask, L., Swanson-Hysell, N., Minnett, R., Koppers, A., Constable, C., Jarboe, N., Gaastra, K., and Fairchild, L., 2016, PmagPy: Software package for paleomagnetic data analysis and a bridge to the Magnetics Information Consortium (MagIC) Database: Geochemistry, Geophysics, Geosystems, v. 17, p. 2450–2463, doi:10.1002/2016GC006307.

Tauxe, L., and Staudigel, H., 2004, Strength of the geomagnetic field in the Cretaceous Normal Superchron: New data from submarine basaltic glass of the Troodos Ophiolite: Geochemistry, Geophysics, Geosystems, v. 5, doi:10.1029/2003GC000635.

Thébault, E. et al., 2015, International geomagnetic reference field: The 12th generation: Earth, Planets, and Space, v. 67, p. 1–19.

Torsvik, T.H. et al., 2012, Phanerozoic polar wander, palaeogeography and dynamics: Earth-Science Reviews, v. 114, p. 325–368.

White, S.M., Crisp, J.A., and Spera, F.J., 2006, Long-term volumetric eruption rates and magma budgets: Geochemistry, Geophysics, Geosystems, v. 7.

Wigley, T., Ammann, C., Santer, B., and Raper, S.C., 2005, Effect of climate sensitivity on the response to volcanic forcing: Journal of Geophysical Research: Atmospheres, v. 110.

Wignall, P., 2005, The link between large igneous province eruptions and mass extinctions: Elements, v. 1, p. 293–297.

Wilkinson, C.M., Ganerød, M., Hendriks, B.W., and Eide, E.A., 2017, Compilation and appraisal of geochronological data from the North Atlantic Igneous Province (NAIP): Geological Society, London, Special Publications, v. 447, p. 69–103.

Willhite, L.N., Jackson, M.G., Blichert-Toft, J., Bindeman, I., Kurz, M.D., Halldórsson, S.A., Harðardóttir, S., Gazel, E., Price, A.A., and Byerly, B.L., 2019, Hot and heterogenous high-3He/4He components: New constraints from proto-Iceland plume lavas from Baffin Island: Geochemistry, Geophysics, Geosystems, v. 20, p. 5939–5967.

Wing, S.L., Harrington, G.J., Smith, F.A., Bloch, J.I., Boyer, D.M., and Freeman, K.H., 2005, Transient floral change and rapid global warming at the Paleocene-Eocene boundary: Science, v. 310, p. 993–996.

Yaxley, G.M., Kamenetsky, V.S., Kamenetsky, M., Norman, M.D., and Francis, D., 2004, Origins of compositional heterogeneity in olivine-hosted melt inclusions from the Baffin Island picrites: Contributions to Mineralogy and Petrology, v. 148, p. 426–442.

Chapter 5

Characterizing the Geomagnetic Field at High Southern Latitudes: Evidence from the Antarctic Peninsula

Coauthors: Joseph Biasi, Caltech; Joseph L. Kirschvink, Caltech

Abstract

We present new paleomagnetic and paleointensity data from the James Ross Island volcanic group, located on the Antarctic Peninsula. Global models of the geomagnetic field rely on high-quality paleomagnetic datasets from all latitudes, but there is a notable lack of data from the 60-70 ºS latitude bin. We collected 251 samples from 31 sites, spanning 0.99–6.8 Ma in age and include positive fold, conglomerate, and baked contact tests. Alternating-field and thermal demagnetization of these samples yields an average pole of -87.7º, 271.1º, α95=7º. When combined with preexisting data from an earlier study on James Ross Island and two studies from Deception Island, we present a revised paleomagnetic pole of -87.5º, 025º, α95=3.6º for the Antarctic Peninsula over the last ~5 Ma. In addition, the C2r/C2n transition may have been recorded at a site on JRI, and further geochronological and paleomagnetic study of these units will refine the age of this reversal. Finally, paleointensity data from three methods (Thellier-Thellier, pseudo-Thellier, and Tsunakawa-Shaw) were collected from all sites. The Thellier-Thellier method had low yields and produced unreliable data, likely due to sample alteration during heating. Results from the Tsunakawa-Shaw and pseudo-Thellier methods were more consistent, and we found average paleointensities of 35 and 65 μT at two sites.

1. Introduction

1.1 The Geomagnetic Field

Earth's magnetic field is often approximated as a geomagnetic axial dipole (GAD) (Merrill and McFadden, 2003). However, it is well known that the GAD hypothesis is not

entirely accurate, and that both short and long-term deviations from the expected GAD field are common (Johnson and McFadden, 2015). The GAD model is supported by an abundance of directional and intensity data from mid- to low-latitudes sites. Presently, there is a clear lack of data from high-latitude sites (Fig. 1). This lack of data represents a significant barrier to understanding the long-term structure of the geomagnetic field, especially over geologic timescales. Therefore, it is not clear if the GAD hypothesis is an accurate approximation of the field at high-latitude sites, even over the last 5 Ma. Other field models such as Model G (McElhinny and McFadden, 1997) and TK03 (Tauxe and Kent, 2004) have also been proposed, which expect a very different geomagnetic field structure at these latitudes.

Accurately determining the long-term structure and behavior of the geomagnetic field is important for several reasons. The geomagnetic field itself is driven by convection in the Earth's core, so the structure of the field is informative of the structure and convection regime of the core (Glatzmaier and Roberts, 1995). Furthermore, understanding the field at high latitudes will aid in interpretation of paleomagnetic data from high latitude sites. Prior to the Cenozoic, much of the Arctic was occupied by continental landmasses (Pease, 2011), and the Antarctic did not form large ice sheets until establishment of the Antarctic circumpolar current at ~33 Ma (Hill et al., 2013; Scher et al., 2015). Several low-latitude sites today were formed at high-latitudes in the distant geologic past, and paleomagnetic data and tectonic reconstructions using these sites necessitate an accurate field model at high latitudes.

1.2 Unknowns

Accumulating more high-latitude data is not an easy task. In the Arctic, most volcanism over the last 10 Ma has been due to seafloor spreading (Cottrell, 2015). This leaves Iceland and a few isolated islands as the only subaerial sites available for paleomagnetic study. In the Antarctic, volcanism is common in West Antarctica over the last 10 Ma (Smellie, 2021a). However, logistical challenges and ice cover has led to very few paleomagnetic studies (e.g. Lawrence et al., 2009; Oliva-Urcia et al., 2016). These problems are only compounded for older periods (>10 Ma), where the exposure of appropriately aged rocks is reduced.

In typical paleomagnetic studies, the directional components of the ancient field vector (e.g., declination (D) and inclination (I)) can be extracted more easily from old rocks than the paleointensity (*F*), because intensity needs to be normalized through intensive rock-magnetic calibration experiments. Despite this, few directional data exist from high latitudes (Fig. 1), which has hampered comparisons between the geomagnetic field at different latitudes.

It follows that there are even fewer reliable measurements of paleointensity at high latitudes. The present-day geomagnetic field has a Virtual Axial Dipole Moment of ~80 ZAm^2, with expected surface intensities of ~30 μT at the equator and ~60 μT at the poles (Cromwell et al., 2018). However, over the last 5 Ma the expected intensities often do not agree with the measured intensities (Cromwell et al., 2015a). Low- to mid-latitude sites give a variety of average intensities, but high-latitude sites show lower-than-expected intensities (Juarez et al., 1998; Tauxe et al., 2013). This model suggests that the long-term average GAD was roughly half the strength of the modern GAD, producing surface

intensities of ~16 μT at the equator and ~32 μT at the poles. However, very few high-latitude sites exist to constrain these field models. At present, most of these studies have focused on Iceland (Arctic) or McMurdo Sound (Antarctic).

Here we report new inclination, declination, and absolute intensity measurements from the James Ross Island volcanic group, on the Antarctic Peninsula (Fig. 2). These data were derived from 28 igneous sites, and range in age from 0.99-6.8 Ma (Table 1). This is only the 2nd dataset of its kind in Antarctica (Lawrence et al., 2009), and provides important constraints on the long-term behavior of the high-latitude geomagnetic field. Furthermore, we use the paleomagnetic data collected in this study to refine the volcanostratigraphy of the James Ross Island volcanic group.

2. Geologic Background

2.1 Tectonic Setting

This study focuses on the James Ross Island volcanic group (JRIVG), located in the northern Antarctic Peninsula (AP, Fig. 2). This area is tectonically complex, with the timing of some events (such as the opening of the Drake Passage) remaining hotly debated (Eagles et al., 2004; Hill et al., 2013; Scher et al., 2015). The AP was originally part of Gondwana until ~125 Ma, when the Falkland plateau began separating from southern Africa (Jokat et al., 2003). The AP remained adjacent to the South American plate until the Eocene, when the continents separated, forming the Scotia plate, Drake passage, and eventually the Antarctic circumpolar current (Dalziel et al., 2013). Subduction of (proto-)Pacific crust under the western side of the AP was ongoing from the Triassic to the

Neogene, which was responsible for voluminous arc magmatism on the peninsula (Pankhurst, 1982; Doubleday et al., 1994; Riley and Leat, 2021). Around ~4 Ma, subduction ceased entirely along the AP (Livermore 2000). Following cessation of subduction, small alkaline volcanoes appeared throughout the peninsula, including the James Ross Island Volcanic Group (Smellie, 1987; Hole, 1988; Hole et al., 1991; Hole and Larter, 1993; Smellie and Hole, 2021). Alkaline volcanoes on the west side of the AP appear to owe their origin to back-arc rifting and extension with some input from the subducting slab, though the origin of several volcanoes in this area is not well known (Haase and Beier, 2021; Smellie, 2021b). The JRIVG shows little slab input and is more similar to intraplate volcanism. Activity in this area is attributed to extension of thin continental lithosphere (Haase and Beier, 2021; Smellie, 2021b).

2.2 James Ross Island

James Ross Island (JRI) has been relatively well studied by Antarctic standards, due to the presence of nearby Argentinian, Czech, and Chilean bases as well as frequent visits by American and British scientists. The geology of the area has been the subject of numerous studies, most of which focused on igneous petrology (e.g. Sykes, 1988; Košler et al., 2009), geochronology (compilation of ages in Smellie, 2021b), glaciology (Carrivick et al., 2012; Engel et al., 2012), sedimentology/stratigraphy (Tobin et al., 2012; Milanese et al., 2020a; Tobin et al., 2020), and paleontology (Olivero, 2012; Roberts et al., 2014). The area consists of a thick Cretaceous-Paleogene sedimentary basin, capped by a large basaltic polygenetic shield volcano along with several smaller outlying volcanoes (Fig. 2, 3a) (Smellie et al., 2013). These units are variably covered by ice caps and glaciers, which

are rapidly retreating in most cases (Engel et al., 2012; Smellie et al., 2013). The nearest exposures of crystalline basement rocks are on the AP.

The volcanic rocks of the area comprise the JRIVG, and consist of hundreds of basalt flows, scoria cones, stocks, dikes, plugs, sills, and hyaloclastite foresets. Eruptive products were variably subaerial, subaqueous, and subglacially emplaced (Smellie, 2021b). Mt. Haddington, which makes up a large portion of James Ross Island, is also the largest volcano in Antarctica both in terms of basal diameter (60–80 km) and total volume (4500 km^3). For comparison, the more well-known Mt. Erebus volcano on Ross Island (near McMurdo station) is less than half the size, with a basal diameter of ~40 km and total volume of 2200 km^3 (Esser et al., 2004; Smellie, 2021b; Smellie and Martin, 2021). Volcanic activity in the JRIVG began at >12 Ma, based on the oldest dated material from the JRIVG (a K-Ar age; Marenssi et al., 2010). The volcanostratigraphy and age-relations between the most easily accessible units have been well established over the course of several studies (e.g. Smellie et al., 2008; Calabozo et al., 2015), though several stratigraphic uncertainties are still present for more inaccessible units.

2.3 Previous Paleomagnetic Studies

One previous paleomagnetic study was done on the JRIVG by Kristjánsson et al. (2005), focusing on use of paleomagnetic data for flow-correlation and volcanostratigraphy. They report alternating field (AF) demagnetization results from 15 sites (59 samples) with accompanying $^{40}Ar/^{39}Ar$ age data in the JRIVG with a mean *I* of -76º, *D* of 352º, and $\alpha 95$ of 7º. Their flows range from 3.95–5.91 Ma in age.

Elsewhere on the Antarctic Peninsula, a limited number of paleomagnetic studies have been done on units that are <10 Ma in age. Scharnberger et al. (1982) report NRM values from 2 sites in the South Shetland Islands. Blundell (1962) report AF demagnetization results from 5 sites in the South Shetland Islands. Valencio & Fourcade (1969) report paleomagnetic results from 5 sites in the South Shetland Islands. More recently, Baraldo et al. (2003) report AF and thermal demagnetization results from 21 sites on Deception Island, spanning the last ~150 ka. Finally, Oliva-Urcia et al. (2016) report thermal demagnetization results from 20 sites on Deception Island. Collectively, these results cover the last ~14 Ma, but are heavily biased towards data from Quaternary deposits on Deception Island.

Comparatively, the volcanic deposits of McMurdo Sound are far better studied. The combined efforts of several studies (e.g. Turnbull, 1959; Mankinen and Cox, 1988; Tauxe et al., 2004; Lawrence et al., 2009) have provided directional and intensity data on >100 lava flows over the last 10 Ma. A recent global compilation of high-quality paleomagnetic data has found that only some studies near McMurdo (Tauxe et al., 2004; Lawrence et al., 2009), and two studies at Deception Island (Baraldo et al., 2003; Oliva-Urcia et al., 2016) meet modern methodology and data quality standards (Cromwell et al., 2018). This leaves a dearth of reliable paleomagnetic data from the Antarctic, which are critical for construction of global geomagnetic field models in the recent and geologic past.

3. Methods

3.1 Fieldwork and Sample Collection

Our expedition's main goal on the February–March, 2016 cruise of the *Nathaniel B. Palmer* was to sample the Cretaceous sediments on and around JRI for magnetostratigraphy and tectonic constraints (Milanese et al., 2019a, 2019b, 2020a, 2020b; Tobin et al., 2020). All igneous samples were therefore taken as targets of opportunity. As a result, we sampled a wide variety of igneous products for this study and did not limit ourselves exclusively to basaltic lava flows. Cores were drilled using a Pomeroy gas-powered drill with water-cooling. Cores (2.54 cm diameter) were oriented using a Pomeroy orienting tool (Fig. 3b). Specimens were cut from each core, which were typically 0.5–1 cm in height. Sun compass measurements were taken whenever possible to calculate declination corrections. Sightings to distant features were taken when sun compass measurements were not available. No block samples were collected for this study. Most sites were accessed via helicopter (Fig. 3c), which was essential to reach the tops of most volcanic mesas in the area. Coastal sites were typically accessed via boats.

3.2 Rock Magnetics

Samples chosen to represent a wide variety of ages and volcanic products were subjected to a variety of rock magnetic tests and experiments, which are described in Kirschvink et al. (2008). This includes progressive AF demagnetization of the NRM up to 120 mT followed by progressive anhysteretic remanent magnetization (ARM) and isothermal remanent magnetization (IRM) acquisition experiments, modified Lowrie-

Fuller tests (Lowrie and Fuller, 1971; Johnson et al., 1975), and Fuller test of NRM (Fuller et al., 2002). All samples were analyzed using a 2G Enterprises vertical SQUID magnetometer and custom ARM/IRM/AF coil setup at the California Institute of Technology. The magnetometer is housed in a shielded room with a background field of ~150 nT.

Measurements of thermal-susceptibility curves were performed with an AGICO Multi-Function Kappabridge instrument. The samples were heated from room temperature at a rate of 9 ºC/minute, at an operating frequency of 976 Hz. Maximum temperatures reached were 700 ºC, and all experiments were run in an Argon atmosphere to minimize oxidation effects. Background 'noise' was removed via the subtraction of a blank sample (run under identical conditions) using AGICO's *Cureval* software. Hysteresis loops were measured at the Tokyo Institute of Technology on a Princeton Instruments MicroMag 3900 vibrating sample magnetometer at room temperature, in fields from -1 to 1 T.

3.3 Paleomagnetic Measurements

All samples were measured on a 2G Enterprises vertical SQUID magnetometer with RAPID automatic sample changer (Kirschvink et al., 2008). After initial NRM measurement, samples were subjected to two thermal cycling steps to 77K in liquid-nitrogen baths in a magnetically shielded vessel (<10 nT in a mu-metal can) for ~15 minutes to remove viscous components that are held in multi-domain magnetite (Muxworthy and McClelland, 2000). Samples were then demagnetized using a 20-step alternating field demagnetization protocol (1.6–90 mT). Sample analysis and best-fit determinations were done using the DemagGUI program as part of the PmagPy software

package (Tauxe et al., 2016). Maximum angle of deviation (MAD) and deviation angle (DANG) statistics are reported to assess goodness of fit (Kirschvink, 1980; Tauxe and Staudigel, 2004) (Table A1).

3.4 Paleointensity Experiments

3.4.1 Thellier-Thellier

In addition to standard demagnetization experiments, we also performed Thellier-Thellier (TT), Pseudo-Thellier (PST), and Tsunakawa-Shaw (TS) paleointensity experiments on subsets of our samples. For our TT experiments (Thellier and Thellier, 1959), we used the same methods and selection criteria of Lawrence et al. (2009), in order to directly compare the two Antarctic datasets (Table A2). After measuring NRMs, and as noted above, each sample was subjected to two liquid nitrogen baths in an attempt to reduce the effects of multidomain grains on later paleointensity experiments. Each Thellier-Thellier experiment then consisted of 11 in-field/zero-field or zero-field/in-field steps (the IZZI protocol; Yu et al. (2004)), at 0-600 ºC. In addition, four pTRM and four pTRM-tail checks were also performed to identify alteration of the samples. All heating steps were done in a magnetically shielded oven in a pure nitrogen atmosphere to minimize oxidation of the samples. In-field steps were done within a 40 μT bias field along the axis of the cores. Overall the Thellier-Thellier experiments yielded results of poor quality, which is discussed in more detail in section 4.4.1.

3.4.2 Pseudo-Thellier

Pseudo-Thellier experiments (Tauxe et al., 1995) were also performed. Unlike the TT technique, this technique involves no heating steps. Instead the NRM is progressively

AF demagnetized, followed by progressively imparting an ARM, and then AF demagnetizing the new ARM. Two new calibrations of the technique were used here, and we have delineated which samples pass the de Groot et al. (2013) and Paterson et al. (2016) selection criteria in Table A3. We used a 40 μT bias field when imparting ARMs. These samples were also subjected to two liquid nitrogen baths prior to AF demagnetization.

3.4.3 Tsunakawa-Shaw

Shaw experiments were performed using the methods and selection criteria of Yamamoto and Yamaoka (2018) (Table A4). This method involves two heating steps, six low-temperature demagnetization steps, and numerous AF demagnetization and ARM-imparting steps in-between. The technique is also known as *low-temperature demagnetization, double heating technique, Shaw* or LTD-DHT-Shaw. The AF demagnetization steps used here are the same as those used in the directional estimations. Laboratory TRMs were imparted by heating samples to 610 ºC for 10-20 minutes and cooling them in a uniform field of 30 μT. ARMs were imparted with a DC bias field of 50 μT in the same direction as the laboratory TRM. Low-temperature demagnetization steps, which are performed before the first AF demagnetization and after imparting the second ARM, were conducted in a similar manner as previously described.

4. Results

4.1 Sampling Overview

In total, 251 paleomagnetic cores were collected from 31 sites that spanned 0.99-6.8 Ma in age. A ‘site’ is defined as one cooling unit such as a lava flow, dike, or sill. Multiple sites in the same area are grouped into ‘locations,’ which are shown in Figure 2.

These samples were collected over the course of the six-week field season in February/March 2016. This is in addition to the >1000 cores taken from Cretaceous-Paleogene sediments in the JRI area in the same timeframe. As discussed earlier, igneous samples were targets of opportunity, and little effort was made to find the 'best' sites to sample. As a result, a wide variety of volcanic and intrusive products were sampled, which are discussed below. Unfortunately, we did not find volcanic glass at our sampling localities, which will become more relevant when discussing paleointensity results (see Section 5.4).

4.1.1 Location Descriptions

Samples from Cockburn Island (Fig. 2(2), 3a) were taken from the lowest flows of an uncorrelated lava-fed delta formation with an age of ~2.9 Ma (see Smellie (2021b) for a review of all JRI age data and associated references). Two flows were sampled at this location.

The Naze (Fig. 2(7), 3b) is a complex locality with multiple flows, sills, dikes, and volcanic necks. The surrounding sediments are extensively altered, suggesting that a large degree of heat transfer or hydrothermal circulation took place during igneous activity here. We sampled five units: three flows, one small sill (Fig. 3b), and one small dike. No samples from the northern portion of the Naze have been dated yet, but a nearby laccolith has a K-Ar age of 3.57 ± 0.34 Ma. It is not clear if this laccolith is cotemporal with other igneous activity on the Naze.

Keltie Head (Fig. 2(5),3c) is the youngest formation that we sampled (0.99 Ma), and we sampled at least two lava flows here. The flows have a distinct taupe color that is

dissimilar to the dark grey or dark brown color of all other lavas that we sampled. It is also clear that the original glassy flow tops are no longer present here, likely due to glaciation.

Taylor Bluff (Fig. 2(10), 4) is another complex locality with multiple igneous products. The bluff is made up of the Taylor Bluff formation, consisting of pillow-breccia foresets (heavily palagonized) which are extensively intruded by dikes of ~2(?) Ma in age (Fig. 4a). Overlying this are Neogene sediments, followed by the Forster Cliffs formation (Smellie et al., 2013). Atop the bluff is an eroded palagonite tuff cone (Fig. 4a). The relationship between the Forster Cliffs formation and the tuff cone is not certain (Fig. 4b, 4c), but based on results from this study, they are cotemporal at this locality (see Section 5.3). We sampled a dike intruding the Taylor Bluff formation (Fig. 4d), an unusual columnar intrusion in the Forster Cliffs formation (Fig. 4b), and the summit tuff cone (~2 Ma; Fig. 4c).

Smellie Peak (also known as Cerro Santa Marta; Fig. 2(9), 5) is the most complex of all the localities that we sampled and has been described in detail by Calabozo et al. (2015). We sampled two lava flows (Fig. 5a) and some pillow basalts (Fig. 5b) from the Smellie Peak formation (5.14 Ma), as well as an eroded scoria cone (Fig. 5b; 5.91 Ma). The two lava flows are probably tilted (Fig. 5a), so we have applied a tilt correction to these units which we measured in the field (160º strike, 18º dip). Some of the pillow basalts that we sampled were brecciated and yielded scattered paleomagnetic directions (see Section 4.3.2). We also sampled a large landslide block of the Lookalike Peaks formation (5.89 Ma) to act as a crude fold test (see Section 4.3.2).

Davies Dome (Fig. 2(3), 6) is a large ice cap sitting atop a volcanic mesa. We sampled four lava flows here, all from the Kipling Mesa formation (~5.36 Ma).

Humps Island (Fig. 2(4)) consists of K-Pg sediments capped by two small volcanoes. The western volcano is better preserved, while only the neck of the eastern volcano is still present (Fig. 7a). We sampled the eastern volcanic neck, which is of unknown age.

Lachman Mesa (Fig. 2(6), 7b) is a prominent lava-capped mesa on the Ulu peninsula. We sampled two flows here, both from the Johnson Mesa formation (5.04 Ma). There was no sun available for orienting, so we used sighting to five landmarks to calculate a declination correction.

Seymour Island (Fig. 2(8), 7c) is composed mostly of K-Pg sediments, but a few JRIVG dikes are also present. We sampled one of these dikes (~6.8 Ma) that formed a prominent ridgeline on the island. It appears that extensive hydrothermal alteration of both the wall rock and dike occurred during intrusion, likely due to the heat from the dike combined with abundant water trapped in the sediments.

Finally, we attempted a baked contact test at Leal Bluff, to the north of Cape Lamb (Fig. 2(1)), using palagonite breccias, a dike, and a connected pillow basalt (Fig. 8). To conduct the test, we collected nine cores from the palagonite (wall rock), five cores from the dike, and six cores from the pillow. The results of the test are discussed in section 4.3.2. These samples are all part of the Sandwich Bluff formation (5.42 Ma).

4.2 Rock Magnetism

Results from rock magnetic experiments are summarized in Figures 9-14. IRM acquisition curves (Fig. 9) show moderate-strongly interacting grains, which is in agreement with results from ARM acquisition curves (Fig. 10). There appears to be no

systematic variability in particle interaction based on rock type. IRM derivative curves (Fig. 9) suggest that CLC 4, CLD 6, NS1 6, TBA 25, and TBA 30 have a single magnetic phase. Two phases are likely to be present in HIA 22, KLH 14, and LCH 2.

Lowrie-Fuller tests (Lowrie and Fuller, 1971) show a mixture of results (Fig. 11), with some samples showing L-type behavior (ARM is more stable; Xu and Dunlop (1995)), some showing H-type behavior (IRM is more stable), and some showing mixed behavior with crossing ARM and IRM curves. L-type samples include CLC 4, CLD 6, and TBA 30. The only H-type sample is NS1 6, and mixed samples include HIA 22, KLH 14, LCH 2, TBA 25. The mixed samples in Figure 11 largely overlap with samples showing multiple phases in Figure 9. NRM is of greater or equal resistance to AF demagnetization as ARM and IRM, with the exception of HIA 22 which shows substantial NRM decay (Fig. 11c), likely due to alteration to maghemite or Fe-oxyhydroxides. L-type behavior can indicate either a small (single-domain) grain size or small dislocation density (Xu and Dunlop, 1995), while H-type behavior indicates the opposite. Once again there appears to be no systematic variation in Lowrie-Fuller results by rock type.

Fuller test results (Fuller et al., 1988) are shown in Figure 12. For thermal remanent magnetization, a ratio of NRM:IRM of ~100 or greater is expected. Larger ratios (1:1000 or more) is indicative of alteration of the sample (Fuller et al., 2002). Five samples (KLH 14, LCH 2, NS1 6, TBA 25, and TBA 30) show relatively little evidence for alteration in these plots. Three samples (CLC 4, CLD 6, and HIA 22) show evidence for alteration, which is in agreement with field observations of the sampling sites.

Hysteresis loops are shown in Figure 13. Three samples (CLC 4, SEA 3, and TBA 30) show evidence for a strong paramagnetic component (Tauxe et al., 1996). Sample CLC

4 is a palagonite breccia, which by its very nature is an altered material (Nayudu, 1964), so we attribute the paramagnetism in this sample to alteration of magnetite to lepidocrocite or similar hydrous iron-oxides (Guyodo et al., 2016). Sample SEA 3 also showed evidence for alteration in the field (see Section 4.1.1), so we again attribute this to alteration. Finally, sample TBA 30 is from a palagonite tuff cone on Taylor Bluff. This cone appears to have been near the surface since its eruption and may have erupted into thin ice or a similarly wet environment, so we again attribute this to alteration. The remaining samples show somewhat similar hysteresis loops that are consistent with a mixture of single domain, pseudo-single domain, and paramagnetic material (Tauxe et al., 1996).

Finally, thermal-susceptibility curves (Fig. 14) show that several samples have Fe-oxyhydroxide components, as evidenced by dissimilar heating and cooling curves (Gehring and Hofmeister, 1994; Özdemir and Dunlop, 1996; Minyuk et al., 2011). Samples CLC 4, HIA 22, NS1 6, and TBA 30 show evidence for dehydration of Fe-oxyhydroxides (e.g. goethite) upon heating, which are irreversibly altered to form (titano)magnetite, which is stable upon cooling (Minyuk et al., 2011). It is important to note that all samples clearly retain a portion of their original magnetite, as evidenced by drops in susceptibility around 580 ºC. The remaining samples show fairly similar heating and cooling curves, though the absolute value of the susceptibility is typically higher after heating due to annealing of grains (Bowles et al., 2013).

Overall, the rock magnetic data presented here show notable differences between samples from lava flows and all other volcanic products. Lava flow samples are generally less susceptible to alteration and show less evidence for paramagnetic material. Beyond

these differences, all samples appear to have a mixture of single domain and pseudo-single domain (titano)magnetite.

4.3 Paleomagnetic Directions

4.3.1 Demagnetization Results

Results from AF demagnetization are summarized in Figures 15, 16, 17, and Tables 2 and A1. In most cases, the samples were flipped every four AF steps to allow for running samples overnight on the RAPID system (in addition to the 252 cores of this study, we also needed to run >1000 sedimentary cores from JRI). This occasionally creates a zig-zag pattern in the orthogonal projections that can create artificially high MAD and DANG values (Fig. 16a). If we had flipped each sample during every step, this zig-zag would not be present. This is evident when looking at thermal demagnetization data from the TT experiments (Fig. 16b). Therefore, whenever AF demagnetization produces a best-fit line with >15 MAD, we have substituted the data with thermal demagnetization data from TT experiments if such a sample is available (Table A1). The differences in direction between the two techniques are negligible (Fig. 16c).

As a result, when determining virtual geomagnetic pole (VGP) positions, we do not include any samples with MAD>15. At the site level, every site has at least two samples, and generally show high-quality results. The median precision parameter (k) is 170, and is >50 for 22/25 sites (Table 2). The median $\alpha 95$ value is 4.2. The main sources of high $\alpha 95$ values in our dataset are either too few samples (Naze dike), eruption during a clearly transitional period (Cockburn Is. Flow 1, Taylor Bluff columns), or hydrothermal alteration

(Humps Island). Five sites were excluded from paleomagnetic pole calculations because they are questionably in-place. This includes the Smellie Peak landslide block (used for a fold test), and the pillow and dike sites on Cape Lamb (see Section 4.3.2).

Overprints are uncommon in our dataset, with only 37/245 samples (15%) showing an overprint direction (Table A1). There appears to be no systematic variation (or lack of variation) in the overprint directions, and therefore little information can be gleaned from such data. Overall, despite sampling a wide variety of volcanic units, most samples were good carriers of a stable remanent magnetization.

4.3.2 Stability Tests

The JRIVG is very young by geologic standards, and as a result has not been tectonically rotated or regionally tilted, has not experienced regional metamorphism, and has not been folded. Therefore, stability tests are probably not needed, and difficult to conduct. We attempted a baked contact test, fold test, and conglomerate test anyway to check for secondary magnetizations.

Using a landslide block, a very crude fold-test (Graham, 1949) was performed near Smellie Peak. The block was roughly 200m in thickness and ~1 km in length, and probably was dislodged during a Holocene glaciation (Smellie et al., 2008). The block is most likely from the Lookalike Peaks formation (Smellie et al., 2013), and yielded an average paleomagnetic direction of 55.8 declination, 39.3 inclination (Fig. 17i), corresponding to a VGP of -6.4º, 352.5º. This direction differs significantly from any expected direction during a normal or reversed polarity period. Unfortunately we were not able to sample an in-place section of the Lookalike peaks formation, so we cannot with 100% confidence

state that the fold-test has been passed. However it seems very unlikely that data of such consistency and quality (k = 2032, $\alpha 95$ = 0.9) would be produced during a transitional period. The Lookalike Peaks formation erupted within the C3An (Gilbert) chron, and the determined age is not within error of a polarity transition (Smellie et al., 2008; Gradstein et al., 2012). Furthermore, paleomagnetic data from the Lookalike Peaks Fm. was collected by Kristjánsson et al. (2005), who found typical reversed directions (Table A5). Therefore we tentatively assume that the fold-test was successfully passed.

Using brecciated pillow basalts, a conglomerate test (Graham, 1949) was also performed at Smellie Peak. Samples SML 16, 17, 18, 19, and 27 were taken from brecciated pillows, while samples SML 20-26 were taken from in-place pillows in the same unit. The brecciated pillows show clearly distinct directions from the in-place pillows (Fig. 17i, Table 2), indicating that the conglomerate test has most likely passed.

Finally, we attempted a baked contact test (Graham, 1949) on a unique exposure of palagonite breccias, a dike, and a pillow basalt on Cape Lamb (Fig. 8). The palagonite was a hyaloclastite breccia prior to low-temperature alteration (Drief and Schiffman, 2004). A dike can be seen directly feeding a pillow basalt at this exposure, but the dike is not very large, and we could not follow it beyond a few meters. Paleomagnetic data from all three units (Fig. 17b) are rather unusual. The majority of the data show a normal/transitional polarity, while four samples from the dike and pillow show a reversed/transitional polarity. Most likely thermal overprinting of the dike and pillow by the hyaloclastite is responsible, as field photos indicate that all cores were marked correctly so the anomalous directions are unlikely to be a result of orientation errors. These hyaloclastite breccias can be emplaced at high temperature (Yamagishi and Dimroth, 1985; Porreca et al., 2014), and

our consistent directions from the contact zone suggest that this is the case. The observed resetting would imply that the dike did not intrude the palagonite, and instead the palagonite incorporated the dike and pillow as a large clast during formation of the palagonite breccias. This is entirely possible from a volcanological perspective (Nayudu, 1964; Yamagishi and Dimroth, 1985), and the dike and pillow could have been produced in the same eruptive event as the hyaloclastite. Overall, we conclude that the baked contact test is passed here, though not in the manner we originally anticipated.

4.3.3 Pole Positions

VGPs from 25 sites are shown in Figure 18a, with normal polarity poles inverted to the southern hemisphere for easier plotting. To determine which poles are transitional (and therefore excluded from further calculations), we used the iterative cutoff calculation of Vandamme (1994). We found the Vandamme cutoff angle to be 32.9º (Table 3) – Poles above 57.1 or -57.1º latitude are therefore assumed to be normal or reversed, respectively. These are then averaged (I=-76.9, D=002.9, $\alpha 95$=3.9) to create a paleomagnetic pole at -87.7º, 271.1º ($\alpha 95$ = 7.0º), which overlaps with the modern geographic north pole. This suggests that no significant tectonic movement of the AP has occurred over the last ~7 Ma, and/or that our dataset is large enough to average out secular variation.

4.4 Paleointensity

Paleointensity results are summarized in Figs. 19-21 and Tables 4, A6-A8. It is important to note that most (if not all) of our samples are not ideal paleointensity recorders. As mentioned above, we collected ‘target of opportunity’ samples. While these samples

are mostly suitable for directional data, they are likely poor recorders of paleointensity. For example, no volcanic glass (the ideal paleointensity carrier in this case; Cromwell et al. (2015b)) was collected, for the simple reason that we did not find any in the localities that we could reach by helicopter and/or zodiac. Despite the non-ideal nature of our sample set, we felt it worthwhile to conduct the paleointensity experiments because of the distinct absence of such data from this latitude. Furthermore, we plan to use these data to guide paleointensity sampling during another expedition to the JRIVG.

4.4.1 Thellier-Thellier

Success rates from Thellier-Thellier experiments were very low (Table A4), and only 9/102 samples met the selection criteria of Lawrence et al. (2009) (Table A2), which are already lower than modern selection criteria standards (Cromwell et al., 2015b). Our low success rates are likely due to the presence of multidomain grains (indicated by two-component Arai plots) and Fe-oxyhydroxides. These minerals consistently de-watered during early stages of the experiments, which altered the 'pTRM gained' significantly and caused the pTRM checks to fail in many samples. The TT results are reported in Table A6 and Figure 19 and show inconsistent results even within individual sites. Therefore, the results from this technique should not be trusted or incorporated into any regional or global data compilations. Recently, a statistical method has been developed to correct for multidomain behavior in Thellier-Thellier experiments (Cych et al., 2021). However, given the ubiquitous alteration that we observed in our samples during the experiments, such a method is not appropriate to apply to this dataset.

4.4.2 Pseudo-Thellier

Pseudo-Thellier experiments had the highest success rates (Figure 20, Table A7), likely because no heating steps are involved. Two sets of selection criteria were implemented here (Table A3). Of the two-hundred samples that were measured, 60 passed the selection criteria of de Groot et al. (2013) and 17 passed the more stringent selection criteria of Paterson et al. (2016). Only five samples passed both sets of selection criteria. In this case, we attribute most of our failed samples to multidomain and pseudo-single domain grain size, as dehydration of hydrous iron-oxides is not a factor in this technique.

These results are of uncertain reliability. Some sites show good internal consistency (Taylor Bluff tuff cone, Smellie Peak pillows) while other sites vary widely in their intensity estimations (Lachman Mesa flows). At best, the relative intensities between some sites can be inferred from the PST data. For example, the Taylor Bluff columns show consistently low intensity values (~5.5 μT) while Flow 1 at Keltie Head was probably erupted during a higher-intensity period (~66 μT). Several samples were successfully duplicated, meaning that multiple specimens from the same core passed the selection criteria. These duplications are all in good agreement with each other, suggesting that errors associated with this technique are systematic, and do not significantly vary from analysis to analysis.

4.4.3 Tsunakawa-Shaw

Success rates from the Shaw method were between the TT and PST success rates (Table A8), likely because the samples are only heated twice during this process. Of the 191 samples analyzed, 38 passed the selection criteria of Yamamoto and Yamaoka (2018) (Figure 21, Table A4). Within-site consistency is better than the TT results, but worse than

the PST results. Similar to the TT technique, we attribute failed samples to large grain size and alteration during heating. The Shaw intensities are generally higher than the TT intensities but are in surprisingly good agreement with the PST intensities. More detailed discussion of these results is in Section 5.4.

5. Discussion

5.1 Combining JRI Datasets

Paleomagnetic results from this study can be combined with the 15 sites from Kristjánsson et al. (2005) (Table A5) to create a combined paleomagnetic pole for the JRIVG. VGPs from both studies are shown in Figure 18b. The resultant paleomagnetic pole (-88.1º, 268.3º, $\alpha 95$ = 5.8º) appears to average-out secular variation and includes the geographic south pole in its envelope of uncertainty. Furthermore, several locations were sampled by both studies, and show good agreement in measured paleomagnetic directions (Tables 2 and A5). Some minor variations between the two studies are likely due to sampling of different units at the same location, which will differ slightly in age. This pole also makes use of the Vandamme (1994) iterative cutoff technique to determine which poles are transitional (Table 3).

5.2 Incorporation into the PSV10 Field Model

Given the young age of the JRIVG, paleomagnetic data from these units is most useful for incorporation into long-term models of the geomagnetic field, as there is little use of these data for tectonic reconstructions. As discussed in Section 2.3, multiple paleomagnetic studies have been done on the AP, spanning the last ~14 Ma. However, a

recent review of global paleomagnetic data by Cromwell et al. (2018) found that only two studies from Deception Island (Baraldo et al., 2003; Oliva-Urcia et al., 2016) met modern standards of data quality. They seem to have missed the JRI study by Kristjánsson et al. (2005), which also meets all of their criteria, but has not been uploaded into the MagIC database yet (https://www2.earthref.org/MagIC).

After combining site-level data from all four studies, the resultant paleomagnetic pole (-87.5°, 025.0°, $\alpha 95$ = 3.6°) is shown in Figure 18c. Again, the iterative cutoff of Vandamme (1994) was used here. Though the pole has a lower $\alpha 95$ uncertainty, it is also slightly farther from the geographic south pole (compared to Fig. 18b). This is caused by the Deception Island studies, which likely did not average-out secular variation. All of their sites are ~150 ka or younger, and most may be younger than ~15 ka (Baraldo et al., 2003; Oliva-Urcia et al., 2016; Smellie, 2021b). Based on their VGPs, the geomagnetic pole was over East Antarctica for much of this time.

After calculating paleomagnetic poles, we can also calculate the associated inclination anomaly (ΔI) and VGP dispersal (S_F). The expected ΔI and S_F will differ depending on which field model is used. Figure 22 shows our data (incorporated into the PSV10 global dataset) and new values for ΔI and S_F in the 60-70º S latitude bin. Overall the new data are consistent with the TK03 field model, though the GAD model is not ruled out entirely. Notably, this latitude bin has very low VGP dispersion, but the reasons for this are not clear. Collectively, the AP data provide a long-term average of the geomagnetic field in this area, so insufficient time for VGP dispersal is not to blame. The S_F from only the JRI studies (Table 3) is not much higher than the S_F when including the Deception Island studies.

5.3 JRIVG Stratigraphy

Most of the volcanostratigraphy of the JRIVG has been established via previous volcanological and geochronological studies (see reviews by Haase and Beier, 2021; Smellie, 2021b). Therefore, this study only presents a few refinements to that stratigraphy. The two uppermost igneous units at Taylor Bluff are the Forster Cliffs formation (2.5 Ma) and a tuff cone (~2 Ma; Fig. 4a, Table 1). However, the paleomagnetic directions from these units (Fig. 17j) are very similar. We suggest that both units were erupted at ~2 Ma at this locality, which may require the creation of a new stratigraphic unit or incorporation of the columnar body that we sampled into the tuff cone unit. The 2.5 Ma age for the Forster Cliffs formation is from a different exposure to the east of Taylor Bluff (Smellie et al., 2013).

Two sites on Stickle Ridge were sampled by Kristjánsson et al. (2005) who found a reversed polarity and an age of 6.16 ± 0.08 Ma (assigned to the Lookalike Peaks formation). While this polarity and age are consistent with the geomagnetic timescale of Cande and Kent (1995), it is not consistent with the more-recent GTS12 timescale (Gradstein et al., 2012) (Fig. 23). The relative accuracy of the Cande and Kent timescale versus the GTS12 timescale could fill an entire paper by itself. However, the GTS12 timescale incorporates more recent data from more sources, and therefore will be used here (Gradstein et al., 2012). Regarding the Kristjánsson data from this period, it is not clear if a geomagnetic excursion was captured, or if the geomagnetic timescales are not correct. The age determination is most likely accurate, because the paleomagnetic sites and the geochronology sampling site are at the same location.

In addition, all of the sites from Davies Dome yielded normal polarities in this study (Table 2). This conflicts with the determined age of the Kipling Mesa formation (5.36 ± 0.05 Ma), which is within the C3r chron, and not within error of a normal polarity period (Gradstein et al., 2012). In this case, both polarity timescales agree that this is a reversed polarity period (Fig. 23). In this case, the disparity may be due to an incorrect age for the Kipling Mesa formation at this location. The 5.36 Ma age for this formation was determined at a different mesa to the southwest (Smellie et al., 2013), so it is possible that the flows here predate the assigned age for this unit.

5.4 Paleointensity Determinations

Given the low success rates and non-ideal nature of our samples, we need to determine if any of our samples are accurate recorders of paleointensity. Sources of error in paleointensity experiments are numerous, often difficult to constrain, and vary depending on the technique that is used. We employed two methods that use heating steps (Thellier-Thellier and Tsunakawa-Shaw), and one method that involves no heating (pseudo-Thellier). Therefore, if similar paleointensities are determined between TT and PST, or TS and PST, then we can conclude that most of the error in the paleointensity determination is due to the sample itself and not due to the method that is employed. This in turn would increase our confidence in the measured paleointensities.

Figure 24 shows the measured paleointensities for samples that passed selection criteria from the PST method and at least one other technique. Samples from Keltie Head and Lachman Mesa show good agreement between the PST and TS methods, suggesting that these results are the most reliable in our study. Since these are only 2/28 sites, it is

difficult to make any definitive conclusions about the strength of the geomagnetic field over the AP during this time period. The Lachman Mesa flow 1 sites yields an average intensity of ~35 μT, which is expected under the long-term field model of Juarez et al. (1998) and Tauxe et al. (2013). The Keltie Head flow 1 site yields an average intensity of ~65 μT, which is more typical of the modern field.

For the remaining samples, they are probably best used as recorders of relative paleointensity between each site, and not for absolute paleointensity determinations. Detailed interpretation of these data, or incorporation into global paleomagnetic models is not advised at this time.

We recommend that future expeditions target the subaerial lava flows which are abundant in the JRIVG, but more difficult to access due to their exposures in steep cliff walls. As we note above, the ideal paleointensity recorder, volcanic glass (Cromwell et al., 2015b), was never found in the places we were able to visit, and hence not sampled. Repeated glacial advances and retreats appear to have removed most flow tops where glass is normally located in subaerial flows. Despite these issues, it is entirely possible that future expeditions to the JRIVG will find volcanic glass, and better recovery of paleointensity data may result from such an expedition. We are therefore not surprised that few of our samples are ideal recorders of paleointensity, and the paleointensity results should be interpreted with caution. We performed these experiments because samples of the JRIVG are difficult to obtain, no other paleointensity data exists from this area, and the use of the RAPID system makes this relatively easy to implement. An abundance of devitrified, altered volcanic glass can be found in the hyaloclastite breccias. Furthermore, the

hyaloclastite breccias have a complex thermal history (see Section 4.3.2), so paleointensity data from them will be of uncertain reliability.

5.5 Timing of Reversal

Our paleomagnetic directional results may have captured a geomagnetic reversal or excursion in this study, allowing for an accurate age determination of this event. Samples from the Taylor Bluff columnar body and tuff cone have transitional directions (Fig. 17j), and their determined age (2.03 ± 0.13 Ma) overlaps with the C2r/C2n transition period (Fig. 23). In addition, the measured paleointensities are among the lowest in the JRIVG (Table 4). As discussed earlier, the paleointensities should be interpreted with caution, but they are consistently low (Tables A7, A8) and support a transitional field in this case. Additional geochronological and paleomagnetic study of these units may help to place better temporal constraints on the C2r/C2n transition.

6. Conclusions

We present new paleomagnetic data from several sites in the James Ross Island volcanic group. These data give a good long-term average of the geomagnetic field over the AP, especially when combined with a previous study of the JRIVG. Incorporation into the PSV10 field model (Cromwell et al., 2018) shows that anomalously low VGP dispersion seems to be a robust result and not an effect of sampling bias. We also found that minor revisions to the stratigraphy at Taylor Bluff are probably necessary, and there are disparities between the measured polarities and measured ages at two localities (Stickle Ridge and Davies Dome). This study most likely found the C2r/C2n transition at Taylor

Bluff, and the age of these units (2.03 ± 0.13 Ma) could be refined with further sampling and geochronological analysis to produce a well-constrained age of this event. Finally, results from paleointensity analysis are generally of low-quality and not recommended for incorporation into global field models at this time. Two sites – Keltie Head Flow 1 and Lachman Mesa Flow 1 – may have produced reliable paleointensity estimates of 65 μT and 35 μT, respectively.

More data are still needed to understand high-latitude geomagnetic field. In the long-term, we are limited by the few volcanic centers at high latitudes. In the short-term, gathering of further data is only limited by logistical concerns and general inaccessibility. We likely sampled ~10% of the exposed units in the JRIVG. A future expedition, that specifically targets the JRIVG for paleomagnetic and paleointensity sampling, is warranted, but would require extensive helicopter support. Reliable absolute paleointensity data still do not exist for this area, and any future study should make this a high priority. Specifically targeting the subaerial lava flows for directional data and targeting volcanic glass for paleointensity information will be the most successful approach.

Supplementary Materials

Supplemental Tables S1-S8, which contain least-squares fits, paleointensity selection criteria, paleointensity results, and VGPs from previous studies, are available with the online version of this thesis.

Acknowledgements

The author would like to thank his fellow team members: Jennifer Buz, David Flannery, Roger Fu, Joe Kirschvink, Ross Mitchell, Joe O'Rourke, Steve Skinner, Sarah Slotznick, David Smith, Frank Sousa, and Tom Tobin for their patience and assistance with sample collection. I also want to thank the crew of the Nathaniel B. Palmer and Air Center Helicopters for their logistical support. Joe Kirschvink is greatly thanked for use of his lab, running hysteresis loops, and advising on this project. This work was funded by NSF Polar Programs grant ANT-1341729 to J. L. Kirschvink.

Table 1: Sampling Locations

# on Map	Locality	Site	Latitude	Longitude	Rock Type	Unit	Age (Ma)	Notes
1	Cape Lamb	Palagonite	-63.8924	302.4051	Palagonite Breccia	Sandwich Bluff Fm.	5.42 ± 0.08	Part of a baked contact test, may not be in-place.
		Dike	-63.8924	302.4051	Basalt	Sandwich Bluff Fm.	5.42 ± 0.08	
		Pillow	-63.8924	302.4051	Basalt	Sandwich Bluff Fm.	5.42 ± 0.08	
2	Cockburn Island	Flow 1	-64.1907	303.1657	Basalt	Uncorrelated	2.9 ± 0.4	
		Flow 2	-64.1907	303.1657	Basalt	Uncorrelated	2.9 ± 0.4	
3	Davies Dome	Flow 1	-63.8840	301.9172	Basalt	Kipling Mesa Fm.	5.36 ± 0.05	Polarity and age do not agree
		Flow 2	-63.8842	301.9178	Basalt	Kipling Mesa Fm.	5.36 ± 0.05	
		Flow 3	-63.8893	301.9243	Basalt	Kipling Mesa Fm.	5.36 ± 0.05	
		Flow 4	-63.8893	301.9243	Basalt	Kipling Mesa Fm.	5.36 ± 0.05	
4	Humps Is.	Volcanic Neck	-63.9860	302.5869	Diabase	Palisade Nunatak Fm.	--	Age unknown
5	Keltie Head	Flow 1	-63.8066	302.3662	Basalt	Keltie Head Fm.	0.99 ± 0.05	
		Flow 2	-63.8070	302.3661	Basalt	Keltie Head Fm.	0.99 ± 0.05	
6	Lachman Mesa	Flow 1	-63.8468	302.1662	Basalt	Johnson Mesa Fm.	5.04 ± 0.04	
		Flow 2	-63.8484	302.1679	Basalt	Johnson Mesa Fm.	5.04 ± 0.04	
7	The Naze	Flow 1	-63.9139	302.5267	Basalt	Uncorrelated	--	Age unknown
		Flow 2	-63.9139	302.5267	Basalt	Uncorrelated	--	Age unknown
		Flow 3	-63.9162	302.5256	Basalt	Uncorrelated	--	Age unknown
		Sill	-63.9151	302.5287	Diabase	Uncorrelated	--	Age unknown
		Dike	-63.9158	302.5272	Diabase	Uncorrelated	--	Age unknown
8	Seymour Is.	Dike	-64.2907	303.2600	Diabase	Palisade Nunatak Fm.	6.8 ± 0.5	
9	Smellie Peak	Landslide Block	-63.9264	302.0972	Basalt	Lookalike Peaks Fm.	5.89 ± 0.09	Not in-place, used as a fold test. Age uncertain.
		Flow 1	-63.9303	302.0847	Basalt	Smellie Peak F.	5.14 ± 0.38	Tilted 160/18
		Flow 2	-63.9304	302.0847	Basalt	Smellie Peak F.	5.14 ± 0.38	Tilted 160/18
		Pillows	-63.9306	302.0823	Basalt	Smellie Peak F.	5.14 ± 0.38	Some samples were from brecciated pillows.
		Scoria Cone	-63.9303	302.0821	Basaltic Lapilli	Scoria Cone	5.91 ± 0.08	
10	Taylor Bluff	Dike	-63.9955	302.3382	Diabase	Taylor Bluff Fm.	1.94 ± 0.47	Intrudes Taylor Bluff Fm.
		Columns	-63.9950	302.3309	Basalt	Forster Cliffs Fm.	2.5 ± 0.07	Possibly 2.03 ± 0.13 Ma
		Tuff Cone	-63.9950	302.3309	Basaltic Lapilli	Tuff Cone	2.03 ± 0.13	

See Smellie (2021b) for a compilation of ages from the JRIVG and associated references.

Table 2: Site-mean Virtual Geomagnetic Poles (VGPs)

Location	Site	n/N	D	I	a95	K	R	VGP Lat	VGP Lon	VGP dm	VGP dp	Polarity*
Cape Lamb	Palagonite	9/9	87.3	-53.8	7.3	51	8.8	-31.6	226.9	10.2	7.1	T
Cockburn Island	Flow 1	3/3	345.4	42.5	38.8	11	2.8	-0.5	109.9	47.8	29.5	T
Cockburn Island	Flow 2	10/11	15.9	-61.7	5.1	89	9.9	-66.8	153.8	7.9	6.1	N
Davies Dome	Flow 1	11/11	12.6	-76.7	2.1	473	11.0	-84.5	225.9	3.9	3.6	N
Davies Dome	Flow 2	13/13	358.6	-79.3	2.8	227	13.0	-84.6	307.2	5.3	5.1	N
Davies Dome	Flow 3	3/3	316	-86.2	4.1	903	3.0	-68.7	316.5	8.1	8.1	N
Davies Dome	Flow 4	6/6	306.6	-82.9	2.1	973	6.0	-69.2	335.0	4.1	4.0	N
Humps Island	Plug	9/9	333.4	-67.6	26.5	5	7.3	-70.5	63.9	44.2	36.9	N
Keltie Head	Flow 1	9/9	355.8	-73.3	2.2	562	9.0	-84.8	97.7	3.9	3.5	N
Keltie Head	Flow 2	8/8	7.5	-70.5	4.1	184	8.0	-80.1	148.5	7.1	6.1	N
Lachman Mesa	Flow 1	12/12	25.7	-73.1	5.2	71	11.9	-76.7	201.0	9.3	8.3	N
Lachman Mesa	Flow 2	8/8	17.4	-75.9	3.6	236	8.0	-82.3	215.8	6.1	-6.6	N
The Naze	Flow 1	9/9	163.8	75.9	3.8	184	9.0	-82.8	29.8	6.5	7.0	R
The Naze	Flow 2	9/9	159.7	77.5	2.6	407	9.0	-81.2	9.2	4.6	4.9	R
The Naze	Flow 3	7/8	184.6	75.3	4.2	203	7.0	-87.4	177.3	7.0	7.7	R
The Naze	Sill	7/8	123.1	86.3	4.6	170	7.0	-67.1	318.6	9.1	9.1	R
The Naze	Dike	2/2	272.4	85.4	24.2	109	2.0	-62.1	282.7	47.9	47.5	R
Seymour Island	Dike	8/9	176.2	71.7	6.6	72	7.9	-82.0	108.0	10.2	11.6	R
Smellie Peak	Flow 1**	9/9	3.3	78.1	5.7	83	8.9	-41.1	303.8	10.1	10.7	T
Smellie Peak	Flow 2**	6/6	322.8	82.3	3.4	382	6.0	-50.8	287.6	6.5	6.6	T
Smellie Peak	Pillows	7/7	256.4	77.3	8.4	53	6.9	-59.5	250.3	14.7	15.7	R
Smellie Peak	Scoria Cone	10/10	171.3	65.9	8.6	33	9.7	-73.6	101.2	14.0	11.5	R
Taylor Bluff	Dike	12/12	198.2	71.1	2.1	422	12.0	-77.7	178.0	3.7	3.2	R
Taylor Bluff	Columns	13/13	351.1	-10.8	18.4	6	11.0	-31.1	112.0	18.6	9.4	T
Taylor Bluff	Tuff Cone	16/17	335	15.5	4	87	15.8	-15.7	96.6	4.1	2.1	T
Not in-place												
Cape Lamb	Dike (R)	3/3	83.9	-35.4	28	20	2.9	-20.2	215.9	32.4	18.7	--
Cape Lamb	Dike (N)	2/2	261.2	47.3	38.4	44	2.0	-29.1	218.2	49.8	32.3	--
Cape Lamb	Pillow (N)	2/2	275.2	38.5	80.3	12	1.9	-17.1	226.8	95.3	56.6	--
Cape Lamb	Pillow (R)	4/4	70.3	-51.1	13.8	45	3.9	-36.8	210.6	18.7	12.6	--
Smellie Peak	Pillow Breccia	4/4	319.8	22.9	69.1	3	2.9	8.2	262.4	39.0	73.4	--
Smellie Peak	Landslide Block	14/15	55.8	39.3	0.9	2032	14.0	-6.4	352.5	1.1	0.6	--

n = number of samples used; N = number of samples measured; D = declination; I = inclination; a95 = 95% confidence interval; K = precision parameter; R = vector sum; dm/dp = 95% confidence interval (elliptical); N/R/T = normal, reversed, transitional

**Transitional poles determined by Vandamme (1994) cutoff angle.*

**Tilt-corrected (160/18)

Table 3: Mean Paleomagnetic Pole Positions

Pole Name	Latitude	Longitude	N	A95	R	K	A	S_F	ΔI	Notes
This Study	-87.7	271.1	19	7	18.3	24.1	34.7	15.85 ± 3.8/4.1	0.80 ± 3.6/2.8	Excludes transitional poles
All JRI	-88.1	268.3	32	5.8	30.5	20.1	37.5	17.687 ± 3.4/3.4	-0.45 ± 3.0/2.6	This study + Kristjánsson et al. (2005)
Antarctic Peninsula	-87.1	029.0	68	3.4	65.4	26	33.6	15.68 ± 1.9/1.9	0.46 ± 2.3/1.6	This study + Kristjánsson et al. (2005) + Olivia-Urcia et al. (2016) + Baraldo et al. (2003)
PSV10	-87.5	025.0	58	3.6	55.9	27.7	32.7	15.38 ± 1.8/2.0	0.49 ± 2.1/1.8	All AP sites that pass PSV10 data criteria

N = number of samples measured; a95 = 95% confidence interval; K = precision parameter; R = vector sum; A = Vandamme (1994) cutoff angle, S_F = VGP dispersion (with 95% bootstrap confidence intervals), ΔI = Inclination anomaly (with 95% bootstrap confidence intervals).

Table 4: Summary of Successful Paleointensity Results

Location	Site	n	Method	Intensity (μT)	St. Dev.
Davies Dome	Flow 1	2	TT	25.0	6.1
	Flow 2	3	TT, Shaw	42.5	6.0
	Flow 3	3	Shaw	67.5	15.4
	Flow 4	5	Shaw, PST	85.2	12.6
Humps Island	Neck	4	PST	10.4	18.5
Keltie Head	Flow 1	11	TT, Shaw, PST	65.0	6.5
	Flow 2	4	Shaw	76.8	7.7
Lachman Mesa	Flow 1	23	TT, Shaw, PST	37.1	13.0
	Flow 2	12	TT, Shaw, PST	44.1	19.1
The Naze	Flow 2	2	TT	19.4	4.4
	Flow 3	1	PST	12.4	--
Seymour Island	Dike	3	PST	7.9	1.6
Smellie Peak	Landslide Block	1	PST	41.6	--
	Flow 1	1	PST	14.0	--
	Flow 2	1	PST	10.6	--
	Pillows	11	Shaw, PST	7.9	5.4
	Scoria cone	16	Shaw, PST	48.0	10.6
Taylor Bluff	Dike	5	PST	60.8	7.6
	Columns	10	Shaw, PST	5.3	2.6
	Tuff Cone	17	PST	8.3	4.8

Abbreviations:
St. Dev. = standard deviation
TT = Thellier-Thellier
Shaw = Tsunakawa-Shaw (LTD-DHT-Shaw)
PST = pseudo-Thellier

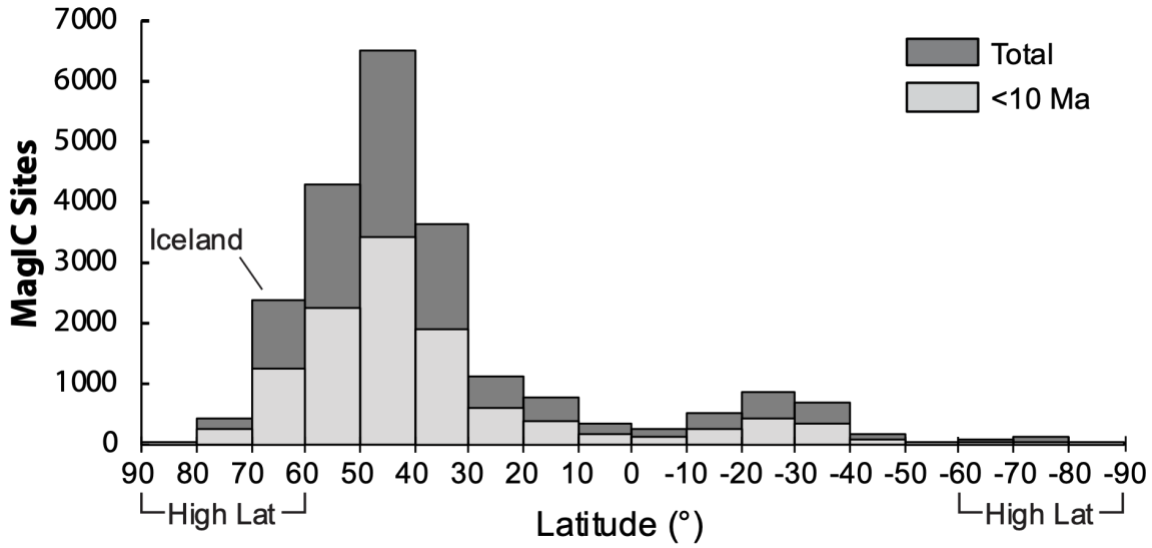

Figure 1 *–MagIC database sites (https://www2.earthref.org/MagIC) with at least one Virtual Geomagnetic Pole (VGP), sorted into 10º latitude bins. Contributions with at least one young (<10 Ma) VGP are in light grey, contributions with only older poles are in dark grey. Note that the large majority of high-latitude data are from Iceland. MagIC method codes DE-DI, DE-POLE, and DE-VGP were used to select the data. Data are from April 2021 or earlier.*

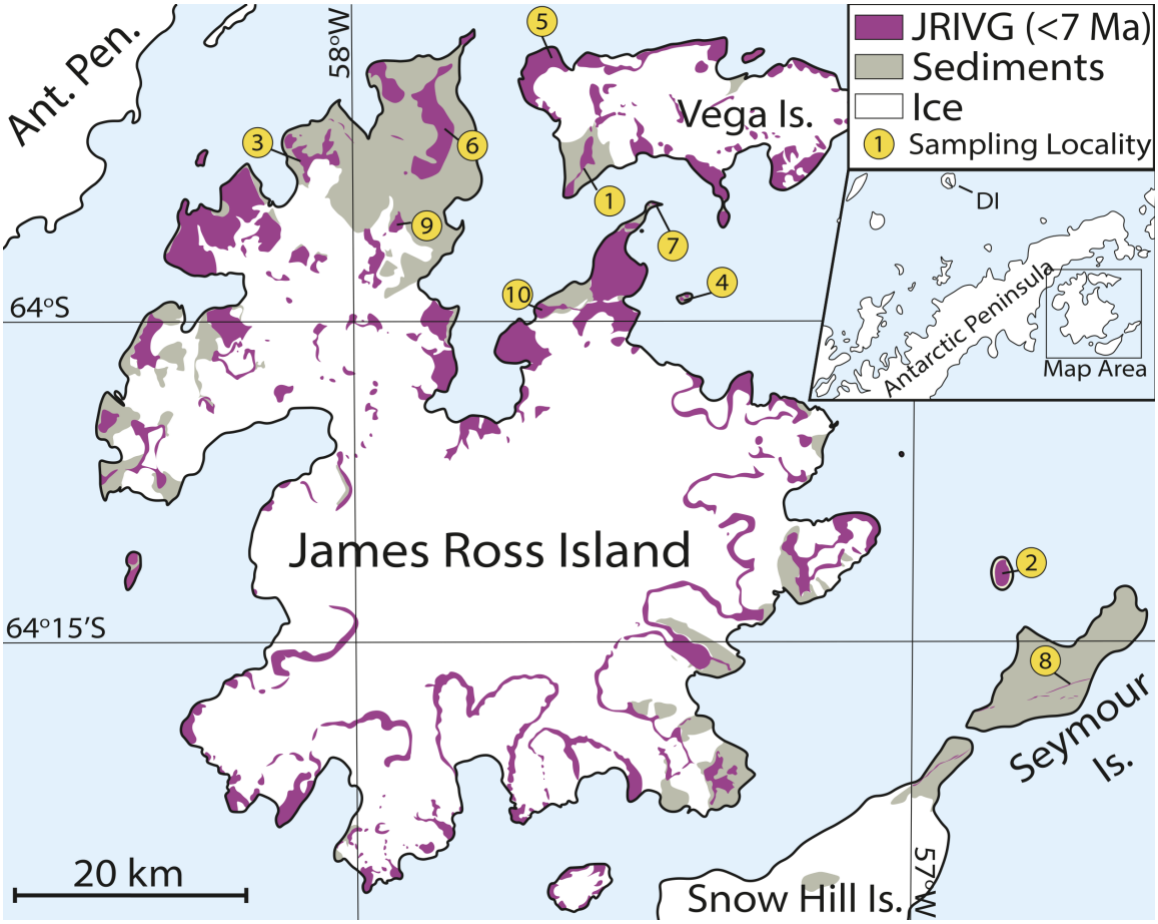

Figure 2 *– Simplified geologic map of James Ross Island and surrounding areas. Numbered sampling localities correlate with Table 1. JRIVG = James Ross Island Volcanic Group. DI = Deception Island. Modified from Smellie et al. (2013).*

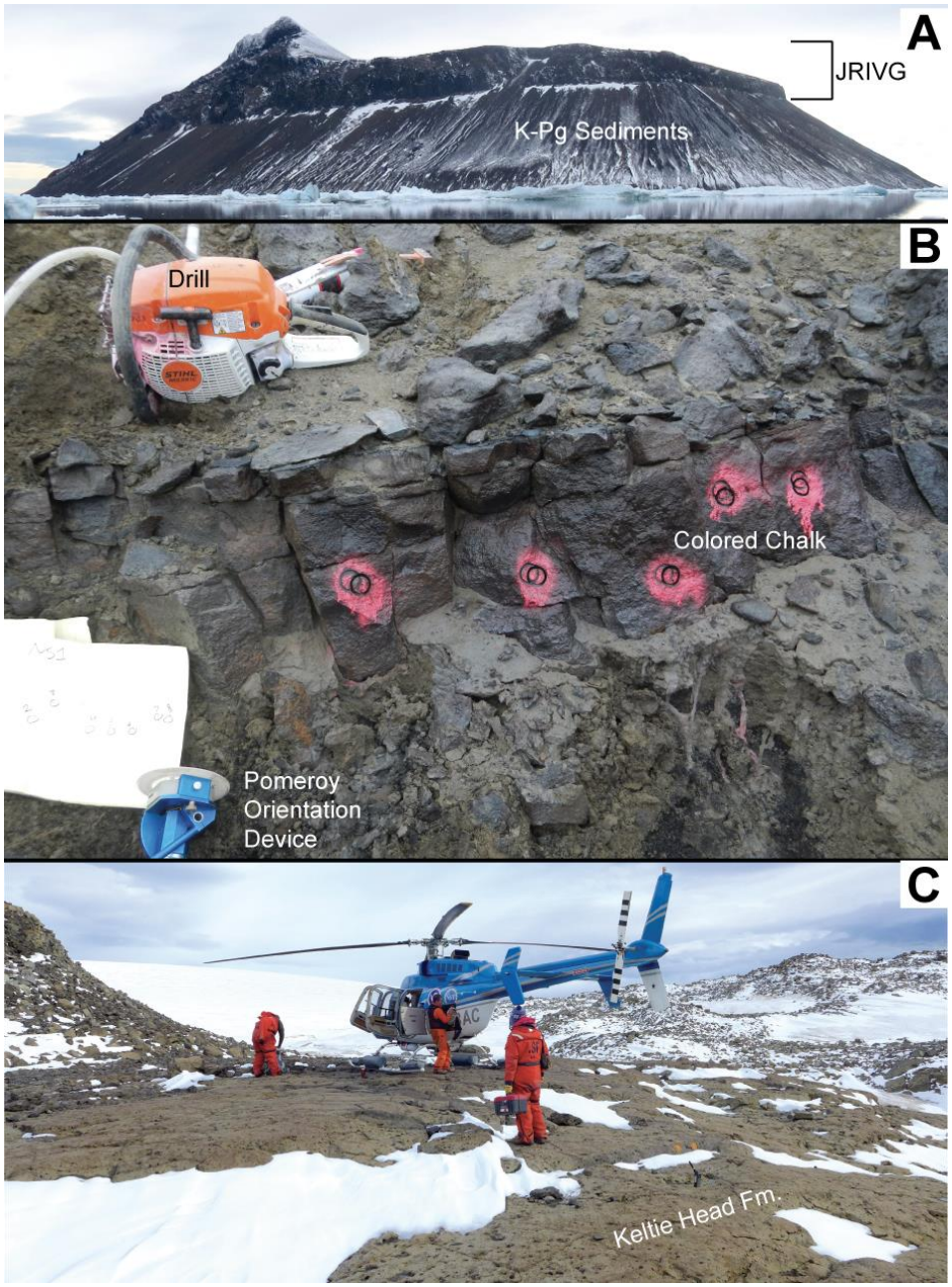

Figure 3 *– **A)** Field photo of Cockburn Island (looking northeast), showing the typical relationship between the James Ross Island volcanic group (JRIVG) and the underlying sedimentary rocks. **B)** Field photo of a small sill at The Naze, showing typical drilling and orienting equipment. Photo credit: Sarah Slotznick. **C)** Photo of a typical lava flow at Keltie Head. Most flows are >1 Ma in age and no longer have glassy or well-preserved flow tops. Helicopter support was essential to reach most sites in this study.*

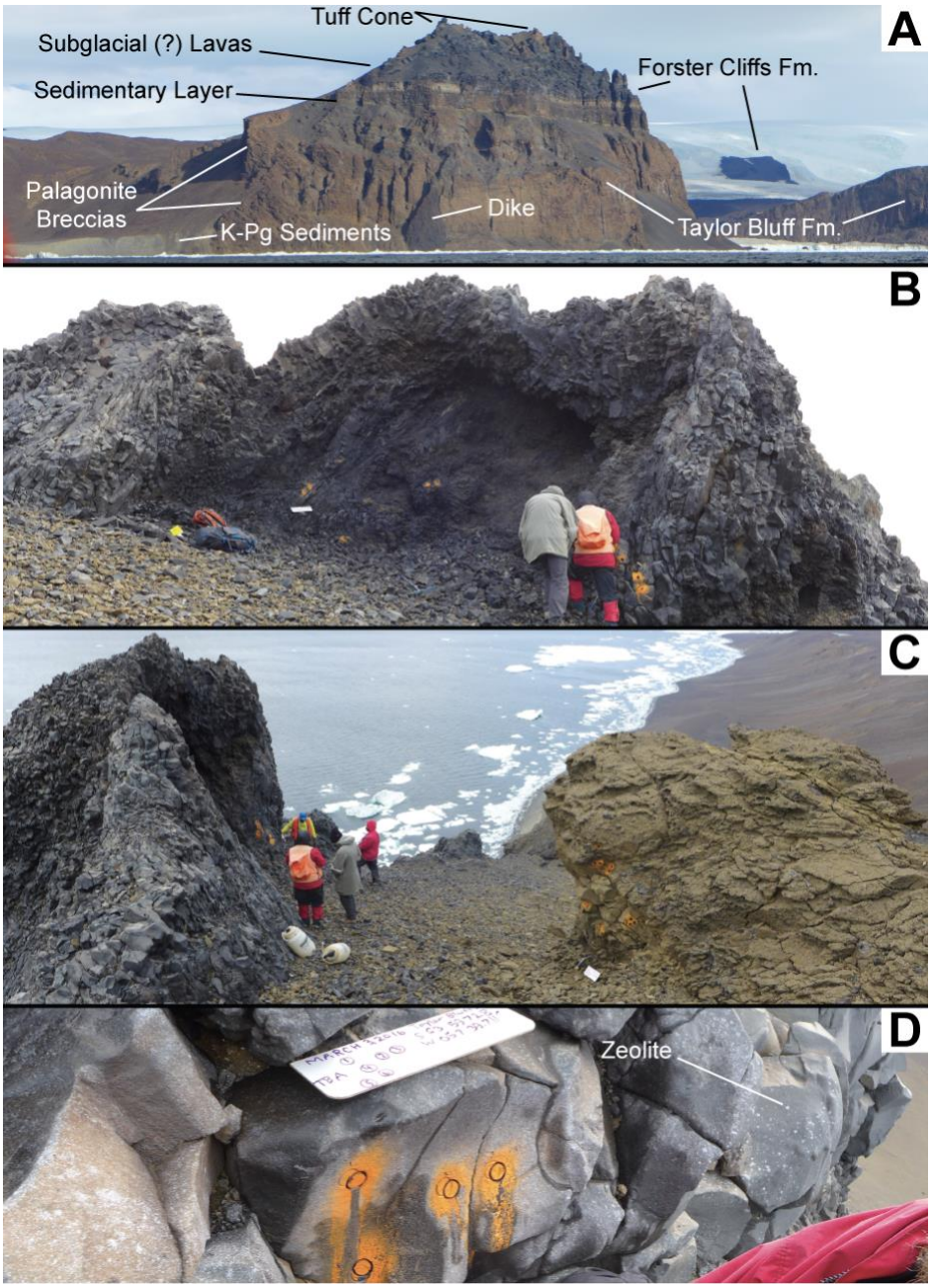

Figure 4 *– **A)** Photo of Taylor Bluff (looking south) showing typical lithologies found in the JRIVG. **B)** Photo of a small columnar intrusion(?) into thin ice, a tuff cone, or both (Smellie et al., 2008), taken near the top of Taylor Bluff. **C)** Photo showing the relation between the intrusion in panel B and a (mostly eroded) tuff cone (seen in panel A). **D)** Photo of paleomagnetic cores taken from a dike on Taylor Bluff. Glassy margins of the dike are no longer present, and zeolites can be seen occasionally filling vesicles.*

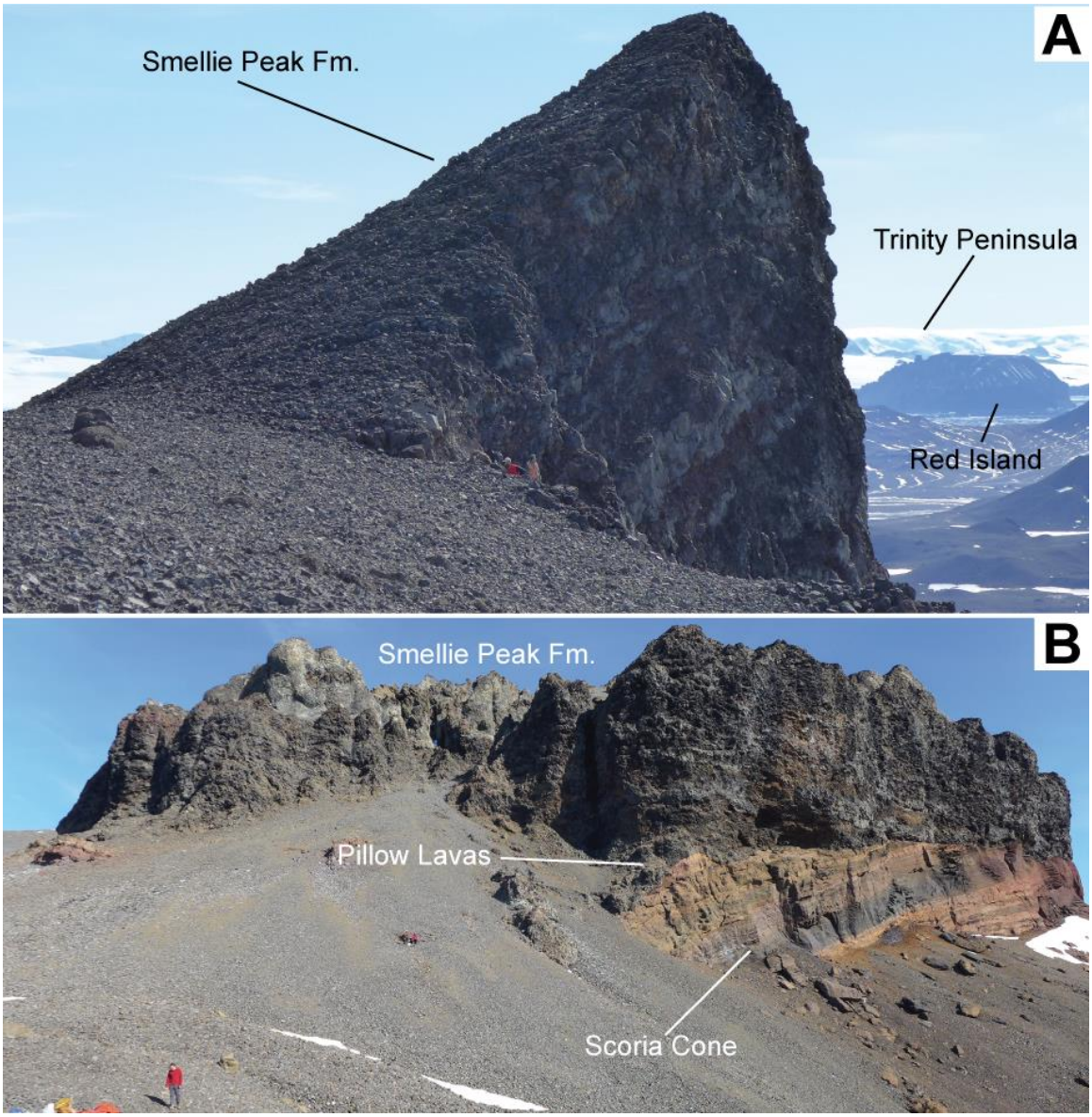

Figure 5 *– **A)** Photo (looking north) of a portion of the Smellie Peak formation. A tilt correction was applied to two lava flows that were sampled here (160º strike, 18º dip).* ***B)*** *Photo of the north-face of Smellie Peak (a.k.a. Cerro Santa Marta, looking southwest. Note the unconformity between the scoria cone and overlying Smellie Peak formation. See Calabozo et al. (2015) for detailed descriptions of this area.*

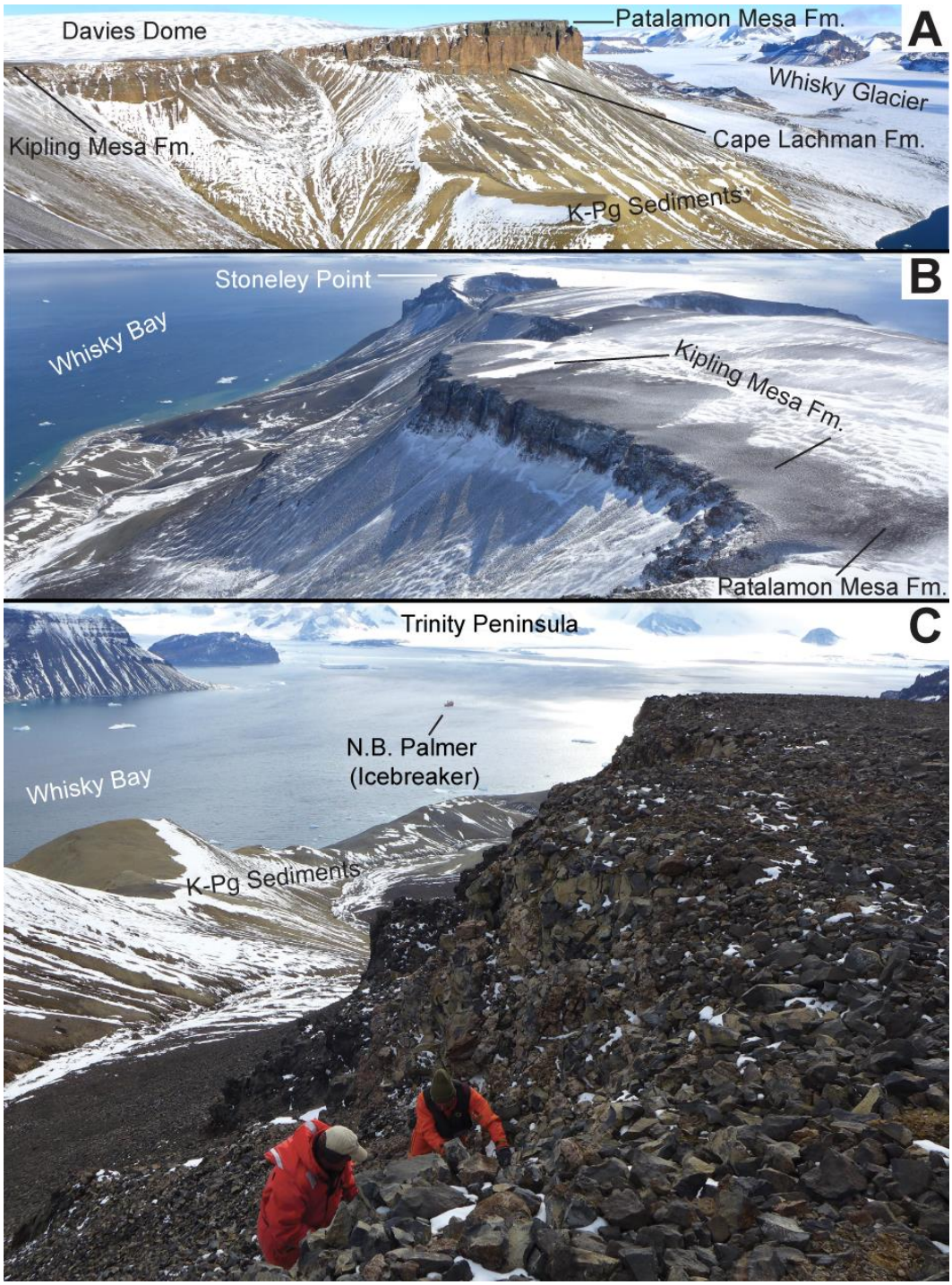

Figure 6 *– **A)** Photo (looking southeast) showing the stratigraphy of the western Davies Dome area. **B)** Photo (looking northwest) showing the main lava-cap that forms a prominent mesa to the west of Davies Dome. **C)** The mesa itself is heavily affected by frost heaving, so in-place outcrops are found at cliff edges.*

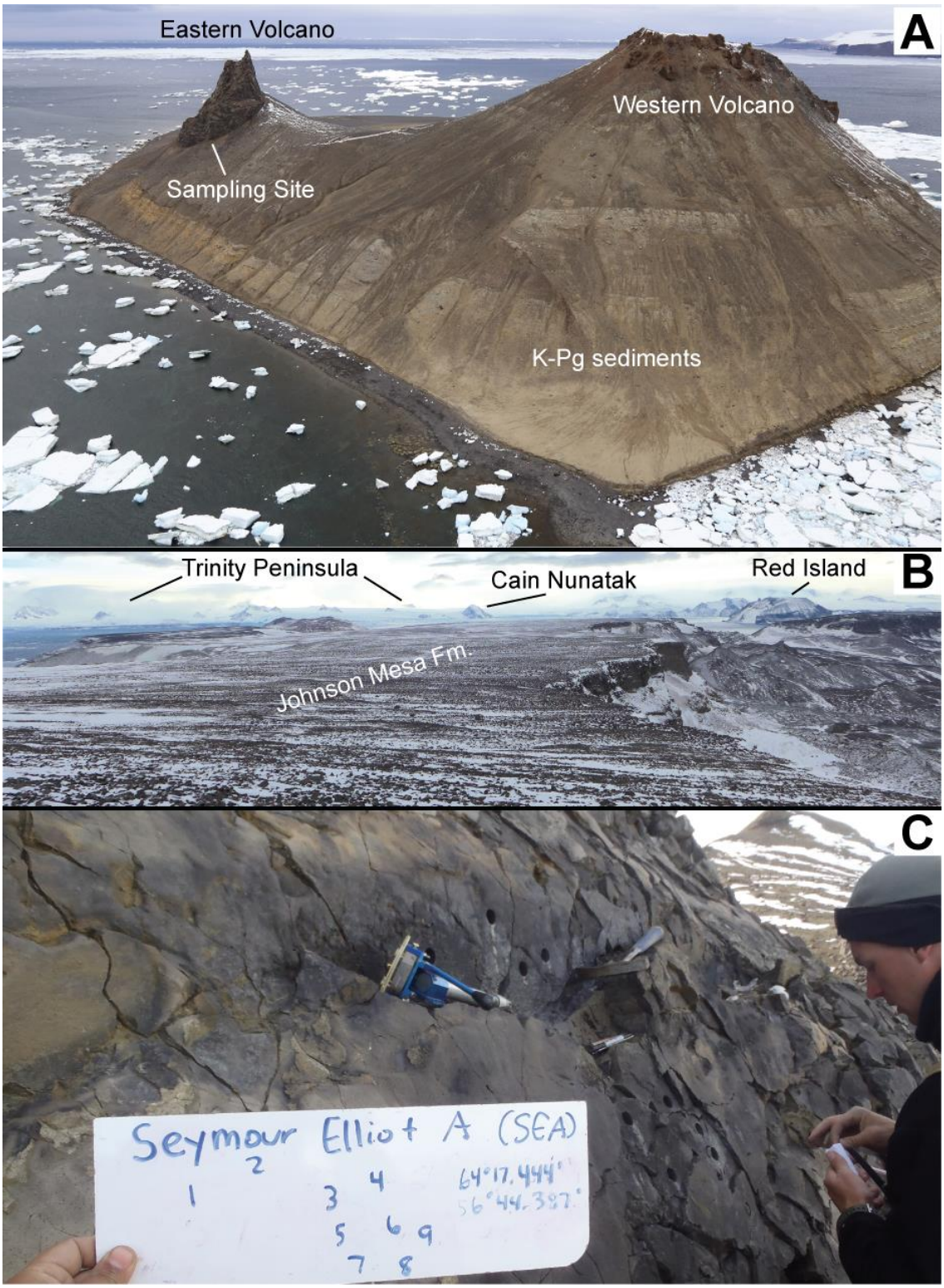

Figure 7 *– **A)** Photo of Humps Island, looking south east. **B)** Photo from atop Lachman Mesa, looking northwest. **C)** Outcrop photo of a dike wall on Seymour Island. Both sides of the dike were sampled. Photo credit: Jennifer Buz.*

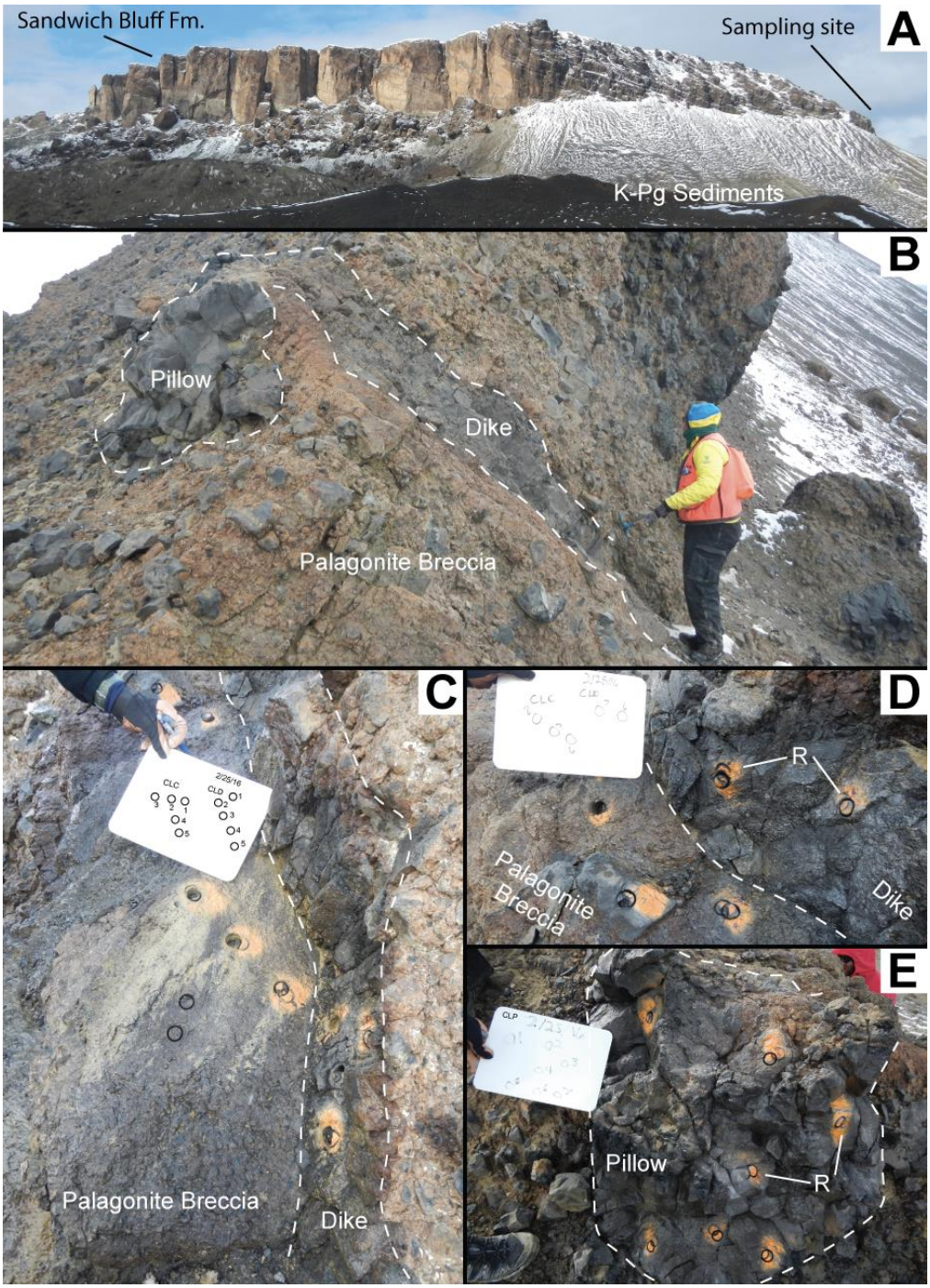

Figure 8 *– **A)** Photo of Leal Bluff, near Cape Lamb, looking east. The lava cap is not well preserved here but the pillow breccia foresets (a common feature in the JRIVG) are clearly visible.* ***B-E)*** *Outcrop photos of the dike, pillow, and palagonite sites. Samples were collected here for a baked contact test, see Section 4.3.2 for discussion. Photo credit: Sarah Slotznick.*

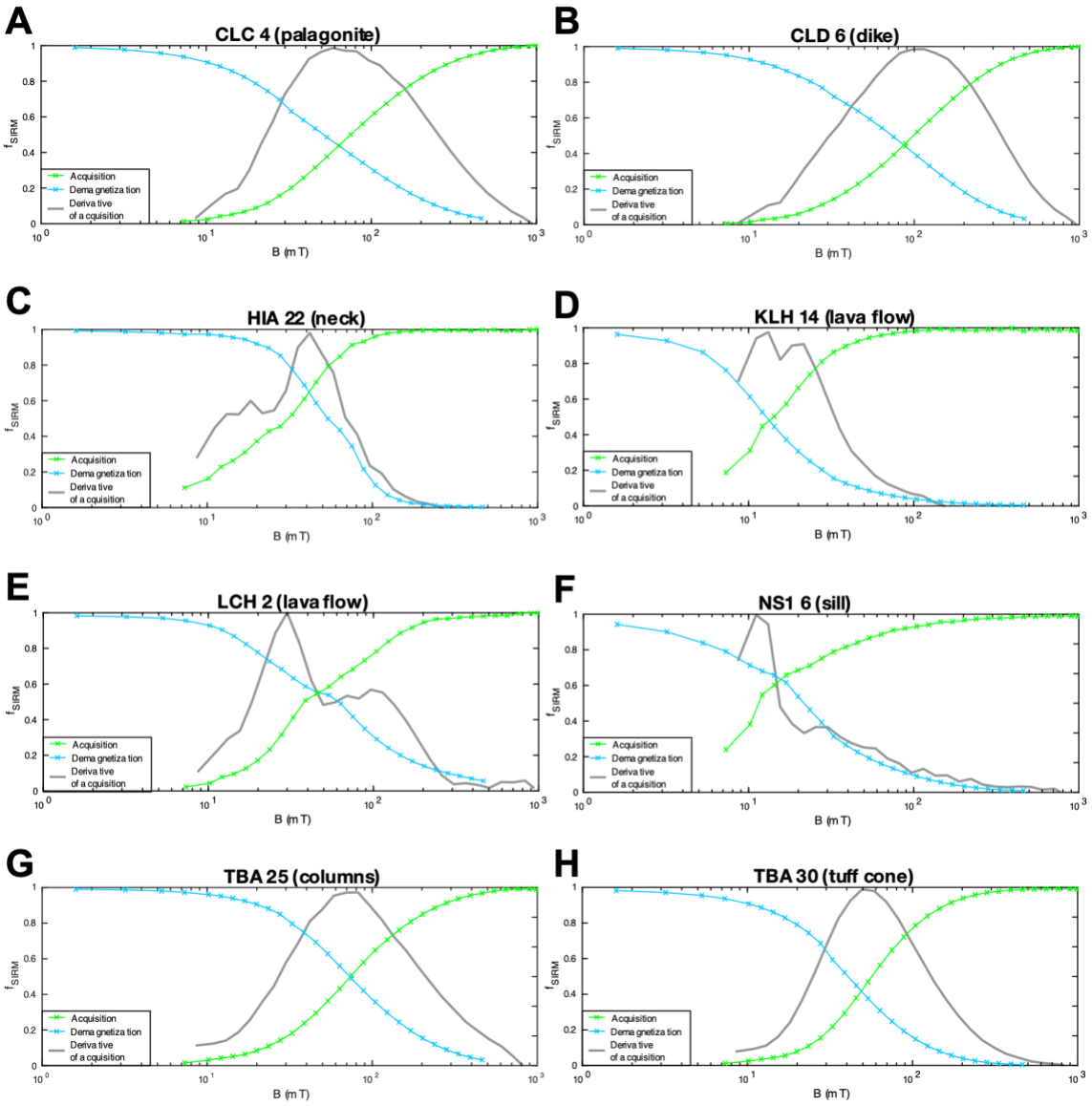

Figure 9 *– IRM acquisition curves of representative JRIVG lithologies. Lower cross-over points (where the curves intersect) signifies greater degrees of particle interaction (Cisowski, 1981). Lava flows have cross-over values of 0.48-0.54, indicating moderate-strong interaction. Other lithologies have crossover values of 0.42-0.63. IRM derivative curves show the presence of one magnetic phase (panel A) or two phases (panel E). See Section 4.2 for discussion.*

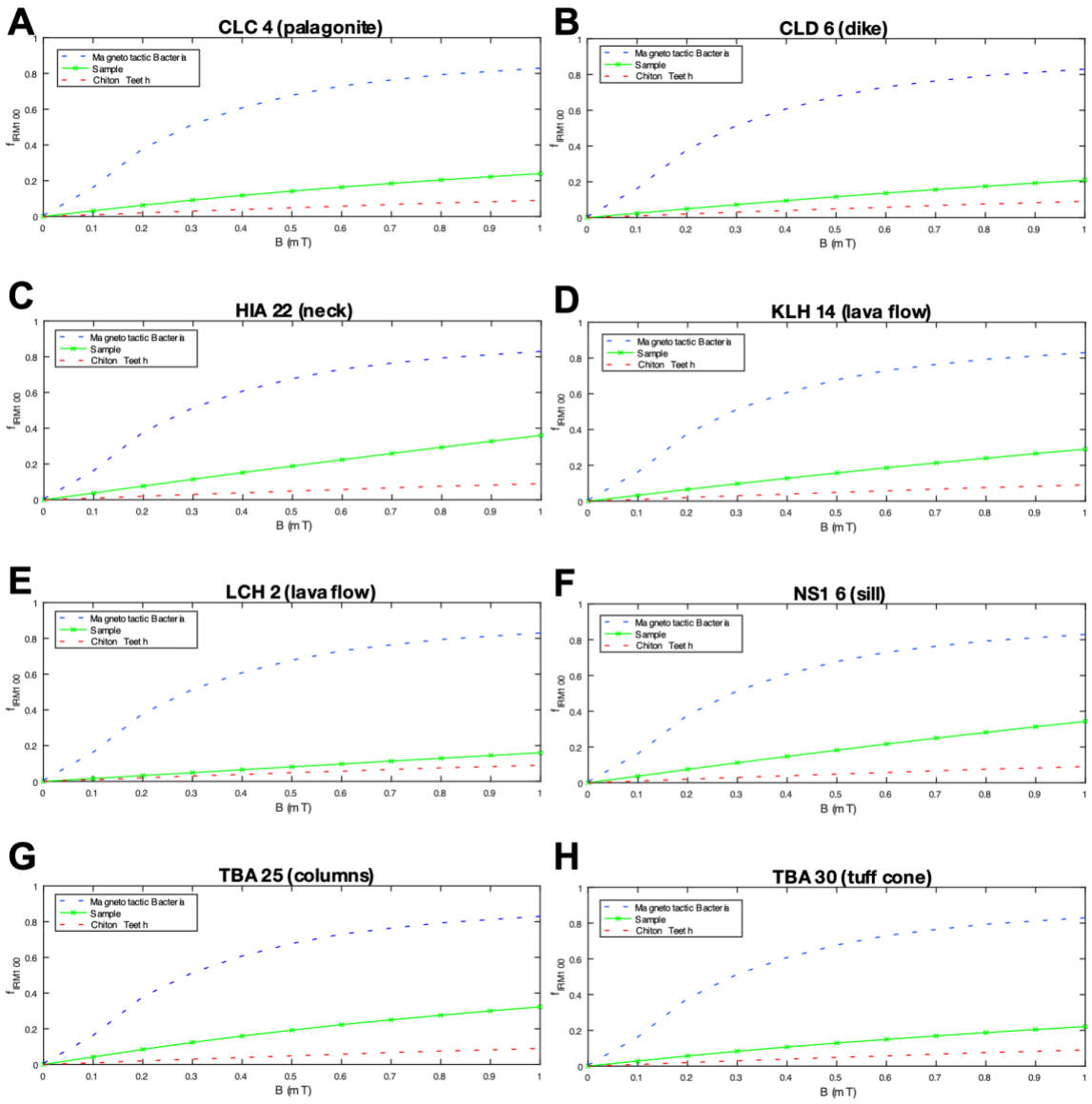

Figure 10 *– ARM acquisition curves of representative JRI lithologies. Reference curves for chiton teeth and magnetotactic bacteria signify strong/weak particle interaction, respectively (Cisowski, 1981; Kobayashi et al., 2006). See Section 4.2 for discussion.*

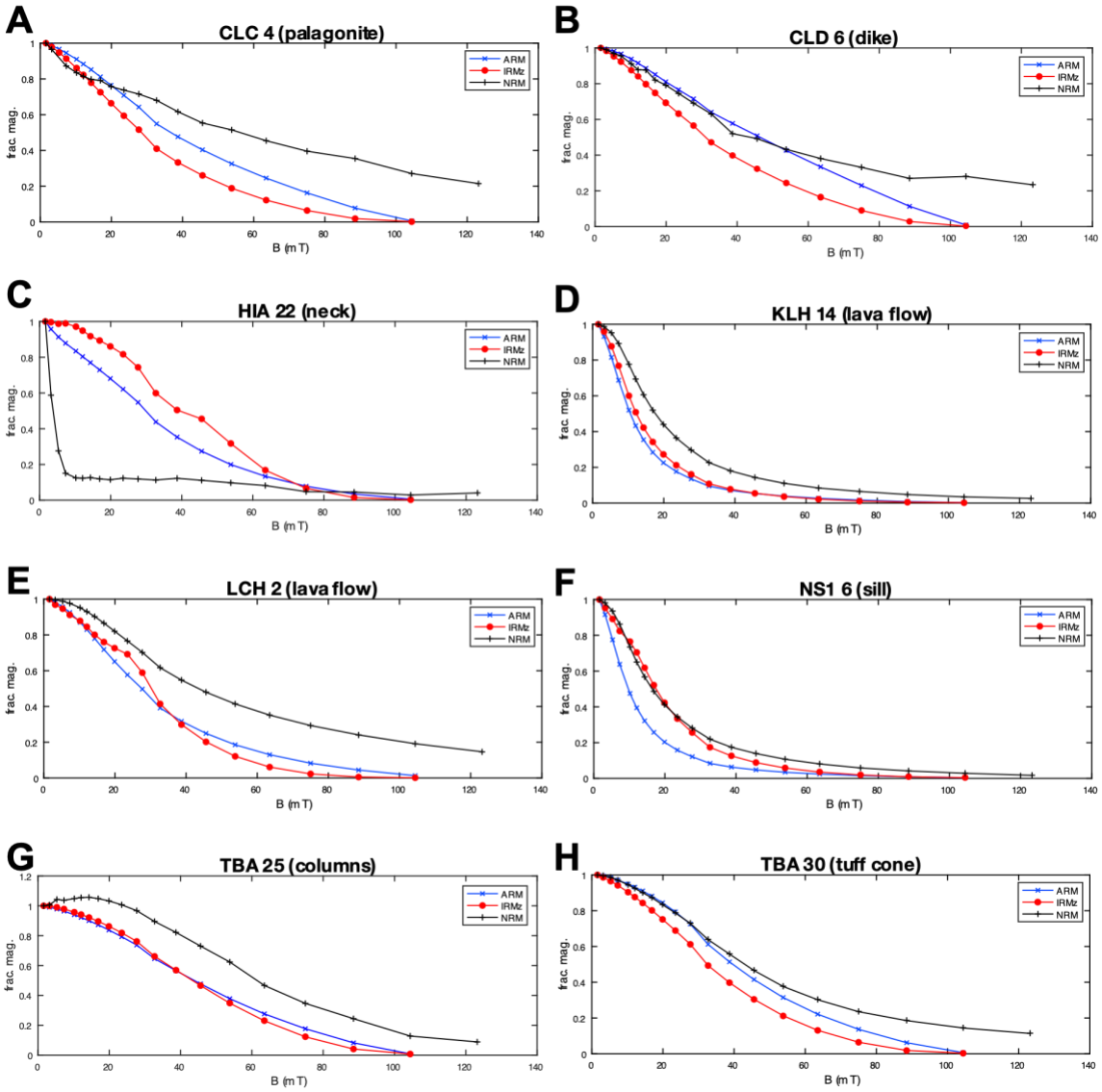

Figure 11 *– Lowrie-Fuller tests of representative JRI lithologies. Overall, a mixture of L- and H-type behavior is seen here (Xu and Dunlop, 1995). See Section 4.2 for discussion.*

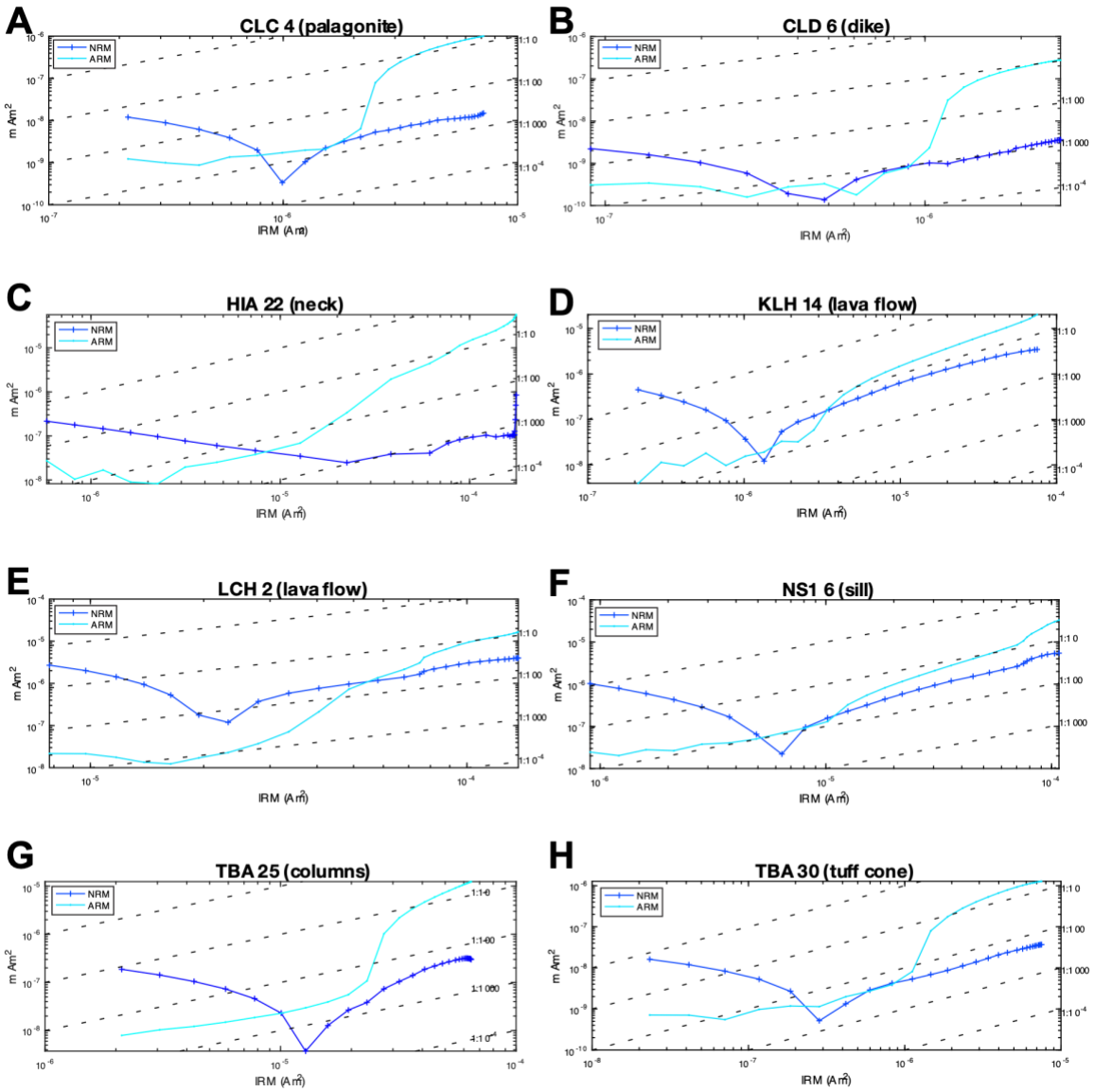

Figure 12 *– Fuller test of NRM (Fuller et al., 1988) on representative JRI lithologies. Some samples show signs of alteration (Fuller et al., 2002), which is expected given their palagonized nature. See Section 4.2 for discussion.*

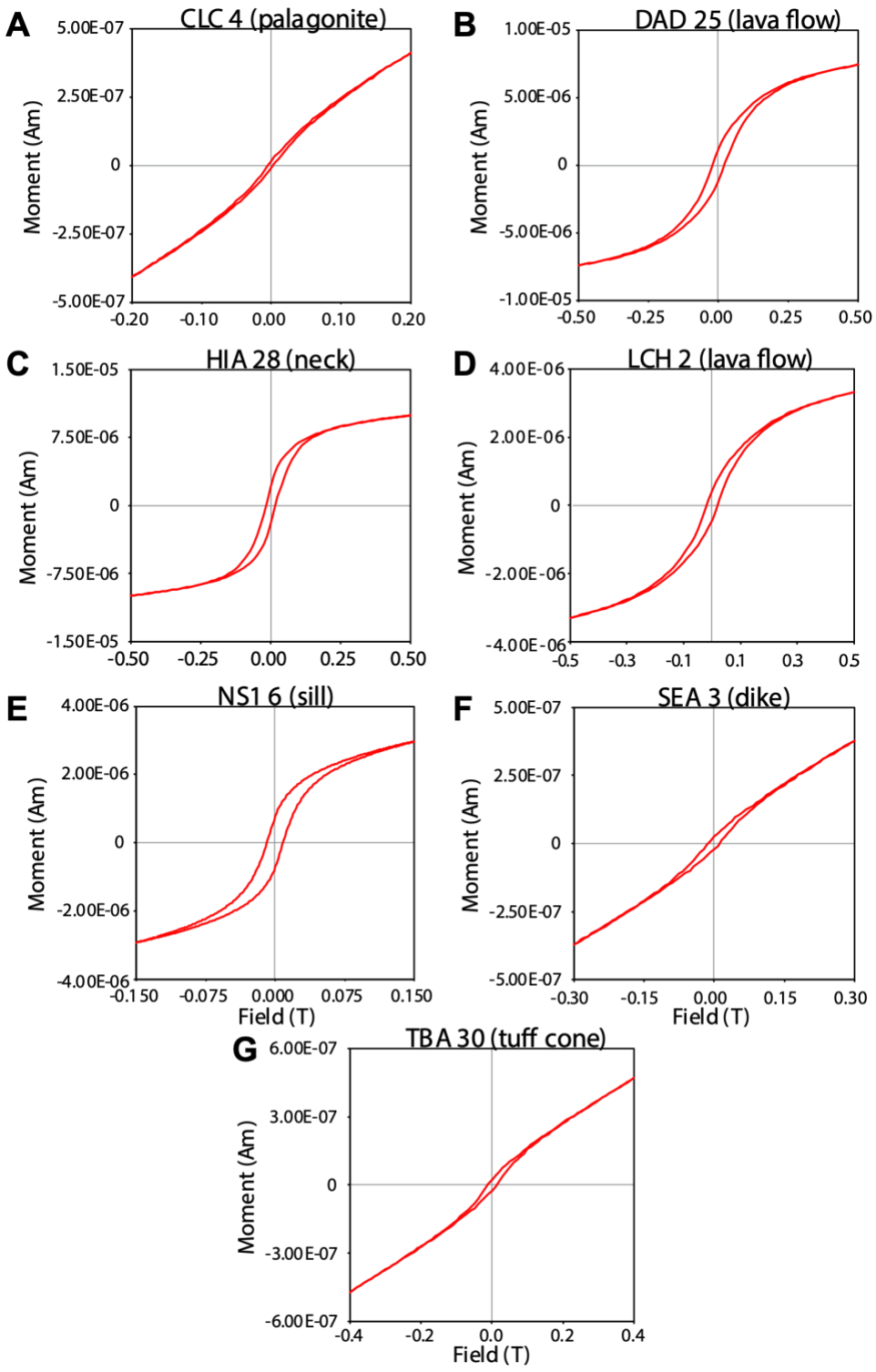

Figure 13 *– Hysteresis loops from representative JRI lithologies. Some samples show strong paramagnetic behavior (panels A, F, G), while the majority show single to pseudo-single domain signatures. See Section 4.2 for discussion.*

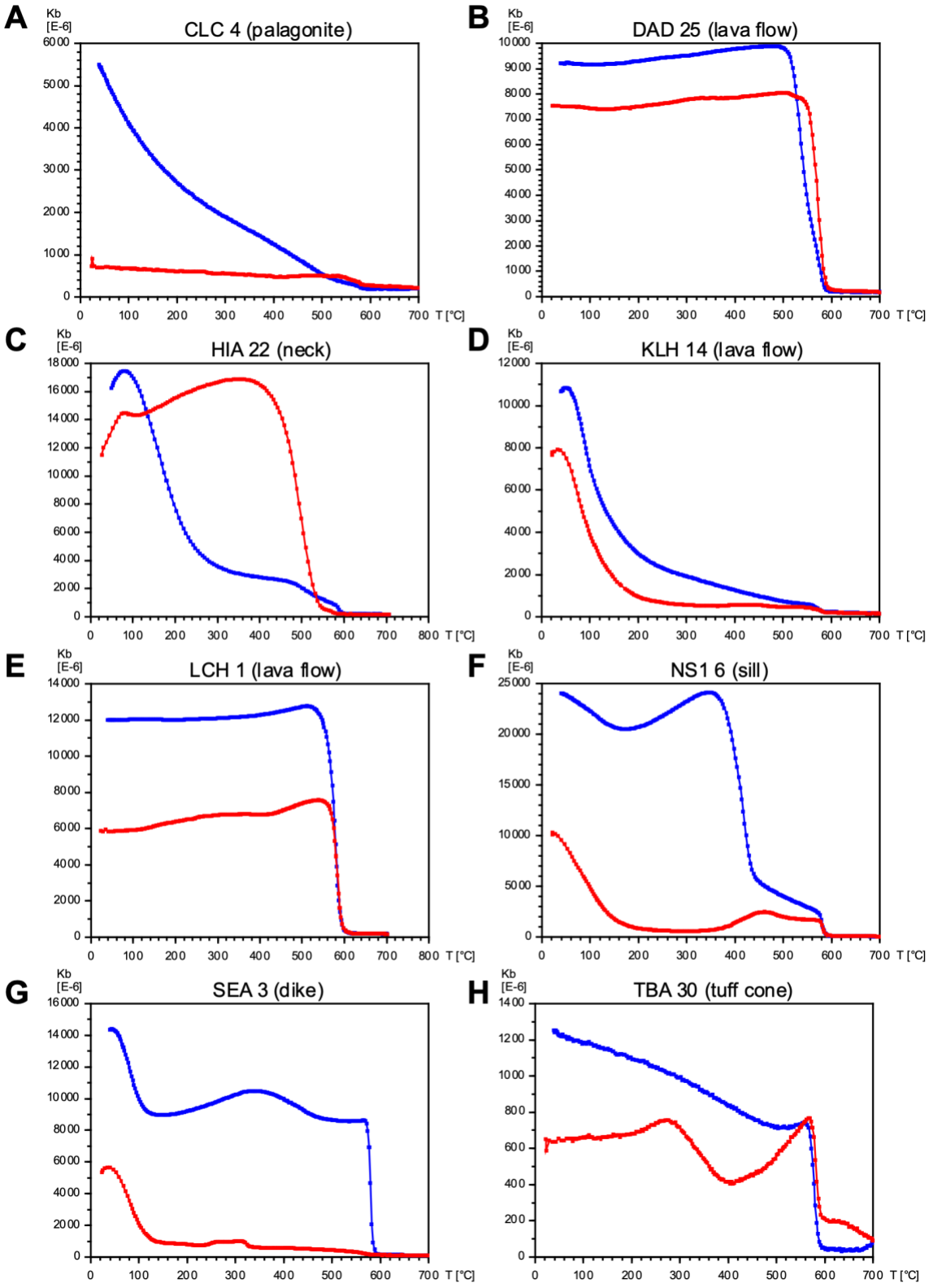

Figure 14 *– Thermal-susceptibility curves from representative JRI lithologies. Heating steps are shown in red, cooling steps are shown in blue. See Section 4.2 for discussion.*

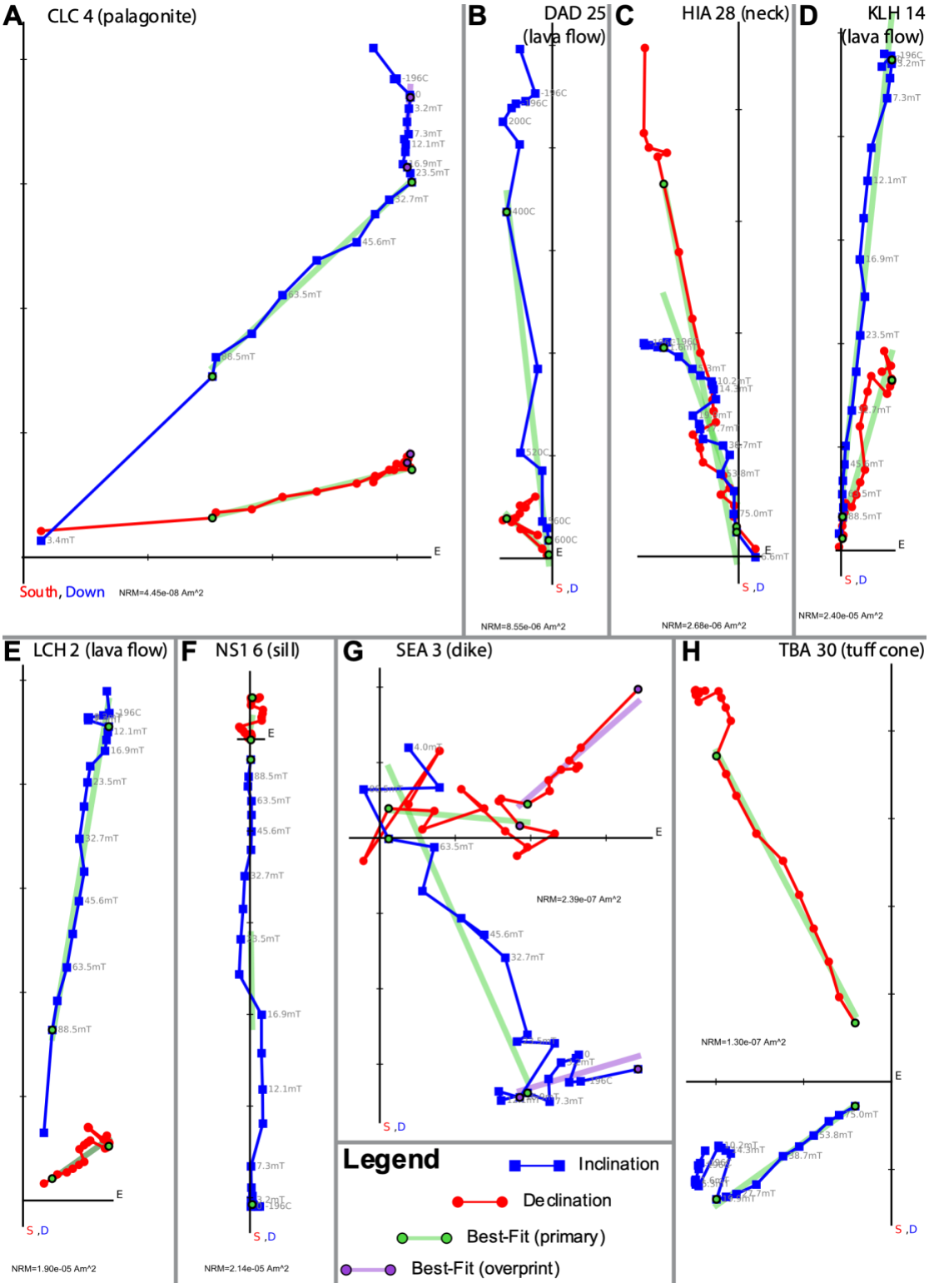

Figure 15 *– Orthogonal projections of representative samples from this study. Declination is shown in red, inclination is shown in blue. Some samples show a zig-zag pattern (e.g. panel F), which is discussed in Section 4.3.1.*

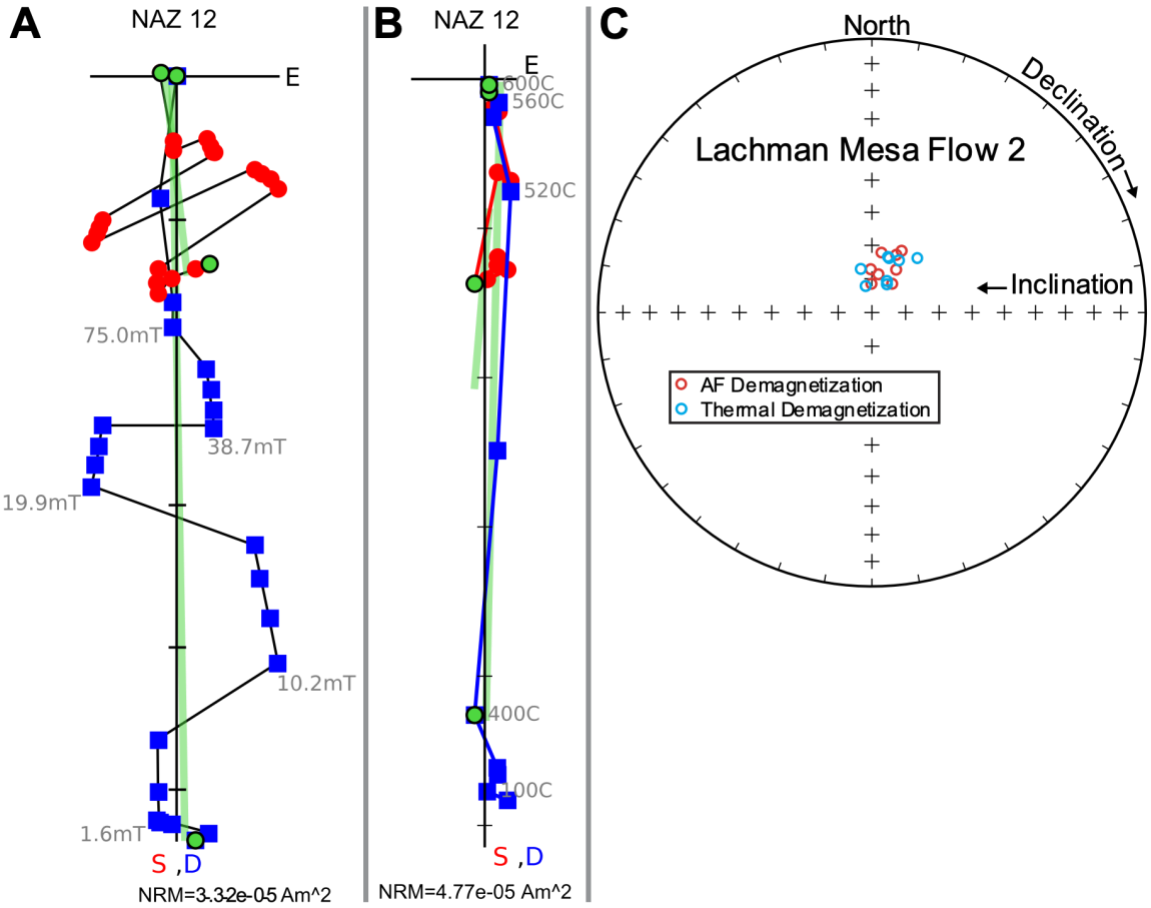

Figure 16 *– Comparison of AF demagnetization data to thermal demagnetization data of different specimens from the same sample.* ***A)*** *A sample from The Naze, showing one of the worst zig-zag patterns seen during AF demagnetization. Symbols as in Figure 15.* ***B)*** *Another specimen from the same core, which was thermally demagnetized during Thellier-Thellier paleointensity experiments.* ***C)*** *Equal area projection showing that least-squares fits at each site are similar regardless of the technique that is used. See Section 4.3.1 for discussion.*

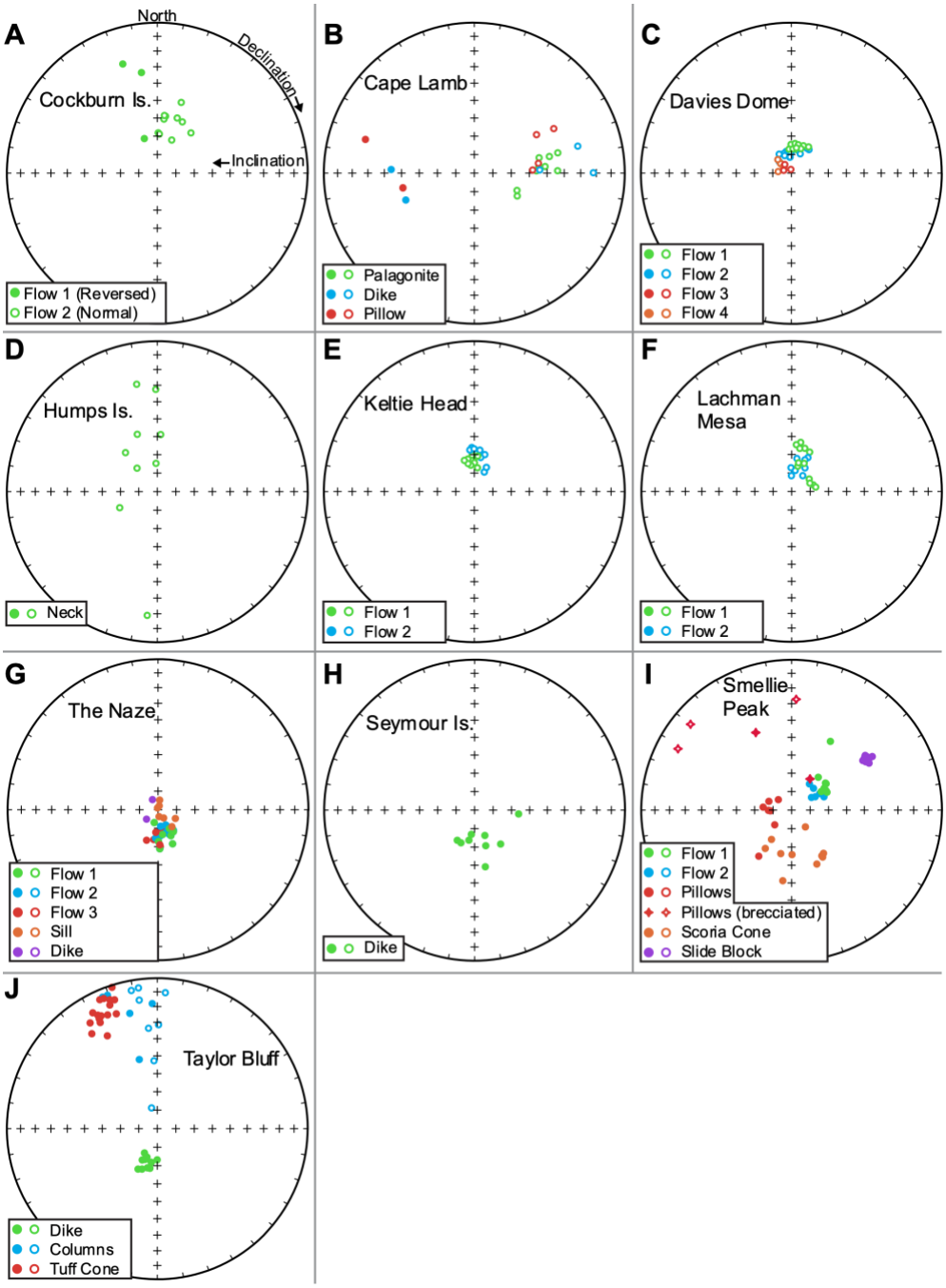

Figure 17 *– Equal area projections showing least-squares best fit directions from each site in this study. Negative inclination (normal polarity) samples are shown with hollow circles, positive inclination (reversed polarity) samples are shown with filled circles. The Cape Lamb pillow and dike, as well as the Smellie Peak slide block, are probably not in-place (Table 2). See Section 4.3.2 for discussion of these sites.*

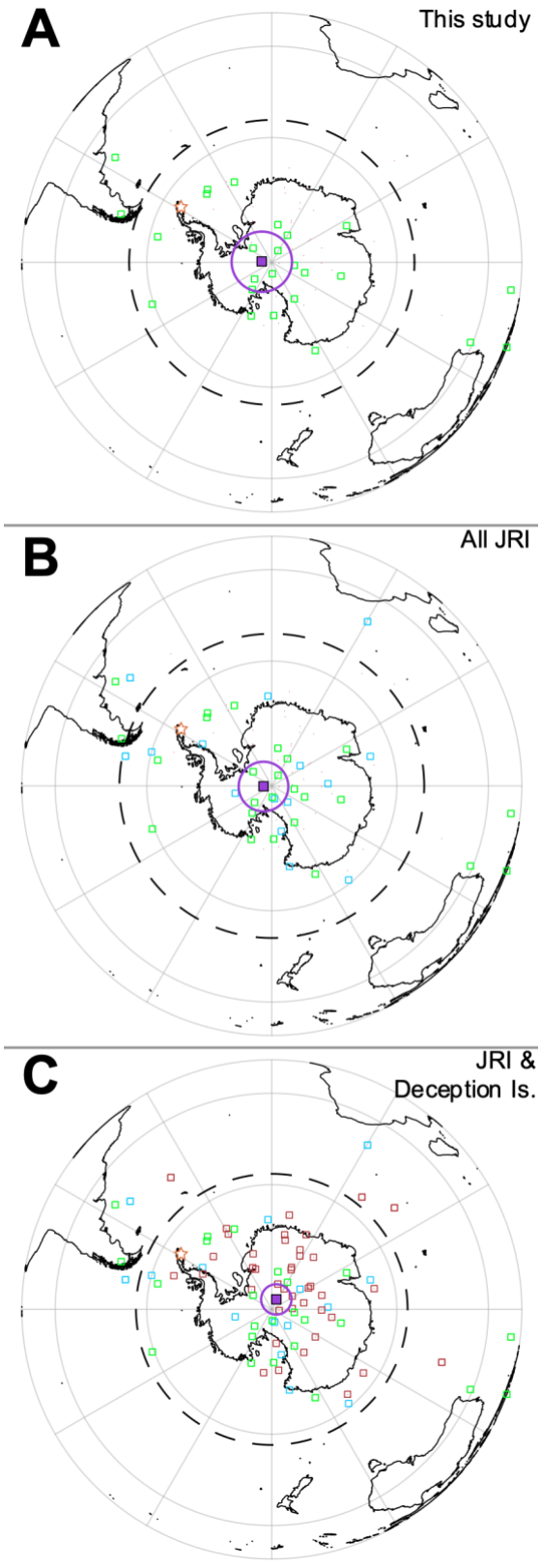

Figure 18 *– **A)** Virtual Geomagnetic Poles (green) from this study. Hollow squares indicate transitional poles, filled squares are normal or reversed. Dashed line is the iteratively calculated cutoff of Vandamme (1994). Purple square and circle are the paleomagnetic pole and α95 confidence interval, respectively. Orange star is the study site (James Ross Island). **B)** Addition of VGPs from Kristjansson et al. (2005) (teal), with a recalculated cutoff angle and paleomagnetic pole. **C)** Addition of young VGPs from Baraldo et al. (2003) and Oliva-Urcia et al. (2016) (red). Only sites that meet the PSV10 selection criteria of Cromwell et al. (2018) are included in the average pole (purple), but all sites are shown here. See Sections 5.1 and 5.2 for discussion.*

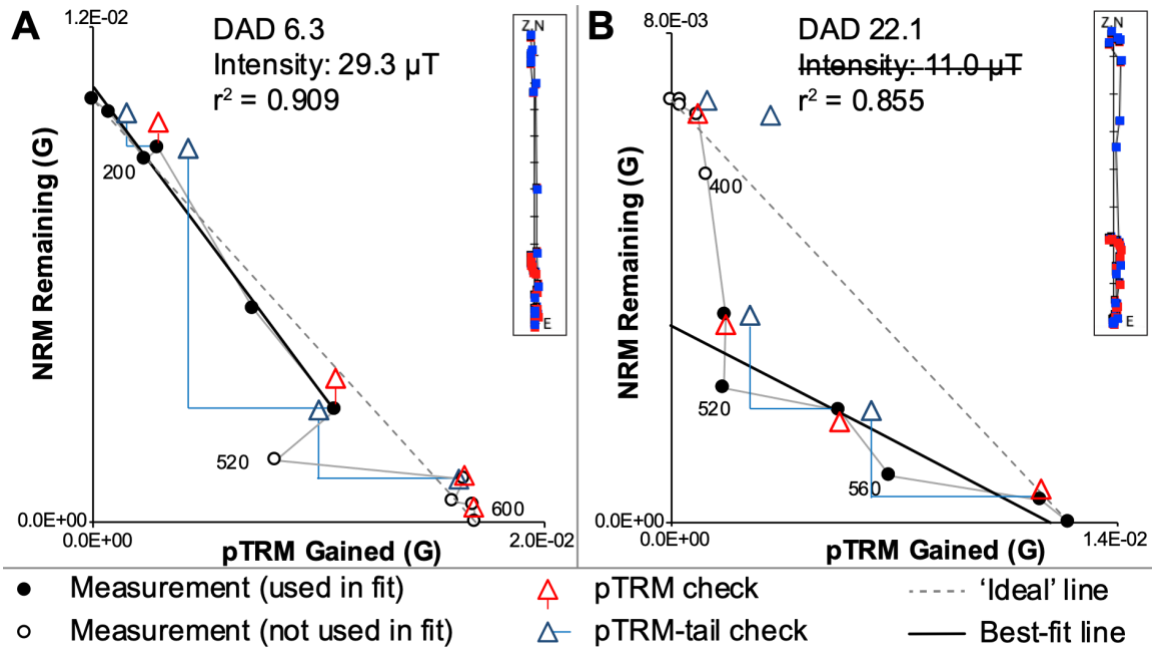

Figure 19 *– Thellier-Thellier results from two flows on Davies Dome.* ***A)*** *A sample that passes the criteria of Lawrence et al. (2009), the associated orthogonal projection is shown in the upper-right.* ***B)*** *Sample that does not pass the selection criteria, showing a two-component Arai plot likely due to multidomain magnetite.*

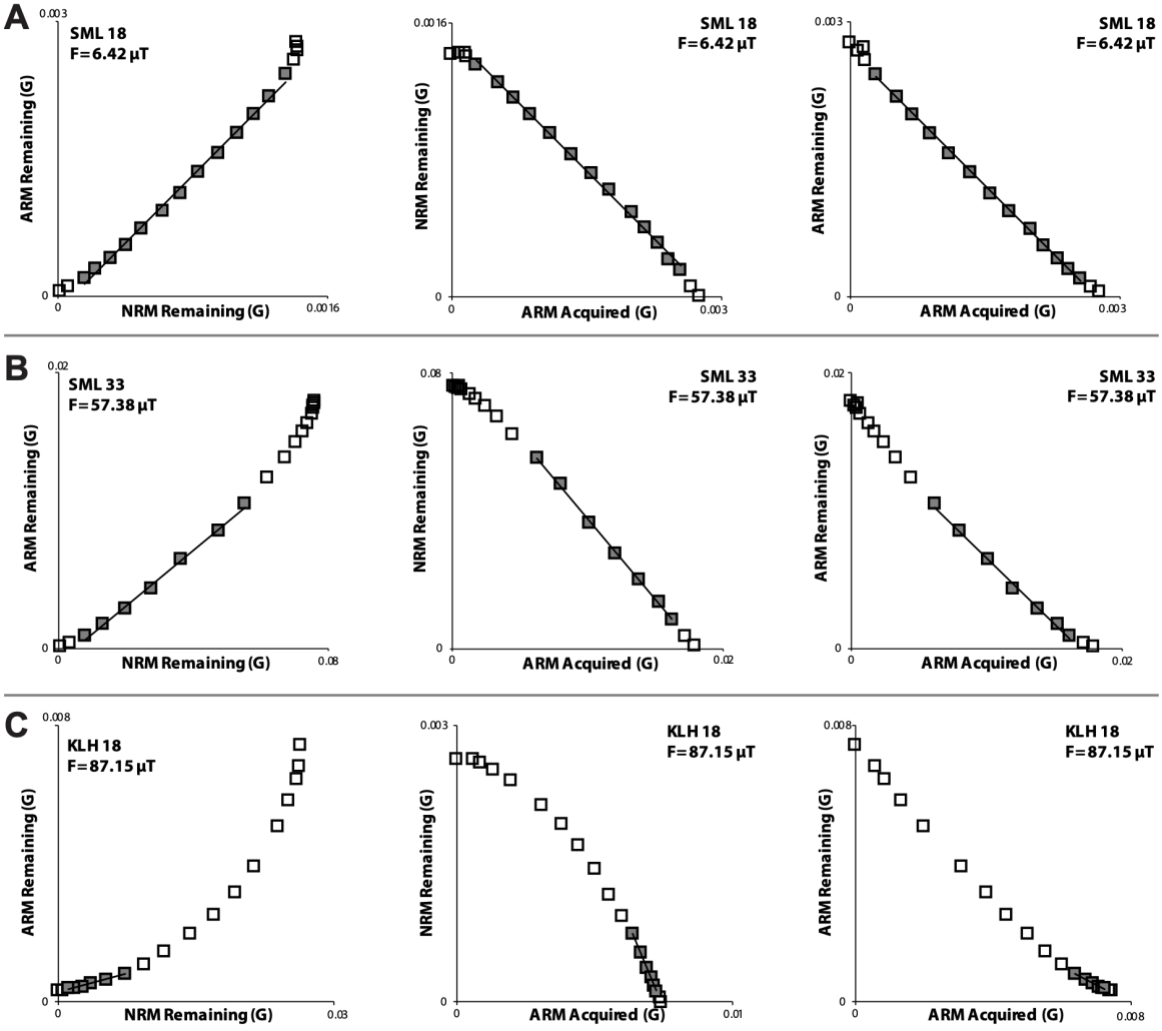

Figure 20 *– Pseudo-Thellier results from three samples.* ***A)*** *High-quality result that passes the selection criteria of Paterson et al. (2016).* ***B)*** *Less reliable result that passes the selection criteria of de Groot et al. (2013).* ***C)*** *Sample that does not pass either set of selection criteria.*

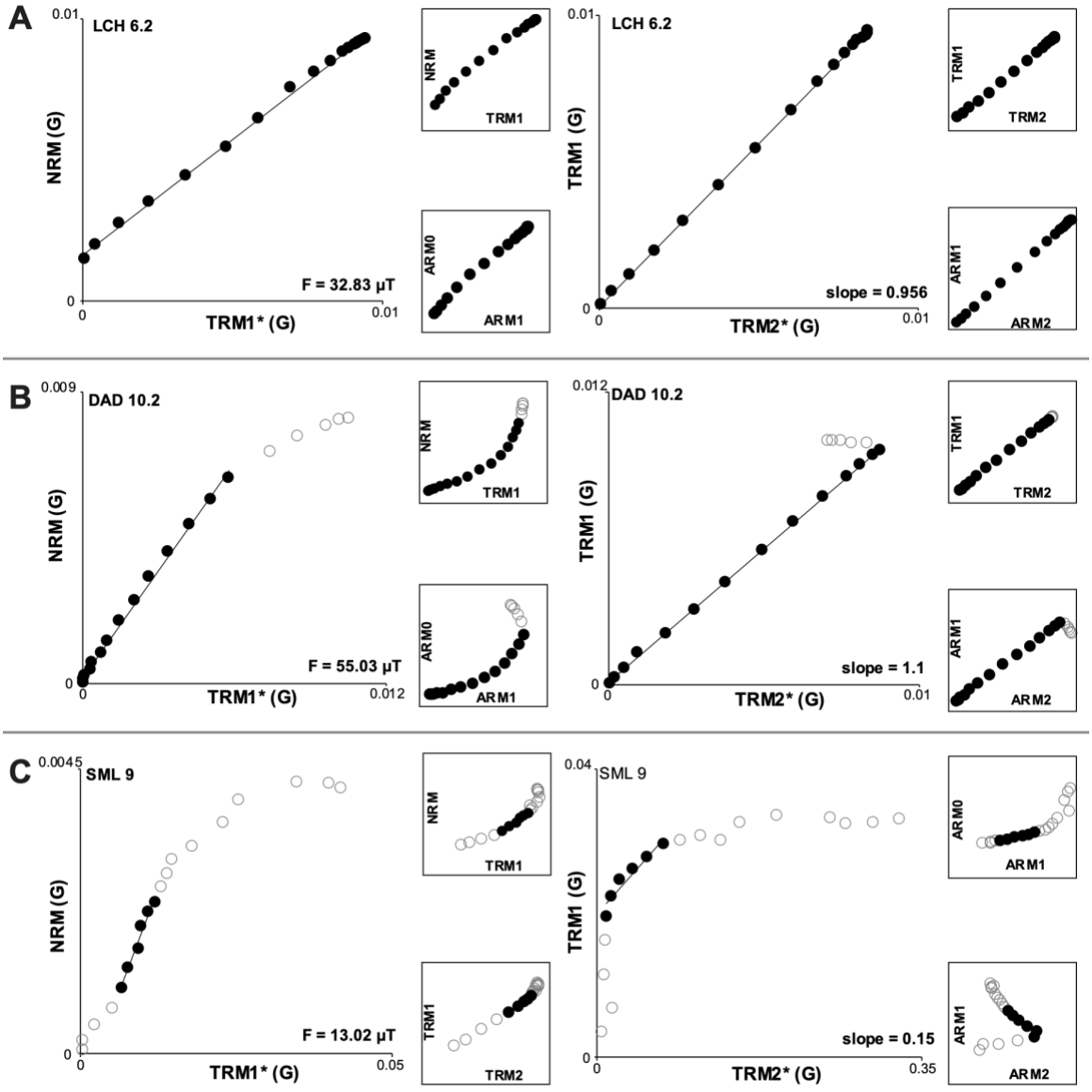

Figure 21 *– Tsunakawa-Shaw results from three samples.* ***A)*** *High-quality result that passes the selection criteria of Yamamoto and Yamaoka (2018).* ***B)*** *A sample that barely passes the selection criteria.* ***C)*** *Sample that does not pass the selection criteria.*

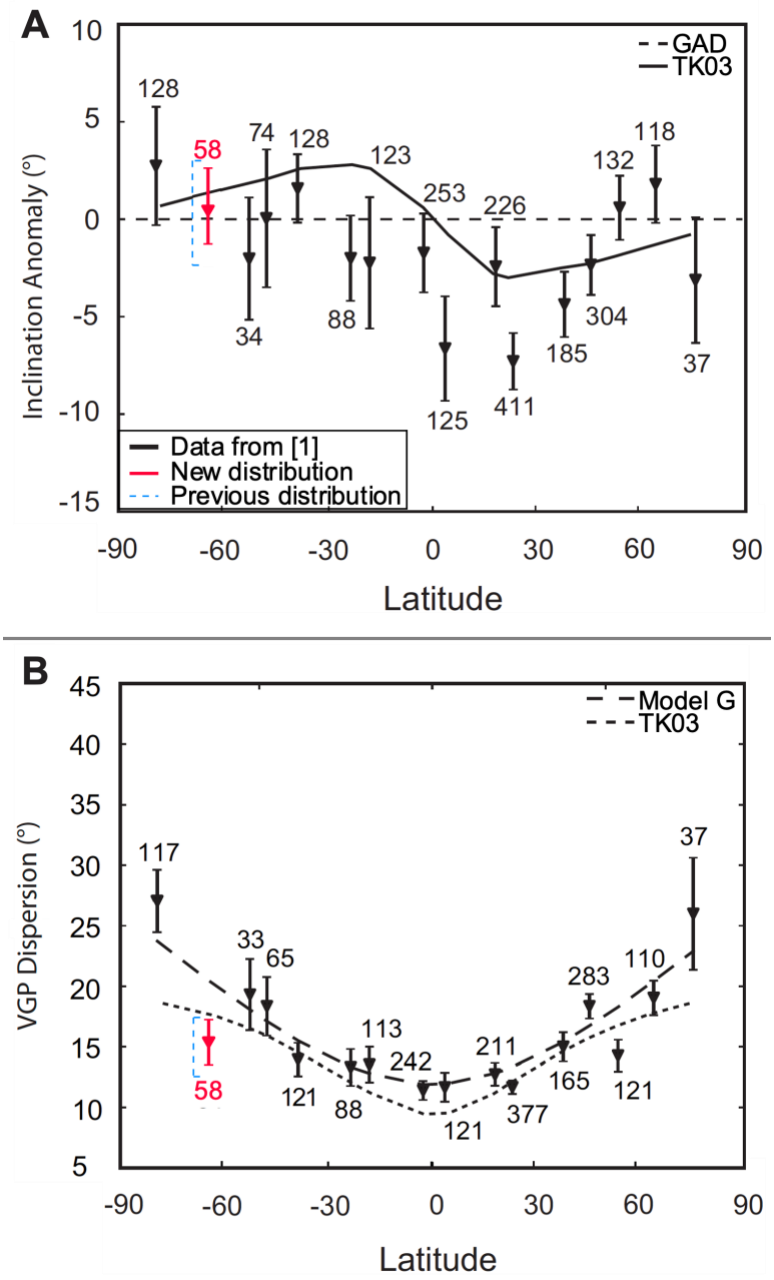

Figure 22 *– **A)** Inclination anomaly and **B)** VGP dispersion data from the PSV10 global data set, lightly modified from Cromwell et al. (2018). Data are organized into 10º latitude bins with average values shown with triangles and bootstrapped 95% confidence bounds shown with vertical bars. Red symbols show the new inclination anomaly and VGP dispersion estimates after incorporating data from this study and Kristjánsson et al. (2005). The original range of estimates by Cromwell et al. (2018) is shown in blue.*

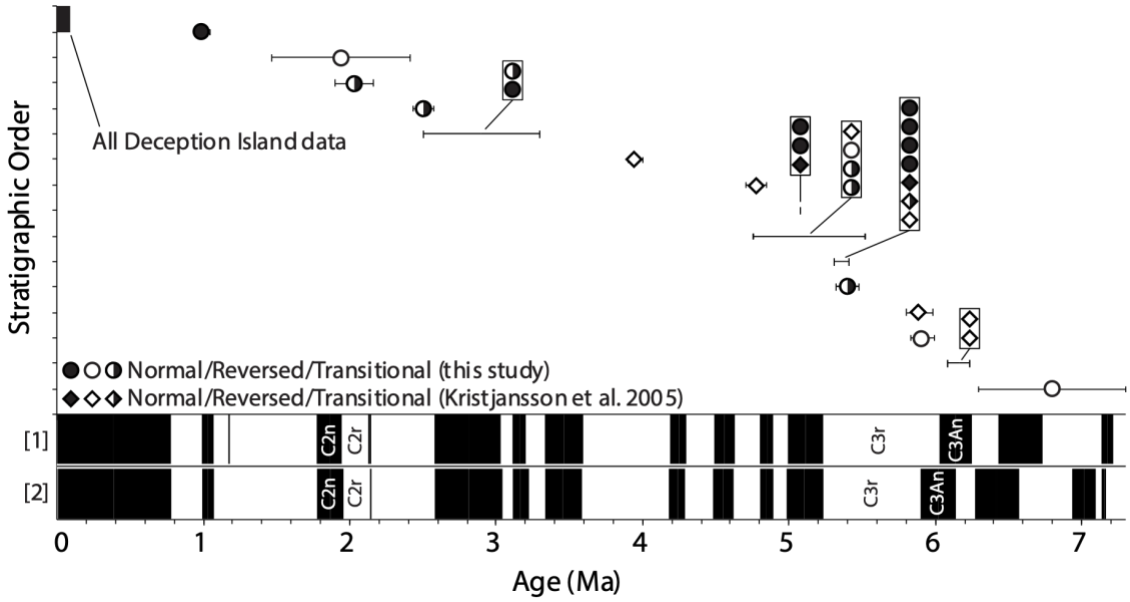

Figure 23 *– Compilation of polarity data from our sites and those of Kristjansson et al. (2005). [1] Geomagnetic polarity timescale of Gradstein et al. (2012). [2] Geomagnetic polarity timescale of Cande and Kent (1995). Stratigraphic order based on Smellie et al. (2013).*

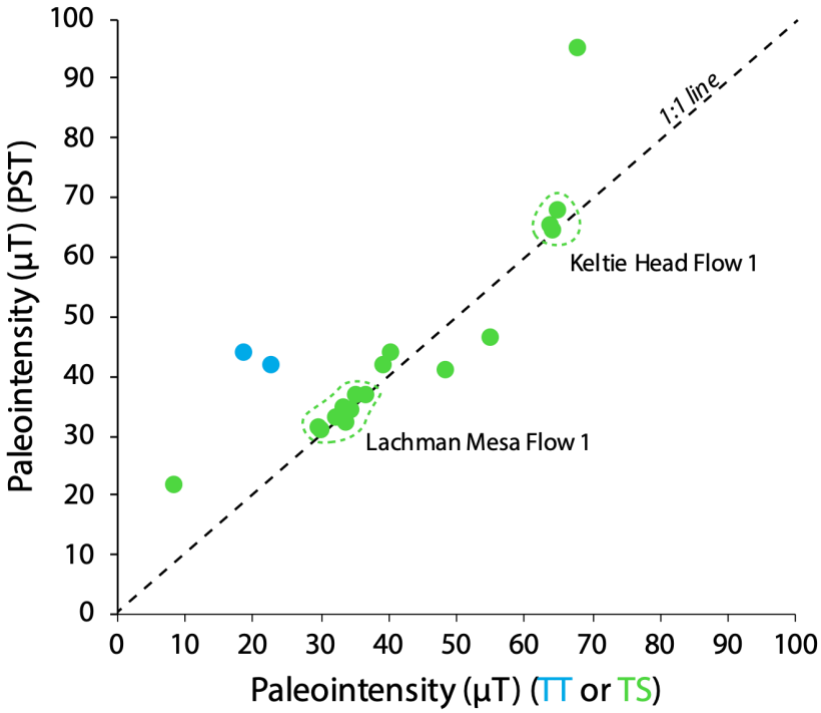

Figure 24 *– Comparison of paleointensity results from different techniques. Results from the pseudo-Thellier method (y-axis) and Tsunakawa-Shaw (green symbols, x-axis) or Thellier-Thellier method (blue symbols, x-axis) will ideally fall on the 1:1 line.*

References

Baraldo, A., Rapalini, A.E., Böhnel, H., and Mena, M., 2003, Paleomagnetic study of Deception Island, South Shetland Islands, Antarctica: Geophysical Journal International, v. 153, p. 333–343.

Blundell, D., 1962, Palaeomagnetic investigations in the Falkland Island Dependencies: British Antarctic Survey, p. 24.

Bowles, J.A., Jackson, M.J., Berquó, T.S., Sølheid, P.A., and Gee, J.S., 2013, Inferred time-and temperature-dependent cation ordering in natural titanomagnetites: Nature Communications, v. 4, p. 1–9.

Calabozo, F.M., Strelin, J.A., Orihashi, Y., Sumino, H., and Keller, R.A., 2015, Volcano–ice–sea interaction in the Cerro Santa Marta area, northwest James Ross Island, Antarctic Peninsula: Journal of Volcanology and Geothermal Research, v. 297, p. 89–108.

Cande, S.C., and Kent, D.V., 1995, Revised calibration of the geomagnetic polarity timescale for the Late Cretaceous and Cenozoic: Journal of Geophysical Research: Solid Earth, v. 100, p. 6093–6095.

Carrivick, J.L., Davies, B.J., Glasser, N.F., Nývlt, D., and Hambrey, M.J., 2012, Late-Holocene changes in character and behaviour of land-terminating glaciers on James Ross Island, Antarctica: Journal of Glaciology, v. 58, p. 1176–1190, doi:10.3189/2012JoG11J148.

Cisowski, S., 1981, Interacting vs. non-interacting single domain behavior in natural and synthetic samples: Physics of the Earth and Planetary Interiors, v. 26, p. 56–62.

Coe, R.S., Grommé, S., and Mankinen, E.A., 1978, Geomagnetic paleointensities from radiocarbon-dated lava flows on Hawaii and the question of the Pacific nondipole low: Journal of Geophysical Research: Solid Earth, v. 83, p. 1740–1756.

Cottrell, E., 2015, Global distribution of active volcanoes, *in* Volcanic Hazards, Risks and Disasters, Elsevier, p. 1–16.

Cromwell, G., Johnson, C., Tauxe, L., Constable, C., and Jarboe, N., 2018, PSV10: A global data set for 0–10 Ma time-averaged field and paleosecular variation studies: Geochemistry, Geophysics, Geosystems, v. 19, p. 1533–1558.

Cromwell, G., Tauxe, L., and Halldórsson, S., 2015a, New paleointensity results from rapidly cooled Icelandic lavas: Implications for Arctic geomagnetic field strength: Journal of Geophysical Research: Solid Earth, v. 120, p. 2913–2934.

Cromwell, G., Tauxe, L., Staudigel, H., and Ron, H., 2015b, Paleointensity estimates from historic and modern Hawaiian lava flows using glassy basalt as a primary source material: Physics of the Earth and Planetary Interiors, v. 241, p. 44–56.

Cych, B.J., Morzfeld, M., and Tauxe, L., 2021, Bias Corrected Estimation of Paleointensity (BiCEP): An improved methodology for obtaining paleointensity estimates: Earth and Space Science Open Archive, p. 30, doi:10.1002/essoar.10506403.1.

Dalziel, I.W., Lawver, L.A., Norton, I.O., and Gahagan, L.M., 2013, The Scotia Arc: Genesis, evolution, global significance: Annual Review of Earth and Planetary Sciences, v. 41.

De Groot, L., Biggin, A., Dekkers, M., Langereis, C., and Herrero-Bervera, E., 2013, Rapid regional perturbations to the recent global geomagnetic decay revealed by a new Hawaiian record: Nature Communications, v. 4, p. 1–7.

Doubleday, P., Leat, P., Alabaster, T., Nell, P., and Tranter, T., 1994, Allochthonous oceanic basalts within the Mesozoic accretionary complex of Alexander Island, Antarctica: Remnants of proto-Pacific oceanic crust: Journal of the Geological Society, v. 151, p. 65–78.

Drief, A., and Schiffman, P., 2004, Very low-temperature alteration of sideromelane in hyaloclastites and hyalotuffs from Kilauea and Mauna Kea volcanoes: Implications for the mechanism of palagonite formation: Clays and Clay Minerals, v. 52, p. 622–634.

Eagles, G., Gohl, K., and Larter, R.D., 2004, High-resolution animated tectonic reconstruction of the South Pacific and West Antarctic Margin: Geochemistry, Geophysics, Geosystems, v. 5.

Engel, Z., Nývlt, D., and Láska, K., 2012, Ice thickness, areal and volumetric changes of Davies Dome and Whisky Glacier (James Ross Island, Antarctic Peninsula) in 1979–2006: Journal of Glaciology, v. 58, p. 904–914, doi:10.3189/2012JoG11J156.

Esser, R.P., Kyle, P.R., and McIntosh, W.C., 2004, 40 Ar/39 Ar dating of the eruptive history of Mount Erebus, Antarctica: Volcano evolution: Bulletin of Volcanology, v. 66, p. 671–686.

Fuller, M., Cisowski, S., Hart, M., Haston, R., Schmidtke, E., and Jarrard, R., 1988, NRM: IRM (s) demagnetization plots: An aid to the interpretation of natural remanent magnetization: Geophysical Research Letters, v. 15, p. 518–521.

Fuller, M., Kidane, T., and Ali, J., 2002, AF demagnetization characteristics of NRM, compared with anhysteretic and saturation isothermal remanence: An aid in the interpretation of NRM: Physics and Chemistry of the Earth, Parts A/B/C, v. 27, p. 1169–1177.

Gehring, A., and Hofmeister, A., 1994, The transformation of lepidocrocite during heating: A magnetic and spectroscopic study: Clays and Clay Minerals, v. 42, p. 409–415.

Glatzmaier, G.A., and Roberts, P.H., 1995, A three-dimensional convective dynamo solution with rotating and finitely conducting inner core and mantle: Physics of the Earth and Planetary Interiors, v. 91, p. 63–75.

Gradstein, F.M., Ogg, J.G., Schmitz, M.D., and Ogg, G.M., 2012, The geologic time scale 2012: Elsevier BV, 1176 p., https://doi.org/10.1016/C2011-1-08249-8.

Graham, J.W., 1949, The stability and significance of magnetism in sedimentary rocks: Journal of Geophysical Research, v. 54, p. 131–167, doi:10.1029/JZ054i002p00131.

Guyodo, Y., Bonville, P., Till, J.L., Ona-Nguema, G., Lagroix, F., and Menguy, N., 2016, Constraining the origins of the magnetism of lepidocrocite (γ-FeOOH): A Mössbauer and magnetization study: Frontiers in Earth Science, v. 4, p. 28.

Haase, K.M., and Beier, C., 2021, Chapter 3.2b Bransfield Strait and James Ross Island: Petrology: Geological Society, London, Memoirs, v. 55, doi:10.1144/M55-2018-37.

Hill, D.J., Haywood, A.M., Valdes, P.J., Francis, J.E., Lunt, D.J., Wade, B.S., and Bowman, V.C., 2013, Paleogeographic controls on the onset of the Antarctic circumpolar current: Geophysical Research Letters, v. 40, p. 5199–5204.

Hole, M., 1988, Post-subduction alkaline volcanism along the Antarctic Peninsula: Journal of the Geological Society, v. 145, p. 985–998.

Hole, M., and Larter, R.D., 1993, Trench-proximal volcanism following ridge crest-trench collision along the Antarctic Peninsula: Tectonics, v. 12, p. 897–910.

Hole, M., Smellie, J.L., and Marriner, G., 1991, Geochemistry and tectonic setting of Cenozoic alkaline basalts from Alexander Island, Antarctic Peninsula, *in* International Symposium on Antarctic Earth Sciences. 5, p. 521–526.

Johnson, H., Lowrie, W., and Kent, D., 1975, Stability of ARM in fine and course grained magnetite and maghemite particles: Geophysical Journal of the Royal Astronomical Society, v. 41, p. 1–10.

Johnson, C.L., and McFadden, P., 2015, 5.11 - The Time-Averaged Field and Paleosecular Variation, *in* Schubert, G. ed., Treatise on Geophysics (Second Edition), Oxford, Elsevier, p. 385–417, doi:10.1016/B978-0-444-53802-4.00105-6.

Jokat, W., Boebel, T., König, M., and Meyer, U., 2003, Timing and geometry of early Gondwana breakup: Journal of Geophysical Research: Solid Earth, v. 108.

Juarez, M., Tauxe, L., Gee, J., and Pick, T., 1998, The intensity of the Earth's magnetic field over the past 160 million years: Nature, v. 394, p. 878–881.

Kirschvink, J., 1980, The least-squares line and plane and the analysis of palaeomagnetic data: Geophysical Journal International, v. 62, p. 699–718, doi:10.1111/j.1365-246X.1980.tb02601.x.

Kirschvink, J.L., Kopp, R.E., Raub, T.D., Baumgartner, C.T., and Holt, J.W., 2008, Rapid, precise, and high-sensitivity acquisition of paleomagnetic and rock-magnetic data: Development of a low-noise automatic sample changing system for superconducting rock magnetometers: Geochemistry, Geophysics, Geosystems, v. 9, doi:10.1029/2007GC001856.

Kobayashi, A., Kirschvink, J.L., Nash, C.Z., Kopp, R.E., Sauer, D.A., Bertani, L.E., Voorhout, W.F., and Taguchi, T., 2006, Experimental observation of magnetosome chain collapse in magnetotactic bacteria: Sedimentological, paleomagnetic, and evolutionary implications: Earth and Planetary Science Letters, v. 245, p. 538–550.

Košler, J., Magna, T., Mlčoch, B., Mixa, P., Nỳvlt, D., and Holub, F., 2009, Combined Sr, Nd, Pb and Li isotope geochemistry of alkaline lavas from northern James Ross Island (Antarctic Peninsula) and implications for back-arc magma formation: Chemical Geology, v. 258, p. 207–218.

Kristjansson, L., Gudmundsson, M., Smellie, J.L., McIntosh, W.C., and Esser, R., 2005, Palaeomagnetic, 40Ar/39Ar, and stratigraphical correlation of Miocene-Pliocene basalts in the Brandy Bay area, James Ross Island, Antarctica: Antarctic Science, v. 17, p. 409.

Lawrence, K., Tauxe, L., Staudigel, H., Constable, C., Koppers, A., McIntosh, W., and Johnson, C., 2009, Paleomagnetic field properties at high southern latitude: Geochemistry, Geophysics, Geosystems, v. 10.

Lowrie, W., and Fuller, M., 1971, On the alternating field demagnetization characteristics of multidomain thermoremanent magnetization in magnetite: Journal of Geophysical Research, v. 76, p. 6339–6349.

Mankinen, E.A., and Cox, A., 1988, Paleomagnetic investigation of some volcanic rocks from the McMurdo volcanic province, Antarctica: Journal of Geophysical Research: Solid Earth, v. 93, p. 11599–11612, doi:https://doi.org/10.1029/JB093iB10p11599.

Marenssi, S.A., Casadío, S., and Santillana, S.N., 2010, Record of Late Miocene glacial deposits on Isla Marambio (Seymour Island), Antarctic Peninsula: Antarctic Science, v. 22, p. 193.

McElhinny, M.W., and McFadden, P.L., 1997, Palaeosecular variation over the past 5 Myr based on a new generalized database: Geophysical Journal International, v. 131, p. 240–252.

Merrill, R.T., and McFadden, P.L., 2003, The geomagnetic axial dipole field assumption: Physics of the Earth and Planetary Interiors, v. 139, p. 171–185.

Milanese, F.N., Olivero, E.B., Raffi, M.E., Franceschinis, P.R., Gallo, L.C., Skinner, S.M., Mitchell, R.N., Kirschvink, J.L., and Rapalini, A.E., 2019a, Mid Campanian-Lower Maastrichtian magnetostratigraphy of the James Ross Basin, Antarctica: Chronostratigraphical implications: Basin Research, v. 31, p. 562–583.

Milanese, F.N., Olivero, E.B., Slotznick, S.P., Tobin, T.S., Raffi, M.E., Skinner, S.M., Kirschvink, J.L., and Rapalini, A.E., 2020a, Coniacian-Campanian magnetostratigraphy of the Marambio Group: The Santonian-Campanian boundary in the Antarctic Peninsula and the complete Upper Cretaceous–Lowermost Paleogene chronostratigraphical framework for the James Ross Basin: Palaeogeography, Palaeoclimatology, Palaeoecology, v. 555, p. 109871.

Milanese, F.N., Rapalini, A., Gallo, L., Franceschinis, P., and Kirschvink, J., 2020b, Large paleomagnetic declination anomalies in the Cerro Nevado (Snow Hill) Island, Antarctic Peninsula: Evidence of hidden tectonic rotations? Revista de la Asociación Geológica Argentina, v. 77, p. 192–206.

Milanese, F., Rapalini, A., Slotznick, S.P., Tobin, T.S., Kirschvink, J., and Olivero, E., 2019b, Late Cretaceous paleogeography of the Antarctic Peninsula: New paleomagnetic pole from the James Ross Basin: Journal of South American Earth Sciences, v. 91, p. 131–143.

Minyuk, P., Subbotnikova, T., and Plyashkevich, A., 2011, Measurements of thermal magnetic susceptibility of hematite and goethite: Izvestiya, Physics of the Solid Earth, v. 47, p. 762–774.

Muxworthy, A., and McClelland, E., 2000, Review of the low-temperature magnetic properties of magnetite from a rock magnetic perspective: Geophysical Journal International, v. 140, p. 101–114.

Nayudu, Y.R., 1964, Palagonite tuffs (hyaloclastites) and the products of post-eruptive processes: Bulletin Volcanologique, v. 27, p. 391–410.

Oliva-Urcia, B., Gil-Peña, I., Maestro, A., López-Martínez, J., Galindo-Zaldívar, J., Soto, R., Gil-Imaz, A., Rey, J., and Pueyo, O., 2016, Paleomagnetism from Deception Island (South Shetlands archipelago, Antarctica), new insights into the interpretation of the volcanic evolution using a geomagnetic model: International Journal of Earth Sciences, v. 105, p. 1353–1370.

Olivero, E.B., 2012, Sedimentary cycles, ammonite diversity and palaeoenvironmental changes in the Upper Cretaceous Marambio Group, Antarctica: Cretaceous Research, v. 34, p. 348–366.

Özdemir, Ö., and Dunlop, D.J., 1996, Thermoremanence and Néel temperature of goethite: Geophysical Research Letters, v. 23, p. 921–924.

Pankhurst, R., 1982, Rb-Sr geochronology of Graham Land, Antarctica: Journal of the Geological Society, v. 139, p. 701–711.

Paterson, G.A., 2011, A simple test for the presence of multidomain behavior during paleointensity experiments: Journal of Geophysical Research: Solid Earth, v. 116.

Paterson, G.A., Heslop, D., and Pan, Y., 2016, The pseudo-Thellier palaeointensity method: new calibration and uncertainty estimates: Geophysical Journal International, v. 207, p. 1596–1608, doi:10.1093/gji/ggw349.

Pease, V., 2011, Eurasian orogens and Arctic tectonics: An overview: Geological Society, London, Memoirs, v. 35, p. 311–324.

Pick, T., and Tauxe, L., 1993, Geomagnetic palaeointensities during the Cretaceous normal superchron measured using submarine basaltic glass: Nature, v. 366, p. 238–242.

Porreca, M., Cifelli, F., Soriano, C., Giordano, G., Romano, C., Conticelli, S., and Mattei, M., 2014, Hyaloclastite fragmentation below the glass transition: An example from El Barronal submarine volcanic complex (Spain): Geology, v. 42, p. 87–90.

Riley, T.R., and Leat, P.T., 2021, Palmer Land and Graham Land volcanic groups (Antarctic Peninsula): Volcanology: Geological Society, London, Memoirs, v. 55.

Roberts, E.M., Lamanna, M.C., Clarke, J.A., Meng, J., Gorscak, E., Sertich, J.J., O'Connor, P.M., Claeson, K.M., and MacPhee, R.D., 2014, Stratigraphy and vertebrate paleoecology of Upper Cretaceous–lowest Paleogene strata on Vega Island, Antarctica: Palaeogeography, Palaeoclimatology, Palaeoecology, v. 402, p. 55–72.

Scharnberger, C., Scharon, L., and Craddock, C., 1982, Paleomagnetism of rocks from Graham Land and western Ellsworth Land, Antarctica: Antarctic Geoscience, C. Craddock, ed, p. 371–375.

Scher, H.D., Whittaker, J.M., Williams, S.E., Latimer, J.C., Kordesch, W.E., and Delaney, M.L., 2015, Onset of Antarctic Circumpolar Current 30 million years ago as Tasmanian Gateway aligned with westerlies: Nature, v. 523, p. 580–583.

Smellie, J.L., 2021a, Antarctic volcanism: Volcanology and palaeoenvironmental overview: Geological Society, London, Memoirs, v. 55.

Smellie, J.L., 2021b, Chapter 3.2a Bransfield Strait and James Ross Island: Volcanology: Geological Society, London, Memoirs, v. 55, doi:10.1144/M55-2018-58.

Smellie, J.L., 1987, Geochemistry and tectonic setting of alkaline volcanic rocks in the Antarctic Peninsula: A review: Journal of Volcanology and Geothermal Research, v. 32, p. 269–285.

Smellie, J.L., and Hole, M.J., 2021, Chapter 4.1a Antarctic Peninsula: Volcanology: Geological Society, London, Memoirs, v. 55, doi:10.1144/M55-2018-59.

Smellie, J.L., Johnson, J.S., McIntosh, W., Esser, R., Gudmundsson, M., Hambrey, M.J., and De Vries, B. van W., 2008, Six million years of glacial history recorded in volcanic lithofacies of the James Ross Island Volcanic Group, Antarctic Peninsula: Palaeogeography, Palaeoclimatology, Palaeoecology, v. 260, p. 122–148.

Smellie, J., Johnson, J., and Nelson, A., 2013, Geological Map of James Ross Island. 1. James Ross Island Volcanic Group: BAS GEOMAP 2 Series Sheet 5. British Antarctic Survey, Cambridge, UK, http://nora.nerc.ac.uk/506743/1/BAS%20GEOMAP%202%2C%20sheet%205%20-%20Geological%20map%20of%20James%20Ross%20Island%20-%20I%20-%20James%20Ross%20Island%20volcanic%20group.pdf.

Smellie, J.L., and Martin, A.P., 2021, Chapter 5.2a Erebus Volcanic Province: Volcanology: Geological Society, London, Memoirs, v. 55, doi:10.1144/M55-2018-62.

Sykes, M.A., 1988, The petrology and tectonic significance of the James Ross Island volcanic group, Antarctica. [PhD Thesis]: University of Nottingham.

Tauxe, L., Gans, P., and Mankinen, E.A., 2004, Paleomagnetism and 40Ar/39Ar ages from volcanics extruded during the Matuyama and Brunhes Chrons near McMurdo Sound, Antarctica: Geochemistry, Geophysics, Geosystems, v. 5, doi:https://doi.org/10.1029/2003GC000656.

Tauxe, L., Gee, J., Steiner, M., and Staudigel, H., 2013, Paleointensity results from the Jurassic: New constraints from submarine basaltic glasses of ODP Site 801C: Geochemistry, Geophysics, Geosystems, v. 14, p. 4718–4733.

Tauxe, L., and Kent, D.V., 2004, A simplified statistical model for the geomagnetic field and the detection of shallow bias in paleomagnetic inclinations: Was the ancient magnetic field dipolar? Timescales of the Paleomagnetic Field, Geophysical Monograph Series, v. 145, p. 101–115.

Tauxe, L., Mullender, T., and Pick, T., 1996, Potbellies, wasp-waists, and superparamagnetism in magnetic hysteresis: Journal of Geophysical Research: Solid Earth, v. 101, p. 571–583.

Tauxe, L., Pick, T., and Kok, Y., 1995, Relative paleointensity in sediments: A pseudo-Thellier approach: Geophysical Research Letters, v. 22, p. 2885–2888.

Tauxe, L., Shaar, R., Jonestrask, L., Swanson-Hysell, N., Minnett, R., Koppers, A., Constable, C., Jarboe, N., Gaastra, K., and Fairchild, L., 2016, PmagPy: Software package for paleomagnetic data analysis and a bridge to the Magnetics Information Consortium (MagIC) Database: Geochemistry, Geophysics, Geosystems, v. 17, p. 2450–2463, doi:10.1002/2016GC006307.

Tauxe, L., and Staudigel, H., 2004, Strength of the geomagnetic field in the Cretaceous Normal Superchron: New data from submarine basaltic glass of the Troodos Ophiolite: Geochemistry, Geophysics, Geosystems, v. 5, doi:10.1029/2003GC000635.

Thellier, E., and Thellier, O., 1959, Sur l'intensité du champ magnétique terrestre dans le passé historique et géologique: Ann. Geophys., v. 15, p. 285–376.

Tobin, T.S. et al., 2020, New evidence of a Campanian age for the Cretaceous fossil-bearing strata of Cape Marsh, Robertson Island, Antarctica: Cretaceous Research, v. 108, p. 104313.

Tobin, T.S., Ward, P.D., Steig, E.J., Olivero, E.B., Hilburn, I.A., Mitchell, R.N., Diamond, M.R., Raub, T.D., and Kirschvink, J.L., 2012, Extinction patterns, δ18 O trends, and magnetostratigraphy from a southern high-latitude Cretaceous–Paleogene section: Links with Deccan volcanism: Palaeogeography, Palaeoclimatology, Palaeoecology, v. 350–352, p. 180–188, doi:https://doi.org/10.1016/j.palaeo.2012.06.029.

Turnbull, G., 1959, Some palaeomagnetic measurements in Antarctica: Arctic, v. 12, p. 151–157.

Valencio, D., and Fourcade, N.H., 1969, Estudio paleomagnetico y petrografico de algunas formaciones cenozoicas de las islas shetland de sur: Antártico Argentino, v. 125, 25 p.

Vandamme, D., 1994, A new method to determine paleosecular variation: Physics of the Earth and Planetary Interiors, v. 85, p. 131–142.

Xu, S., and Dunlop, D.J., 1995, Toward a better understanding of the Lowrie-Fuller test: Journal of Geophysical Research: Solid Earth, v. 100, p. 22533–22542.

Yamagishi, H., and Dimroth, E., 1985, A comparison of Miocene and Archean rhyolite hyaloclastites: Evidence for a hot and fluid rhyolite lava: Journal of Volcanology and Geothermal Research, v. 23, p. 337–355.

Yamamoto, Y., and Yamaoka, R., 2018, Paleointensity study on the Holocene surface lavas on the island of Hawaii using the Tsunakawa–Shaw method: Frontiers in Earth Science, v. 6, p. 48.

Yu, Y., and Tauxe, L., 2005, Testing the IZZI protocol of geomagnetic field intensity determination: Geochemistry, Geophysics, Geosystems, v. 6.

Yu, Y., Tauxe, L., and Genevey, A., 2004, Toward an optimal geomagnetic field intensity determination technique: Geochemistry, Geophysics, Geosystems, v. 5.